
Measurements of
the Neutral Current $e^\pm p$ Cross Sections
Using Longitudinally Polarised Lepton
Beams
at HERA II

Dissertation der Fakultät für Physik
der
Ludwig-Maximilians-Universität München

vorgelegt von
Andriy Nikiforov

München, 18th January 2007

1. Gutachter: Prof. Dr. Christian Kiesling

2. Gutachter: Prof. Dr. Dorothee Schaile

Tag der mündlichen Prüfung: 15.03.07

Abstract

This thesis presents inclusive $e^\pm p$ single and double differential cross sections for neutral current deep inelastic scattering measured as functions of the four-momentum transfer squared Q^2 and the Bjorken variable x in interactions of longitudinally polarised leptons with unpolarised protons using the H1 detector at HERA II. An overview of the phenomenology of deep inelastic scattering is given and the experimental apparatus as well as the measurement and analysis procedures are described. The analysis is based on e^+p data taken in 2003-04 and e^-p data taken in 2005 at a centre-of-mass energy of $\sqrt{s} = 318$ GeV, with integrated luminosities of 47.6 pb^{-1} and 98.4 pb^{-1} for the e^+p and e^-p samples, respectively. The cross sections are measured in the range of $200 < Q^2 < 20\,000 \text{ GeV}^2$ and $0.0032 < x < 0.65$. The measurements are used to study polarisation effects in neutral current interactions and to determine the structure function $x\tilde{F}_3$. The new HERA II data are combined together with previously published data from HERA I to determine the structure function $x\tilde{F}_3$ with improved precision. Furthermore, this measurement is combined with the corresponding ZEUS measurement to provide the most accurate measurement of the interference structure function $xF_3^{\gamma Z}$, which is sensitive to the valence quark distributions down to low values of x . The data on polarised cross section asymmetries A^\pm are also combined with the ZEUS data. This leads to the first observation of parity violation in neutral current $e^\pm p$ scattering at distances down to 10^{-18} m. The data are well described by the Standard Model predictions.

Kurzfassung

Diese Doktorarbeit stellt einfach- und doppelt-differentielle inklusive $e^\pm p$ Wirkungsquerschnitte für den neutralen Strom in tief-inelastischer Streuung als Funktion des quadrierten Viererimpulsübertrags Q^2 und der Bjorken-Variable x vor, die bei der Wechselwirkung von longitudinal polarisierten Leptonen mit unpolarisierten Protonen mit dem H1-Detektor bei HERA II gemessen wurden. Es wird ein Überblick über die Phänomenologie der tief-inelastischen Streuung gegeben und der experimentelle Aufbau und das Vorgehen bei der Messung und der Analyse beschrieben. Die Analyse basiert auf e^+p -Daten aus Jahren 2003 und 2004, sowie auf e^-p -Daten, die im Jahr 2005 bei einer Schwerpunktsenergie von $\sqrt{s} = 318$ GeV genommen wurden. Dabei betrug die integrierte Luminosität 47.6 pb^{-1} beziehungsweise 98.6 pb^{-1} für die e^+p - und e^-p -Datensätze. Der kinematische Bereich der Analyse wird durch $200 < Q^2 < 20\,000 \text{ GeV}^2$ und $0.0032 < x < 0.65$ definiert. Mithilfe der Messungen werden Polarisierungseffekte bei Wechselwirkungen des neutralen Stroms untersucht und die Strukturfunktionen $x\tilde{F}_3$ bestimmt. Die HERA II-Daten werden zusammen mit zuvor veröffentlichten HERA I-Daten benutzt, um die Strukturfunktion $x\tilde{F}_3$ mit erhöhter Genauigkeit zu bestimmen. Zudem wird die Messung mit der ZEUS-Messung kombiniert, um somit die bestmögliche Messung der bis hin zu niedrigen Werten von x auf die Valenzquarkverteilung sensitiven Interferenzstrukturfunktion $xF_3^{\gamma Z}$ zu erhalten. Die Daten betreffend die Asymmetrie polarisierter Wirkungsquerschnitte A^\pm , ebenfalls kombiniert mit den entsprechenden ZEUS-Daten, führen zur ersten Beobachtung von Paritätsverletzung bei der Streuung durch neutralen Strom in $e^\pm p$ -Streuung bei Abständen von 10^{-18} m. Die Daten werden gut durch das Standardmodell beschrieben.

Contents

1	Introduction	1
2	Theoretical Framework	5
2.1	Deep Inelastic Scattering	5
2.1.1	Kinematics of electron-proton scattering	6
2.1.2	DIS Cross Sections	7
2.2	Bjorken Scaling	9
2.3	The Quark Parton Model	9
2.4	Quantum Chromodynamics	11
2.4.1	Running Coupling Constant and Asymptotic Freedom	11
2.4.2	Scaling Violations in QCD	12
2.4.3	QCD Hard Scattering Factorisation	15
2.4.4	The DGLAP Evolution Equations	16
2.4.5	Longitudinal Structure Function in QCD	18
2.5	The Neutral Current Cross Section	19
2.5.1	The Born Cross Section and Structure Functions	19
2.5.2	The Reduced Cross Section	21
2.5.3	The Single Differential Cross Sections	21
2.5.4	Structure Functions in the Quark Parton Model	21
2.6	The Charged Current Cross Section	22
2.7	Electroweak Physics with Polarised e^\pm Beams	24
2.8	Radiative corrections	26
3	HERA and the H1 Detector	29
3.1	HERA Accelerator	29
3.2	The Luminosity Upgrade Project at HERA	30
3.3	Polarisation at HERA	32
3.3.1	The Sokolov-Ternov Effect in a Constant Magnetic Field	32
3.3.2	Spin Rotators and Longitudinal Polarisation at HERA	33
3.3.3	Depolarisation Effects	34
3.3.4	Polarisation Measurement	35
3.4	Backgrounds After the HERA Upgrade	38
3.5	H1 Detector	40
3.6	Calorimetry	42
3.6.1	Liquid Argon Calorimeter	44
3.6.2	The “Spaghetti” Calorimeter	47
3.7	Tracking	49
3.7.1	Central Tracking Detector	51
3.7.2	The Forward Tracking Detector	54
3.8	The Muon System	55

3.9	Time-of-Flight Counters	56
3.10	Luminosity System	57
3.11	Trigger System	59
3.11.1	Trigger Level One	59
3.11.2	Trigger Level Two	65
3.11.3	Trigger Level Three	65
3.11.4	L45 Processing	66
3.11.5	The NC Stubtriggers	66
3.12	Offline Analysis and H1OO	67
4	Monte Carlo Simulation	71
4.1	Generation of DIS Events	71
4.2	Generation of Background Events	72
4.3	Simulation of the H1 Detector	74
5	Kinematics Reconstruction and Coverage of the Phase Space	75
5.1	Reconstruction of Kinematic Variables	75
5.2	Coverage of the Kinematic Phase Space	79
6	Data Treatment	81
6.1	Electron Identification	81
6.2	Electron Finding Efficiency	83
6.3	Interaction Vertex	84
6.3.1	Vertex Re-weighting in MC	85
6.4	Vertex and Track Link Requirements	86
6.5	Electron Angle Measurement	91
6.5.1	Track Extrapolation	91
6.5.2	Alignment of the LAr Calorimeter	92
6.5.3	Azimuthal and Polar Electron Angles	94
6.6	Electron Energy Measurement	96
6.6.1	Electron Energy Calibration	97
6.6.2	Electron Energy Resolution	101
6.7	Hadronic Energy Measurement	101
6.7.1	The HADROO2 Algorithm	102
6.7.2	Calibration of Hadronic Energy	105
6.8	Determination of the Trigger Efficiency	107
6.8.1	<i>LAr_electron_1</i> TE Efficiency	107
6.8.2	Timing Condition	110
6.8.3	Veto Conditions	110
6.8.4	Trigger Efficiency	112
6.9	Fiducial Volume Definition	112
6.10	Rejection of Non- <i>ep</i> Background	112
7	Selection of NC Events	117
7.1	Run Selection	117
7.1.1	Polarisation Selection	117
7.2	Event Yield	119
7.3	Neutral Current Selection Criteria	120
7.4	Neutral Current Data Samples	120

8	Cross Section Measurement Procedure	125
8.1	Bin Definitions in $x - Q^2$ Plane	125
8.2	Purity, Stability and Acceptance	126
8.3	Extraction of Cross Section	128
8.4	Systematic Uncertainties	130
8.5	Q^2 Bins Combination of $e^\pm p$ Cross Sections for Determination of $x\tilde{F}_3$	131
8.6	Combination of Cross Sections From Different Measurements	134
9	NC Cross Section Results	135
9.1	The e^+p and e^-p Double Differential Cross Sections $d^2\sigma/dxdQ^2$. . .	135
9.2	The e^+p and e^-p Single Differential Cross Sections $d\sigma/dQ^2$	139
9.3	Electroweak Effects at High Q^2	139
9.4	Polarisation Asymmetry	145
9.5	Structure Function $x\tilde{F}_3$	149
10	Summary and Outlook	155
10.1	Summary of the Analysis	155
10.2	Outlook	156
A	Trigger Fiducial Cuts	159
B	Events in the H1 Detector	161
C	Tables of Results	163

Chapter 1

Introduction

The ultimate goal of high energy physics is to understand and describe the structure of matter and the underlying interactions. This view was already expressed by Newton in the introduction to his book “Optics”:

Now the smallest particles of matter cohere by the strongest attraction, and compose bigger particles of weaker virtue; and many of these may cohere and compose bigger particles whose virtue is still weaker, and so on for diverse successions, until the progression ends in the biggest particles on which the operations in chemistry, and the colors of natural bodies depend, and which by cohering compose bodies of a sensible magnitude. There are therefore agents in nature able to make the particles of bodies stick together by very strong attractions. And it is the business of experimental philosophy to find them out.

The fundamental constituents of matter as we know them today, leptons and quarks, are fermions arranged into generations characterised by lepton numbers and quark flavour types, respectively. Leptons are free particles that can be detected. Quarks, on the other hand, only exist in bound states – hadrons. The existence of quarks can be inferred from experimental measurements of the properties of particle interactions and hadron production.

In our present knowledge there are three generations of leptons: the electron (e) and the electron neutrino (ν_e), the muon (μ) and the muon neutrino (ν_μ), and the tau (τ) and the tau neutrino (ν_τ). The quarks likewise fall into three paired groups: down (d) and up (u), strange (s) and charm (c), bottom (b) and top (t).

The fermions interact with each other through the exchange of *gauge bosons*. Four types of interaction are known in Nature: these are the gravitational, electromagnetic, weak and strong forces. Gravitation has little or no bearing in the realm of particle physics, since the gravitation interaction is by far the weakest of the four. The electromagnetic interaction is mediated by the photon. The weak interaction involves the exchange of heavy gauge bosons, Z^0 , W^+ and W^- . The strong interaction is mediated by eight gluons g . Each type of the interactions is characterised by a charge (electric, weak or strong charge). Neutrinos, which carry no electric charge, interact only weakly. Charged leptons take part in weak and electromagnetic interactions. Only quarks take part in all known interactions of the micro-world.

The theoretical framework which allows us to describe all particles and their inter-

actions observed to date is based on gauge theories. The weak and electromagnetic interactions are unified within the so-called *electroweak theory*. The strong interactions are embedded in the framework of *Quantum Chromodynamics*. The combination of the two constitutes what is generally known as the Standard Model of particles and interactions.

The advantage of lepton-nucleon collisions in studying the structure of matter lies in the fact that leptons are point-like objects and their electroweak interactions are well understood. The point-like, partonic substructure of the nucleon was first firmly established (in the late sixties) in the pioneering SLAC experiment [1, 2] in which the spectrum of electrons scattered off a nucleon target was measured. This experiment was very similar in its essence to the famous Rutherford experiment [3] which established the structure of atoms. In a scattering in which an electron of initial four momentum k emerges with four momentum k' , the exchanged virtual photon has a mass $q^2 = (k - k')^2 = -Q^2$ and correspondingly a Compton wavelength of $\hbar/\sqrt{Q^2}$. Thus for different values of Q^2 the interaction is sensitive to structures at different scales.

In the following years various experiments of lepton nucleon deep inelastic scattering [30–34] (DIS) have played a significant role in understanding the partonic structure of the proton and constraining the parameters of the electroweak theory. Since the start of the operation of the electron-proton collider HERA at DESY, Hamburg, the two experiments H1 and ZEUS made possible to probe the structure of the proton at much higher energies and to investigate electroweak phenomena in the DIS interactions.

In this thesis a measurement of the high Q^2 neutral current cross section for the scattering of longitudinally polarised electrons (positrons) on unpolarised protons, $\sigma(e^\pm p \rightarrow e^\pm X)$, is presented. It is based on data collected by the H1 detector during the years 2003-2005. The data consist of samples taken with left-handed and right-handed polarised electrons and positrons. Deep inelastic neutral current scattering at very high Q^2 is sensitive to electroweak effects mainly due to the interference of photon and Z boson exchange which dominates over pure Z exchange effects in most of the kinematic range covered at HERA. Access to electroweak effects is enabled by measuring charge and polarisation cross section differences by which the pure photon exchange part is removed. The charge asymmetry accesses the valence quark distributions at high Q^2 and is sensitive to the axial-vector weak quark couplings to the Z boson and to the sign of the electric quark charges. The polarisation asymmetry measures the product of vector and axial-vector couplings and at HERA is sensitive to parity violation at spatial dimensions down to 10^{-18} m.

The thesis is organised as follows:

- Chapter 2 presents a theoretical basis of the deep inelastic ep scattering. The cross sections of neutral current scattering and their dependence on the proton structure functions and on the electroweak parameters are discussed.
- In the third chapter, the HERA collider and the H1 experiment are described with particular attention paid to the components used in this analysis.

-
- The fourth and fifth chapter are devoted to Monte Carlo simulation and the reconstruction of the event kinematics, respectively.
 - Chapter 6 represents the main part of the data analysis and explains the event identification and reconstruction. Discussion on detailed understanding of detector calibration and efficiency determination, needed for precise measurement of $e^\pm p$ interactions, is presented.
 - Chapter 7 describes the selection of the neutral current DIS events and summarises the data sample used for the cross section measurement.
 - Chapter 8 discusses the procedure used to measure the cross sections. It describes the relevant systematic uncertainties and their implications on the cross section measurement.
 - Chapter 9 presents results of the cross section, cross section polarisation asymmetry and $x\tilde{F}_3$ structure function measurements.
 - Finally, results of this thesis are summarised in chapter 10.

Chapter 2

Theoretical Framework

2.1 Deep Inelastic Scattering

The term *deep inelastic scattering* (DIS) denotes the process in which a lepton, either charged (e, μ) or neutral (ν_e, ν_μ), scatters off a nucleon (p, n), involving a large momentum transfer (four momentum transfer squared, Q^2 , above few GeV^2).

At HERA the electron or positron interacts with a proton exchanging a space-like virtual boson. According to the type of exchanged boson the DIS processes are classified as:

- **neutral current** process (NC DIS) $ep \rightarrow eX^1$, mediated by the exchange of neutral gauge bosons, i.e. the photon and the Z^0 boson. At virtuality $Q^2 \ll M_Z^2$, where M_Z is the mass of the Z^0 boson, the cross section is dominated by single-photon exchange since the Z^0 boson exchange is suppressed by its large mass in the propagator.
- **charged current** process (CC DIS) $ep \rightarrow \nu_e X$, mediated by the exchange of the charged gauge bosons W^\pm .

If the hadrons produced in the final state X are not differentiated, the type of reaction is called *inclusive*.

Denoting k and k' as the four vectors of the initial and final electron, P as the four vector the incoming proton, (see figure 2.1), the kinematic variables describing the lepton nucleon scattering are

$$Q^2 = -q^2 = -(k - k')^2, \quad (2.1)$$

$$s = (P + k)^2, \quad (2.2)$$

$$W^2 = (P + q)^2, \quad (2.3)$$

$$x = \frac{Q^2}{2P \cdot q}, \quad (2.4)$$

$$y = \frac{q \cdot P}{k \cdot P}, \quad (2.5)$$

$$\nu = \frac{q \cdot P}{m_p}. \quad (2.6)$$

¹The label “ X ” denotes all possible hadronic final states.

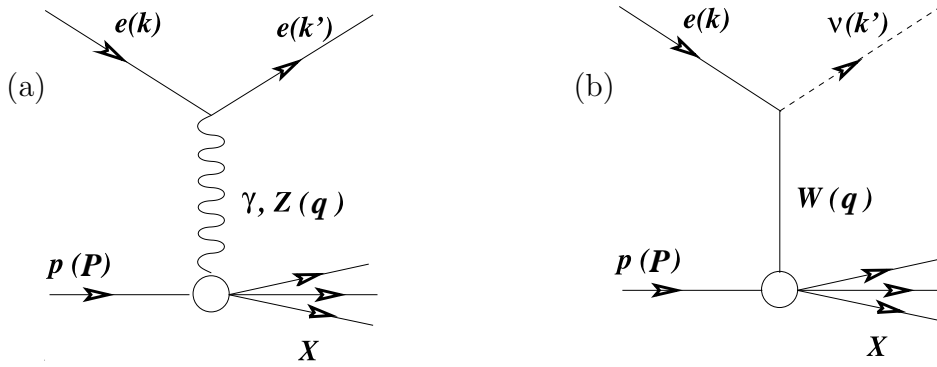


Figure 2.1: Diagrams of electron proton scattering via photon or Z exchange for neutral current interactions (a) and W exchange for charged current interactions (b). The four-momentum vectors of the particles are given in parentheses.

The variables s and W^2 are the centre-of-mass energy squared of the electron-proton and intermediate boson-proton systems, respectively. The negative square of the four momentum transfer (the mass squared of the virtual boson), $Q^2 > 0$, determines the hardness, or in other words, the resolving power of the interaction. The exchanged boson plays the role of a “partonometer” with a resolution Δb ,

$$\Delta b \sim \frac{\hbar c}{\sqrt{Q^2}} = \frac{0.197}{\sqrt{Q^2 [\text{GeV}^2]}} \text{ fm.} \quad (2.7)$$

The meaning of ν is best understood in the rest frame of the target, in which ν is just the energy of the intermediate boson ($\nu = E - E'$). The Lorentz invariant variable y corresponds to the fraction of the lepton’s energy lost in the nucleon rest frame ($y = \frac{\nu}{E}$). It measures the inelasticity of the interaction and its distribution reflects the spin structure of the interaction. The variable x is a dimensionless variable introduced by Bjorken [4].

2.1.1 Kinematics of electron-proton scattering

The variables used in describing the properties of inclusive electron-proton scattering are defined by equations (2.1)-(2.6). Here, their meaning is discussed in more detail, assuming that the masses of the incoming and scattered leptons are negligible.

The variable $s = (P + k)^2 \simeq m_p^2 + 2P \cdot k$ is the square of the ep centre-of-mass energy. The energy variable W , defined as the centre-of-mass energy of the virtual boson-proton system, corresponds to hadronic system recoiling against the scattered lepton,

$$W^2 = (P + q)^2 = m_p^2 - Q^2 + 2P \cdot q = ys - Q^2 + m_p^2(1 - y). \quad (2.8)$$

The Lorentz invariant variable y can be expressed as:

$$y = 1 - \frac{E'}{E} \sin^2 \frac{\theta}{2}, \quad (2.9)$$

where E, E' are the energies of the incoming and scattered leptons and θ is the angle between them. The most general limits on y are:

$$0 \leq y \leq 1. \quad (2.10)$$

The variable y is a measure of the fraction of the energy transferred from the electron to the hadronic system. The limits on x can be readily deduced from the following:

$$x = \frac{Q^2}{2P \cdot q} = \frac{Q^2}{W^2 + Q^2 - m_p^2}, \quad (2.11)$$

where the relation (2.8) was used. Since $Q^2 \geq 0$ and W^2 cannot be smaller than m_p^2 the upper limit on x is one. The lower limit is determined by Q^2 and the maximum W^2 available in the interaction. For $s \rightarrow \infty$ the minimum accessible x approaches zero. Thus,

$$0 \leq x \leq 1. \quad (2.12)$$

The interpretation of x is easiest in the Quark Parton Model [5] (QPM) language. Define z as the fraction of the proton momentum carried by the struck quark and p' as the four momentum of the outgoing quark. If we assume that the quark masses are zero as it considered in QPM (i.e. $(zP)^2 = p'^2 = 0$) then

$$p'^2 = (zP + q)^2 = 2zP \cdot q - Q^2 = 0. \quad (2.13)$$

It can be readily seen that $z = x$. Thus, in QPM x is the fraction of the proton momentum carried by the struck massless quark. Note also that for $Q^2 \ll W^2$,

$$x \simeq \frac{Q^2}{W^2}, \quad (2.14)$$

and for fixed values of Q^2 , high W corresponds to low x .

The value of Q^2 depends on kinematics of the scattered lepton and is given by

$$Q^2 = 2EE'(1 - \cos \theta), \quad (2.15)$$

where θ is the angle between the initial and scattered lepton. This expression is valid in all frames of reference. The larger the scattering angle and the larger the energy of the scattered lepton, the larger the Q^2 . The maximum Q^2 is limited by s ,

$$Q^2 = xy(s - m_p^2), \quad (2.16)$$

and occurs when both x and y tend to one. For a given Q^2 the lowest x is achieved when $y = 1$ and the lowest y when $x = 1$. Thus, kinematically the small values of x are associated with large values of y and vice versa.

2.1.2 DIS Cross Sections

The cross section for the scattering of polarised leptons on protons can be expressed in terms of the products of leptonic and hadronic tensors associated with the coupling of the exchanged bosons at the upper and lower vertices in figure 2.1 [6].

$$\frac{d^2\sigma}{dxdy} = \frac{2\pi y\alpha^2}{Q^4} \sum_j \eta_j L_j^{\mu\nu} W_{\mu\nu}^j. \quad (2.17)$$

For neutral current process, the summation is over $j = \gamma, Z$ and γZ representing photon and Z exchange and the interference between them, whereas for charged current interactions there is only W exchange, $j = W$. $L_{\mu\nu}$ is the lepton tensor associated with the coupling of the exchange boson to the leptons. For incoming leptons of charge $e = \pm 1$ and helicity $\lambda = \pm 1$ [7],

$$\begin{aligned} L_{\mu\nu}^\gamma &= 2(k_\mu k'_\nu + k'_\mu k_\nu - k \cdot k' g_{\mu\nu} - i\lambda \varepsilon_{\mu\nu\alpha\beta} k^\alpha k'^\beta), \\ L_{\mu\nu}^{\gamma Z} &= (v_e + e\lambda a_e) L_{\mu\nu}^\gamma, \\ L_{\mu\nu}^Z &= (v_e + e\lambda a_e)^2 L_{\mu\nu}^\gamma, \\ L_{\mu\nu}^W &= (1 + e\lambda)^2 L_{\mu\nu}^\gamma, \end{aligned} \quad (2.18)$$

where $v_e = -\frac{1}{2} - 2e \sin^2 \theta_W$, $a_e = -\frac{1}{2}$.

The factors η_j in equation (2.17) denote the ratios of the corresponding propagators and couplings to the photon propagator and coupling squared

$$\begin{aligned} \eta_\gamma &= 1; \quad \eta_{\gamma Z} = \left(\frac{G_F M_Z^2}{2\sqrt{2}\pi\alpha} \right) \left(\frac{Q^2}{Q^2 + M_Z^2} \right); \quad \eta_Z = \eta_{\gamma Z}^2; \\ \eta_W &= \frac{1}{2} \left(\frac{G_F M_W^2}{4\pi\alpha} \frac{Q^2}{Q^2 + M_W^2} \right)^2, \end{aligned} \quad (2.19)$$

where G_F is the Fermi coupling constant, α is fine structure constant and M_W is the W boson mass.

The hadronic tensor for an a priori unknown structure of the proton cannot be calculated from first principles. It is therefore presented in terms of structure functions, the four-momenta at the hadronic vertex, P and q , and the metric tensor $g_{\mu\nu}$ [7]:

$$W_{\mu\nu} = (-g_{\mu\nu} + \frac{q_\mu q_\nu}{q^2}) F_1(x, Q^2) + \frac{\hat{P}_\mu \hat{P}_\nu}{P \cdot q} F_2(x, Q^2) - i\varepsilon_{\mu\nu\alpha\beta} \frac{q^\alpha P^\beta}{2P \cdot q} F_3(x, Q^2), \quad (2.20)$$

where

$$\hat{P}_\mu = P_\mu - \frac{P \cdot q}{q^2} q_\mu. \quad (2.21)$$

The cross sections for neutral and charged current deep inelastic scattering can be written in terms of the structure functions in the generic form [7]

$$\frac{d^2\sigma^i}{dxdy} = A^i \left\{ \left(1 - y - \frac{x^2 y^2 M^2}{Q^2}\right) F_2^i + y^2 x F_1^i \mp \left(y - \frac{y^2}{2}\right) x F_3^i \right\}, \quad (2.22)$$

where $i = \text{NC}, \text{CC}$ corresponds to neutral current ($ep \rightarrow eX$) or charged current ($ep \rightarrow \nu X$) processes, respectively. A^i is a process dependent constant. For the CC process A^{CC} contains the polarisation dependence of the cross section, while for NC the polarisation dependence enters via structure functions. In the last term, the “−” sign is taken for an incoming e^+ and the “+” sign for an incoming e^- .

2.2 Bjorken Scaling

The modern history of the DIS experiments started in the early sixties when the first results on the scattering of high energy electrons ($7 < E_e < 17$ GeV) off nuclear targets were obtained at the Stanford Linear Accelerator Centre (SLAC) [1,2]. The remarkable outcome of these experiments was that the structure function F_2 , measured at fixed $x \simeq 0.25$, showed very little dependence on Q^2 , but depends only on the variable x (see figure 2.2). This kind of behaviour was termed scale invariance or *scaling* and was predicted by Bjorken [4]. The explanation of this phenomenon has been given within the Quark Parton Model.

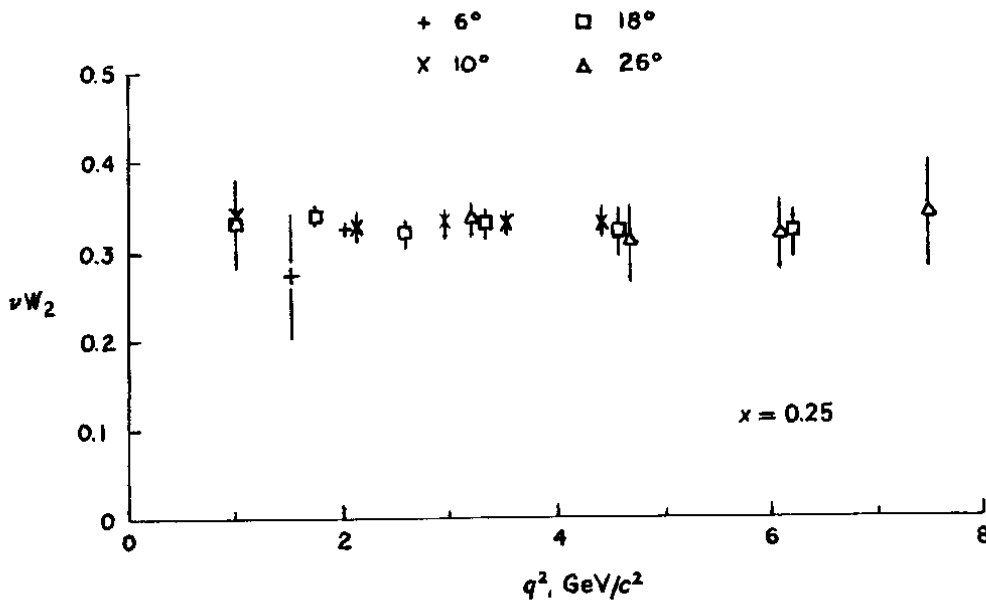


Figure 2.2: Observation of scaling: independence of the structure function $\nu W_2 = F_2$ of Q^2 . The Bjorken variable x is kept fixed, $x = 0.25$.

Scaling, the Q^2 independence of the structure function F_2 , suggested the existence of pointlike scattering centres in the proton. That the proton itself is not a pointlike Dirac particle was already known since the 1930s from the measurement of the anomalous magnetic moment of the proton [8], and later in the 1950s substantiated by Hofstadter *et al.* [9] in the pioneering electron proton scattering experiment.

2.3 The Quark Parton Model

The Quark Parton Model is the theoretical model in which hadrons, such as the proton, are made up of point-like “partons”. In this model, the cross section of deep inelastic ep scattering is expressed as the incoherent sum of elementary elastic electron-parton scattering processes. The partons are associated with either constituent or sea quarks [10,11].

The incoherence of these elastic scattering processes, i.e. neglecting the parton-parton interactions and treating them as quasi-free, is justified if the calculations are carried

out in a frame where the proton moves with infinite momentum. In this infinite momentum frame [4], the electron parton scattering process can be shown to take place on a much shorter time scale as the parton-parton interactions.

A parton carries a certain fraction of the proton's momentum which is identified with the Bjorken scaling variable x . The number of partons dn of a certain flavour i encountered in the interval between x and $x + dx$ is parameterised by a *parton distribution function* (PDF) $q_i(x)$: $dn = q(x)dx$. The momentum fraction dp of the protons momentum carried by these partons is then given by $dp = xq_i(x)dx$.

The proton consists of two u and one d valence quarks, therefore the counting rules

$$\int_0^1 dx(u(x) - \bar{u}(x)) = 2 \quad \int_0^1 dx(d(x) - \bar{d}(x)) = 1 \quad (2.23)$$

must be satisfied. Here, $u(x)$ ($\bar{u}(x)$) and $d(x)$ ($\bar{d}(x)$) are parton distribution functions of the (anti-)quark u (\bar{u}) and d (\bar{d}), respectively.

The deep inelastic scattering cross section, $\sigma_{ep \rightarrow eX}$, can be written as a convolution of PDFs with the (calculable) elastic electron parton cross sections $\sigma_{eq_i \rightarrow eq_i}$ weighted by the electric charge squared, e_i^2 , of the parton and summed over all charged parton flavours i :

$$\left(\frac{d\sigma}{dx dQ^2} \right)_{ep \rightarrow eX} = \sum_i \int dx e_i^2 q_i(x) \left(\frac{d\sigma}{dx dQ^2} \right)_{eq_i \rightarrow eq_i}. \quad (2.24)$$

For the spin 1/2 partons the Callan-Gross [12] relation holds:

$$2xF_1(x) = F_2(x), \quad (2.25)$$

and for pure electromagnetic processes the structure functions F_1 and F_2 can be expressed then as:

$$F_1(x) = \frac{1}{2} \sum_i e_i^2 [q_i(x) + \bar{q}_i(x)], \quad F_2(x) = \sum_i e_i^2 x [q_i(x) + \bar{q}_i(x)]. \quad (2.26)$$

The difference $F_L = F_2 - 2xF_1$ is referred to as the *longitudinal structure function*. It is zero in QPM, which means that partons cannot interact with longitudinally polarised photons [13].

Although the experimental observation at SLAC of the Bjorken scaling behaviour and of the Callan-Gross relation in the late 1960's confirmed the Quark Parton Model, contradictions soon arose. If the proton would be solely constituted of charged quarks, the integration of the parton densities over all partons inside the proton and over the whole kinematic range of x should be equal to unity:

$$\int_0^1 dx x \sum_i q_i(x) = 1 \quad (2.27)$$

As the experimental value turned out to be approximately one half [14], it was concluded that half of the proton momentum was carried by neutral particles. These particles were identified as *gluons* and directly observed in 3-jet events at PETRA in 1979 [15]. In addition, the Quark Parton Model does not explain other experimental results like logarithmic violation of the scaling behaviour, non-zero longitudinal structure function, quark confinement, etc. These effects were successfully explained within the framework of *Quantum Chromodynamics*.

2.4 Quantum Chromodynamics

The field theory of strong interaction, *Quantum Chromodynamics* (QCD) [16] is a local non-Abelian gauge theory, based on the $SU(3)$ gauge group. QCD is a phenomenologically richer theory than QPM, and has the following characteristics:

- The charge of the strong interaction is a new quantum number called *colour* with three degrees of freedom (red (r), green (g) and blue (b) and the corresponding anti-colours.) Each quark carries, besides its electric and weak charge, a colour charge.
- The gauge bosons of the strong interactions are eight massless gluons with no electric nor weak charge. As a consequence of the non-Abelian nature of QCD gluons carry colour charges and are therefore able to self-interact, producing three-gluon as well as four-gluon vertices.
- The strong interaction is characterised by a strong coupling constant α_s .
- All physically observable states are colourless, i.e. they are colour singlets, and furthermore $q\bar{q}$ and qqq states form mesons and baryons. Quarks and gluons carry colour charge and therefore do not appear as free particles but only in colourless hadronic bound states. This behaviour is known as “*colour-confinement*”.

2.4.1 Running Coupling Constant and Asymptotic Freedom

In gauge field theory, the strong interaction is mediated by mediator particles which could, as neutral partons, account for the observed missing momentum in the proton. However, the field theoretical description of deep inelastic scattering was long troubled by the fact that the QPM assumption of quasi-free partons in the proton implied that the coupling strength of the interaction be small at short-distances (high momentum transfer regime) and large at long distances. This leads to the confinement of quarks in hadrons. To account for these changes, the coupling strength should vary, “running”, with the momentum transfer (*running coupling constant*).



Figure 2.3: Loop diagrams.

A running coupling constant is indeed expected in quantum field theories. The Q^2 dependence arises from the fact that in higher orders of the theory, infinities arise for example due to fermion loop diagrams in the boson propagator as depicted in figure 2.3 (right). These infinities are removed by a renormalisation procedure which introduces a renormalisation scale μ^2 at which the *ultraviolet* loop divergences are subtracted out. This leads to a dependence of the renormalised coupling constant α on the renormalisation scale μ^2 .

However, physical observables $R(Q^2/\mu^2, \alpha_s)$ when computed up to all orders of perturbation theory should not depend on an arbitrary renormalisation scale. Any explicit dependence of R on μ^2 should therefore be cancelled by the dependence of α_s on μ^2 . This is mathematically expressed by the following equation:

$$\mu^2 \frac{\partial R}{\partial \mu^2} + \mu^2 \frac{\partial \alpha_s}{\partial \mu^2} \frac{\partial R}{\partial \alpha_s} = 0. \quad (2.28)$$

This is called the *renormalisation group equation*. If physical quantities are computed to fixed order, residual dependences of the observables will remain due to missing higher order diagrams. This residual scale dependence must be estimated as part of the theoretical uncertainty for an observable.

The dependence of the strong coupling constant α_s on the renormalisation scale μ^2 can be computed by observing that the partial derivative $\partial\alpha_s/\partial\mu^2$ of equation 2.28 can itself be expressed in a power series of $\alpha_s(\mu^2)$ and so-called β functions which are calculable in QCD:

$$\mu^2 \frac{\partial\alpha_s}{\partial\mu^2} = \alpha_s \beta(\alpha_s) = -\beta_0 \frac{\alpha_s^2}{4\pi} - \beta_1 \frac{\alpha_s^3}{16\pi^2} + \dots \quad (2.29)$$

with

$$\beta_0 = (33 - 2n_f)/3 \quad \beta_1 = 102 - \frac{38}{3}n_f, \quad (2.30)$$

where β_0 and β_1 are the first coefficients occurring in the expansion and n_f denoting the number of active flavours, i.e. the quark flavours with masses smaller than μ .

In the one-loop approximation, i.e. regarding only the term with β_0 , the coupling constant α_s can be written in terms of the renormalisation scale as

$$\alpha_s(\mu^2) = \frac{\alpha_s(\mu_0^2)}{1 + b \cdot \alpha_s(\mu_0^2) \ln(\mu^2/\mu_0^2)}, \quad (2.31)$$

where $b = \beta_0/4\pi = (33 - 2n_f)/12\pi$ and μ_0^2 being a suitably chosen reference scale.

At small distance, large energy scale ($\mu^2 \rightarrow \infty$), the coupling between quarks and gluons becomes small, $\alpha_s \rightarrow 0$, and the quarks inside a proton can be treated as quasi-free particles. This behaviour is called “*asymptotic freedom*”. This property is unique to non-Abelian gauge theories. For $\mu^2 \rightarrow 0$, the coupling is seen to diverge. This can be viewed as a reason for the confinement of quarks and gluons inside hadrons. However, confinement is not completely yet understood since the increase of the coupling constant prohibits the use of perturbation theory of the region of μ^2 below a few GeV².

2.4.2 Scaling Violations in QCD

In figure 2.4 the proton structure function $F_2(x, Q^2)$ is shown as a function of Q^2 for various fixed values of x . The scaling behaviour, expected in the naive QPM, is observed only for values of Bjorken x about 0.13. In all other x -regions F_2 depends approximately logarithmically on Q^2 .

The rise of the proton structure functions with increasing Q^2 at low x and the decrease at high x are a feature of the gluon interactions in Quantum Chromodynamics: the quarks inside the proton continuously emit gluons, which may then fluctuate into virtual quark anti-quark pairs. These virtual quark anti-quark pairs are termed “*sea quarks*” and are distinguished from the original quark content of the proton in the static Quark Parton Model, the “*valence quarks*”.

The extent to which the virtual quarks contribute to the electron-proton scattering cross-section depends on the resolution parameter Q^2 with which the proton is

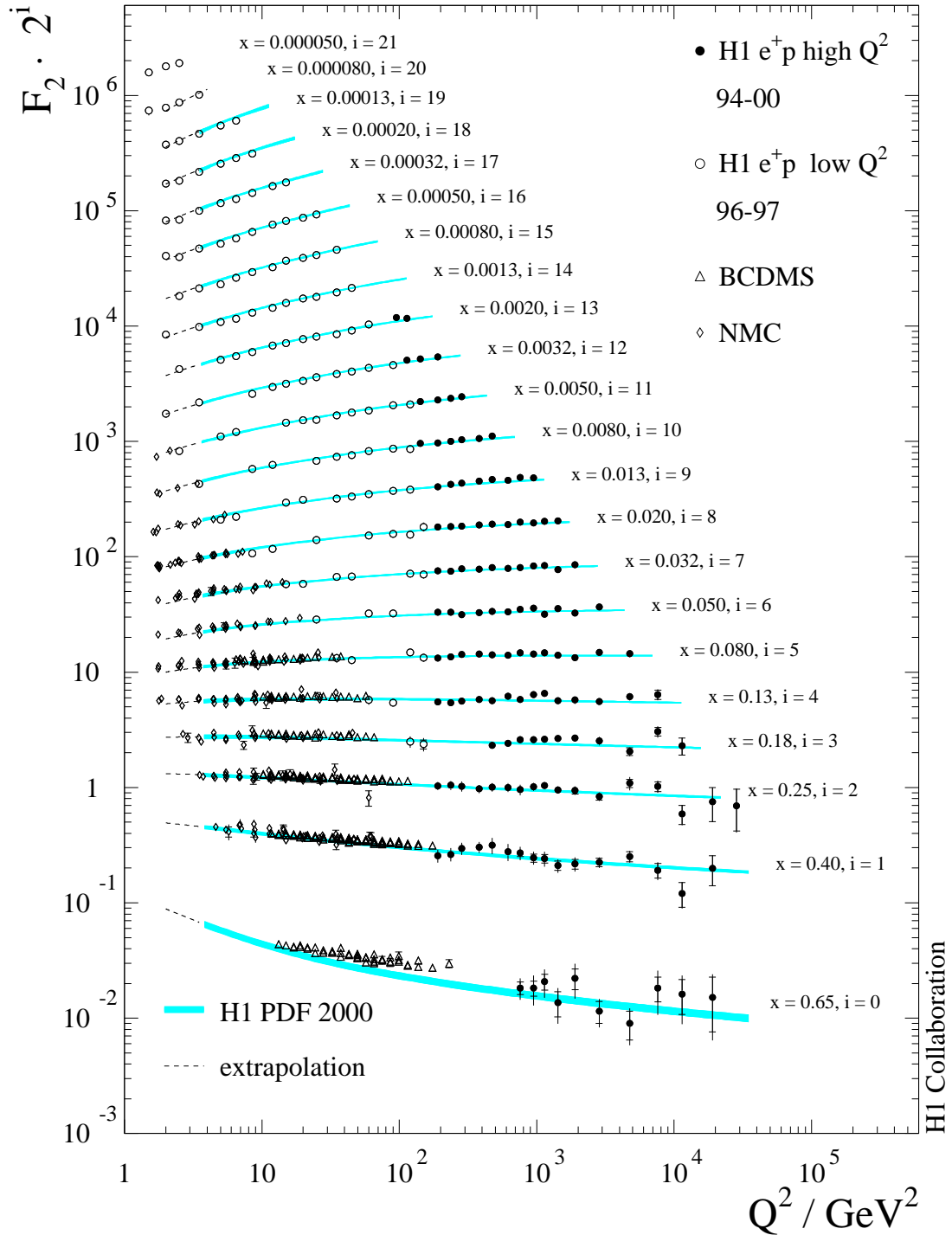


Figure 2.4: Measurement of the proton structure function $F_2(x, Q^2)$ (solid points) as a function of Q^2 at fixed x by H1 and fixed target experiments BCDMS and NMC. The result are compared with the corresponding Standard Model expectation determined from the H1 PDF 2000 fit [85] (error bands).

Parton Densities and Scale

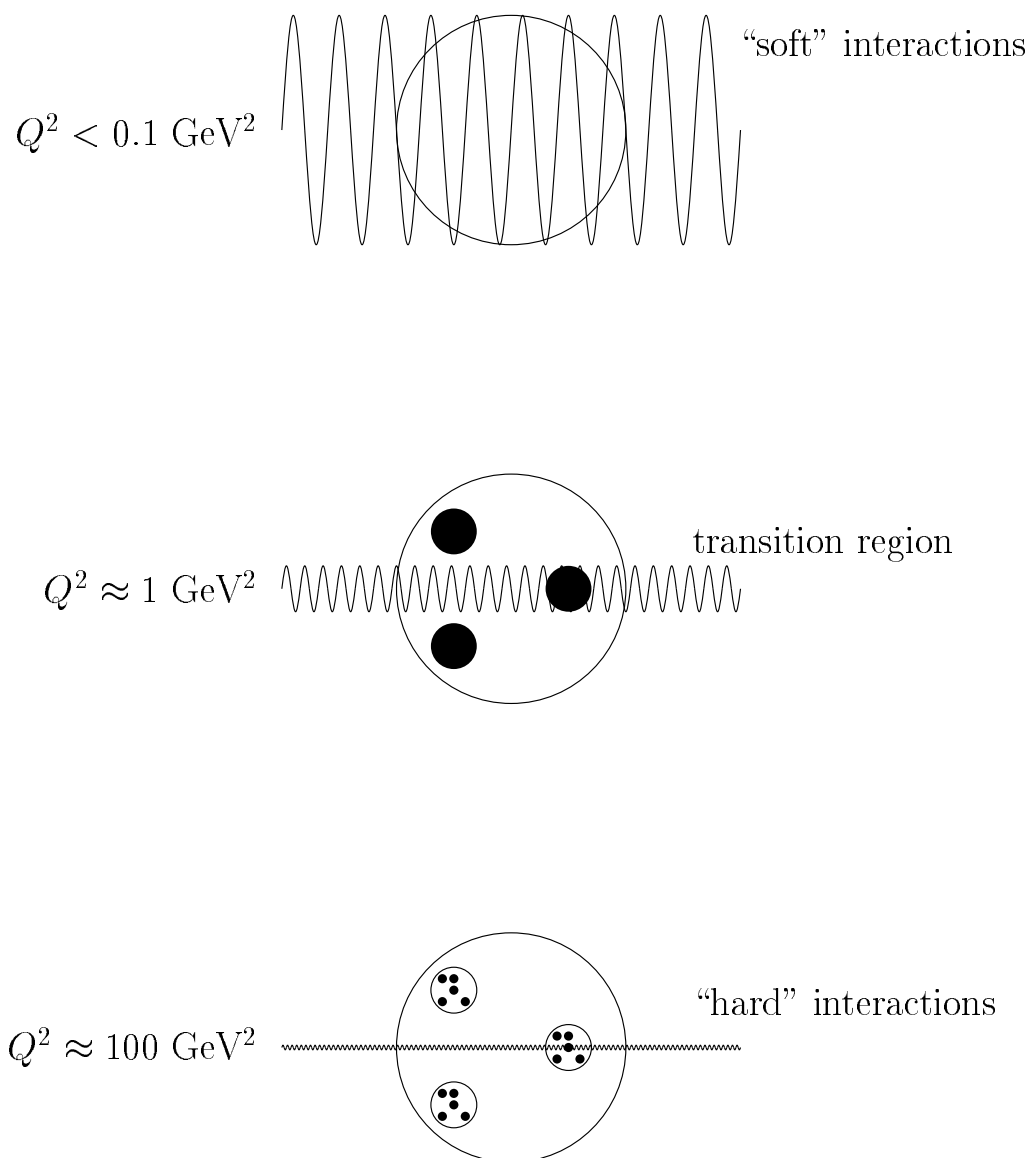


Figure 2.5: Schematic representation of photon-proton scattering for increasing photon virtuality Q^2 . As Q^2 increases, the photon probes smaller transverse distances and is able to resolve the structure of the proton. With further increase in Q^2 , more quarks and gluons are resolved inside the proton.

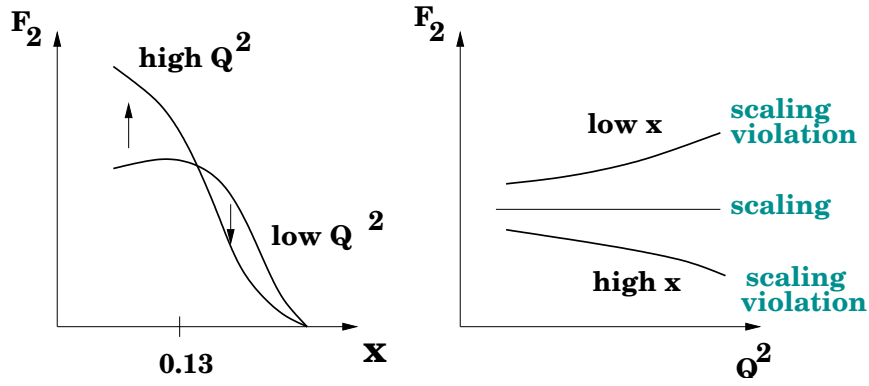


Figure 2.6: Sketch of the variation of F_2 as a function of x and Q^2 .

probed: with increasing Q^2 , the photon emitted by the electron is more likely to find the proton in a state in which one of the valence quarks has radiated off one or more gluons and is surrounded by a cloud of virtual quark anti-quark pairs (see figure 2.5 for illustration). In this case, the photon may scatter off one of the sea quarks, which typically carry on a small fraction x of the proton's momentum, explaining the rise of the proton structure function at low x (see figure 2.6).

If the photon, however, scatters off the valence quark that has radiated off the gluons, the struck quark carries on average a smaller fraction x of the proton's momentum than it would, had it not emitted any gluons. In other words, with increasing resolution Q^2 the photon starts to resolve quantum loops and the probability to scatter off a parton with low fraction x increases.

2.4.3 QCD Hard Scattering Factorisation

In QCD, additional infinities arise connected to the so-called “*infrared divergences*” due to gluon radiation off quark lines when the gluon is almost collinear with the quark. These diagrams give rise to large divergent logarithms in the perturbation series.

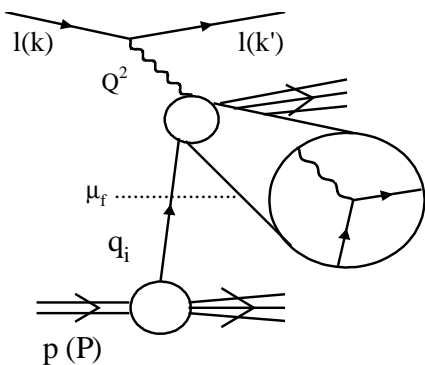


Figure 2.7: Factorisation in QCD.

These divergences are connected to the “soft”, i.e. long range or low momentum regime of QCD and are thus not perturbatively tractable. They are renormalised in analogy to the ultraviolet divergences described above, introducing an additional factorisation scale μ_f^2 into the theory. For momentum transfers $Q^2 > \mu_f^2$, α_s is taken to be small and perturbation theory is applicable; this is the regime of short range, high momentum transfer (“hard”) interactions. Processes belonging to the “soft” regime, $Q^2 < \mu_f^2$ are absorbed in the renormalised parton distribution functions which now depend on the factorisation scale, μ_f^2 .

The separation of “hard” and “soft” scale processes is called *factorisation* [26]. The

cross section (σ_{ep}) then can be written as a convolution of partonic hard scattering cross sections (σ_{lq}) with probability functions, q_i , for finding the incoming partons in a given hadron, schematically

$$\sigma_{ep} = \sum_f q_i \otimes \sigma_{lq} \quad (2.32)$$

and consequently, it can be sketched as in figure 2.7.

The non-perturbative part, namely the part related to the structure functions, has to be determined by fitting experimental data. Nevertheless, the PDFs thus defined are completely process-independent and can therefore be measured in one process and applied to another. This universality property means that the PDFs of the proton measured at HERA should be able to describe any other process involving protons, whether it be ep interactions at HERA, $p\bar{p}$ interactions at the Tevatron, or pp interactions at the LHC.

2.4.4 The DGLAP Evolution Equations

Although the PDFs themselves are not calculable from first principles it is still possible to apply pQCD in calculating their evolution in Q^2 or x or both. Several evolution schemes exist, most notably the DGLAP [17–20], BFKL [21, 22] and CCFM [23–25] schemes, each having different regions of applicability. The DGLAP evolution scheme has been proven to describe all structure function measurements at HERA, see e.g. [85].

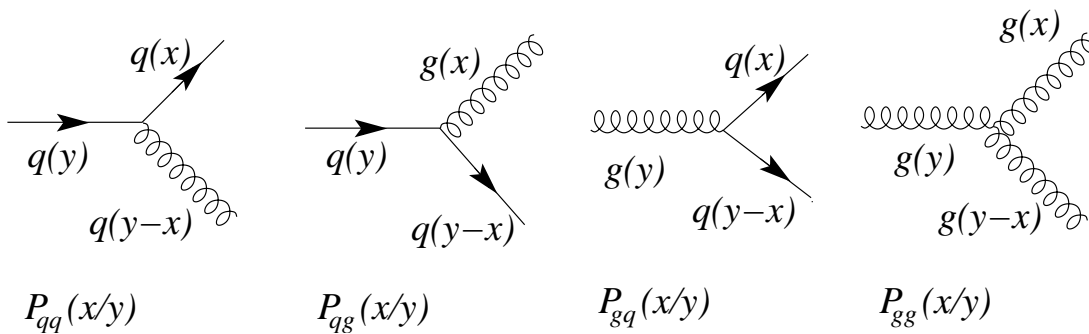


Figure 2.8: Splitting functions P_{ij} , denoting the probabilities for a parton j with momentum fraction y to emit a parton i with momentum fraction x .

The DGLAP evolution equations describe the evolution in $\ln Q^2$ of the PDFs discussed in section 2.4.3. In addition to the quark PDFs considered there, gluon PDFs, $g(x, \mu^2)$, need to be defined, giving the probability of finding a gluon emitted inside the hadron carrying a fraction x of the hadron's momentum. The DGLAP equations then have the form [6]:

$$\frac{\partial q(x, t)}{\partial t} = \frac{\alpha_s(t)}{2\pi} \int_x^1 \frac{dy}{y} \left[q(y, t) P_{qq}\left(\frac{x}{y}\right) + g(y, t) P_{qg}\left(\frac{x}{y}\right) \right], \quad (2.33)$$

$$\frac{\partial g(x, t)}{\partial t} = \frac{\alpha_s(t)}{2\pi} \int_x^1 \frac{dy}{y} \left[q(y, t) P_{gq}\left(\frac{x}{y}\right) + g(y, t) P_{gg}\left(\frac{x}{y}\right) \right], \quad (2.34)$$

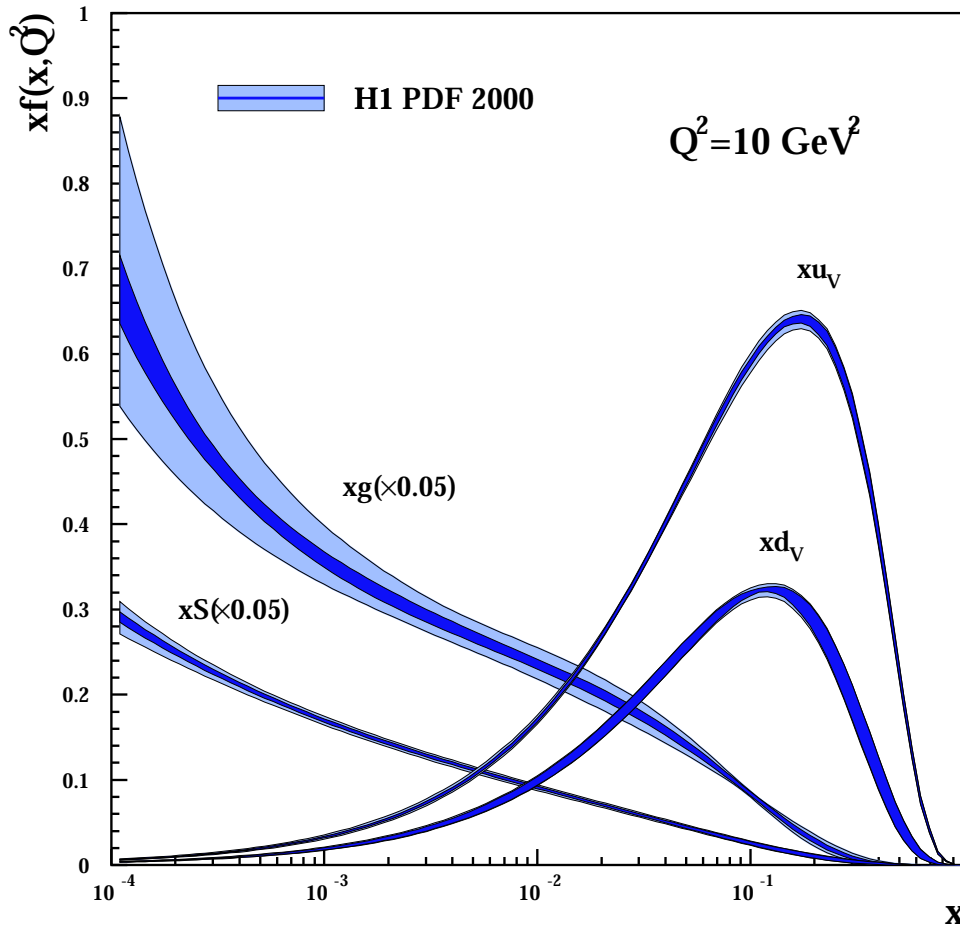


Figure 2.9: The H1 PDF 2000 fit [85] for the valence quarks xu_v and xd_v , the sea quarks xS and the gluon xg . The distributions are shown at $Q^2 = 10 \text{ GeV}^2$. The bands represent estimates of the experimental and theoretical uncertainties. Gluon and sea quark densities are scaled down by a factor of 20.

where $t = \ln(Q^2/\mu_0^2)$ and $P_{ij}(x/y)$ are the splitting functions which represent the probability of finding a parton i with momentum x originating from a parton j with momentum y . For example, the gluon Bremsstrahlung process $q \rightarrow qg$ which modifies the quark distributions is represented by two splitting functions $P_{qq}(x/y)$ and $P_{gq}(x/y)$, and modifications to the gluon distributions by $P_{gq}(x/y)$ and $P_{gg}(x/y)$, as shown in figure 2.8.

There are currently two distinct approaches to extract PDFs from existing data. The first one is the global fit that is practiced by the MRST [35] and CTEQ [36] collaborations. The data set in this case includes deep inelastic scattering, Drell-Yan (DY) pair production in fixed target and collider experiments, and Tevatron jet cross sections. While such an approach benefits from the wealth of data, its drawback is that inconsistent data may influence the quality of the fit. In addition, going beyond the next-to-leading order within this framework is difficult since very few partonic processes are currently known through NNLO in perturbative QCD.

A different approach to extracting PDFs was suggested by Alekhin [37]. The data set in this case is restricted to deep inelastic scattering. Higher order QCD corrections can

be included consistently within this approach since the QCD corrections to DIS coefficient functions and DGLAP splitting functions are known through NNLO [38,39]. The disadvantage of the DIS-based approach is that the DIS data are only sensitive to certain combinations of PDFs. Consequently, not every parton distribution function can be reliably constrained. This leads to large, approximately 20%, errors on sea quark and gluon distributions at relatively large values of the Bjorken variable x , $x \gtrsim 0.1$ [40].

This analysis uses the parton densities of the proton extracted by performing a NLO QCD fit to the H1 NC and CC data [85]. The parton densities are parameterised using polynomial functions in x at an initial scale $Q_0^2 = 4 \text{ GeV}^2$. The parton densities are then evolved in Q^2 using the NLO DGLAP equations and fitted to the experimental data. The results of the H1 PDF 2000 fit are shown in figure 2.9 at $Q^2 = 10 \text{ GeV}^2$. The gluon and sea quark densities are seen to dominate at low x (they are shown scaled down by a factor of 20 in the plot). The valence quark can be seen to contribute at high x ($x \gtrsim 0.2 \div 0.3$). The bands represent estimates of the experimental and theoretical uncertainties of the fit.

2.4.5 Longitudinal Structure Function in QCD

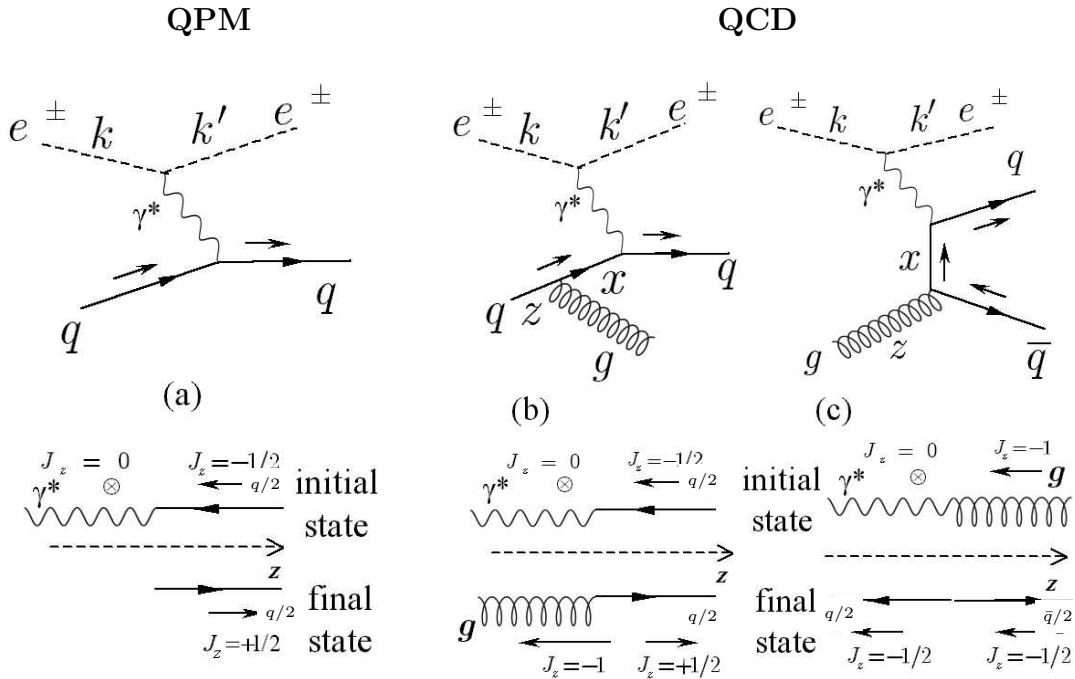


Figure 2.10: Helicity and angular momentum conservation at the hadronic vertex in Quark Parton Model (QPM) and Quantum Chromodynamics (QCD).

Because of conservation of helicity H and angular momentum J at the quark vertex the interaction of a longitudinally polarised virtual photon in the naive QPM is not possible, see figure 2.10(a), which means that $F_L = 0$. On the other hand in QCD, the quark can radiate a gluon, figure 2.10(b), or a gluon can split to quark anti-quark pair, figure 2.10(c). This leads to two particles in the final state, and there is no difficulty to conserve both helicity and angular momentum at the same time. Thus,

in the framework of QCD, a non-zero F_L is allowed. In NLO F_L is given by [27, 28]

$$F_L(x, Q^2) = \frac{\alpha_s}{4\pi} x^2 \int_x^1 \frac{dz}{z^3} \left[\frac{16}{3} \sum_q (q + \bar{q}) + 8 \sum_q e_q^2 \left(1 - \frac{x}{z}\right) \cdot zg \right], \quad (2.35)$$

where the first sum in the integral corresponds to the graph of the gluon radiation off a quark, figure 2.10(b). The second sum corresponds to gluon splitting into a quark anti-quark pair, figure 2.10(c), and demonstrates the sensitivity of the longitudinal structure function to the gluon distribution function. At low x the gluon term dominates and the measurement of F_L can be used to determine the gluon distribution inside the proton [29].

2.5 The Neutral Current Cross Section

2.5.1 The Born Cross Section and Structure Functions

The Born cross section for the deep inelastic ep scattering neutral current process $e^\pm p \rightarrow e^\pm X$ is given by [7]

$$\frac{d^2\sigma_{NC}^\pm}{dx dQ^2} = \frac{2\pi\alpha^2}{x} \left[\frac{1}{Q^2} \right]^2 \phi_{NC}^\pm(x, Q^2), \quad (2.36)$$

with

$$\phi_{NC} = Y_+ \tilde{F}_2^\pm(x, Q^2) - y^2 \tilde{F}_L^\pm(x, Q^2) \mp Y_- x \tilde{F}_3^\pm(x, Q^2), \quad (2.37)$$

where $\alpha = e^2/4\pi$ is the electromagnetic coupling constant. The essential Q^{-4} dependence of the cross section accommodates for the Rutherford type scattering behaviour being characteristic for elastic scattering of point-like charged particles. The structure function term, ϕ_{NC} , accounts for the details of the ep interaction: The three non-negative generalised structure functions $\tilde{F}_2(x, Q^2)$, $x\tilde{F}_3(x, Q^2)$ and $\tilde{F}_L(x, Q^2)$ contain the information about parton structure of the proton and the couplings between the fermions and the exchanged boson. The longitudinal lepton beam polarisation enters implicitly via the structure functions. The “ \mp ” sign in front of the $x\tilde{F}_3$ term signals the opposite contribution to the cross section for e^+p and e^-p scattering.

The explicit y dependence, which is due to the helicity dependence of electroweak interactions, is contained in the functions

$$Y_\pm = 1 \pm (1 - y)^2, \quad (2.38)$$

with y related to the electron scattering angle in the eq rest frame, θ^* , as

$$y = \frac{1 - \cos\theta^*}{2}. \quad (2.39)$$

The longitudinal structure function \tilde{F}_L describes the absorption of a longitudinally polarised vector boson and vanishes for point-like spin one-half particles in the limit of negligible quark masses and zero intrinsic transverse momenta in the proton. However, QCD effects such as gluon radiation lead to a small contribution of \tilde{F}_L in the kinematic region of small x and highest y (see section 2.4.5). Since this analysis is restricted to $y < 0.9$ and covers very high momentum transfers which require large values of x , \tilde{F}_L yields a minor contribution to the cross section and is neglected in

the following discussion of the structure functions. However, \tilde{F}_L may in principle be decomposed in a similar way as it will be done below for \tilde{F}_2 . Certainly, the \tilde{F}_L contribution is taken into account in the cross section calculations performed in this analysis.

The cross section depends on the squared absolute value of the sum of the amplitudes of the contributing electroweak matrix elements,

$$\frac{d^2\sigma}{dx dQ^2} \propto \left| \begin{array}{c} e \quad \sim e_e \quad e \\ \quad \quad \quad \gamma \\ q \quad \sim e_q \quad q \end{array} + \begin{array}{c} e \quad \sim (v_e, a_e) \quad e \\ \quad \quad \quad Z^0 \\ q \quad \sim (v_q, a_q) \quad q \end{array} \right|^2. \quad (2.40)$$

Thus, the generalised structure functions can be separated into the contribution arising from pure γ and pure Z^0 exchange as well as from γZ^0 interference [7]:

$$\tilde{F}_2^\pm = F_2 - (v_e \pm P_e a_e) \kappa_Z F_2^{\gamma Z} + (v_e^2 + a_e^2 \pm 2P_e v_e a_e) \kappa_Z^2 F_2^Z, \quad (2.41)$$

$$x\tilde{F}_3^\pm = -(a_e \pm P_e v_e) \kappa_Z x F_3^{\gamma Z} + (2v_e a_e \pm P_e (v_e^2 + a_e^2)) \kappa_Z^2 x F_3^Z, \quad (2.42)$$

The explicit indication of the x and Q^2 dependence are omitted for simplicity. The “ \pm ” signs refer to the charge of the lepton beam. P_e denotes the longitudinal polarisation of the lepton beam and is defined as

$$P_e = \frac{N_R - N_L}{N_R + N_L}, \quad (2.43)$$

where N_R and N_L are the number of right-handed and left-handed leptons in the beam, respectively.

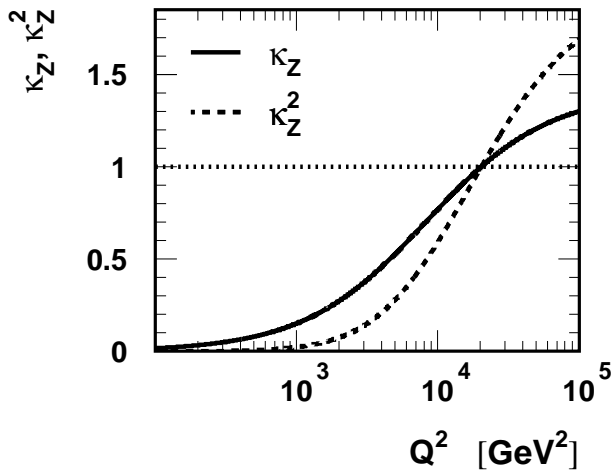


Figure 2.11: Q^2 dependence of κ_Z , the ratio of the couplings and propagators of the Z^0 to those of the photon, and of κ_Z^2 .

The factor κ_Z denotes the ratio of the couplings and propagators of the Z^0 to those of the photon,

$$\kappa_Z(Q^2) = \frac{1}{4\sin^2(\theta_W)\cos^2(\theta_W)} \frac{Q^2}{Q^2 + M_Z^2} \approx 1.41 \frac{Q^2}{Q^2 + M_Z^2}. \quad (2.44)$$

Therefore, the relative magnitudes of the cross sections corresponding to $(\gamma, \gamma Z^0, Z^0)$ exchange behave like $(1, \kappa_Z, \kappa_Z^2)$ depending on Q^2 as displayed in figure 2.11.

The structure functions $F_2, F_2^{\gamma Z}, F_2^Z, xF_3^{\gamma Z}$ and xF_3^Z of equations (2.41)-(2.42) characterise solely the proton as seen by a neutral boson, independent of what the counterpart of the interaction (here an electron) is. The electromagnetic structure function F_2 originates from pure photon exchange and is the dominant contribution to the cross section in the bulk of the kinematic phase space accessible at HERA. The structure functions $F_2^{\gamma Z}$ (F_2^Z) and $xF_3^{\gamma Z}$ (xF_3^Z) represent the γZ^0 interference (pure Z^0) terms of \tilde{F}_2 and $x\tilde{F}_3$, respectively. The γZ^0 interference contribution is noticeable already at intermediate Q^2 values of a few 1000 GeV². However, both γZ^0 and Z^0 exchange yield important contributions to the cross section only at very large Q^2 , $Q^2 \gtrsim M_Z^2$.

Since there are no assumptions made on the proton structure, the equations (2.41)-(2.42) provide the most general form of the proton structure functions for the electroweak boson exchange with unpolarised protons.

2.5.2 The Reduced Cross Section

For the presentation and discussion of the data, it is convenient to introduce the so-called *reduced* cross section, defined by

$$\tilde{\sigma}(x, Q^2) = \frac{xQ^4}{2\pi\alpha^2 Y_+} \frac{d^2\sigma}{dx dQ^2} = \tilde{F}_2(x, Q^2) \mp \frac{Y_-}{Y_+} \cdot x\tilde{F}_3(x, Q^2) - \frac{y^2}{Y_+} \cdot \tilde{F}_L(x, Q^2). \quad (2.45)$$

The propagator term as well as the couplings are divided out to obtain essentially the effects of the parton distribution functions. In most of the kinematic range the relation $\tilde{\sigma} \approx \tilde{F}_2$ holds to a very good approximation.

2.5.3 The Single Differential Cross Sections

The single differential cross section as function of Q^2 is obtained by integration of equation 2.36 over the allowed kinematic phase space in x :

$$\left. \frac{d\sigma}{dQ^2} \right|_{Q_0^2} = \int_x \left. \frac{d^2\sigma}{dx dQ^2} \right|_{Q_0^2} dx. \quad (2.46)$$

The single differential cross section as function of x is defined in a similar way:

$$\left. \frac{d\sigma}{dx} \right|_{x_0} = \int_{Q^2} \left. \frac{d^2\sigma}{dx dQ^2} \right|_{x_0} dQ^2. \quad (2.47)$$

2.5.4 Structure Functions in the Quark Parton Model

In the Quark Parton Model, the contributions to the structure functions F_i can be expressed in terms of the quark distribution functions $q(x, Q^2)$ of the proton, where $q = u, \bar{u}, d, \bar{d}$, etc. The quantity $q(x, Q^2)dx$ is the number of quarks (or antiquarks) of definite flavour carrying a momentum fraction between x and $x + dx$ of the proton's

momentum in a frame in which the proton momentum is infinite.

For the neutral current processes $ep \rightarrow eX$,

$$[F_2, F_2^{\gamma Z}, F_2^Z] = x \sum_q [e_q^2, 2e_q v_q, v_q^2 + a_q^2](q + \bar{q}), \quad (2.48)$$

$$[F_3^\gamma, F_3^{\gamma Z}, F_3^Z] = \sum_q [0, 2e_q a_q, 2v_q a_q](q - \bar{q}), \quad (2.49)$$

where $v_q = \pm \frac{1}{2} - 2e_q \sin^2 \theta_W$ and $a_q = \pm \frac{1}{2}$, with \pm according to whether q is u - or d -type quark respectively [7].

2.6 The Charged Current Cross Section

The charged current cross section can be written as

$$\frac{d^2 \sigma_{CC}^\pm}{dx dQ^2} = (1 \pm P_e) \frac{G_F^2}{2\pi x} \left[\frac{M_W^2}{Q^2 + M_W^2} \right]^2 \phi_{CC}^\pm(x, Q^2). \quad (2.50)$$

We see that the CC cross section has a structure very similar to the NC cross section, equation 2.36, the only difference being that the fine structure constant α is replaced by the Fermi coupling constant G_F and the photon propagator term $1/Q^4$ is replaced by the corresponding W propagator. This propagator structure tells us immediately that the CC cross section is much smaller than the NC one, and comparable in size to NC cross section only for $Q^2 \gtrsim M_W^2$. The term $\phi_{CC}(x, Q^2)$ can be decomposed into structure functions in exactly the same way as ϕ_{NC} [7]:

$$\phi_{CC}^\pm = \frac{1}{2}(Y_+ \tilde{W}_2^\pm \mp Y_- x \tilde{W}_3^\pm - y^2 \tilde{W}_L^\pm). \quad (2.51)$$

In terms of PDFs the term ϕ_{CC}^\pm can be written as [7]:

$$e^+ : \quad \phi_{CC}^+ = x[(\bar{u}(x) + \bar{c}(x)) + (1-y)^2(d(x) + s(x))], \quad (2.52)$$

$$e^- : \quad \phi_{CC}^- = x[(u(x) + c(x)) + (1-y)^2(\bar{d}(x) + \bar{s}(x))]. \quad (2.53)$$

These expressions are exact in LO QCD. In order to take into account quark mixing, the individual terms would have to be weighted by the relevant squared matrix elements of the CKM matrix [41]. Since for an incoming positron the exchanged W boson has positive charge, the cross section is sensitive to down-type quarks and up-type antiquarks. In case of electrons the CC cross section is sensitive to up-type quarks and down-type antiquarks. Thus, we see that CC interactions can distinguish flavours, which is not possible for photon exchange in NC interactions.

An interesting aspect to study in NC and CC deep inelastic scattering is the helicity dependence of the cross sections. The experiments at HERA are sensitive to the contribution from Z and W exchange, and thus to electroweak effects. For CC in particular, only left(right)-handed (anti)quarks participate in the weak part of the interaction. Since certain spin configurations are forbidden by angular momentum conservation, an asymmetry in the positron scattering angle θ_e^* defined in the positron-quark centre-of-mass system appears. The weighting factor $(1-y)^2$ in ϕ_{CC} for down-type quarks can be understood because of the relation $\cos^2(\theta_e^*/2) = 1-y$

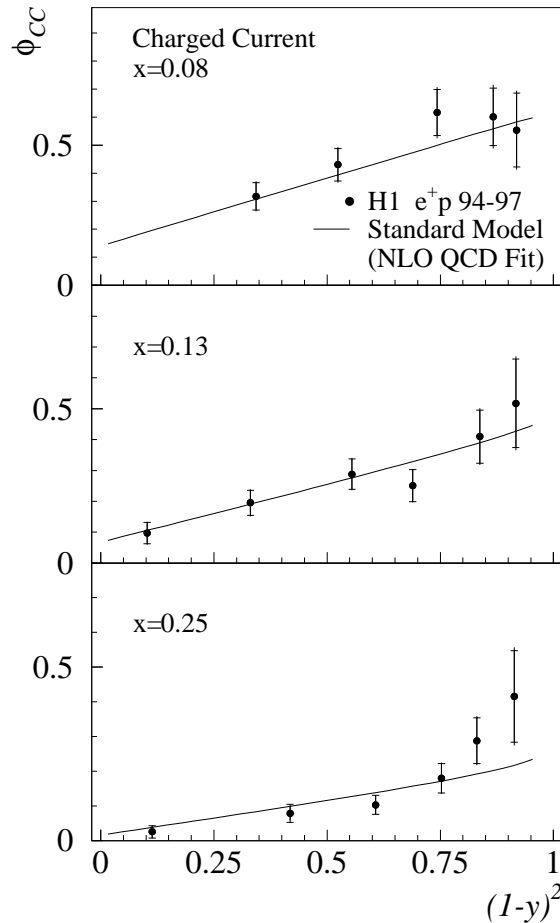


Figure 2.12: Measurement of the CC cross section term ϕ_{CC} by H1 as function of $(1-y)^2$, together with a NLO QCD fit [84].

(see equation 2.39). In figure 2.12 the H1 measurement of the cross section term ϕ_{CC} is shown as a function of $(1-y)^2$, for various bins in the large x region. In leading order we expect a dependence proportional to $(1-y)^2$ from positron-quark (d, s) scattering, and isotropic distribution from positron-antiquark (\bar{u}, \bar{c}) scattering. In fact we observe an almost linear dependence of ϕ_{CC} , with a finite offset, which decreases with increasing x . Therefore these measurements can help to constrain strongly the various quark contributions.

The measurement of the Q^2 dependence of the NC and CC cross sections up to the highest values of Q^2 allow for a beautiful visualisation of the *unification of electromagnetic and weak* interactions. This is illustrated in figure 2.13. At low Q^2 , virtual photon exchange dominates the NC interactions, and CC events are suppressed by many orders of magnitude. However, with increasing Q^2 both cross sections approach each other, showing that the electromagnetic and weak contributions become of similar size. Note the fact that for large Q^2 the CC cross section for electrons is higher than for positrons. This is due to the W^- (W^+) boson exchange, which couples to up (down)-type quarks in the case of electrons (positrons). Those are more abundant in the proton than down-type quarks. In addition, for positron scattering the helicity structure of the interaction leads to an additional suppression. In the highest Q^2 region also the NC cross section is larger for electrons than for positrons. In this region

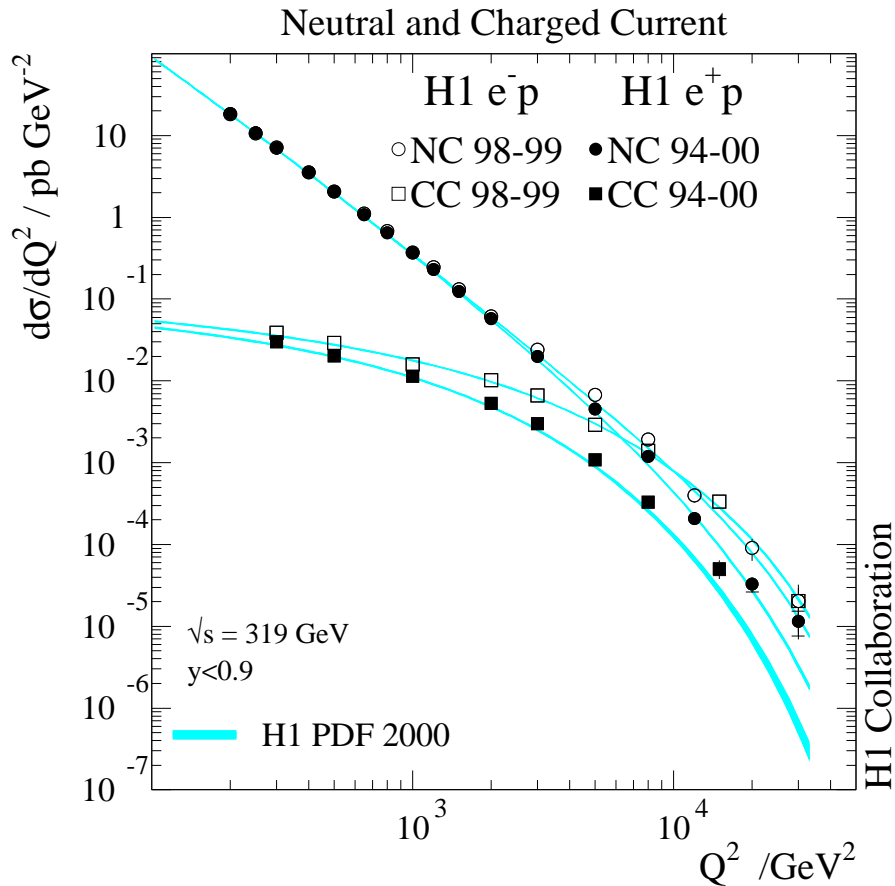


Figure 2.13: The Q^2 dependencies of the NC (circles) and CC (squares) cross sections $d\sigma/dQ^2$, measured with the H1 detector [85]. The e^+p collisions are shown as full symbols, e^-p as open symbols. The results are compared to the Standard Model expectations determined from the H1 PDF 2000 fit (bands).

the interference between photon and Z exchange becomes relevant, which explains the observed asymmetry.

2.7 Electroweak Physics with Polarised e^\pm Beams

In the Standard Model, charged current interactions proceed exclusively via left-handed currents, i.e. the CC cross section vanishes for right-handed electrons and left-handed positrons. The total CC cross sections with different polarisations for e^+p and e^-p are presented in figure 2.14. The measurements agree with the SM predictions and exhibit the expected linear dependence as a function of the polarisation. The result of the measurements excludes the existence of charged currents involving right handed fermions mediated by a hypothetical boson of mass below 180-208 GeV at 95% confidence level, assuming SM couplings and a massless right handed ν_e [48].

The SM predicts a difference in the NC cross section for leptons with different helicity states arising from the chiral structure of the neutral electroweak exchange. The corresponding SM predictions are shown in figure 2.15. The dependence of the NC cross section on the longitudinal lepton polarisation arises mainly from the γZ inter-

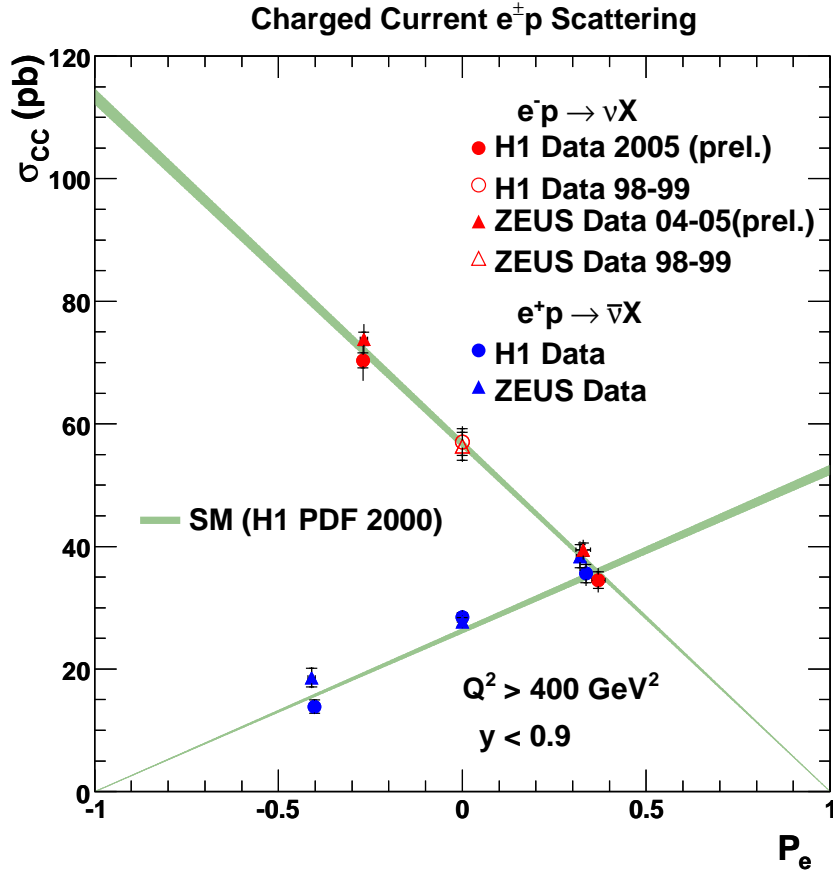


Figure 2.14: The dependence of the e^-p and e^+p CC cross sections on the lepton beam polarisation, P_e . The data [117, 118] are compared to the Standard Model prediction obtained using the H1 2000 PDF fit.

ference terms. The bulk of the cross section is dominated by γ exchange and thus is independent of P_e and is the same for e^+p and e^-p scattering. Only at large Q^2 a sensitivity of the cross sections to the polarisation shows up: the NC cross section becomes dependent on the helicity and the electric charge of the lepton.

Since different combinations of quark flavours enter with different coupling constants into the cross sections, one can use these measurements to determine separately the parton distribution functions for up - and $down$ -type quarks, provided the electroweak couplings of quarks to the Z -boson are known. In turn, assuming values for parton distribution functions, one can extract information on these couplings. Figure 2.16 shows results of a fit to simulated data based on 250 pb^{-1} per beam to vector and axial-vector couplings of the light quarks. Polarisation is very important for such a measurement and helps to improve the precision of the vector-type couplings for a factor of roughly three (using lepton beam with polarisation of 50%) compared to the case with unpolarised beams [50].

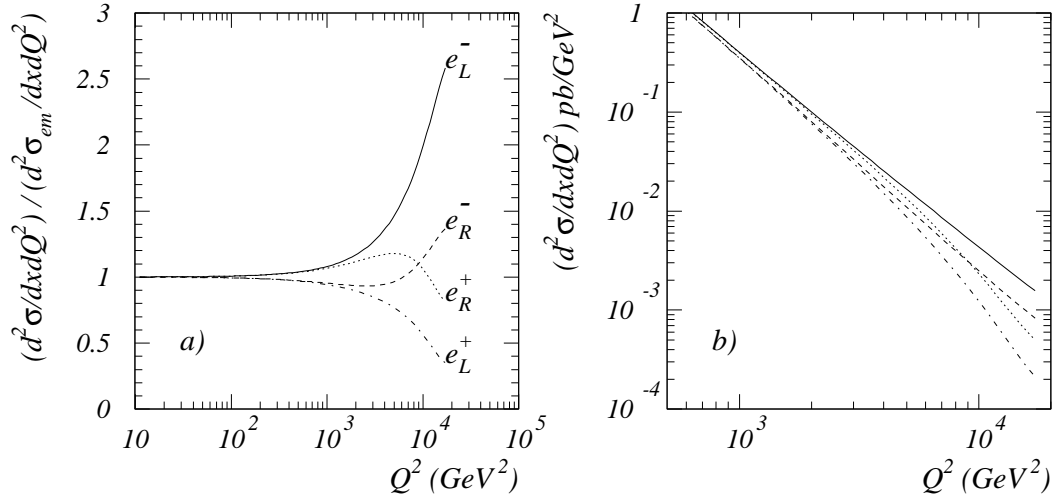


Figure 2.15: NC cross sections $d^2\sigma/dxdQ^2$ at $x = 0.2$ as a function of Q^2 for different charge and polarisation assignments. The left part shows the cross sections normalised to the one-photon exchange which is independent of charge and polarisation, right part displays the absolute cross sections [49].

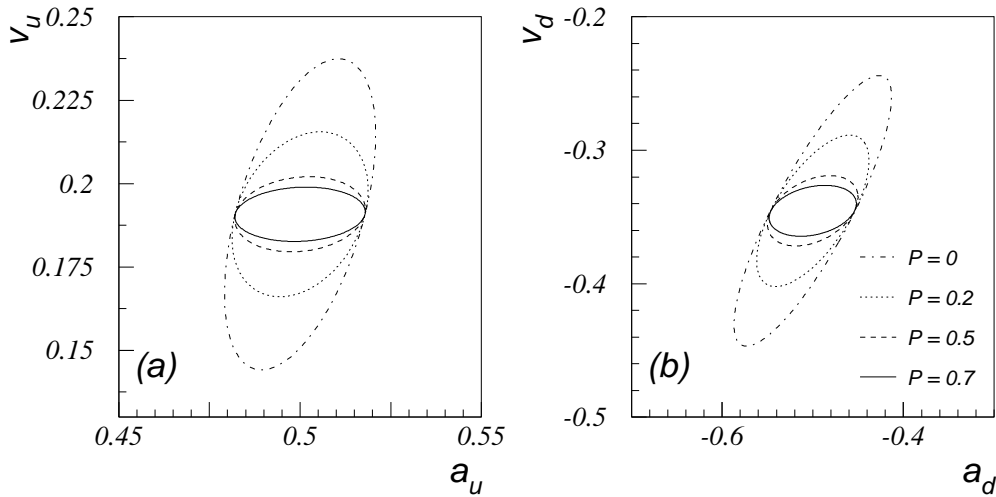


Figure 2.16: Results of the fit to vector and axial-vector electroweak couplings of light quarks for up -quarks assuming fixed $down$ -quark couplings (left) and for $down$ -quarks assuming fixed up -quark couplings with different degree of longitudinal polarisation [49].

2.8 Radiative corrections

To perform cross section measurements and compare them with theoretical calculations it is necessary to take into account the effects of QED radiative processes. This is typically done by correcting the measured cross sections for QED radiative effects, either by using event simulation packages which include radiative effects, or from analytical calculations. The ratio between the radiative cross sections and the Born cross sections are used as correction factors.

First order QED radiative processes from the electron are shown in figure 2.17. They include initial state radiation (ISR), final state radiation (FSR) and virtual loop corrections. There are also radiative effects for the proton, or the quarks. Since they are much smaller in a magnitude these effects typically not corrected for.

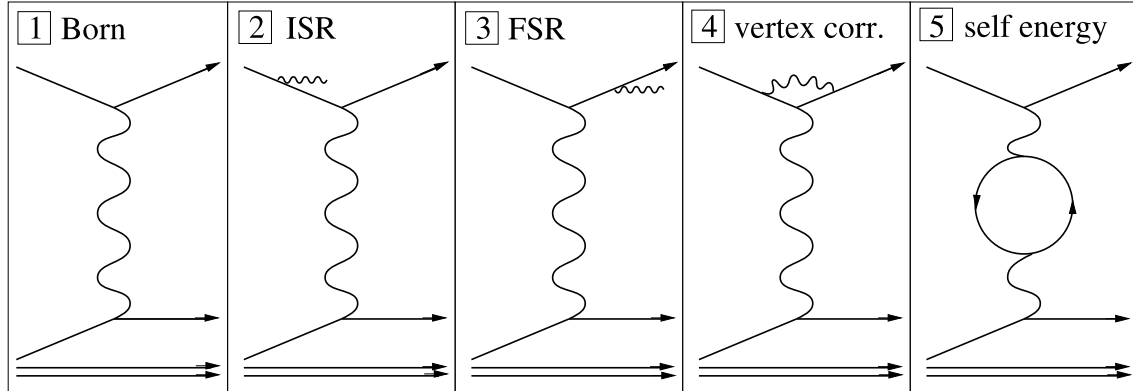


Figure 2.17: Diagrams showing the different LO QED corrections to the Born diagram.

For ISR, the energy of the interacting electron is effectively lowered. The *apparent* x and Q^2 calculated with the electron variables are no longer the same as the x and Q^2 one would calculate from the quark vertex. QED radiation therefore causes shifts in the reconstructed kinematic variables. The shifts depend on the choice of the reconstruction method. Methods relying more on the hadronic system are typically less sensitive to the radiative effects.

To compare experiment with the SM predictions in equation (2.36) the cross section must therefore be corrected to the Born level (no QED radiation). These corrections are typically small, since the QED coupling constant appears, and can be treated as a multiplicative correction. The differential cross section for NC DIS can be approximated as

$$\frac{d^2\sigma^{NC}}{dx dQ^2} = \frac{d^2\sigma^{Born}}{dx dQ^2} (1 + \Delta^{QED}). \quad (2.54)$$

Additional corrections, $1 + \Delta^{weak}$, arise from the effects of the photon-lepton vertex corrections combined with the self energies of the external fermion lines and the effects of the fermion loops of the exchanged photon self energy. The weak corrections are typically less than 1% [85] and have not been applied to the measured cross sections.

Chapter 3

HERA and the H1 Detector

The analysis of this thesis is based on data which were taken in the years 2003-05 with the H1 experiment at the HERA ep collider. This chapter introduces the HERA collider and the detector components of the H1 experiment which are relevant for the investigation of neutral current events.

3.1 HERA Accelerator

The “*Hadron-Electron-Ring-Anlage*”¹, HERA, at the DESY² laboratory in Hamburg is the only facility worldwide to provide colliding beams of electrons and protons. It is designed to accelerate electrons (or positrons) and protons to an energy of 27.5 GeV and 920 GeV, respectively.

The magnetic guide field for the HERA electron ring operates at ambient temperatures, while the proton ring is super-conducting. The two beam pipes merge into one at two opposite areas along the circumference. The beams are made to collide at zero crossing angle to provide ep interactions for the experiments H1 [42] and ZEUS [43]. The H1 detector will be described in more detail in the further sections. The electrons (positrons) and protons are bunched, with bunches separated by 96 ns. Several bunches are left unpaired (i.e., the corresponding bunch in the other beam is empty) for background studies. The electron (positron) beam is naturally polarised in the transverse direction via the Sokolov-Ternov effect [46]. In the end of the year 2000, during the HERA luminosity upgrade (cf. section 3.2), pairs of spin rotators were installed in the beamline around the H1 and ZEUS detectors transforming transversely polarised leptons into longitudinally polarised ones.

The performance of the collider is characterised by the *luminosity*. At HERA, the *instantaneous* luminosity depends on the bunch-crossing frequency f , the numbers of particles N_e and N_p in the electron and proton bunches and the collimation of the beams in the transverse direction σ_x and σ_y ,

$$\mathcal{L} = \frac{f \cdot N_e \cdot N_p}{4\pi \cdot \sigma_x \cdot \sigma_y}, \quad \left[\frac{1}{\text{cm}^2 \cdot \text{s}} \right]. \quad (3.1)$$

The number of the expected interactions, N , in the collision region of an experiment

¹“Anlage” is the German word for “facility”.

²Deutsches Elektronen-Synchrotron.

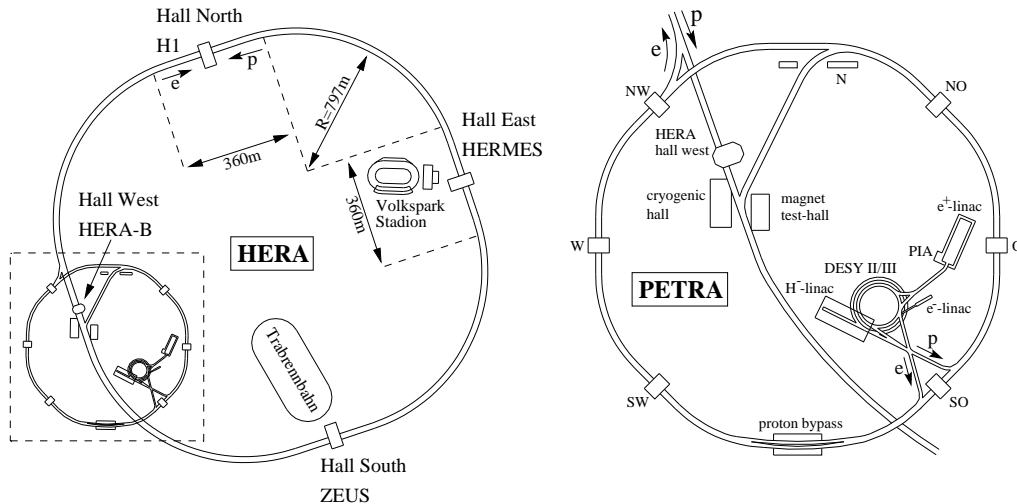


Figure 3.1: The HERA storage ring with two collider experiments (H1, ZEUS) and two fixed target experiments (HERA-B [44], HERMES [45]). On the right-hand side of the picture an enlarged view of the pre-accelerators for HERA (DESY II/III and PETRA) is shown.

is proportional to the *integrated* luminosity:

$$L = \int \mathcal{L} dt \quad (3.2)$$

and is related to the cross-section σ of any given process by:

$$N = L \cdot \sigma \quad (3.3)$$

3.2 The Luminosity Upgrade Project at HERA

The peak luminosity of the HERA ring was $1.79 \times 10^{31} \text{cm}^{-2} \text{s}^{-1}$ in the year 2000. To increase the luminosity and to allow collecting significantly more data, the HERA II upgrade project of the collider ring has been carried out in 2000-2002. An improved sensitivity for detecting non Standard Model physics and an extension of the range of physics experiments to higher Q^2 phenomena compared to HERA I are the goals of the upgrade. The luminosity was increased by approximately a factor of tree to about $4.80 \times 10^{31} \text{cm}^{-2} \text{s}^{-1}$. HERA II delivers about 200pb^{-1} per year, compared to an integrated luminosity of $\simeq 100 \text{pb}^{-1}$ collected by each of the colliding experiments from 1993 to 2000 (see figure 3.2).

A higher luminosity can be reached by increasing the number of particles N_e , N_p and/or by decreasing the beam cross section $\sigma_{x,y}$ (see equation (3.1)). The HERA accelerator was modified at two major points:

- It was equipped with four new super-conducting focusing magnets close to the experiments H1 and ZEUS to decrease $\sigma_{x,y}$. Two magnets were installed in the H1 detector area for focusing the electron beam, one in the forward region (“GO” magnet see figure 3.9) and one in the backward region (“GG” magnet). Forward direction corresponds to the incoming proton direction. To create space

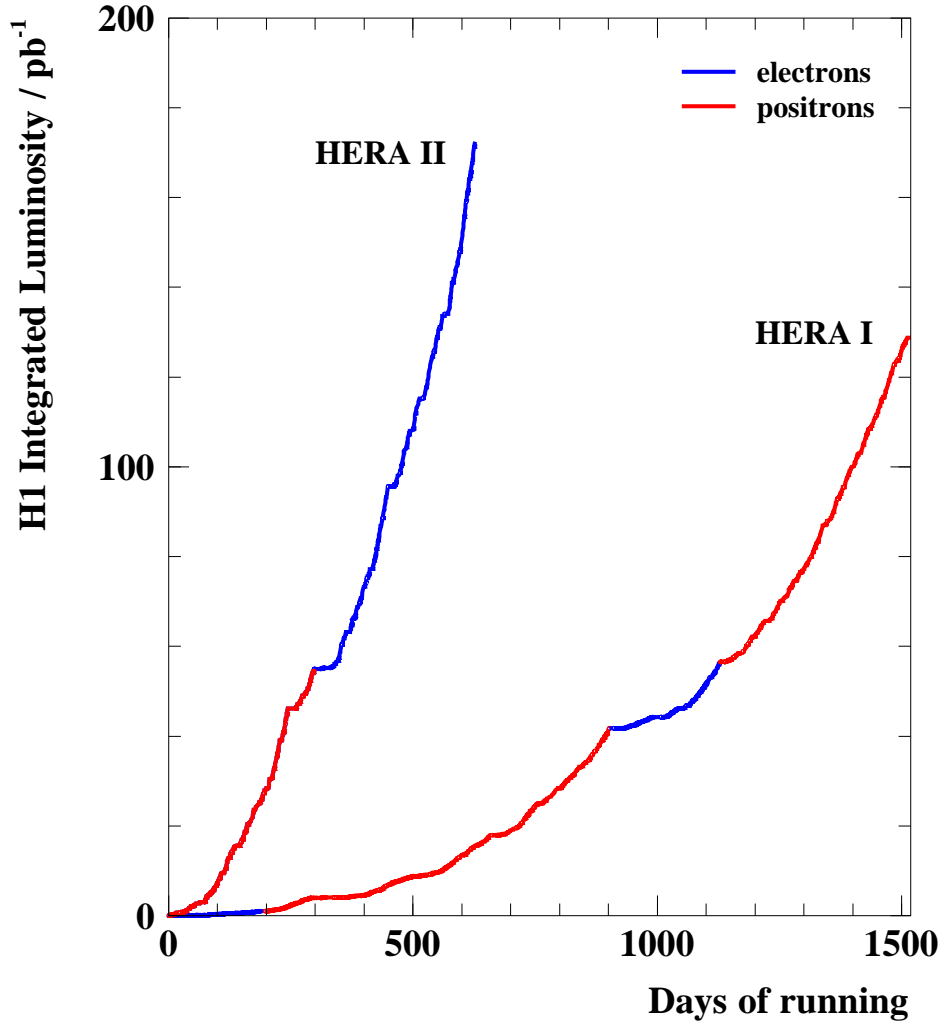


Figure 3.2: The H1 integrated luminosity as function of time for HERA I and HERA II periods, up to the end of the year 2005.

for these magnets, significant changes to the inner part of the H1 detector were necessary. The vacuum beam pipe in the detector had to be changed. Since the new beam pipe has an elliptic design, the innermost detectors had to be adapted to the beam pipe geometry.

- HERA was upgraded to be able to operate with the highest possible beam currents. The goal is to increase the proton current I_p up to 135 mA and the electron beam I_e to 55 mA. In practice due to background conditions in 2003-05 HERA was operating with about the same currents as in the year 2000 (see table 3.1).

Dipole magnets in the new super-conducting focusing magnets are used to steer the electron beam. As a result, a high amount of synchrotron radiation is produced near the experiments that cause degradation of the vacuum quality inside the beam pipe and hence leads to an increased number of beam-gas collisions. The new background situation is explained in more detail in section 3.4. The HERA *upgrade project* is described in detail in [56].

	HERA I		HERA II	
	<i>e</i> -beam	<i>p</i> -beam	<i>e</i> -beam	<i>p</i> -beam
Beam energy	27.5 GeV	920 GeV	27.5 GeV	920 GeV
Nr. of bunches, tot./collid.	189/174	180/174	189/174	180/174
Particles per bunch	3.5×10^{10}	7.3×10^{10}	4.0×10^{10}	10.3×10^{10}
Max. beam current	52 mA	109 mA	42 mA	102 mA
Beam dimensions, $\sigma_x \times \sigma_y, (\mu m \times \mu m)$	192×50	189×50	112×30	112×30
Average luminosity	$6.47 \times 10^{30} \text{cm}^{-2} \text{s}^{-1}$		$17.20 \times 10^{30} \text{cm}^{-2} \text{s}^{-1}$	
Peak luminosity	$17.90 \times 10^{30} \text{cm}^{-2} \text{s}^{-1} \text{A}^{-2}$		$48.01 \times 10^{30} \text{cm}^{-2} \text{s}^{-1} \text{A}^{-2}$	

Table 3.1: Operational parameters of HERA I and HERA II as it was achieved in 2000 and 2005, respectively.

3.3 Polarisation at HERA

The electrons at HERA become transversely polarised through the emission of synchrotron radiation (the Sokolov-Ternov effect). This section describes the theoretical aspects of the polarisation at HERA and the polarisation measurement.

3.3.1 The Sokolov-Ternov Effect in a Constant Magnetic Field

Electrons which move in a magnetic field can have two spin states, up or down, with respect to the field direction. Two states are separated by the energy

$$E = \left| \frac{g}{2} \right| h \gamma^2 \omega_0, \quad (3.4)$$

where ω_0 is the revolution frequency, γ is the Lorentz factor and g is the gyromagnetic ratio of the electron:

$$g = \frac{2|\mu|}{\hbar}, \quad (3.5)$$

where μ is the electron magnetic moment.

During the motion on curved orbits, such as those prescribed by the magnetic guide fields of a storage ring, electrons emit synchrotron radiation. By calculating transition rates in terms of exact Dirac wavefunctions for electrons moving in a homogeneous magnetic field, it is found that a very small fraction of the emitted photons will cause a spin-flip between the “up” and “down” quantum states of the electrons’ spin. For electrons with spins initially aligned along the magnetic field the probabilities for transitions from the up-to-down state and down-to-up state differ, leading to the build-up of polarisation antiparallel to the field. Positrons become polarised parallel to the field. The transition rates for electrons are [46]

$$\omega_{\uparrow\downarrow} = \frac{5\sqrt{3}}{16} \left(1 + \frac{8}{5\sqrt{3}} \right) c \lambda_c r_0 \frac{\gamma^5}{\rho^3}, \quad (3.6)$$

$$\omega_{\downarrow\uparrow} = \frac{5\sqrt{3}}{16} \left(1 - \frac{8}{5\sqrt{3}} \right) c \lambda_c r_0 \frac{\gamma^5}{\rho^3}, \quad (3.7)$$

where the arrows indicate the relative directions of the spin in the initial and final states. For positrons plus and minus signs are interchanged here. ρ denotes the bending radius of the magnetic field,

$$\lambda_c = \hbar/(m_e c) = 3.8616 \cdot 10^{-13} \text{ m}$$

is the reduced electron Compton wavelength and

$$r_0 = e^2/(4\pi\epsilon_0 m_e c^2) = 2.81179 \cdot 10^{-15} \text{ m}$$

is the classical electron radius.

An initially unpolarised electron (positron) beam gradually becomes polarised following an exponential law

$$P(t) = P_{max,ST}(1 - e^{-t/\tau_{ST}}) \quad (3.8)$$

where the maximum attainable (equilibrium) polarisation is given by

$$P_{max,ST} = \frac{\omega_{\uparrow\downarrow} - \omega_{\downarrow\uparrow}}{\omega_{\uparrow\downarrow} + \omega_{\downarrow\uparrow}} = \frac{8}{5\sqrt{3}} \sim 92.38\% \quad (3.9)$$

and the build-up time is

$$\tau_{ST} = \frac{8}{5\sqrt{3}} \frac{\rho^3}{c\lambda_c r_0 \gamma^5}. \quad (3.10)$$

The build-up time depends strongly on the energy (γ^{-5}) and the bending radius (ρ^3). For HERA at an operating electron beam energy of $E_e \approx 27$ GeV one gets $\tau_{ST} \approx 40$ min. This is a very long time, to be compared to the time interval between two photon emissions about 10^{-8} s, reflecting the small spin-flip probability.

3.3.2 Spin Rotators and Longitudinal Polarisation at HERA

Most of the electroweak physics that can be done with polarised beams requires polarisation in the beam direction, i.e. longitudinal polarisation. This is achieved by bringing the natural transverse polarisation of the leptons into a longitudinal polarisation at the interaction region using special magnet arrangements – so called *spin rotators*. Since the generation and maintenance of the naturally occurring polarisation requires that the polarisation direction be vertical, the spins of the longitudinally polarised leptons must be rotated back to the vertical direction behind interaction regions of the HERA experiments. These pairs of spin rotators have been installed around H1 and ZEUS during the HERA II upgrade project, while HERMES was already equipped by rotators in the HERA I period.

The HERA spin rotators are designed to operate in the electron beam energy range from 26.8 GeV to 39 GeV [51]. They consist of a chain of interleaved horizontal and vertical bending magnets. An illustration of the magnet lattice and the spin transformations in the rotator region on the upstream (left) side of the East interaction point (HERMES area) is shown in figure 3.3.

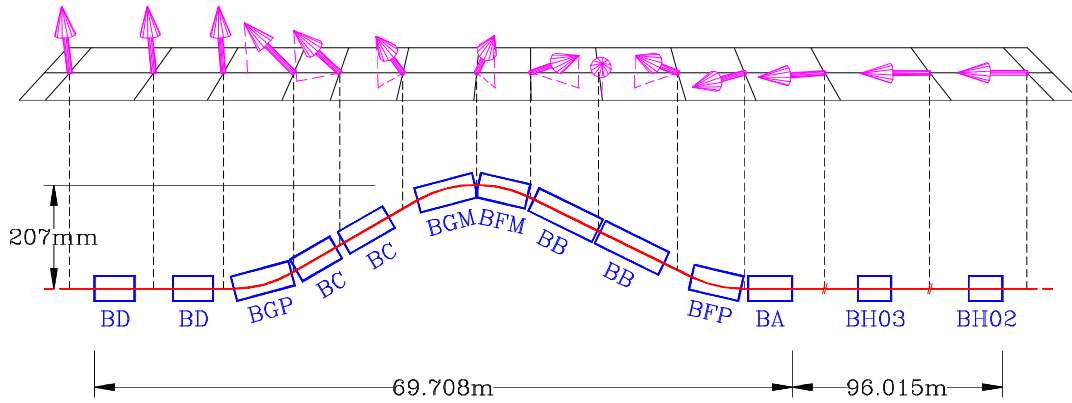


Figure 3.3: The left half of the rotator pair in the East hall (HERMES experiment). The magnets BH03 and BH02 are not part of the rotator, but are needed to complete the spin rotation into the longitudinal direction. On the opposite side of the IP a similar magnet arrangement with reversed radial fields (BF and BG magnets) brings the polarisation back to the vertical direction.

3.3.3 Depolarisation Effects

In addition to the Sokolov-Ternov effect producing the transverse polarisation, there can be spin diffusion, i.e. depolarisation due to the stochastic excitation of the electron orbits by emission of synchrotron radiation photons. The depolarisation is especially strong if the resonance condition

$$\nu = k + m_x Q_x + m_z Q_z + m_s Q_s \quad (3.11)$$

is satisfied where k , m_x , m_z , m_s are integers, the $Q_{x,z,s}$ are orbital tunes and ν , called the spin tune, is the number of spin precessions per turn on the closed orbit [52].

In a perfectly aligned planar ring the equilibrium spin axis is vertical, the beam would have almost zero vertical emittance and the depolarisation would actually almost vanish. But in a real ring with their misalignments, the closed orbit is distorted and the equilibrium spin axis defined along the closed orbit is tilted from the vertical and the spin diffusion can then take place [52]. This depolarisation is combated by the application of *harmonic spin-orbit corrections* using special families of closed “bumps” to return the equilibrium spin axis to the vertical.

The installation of spin rotators itself can result in additional strong depolarisation even in an ideal ring. One reason is that between the rotators the spin axis is horizontal and can be considered to be maximally tilted. Another reason is that there is local vertical dispersion inside the rotators so that synchrotron radiation emission in the rotators excites vertical betatron motion. In principle, these two consequences of the presence of rotators can, in HERA, be largely eliminated by a special choice of optics called “*strong spin matching*”. In practice, there is a compromise in accelerator optic settings between better polarisation and maximum specific luminosity.

Another source of depolarisation is the effect of the proton bunch charge on the electron bunch polarisation. This phenomenon, named *beam-beam* effect, can be viewed as a quadrupole magnet effect on the electron beam.

3.3.4 Polarisation Measurement

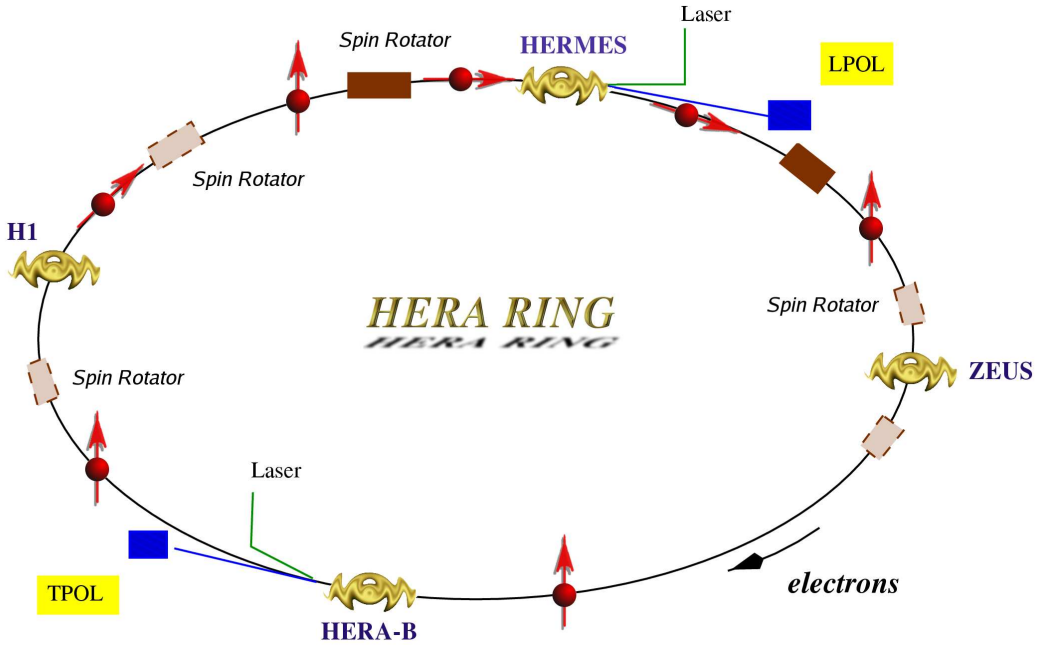


Figure 3.4: Schematic view of the HERA ring after upgrade.

The degree of polarisation is continuously measured by two independent polarimeters, both making use of the polarisation dependence of Compton scattering. The *Transverse Polarimeter* (TPOL) [53] is located near the HERA-B interaction region where the polarisation vector is oriented vertically, and the *Longitudinal Polarimeter* (LPOL) [54,55] is located between the HERMES spin rotators, where the polarisation vector is oriented along the beam axis (see figure 3.4).

Transverse Polarimeter

TPOL measures *spatial asymmetries* in the vertical plane of the distribution of single backscattered Compton photons arising when circularly polarised photons scatter off vertically polarised electrons. The shift of the mean vertical position of the photon distribution, when switching between left (L) and right (R) circular laser light polarisation, is proportional to the vertical polarisation component P_z of the electrons. In particular at the position of the photon detector, 65 m away from the interaction, the photon spot size is of the order of 0.3 mm in the vertical plane and the shift between the centroids is typically about 140 μm [51]. The vertical positions of the photons are recorded with a vertically segmented calorimeter by energy sharing in the upper and lower halves. By forming the shower energy asymmetry $\eta = (E_{up} - E_{down}) / (E_{up} + E_{down})$, where η is related to the vertical position through a parameterization, P_z can be obtained through the difference of the mean values $\langle \eta \rangle$ when switching the light polarisation

$$\Delta\eta(E_\gamma) = \frac{\langle \eta \rangle_L - \langle \eta \rangle_R}{2} = P_z \Delta S_3 \Pi_\eta(E_\gamma). \quad (3.12)$$

Here, ΔS_3 is the difference in the circular polarisation of the laser light. $\Pi_\eta(E_\gamma)$ is the so called analysing power, which depends on the Compton cross section as well

as detector and electron beam parameters and has to be checked through calibration.

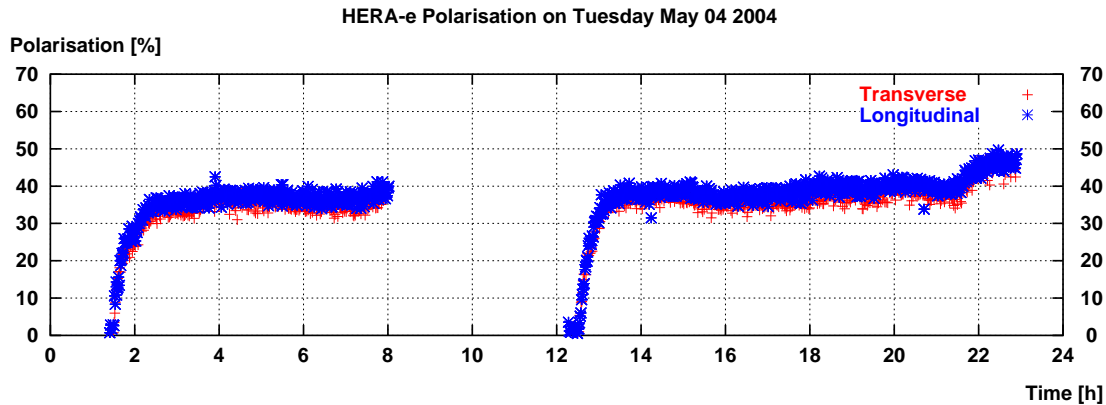


Figure 3.5: Typical HERA II longitudinal and transverse polarisation as a function of time.

Longitudinal Polarimeter

A schematic overview of the Longitudinal Polarimeter arrangement is shown in figure 3.6. A circularly polarised photon beam from a pulsed laser is focused on the HERA electron beam. The laser-electron interaction point is located between the two bending magnets BH39 and BH90 at 39 m and 90 m from the HERMES target, respectively. A calorimeter measures the energy of the back scattered Compton photons for each laser pulse. The polarisation measurement is based upon asymmetries in the energy distributions of the backscattered photons for different light helicity states.

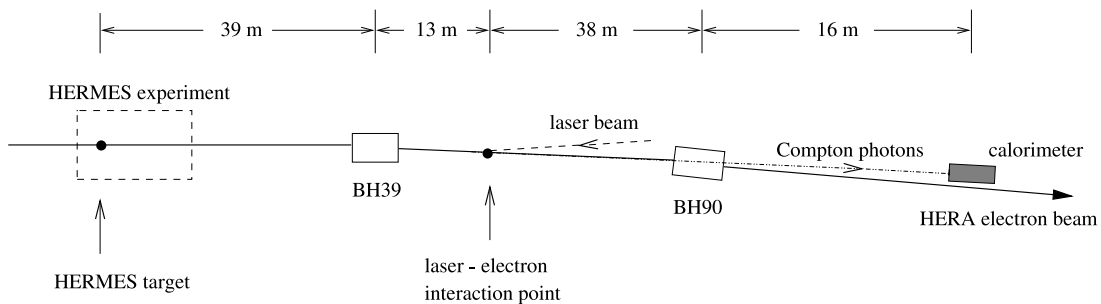


Figure 3.6: Schematic overview of the Longitudinal Polarimeter in the HERA East section.

The detector can be operated in two different modes, the *single-photon* and the *multi-photon* mode. In contrast to the single-photon mode, in which the energy of each individual Compton photon is analysed, in the multi-photon mode one measures the total energy deposited in the detector by many Compton photons per laser pulse interaction with an electron bunch. The multi-photon mode was chosen as the standard mode of operation to provide high statistics single bunch measurements in real time, and to overwhelm the bremsstrahlung backgrounds originating from the residual vacuum pressure in the straight section between the two dipole magnets BH39

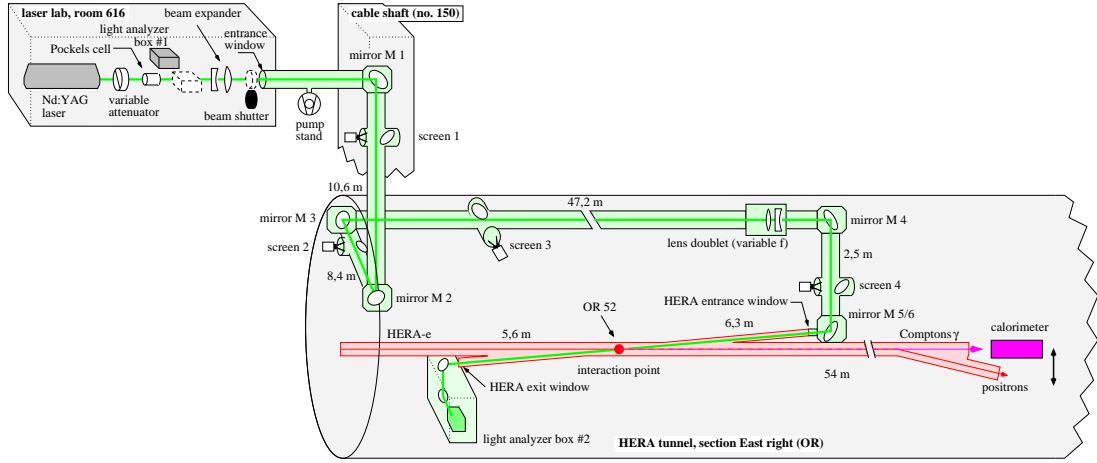


Figure 3.7: Layout of the longitudinal polarimeter at HERA. The laser beam is brought inside the electron vacuum beam pipe by an entrance window. Compton photons are scattered back in the direction of the electron beam within a very narrow angular cone. The back-scattered photons escape the beam pipe through an exit window located at the end of the right section and enter a calorimeter ≈ 60 m downstream from the laser beam-electron interaction point. An optical bench is located on the other side of the interaction point to stop the laser beam and to measure the light polarisation.

and BH90. The single-photon mode is used for test and diagnosis purposes only.

The advantages of running in single-photon mode would be twofold. The asymmetries are larger, and the energy spectra can be compared to the Compton cross sections.

In the single-photon mode, the asymmetry can be written as

$$A_s(E_\gamma) = \frac{(d\sigma/dE_\gamma)_{\frac{3}{2}} - (d\sigma/dE_\gamma)_{\frac{1}{2}}}{(d\sigma/dE_\gamma)_{\frac{3}{2}} + (d\sigma/dE_\gamma)_{\frac{1}{2}}} = P_c P_e A_z(E_\gamma), \quad (3.13)$$

where $(d\sigma/dE_\gamma)_{\frac{1}{2}}$ and $(d\sigma/dE_\gamma)_{\frac{3}{2}}$ are the cross sections for the electron-photon configurations where the incident spins are antiparallel and parallel, respectively, and $P_c = \frac{1}{2}(|P_{+1}| + |P_{-1}|)$ is the average circular light polarisation.

The electron beam polarisation is determined by fitting the energy spectra for the two spin configurations using a simulation that includes the response function and resolution of the detector.

In multi-photon mode a large number of Compton photons is produced each time a laser pulse interacts with an electron bunch. These photons are detected together by the calorimeter, which measures their energy sums $I_{\frac{1}{2}}$ and $I_{\frac{3}{2}}$ for the spin- $\frac{1}{2}$ and spin- $\frac{3}{2}$ electron-photon configurations, respectively. An energy asymmetry is formed as

$$A_m = \frac{I_{\frac{3}{2}} - I_{\frac{1}{2}}}{I_{\frac{3}{2}} + I_{\frac{1}{2}}} = P_c P_e A_p, \quad (3.14)$$

where A_p is the analysing power of the process:

$$A_p = \frac{\Sigma_{\frac{3}{2}} - \Sigma_{\frac{1}{2}}}{\Sigma_{\frac{3}{2}} + \Sigma_{\frac{1}{2}}} \quad (3.15)$$

with

$$\Sigma_i = \int_{E_{\gamma,min}}^{E_{\gamma,max}} (d\sigma/dE_{\gamma})_i E_{\gamma} r(E_{\gamma}) dE_{\gamma}, \quad i = \frac{1}{2}, \frac{3}{2}. \quad (3.16)$$

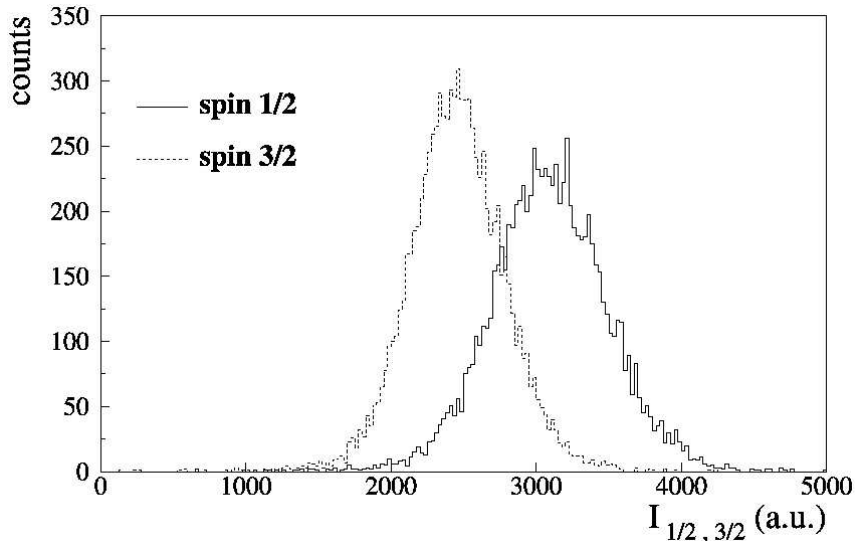


Figure 3.8: Spectra collected in multi-photon mode for the spin- $\frac{1}{2}$ (dashed histogram) and spin- $\frac{3}{2}$ (solid histogram) configurations for a specific electron bunch with polarisation of 0.59.

The longitudinal beam polarisation was determined by evaluating the calorimeter signals for every bunch individually. Switching between the two light helicity states results in the two energy distributions for the corrected calorimeter signals $I_{\frac{1}{2}}$ and $I_{\frac{3}{2}}$, displayed in figure 3.8 for an individual bunch. The longitudinal polarisation of each bunch is determined from the asymmetry of the means of these two energy distributions divided by the analysing power and the measured circular light polarisation (equation (3.14)). This calculation is provided every minute. The longitudinal beam polarisation is finally computed as the mean of individual bunch polarisations weighted by the corresponding time-averaged bunch currents.

3.4 Backgrounds After the HERA Upgrade

The HERA upgrade leads on one hand to an about three times higher instantaneous luminosity, on the other hand, however, the backgrounds has increased significantly. The number of events where protons interact with the residual gas inside the beam pipe or with the beam pipe wall (beam-gas or beam-wall collisions) increased by a factor of about ten compared to HERA I. The high background rate causes the danger of permanent radiation damage of all components of the detector located close to the beam line. For this reason, the collider experiments and HERA investigated ways to reduce the backgrounds.

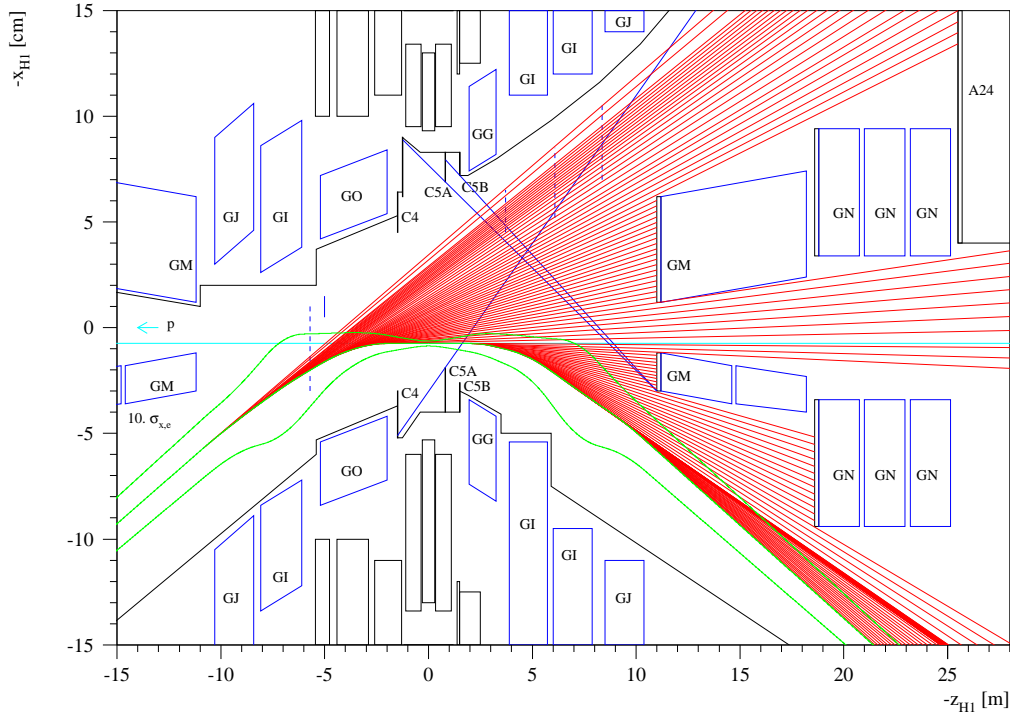


Figure 3.9: Synchrotron radiation in the horizontal plane in the region around the H1 detector shown as tangential lines. Angles with respect to the H1 z -axis are enlarged. The high amount of synchrotron radiation leads to a increased pressure near the absorber.

Reasons for a higher background:

1. Synchrotron radiation: One major component of the upgrade was the installation of stronger focusing magnets close to the interaction point. Additionally, these new superconducting magnets bend the electrons with dipole magnets into the proton beam direction and separate them after the nominal interaction point (see figure 3.9, GO and GG magnets). This early separation is necessary to avoid deflecting the electrons in the proton focusing magnets (GM at ± 10.8 m). As a consequence of bending the electrons in the strong focusing dipole magnets, *synchrotron radiation* is emitted by the (accelerated) electrons. To adapt the increase of the synchrotron radiation a new electron beam pipe was installed. Figure 3.9 shows the new beam pipe geometry and the resulting synchrotron radiation in the region close to the interaction point (IP). The electron beam is steered in such a way that no collimator or beam pipe wall less than 10.8 m from the IP is hit by direct synchrotron radiation. At 10.8 m from the IP, the proton focusing magnet (GM) is installed. At this magnet, parts of the synchrotron radiation is backscattered into the H1 detector. To avoid hitting the H1 detector with synchrotron radiation, collimators are installed, shown in figure 3.9 (C5A, C5B). They have been modified during HERA II upgrade project to account for new radiation conditions.
2. To reduce the amount of backscattered synchrotron radiation a copper absorber is placed in front of the GM magnet at 10.8 m. The high level of synchrotron radiation leads to an increased pressure close to this absorber. Since high energy photons from the synchrotron radiation knock off particles from the inner beam

pipe surface and absorber, the pressure of the residual gas in the beam pipe rises with an increasing electron current in the HERA accelerator, deteriorating significantly the vacuum in the IP.

3. As a consequence of the increased number of beam-gas particles (“bad” vacuum) in the backward region of the H1 detector, the number of collisions of protons with these gas molecules increases (“*beam-gas*” interactions).
4. In collisions between the beam protons and gas nuclei the protons lose their energy giving a rise to the so-called “*off-momentum particles*”. These off-momentum particles are generated in the backward region and may collide with the collimators C5A and C5B. These collisions have to be identified as background events.
5. “*Beam-halo muons*” are produced far up-stream from the IP, via the decay of mesons, generated in collisions of off-momentum particles with elements of the magnetic guide field. These muons are passing through the calorimeters parallel to the proton beam direction. Such events have clear topological signatures and are rejected by the background finders (see section 6.10).

To reduce the pressure of the residual gas in the beam pipe, a powerful ion-getter vacuum pump was installed near the collimator C5B. With this pump, the vacuum can be improved by approximately a factor of two. After months of HERA II running the background conditions improved significantly as vacuum became better. Nevertheless, the HERA II background situation requires more sophisticated procedures to separate background events from *ep*-interactions.

A more detailed description of the reasons for, and investigations of, the background situation at HERA II can be found elsewhere [57, 58].

3.5 H1 Detector

The H1 detector [42] is built around the northern interaction point of the HERA ring. It is a general purpose detector designed to measure the direction, energy and charge of the particles originating from the *ep* collisions in its centre. The detector is asymmetric in the *z*-direction, reflecting the difference of the electron and proton beam energies. Due to the higher energy of the proton beam the centre of mass of the electron-proton collisions is *boosted* along the proton direction. Correspondingly, the instrumentation of the H1 detector is predominantly concentrated in the *forward region*, defined as the direction of the incoming proton beam. The *backward region* is less densely instrumented and dedicated mainly to the detection of the scattered electron.

A three-dimensional representation of the H1 detector and the H1 coordinate system ³ can be seen in figure 3.5. The beampipe [1] is surrounded by the central [2]

³The origin of the right-handed H1 coordinate system is located at the nominal interaction point where the bunch-crossing of the electron and proton beam takes place. The *z*-axis is chosen in direction of the proton beam, with the polar angle θ defined with respect to the beam-axis in the proton direction. The *x*-axis points to the centre of the HERA ring and the *y*-axis vertically upwards. The azimuthal angle ϕ is defined with respect to the *x*-axis.

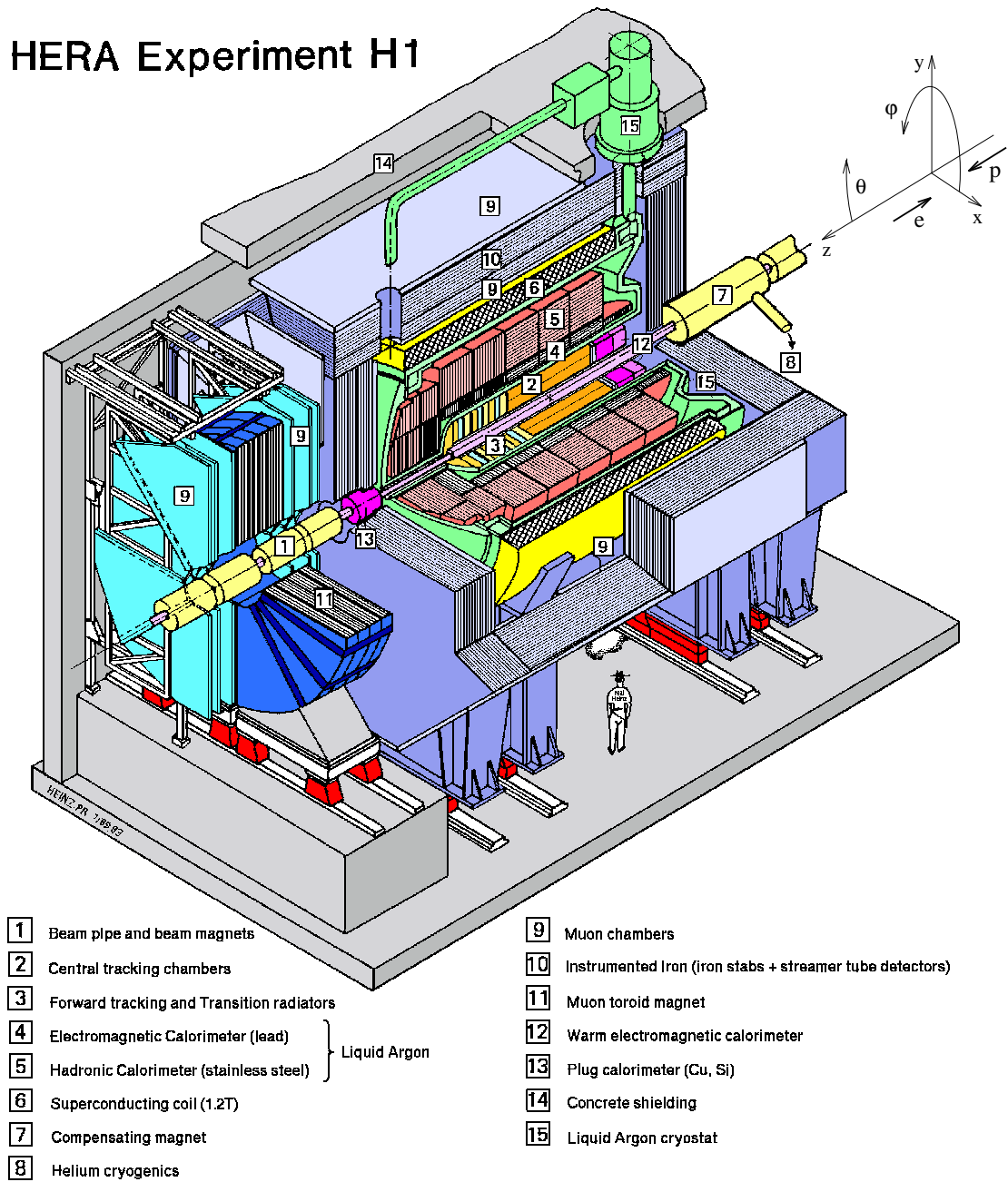


Figure 3.10: Schematic view of the H1 detector. The H1 coordinate system is indicated in the top right corner.

and forward [3] tracking⁴ detectors. Situated around the trackers is the Liquid Argon calorimeter⁵ (LAr), which is made up of an electro-magnetic section [4] and a hadronic section [5]. The LAr is in turn surrounded by a superconducting solenoid magnet [7] which provides an axial field of 1.15 T. The instrumented iron return yoke of the magnet [10] is used to detect muons and hadronic showers that escape the LAr. The Forward Muon Detector [11] covers small angles in the direction of the outgoing protons. The very forward and backward directions are covered by the PLUG [13] and SPACAL [12] calorimeters, respectively, which are situated outside the trackers. The Proton Remnant Tagger (PRT), a detector used in diffractive studies, is situated 24 m downstream of the IP, in the forward direction. The Forward Proton Spectrometer (FPS) is made of four Roman Pots (insertions to the beam pipe, housing scintillating fibre hodoscopes) located between 50 m and 100 m in the forward direction. The pots are used to detect scattered final state protons. The Electron Tagger (ET) and Photon Detector (PD) are positioned upstream the beampipe in the $-z$ direction for the determination of the luminosity by measuring the rate of Bethe-Heitler ($ep \rightarrow ep\gamma$) interactions. The ET is also used to tag photoproduction ($Q^2 \sim 0$) events.

In total, the H1 detector measures approximately $12 \times 10 \times 15 \text{ m}^3$ (length \times width \times height) and weighs about 2800 tons. A more detailed description of the H1 detector can be found in [63]. In the following sections attention is mostly placed on the components important to this analysis.

3.6 Calorimetry

The H1 detector was designed to provide clear identification and precise measurement of electrons, muons and penetrating neutral particles together with good performance in the measurement of jets with high particle densities. These requirements were best met by a calorimeter inside a large coil to minimise both the amount of dead material in front of the electromagnetic calorimeter and the overall size and weight of the calorimeter.

All calorimeters in H1 rely on the same detection principle: each detector is constructed of alternating layers of *passive absorber* material and *active sampling* medium. The function of the absorber layers is to absorb the energy of the incident particle. For this purpose the absorber layers are built of dense materials that have a small mean path length between subsequent interactions of incident particles, so as to stop the incident particle after a short distance and to contain the resulting electromagnetic and hadronic *showers* in a small volume, making possible more compact calorimeters. High energy particles entering an absorbing layer undergo interactions with the constituent nuclei, resulting in the production of secondary particles. These in turn interact with the next absorbing layer, resulting in a shower of tertiary particles. This process carries on until no further production of the shower particles is possible. The charged particles produced in the shower ionise the atoms of the sampling layers and

⁴A reconstructed trajectory of a charged particle is called a *track*.

⁵The name *calorimeter* is derived from the Latin word “calor” (heat), and is used as a general term for detectors that reconstruct particle energies by measuring the development of electromagnetic or hadronic showers (see section 3.6).

produced free electrons (or photons) form the signal that is read out. The readout signal, integrated over all layers, is proportional to the energy of the original incident particle.

As the cross-section for electromagnetic interactions is proportional to the atomic charge number squared Z^2 , while the rate of hadronic interactions is roughly proportional to the atomic mass A , high Z (A) materials are chosen for the absorber material of the electromagnetic (hadronic) sections of sampling calorimeters.

Electrons and photons lose their energy in the absorbing material via bremsstrahlung, $ep \rightarrow ep\gamma$, and pair production, $\gamma p \rightarrow e^+e^-p$, respectively. The secondary particles themselves interact electromagnetically, thus showers develop rapidly. The longitudinal progress of an electromagnetic shower is characterised by the *radiation length* of the absorbing layer, X_0 , which is the mean distance over which an electromagnetic particle will fall to $1/e$ of its total energy.

Hadrons interact strongly with the nuclei of the absorbing layers, resulting in a shower composed of secondary hadrons. The characteristic length of a hadronic shower is given by the *interaction length* of the absorbing layer, λ . The energy contained within the shower consists of a component formed from π^0 mesons produced in the nuclear interactions decaying to photon pairs, which then shower electromagnetically. The secondary charged hadrons (mainly π^\pm mesons) also undergo Coulomb scattering in the absorber. A typical secondary hadron is produced with a transverse momentum of ~ 350 MeV, so that hadronic showers tend to be more spread out laterally than electromagnetic ones. These features make a hadronic shower topologically distinguishable from an electromagnetic shower. Furthermore, in a sampling calorimeter using steel/lead and liquid argon, such as the LAr calorimeter at H1, about 30% of the energy involved in the hadronic shower development is lost in nuclear excitation and breakup; this energy is not visible in the hadronic shower so that the detector response to hadronic energy is lower than that for electrons. Therefore the hadronic energy response is corrected in software [62].

Lead, the material most often used as absorber in electromagnetic calorimeters, has a radiation length of $X_0 \approx 0.56$ cm. For hadronic calorimeters often either lead or iron/steel are used which both have a hadronic interaction length of $\lambda \approx 17$ cm. Since λ is about one order of magnitude larger than X_0 for most materials, hadronic showers are of significantly larger longitudinal extent than electromagnetic showers. As a consequence, much deeper calorimeters are necessary to contain hadronic showers, and electromagnetic calorimeters are placed before hadronic ones, closer to the interaction point.

In the H1 detector, calorimetry is provided by four individual detectors. The main calorimeter is the *Liquid Argon Calorimeter* (LAr), which covers the forward and central regions. Energy leaking out of the Liquid Argon calorimeter is registered in the hadronic *Tail Catcher* (TC), installed in the instrumented iron return yoke of the solenoid. However, it is not used in this analysis due to its mediocre energy resolution. The LAr is complemented in the backward direction by the *Spaghetti calorimeter* (SpaCal). The Plug Calorimeter, situated in the very forward region, fills the gap between the LAr and the beam-pipe, covering $1.9^\circ < \theta < 3.2^\circ$. This subdetector is not used in this analysis.

3.6.1 Liquid Argon Calorimeter

The Liquid Argon (LAr) calorimeter is the most important detector component for the present analysis. It provides an identification and measurement of the scattered electron at high Q^2 and (together with the tracker and SpaCal) the measurement of the hadronic final state. The LAr calorimeter covers the polar angle range of $4^\circ \lesssim \theta \lesssim 153^\circ$ and is housed in a single cryostat. The superconducting solenoid is located outside of the cryostat to minimise the amount of inactive material in front of the calorimeter.

The LAr technique offers the advantages of good stability, ease of electronic calibration, good homogeneity of the response and fine granularity. These properties allow for the identification of electrons and the precise measurement of their energies and positions as well as the accurate measurement of the hadronic energy flow. The structure of the LAr calorimeter and measurement procedure of the electromagnetic and hadronic energy are described below. More details can be found in [65].

Structure of the LAr Calorimeter

The LAr calorimeter is a sampling calorimeter which consists of an inner, fine granulated electromagnetic section followed by a hadronic part with coarser granulation. Figure 3.11 shows a vertical cut along the beam axis of the LAr calorimeter. It is divided along the z -direction into eight self-supporting wheels, named according to their position w.r.t. nominal interaction point: *Backward Barrel* (BBE), *Central Barrel* (CB1, CB2, CB3), *Forward Barrel* (FB1, FB2), *Outer Forward* (OF) and *Inner Forward* (IF). The BBE consists of an electromagnetic section only, the OF only of two hadronic sections. In φ -direction, each wheel is segmented into from eight identical units, the so-called *octants*. Figure 3.12 shows a transverse cross section of a central barrel wheel with the typical octagon structure. In the BBE for a better approximation of the circle, the structure of the octants has 16-fold polygonal surface of the calorimeter front. The insensitive areas between the modules are called “ z -cracks” (between wheels) and “ φ -cracks” (between octants).

The LAr calorimeter is built up of absorber plates, the space between the plates is filled with liquid argon as active medium supplemented by high voltage and read-out electrodes. To obtain a uniform energy resolution, the orientation of the plates is arranged such that the angle of incidence of particles originating from the ep interaction point is always larger than 45° . The electromagnetic section consists of 2.4 mm lead absorber plates. The LAr active gap thickness is 2.35 mm on average. The absorption length of the electromagnetic part varies between 22 and 30 radiation lengths (X_0) in the central and forward directions, respectively. The absorber material in the hadronic section consists of 19 mm thick stainless steel plates with an active double gap of 2.4 mm filled with liquid argon. The total amount of absorbing material of the calorimeter corresponds to about 5 to 8 hadronic interaction lengths (λ).

The LAr calorimeter is segmented into about 45000 read-out cells to enable a good spatial resolution of the deposited energies. The segmentation is coarse in the back-

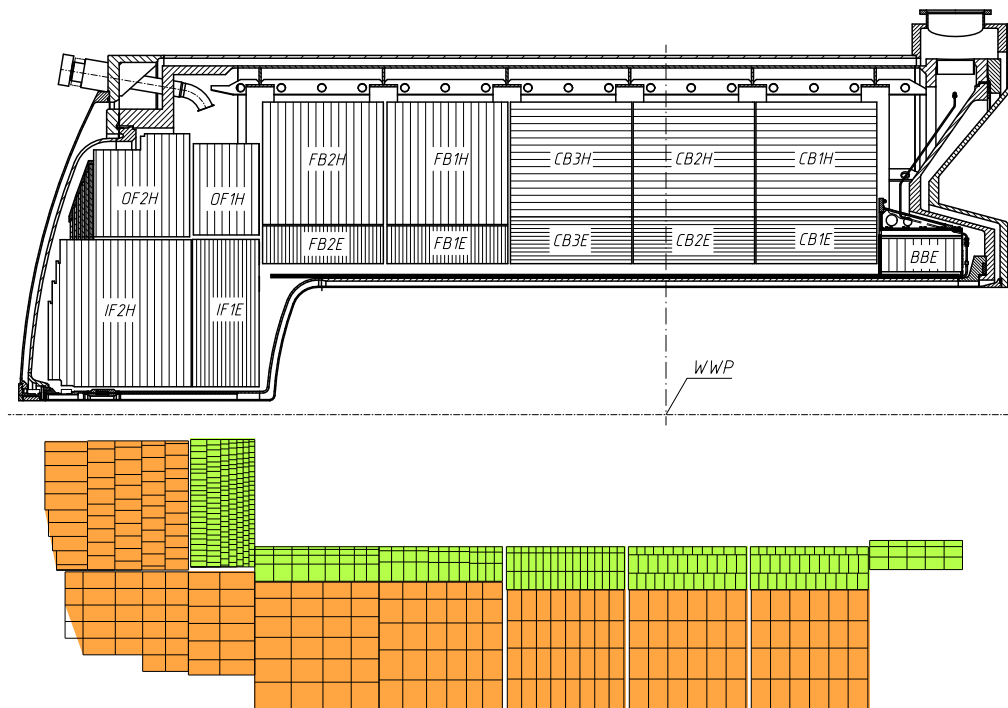


Figure 3.11: Longitudinal cross section of the LAr calorimeter. The upper half shows the sampling structure with the orientation of absorber plates. The read-out cell structure is indicated in the lower part. “WWP” denotes the nominal interaction point.

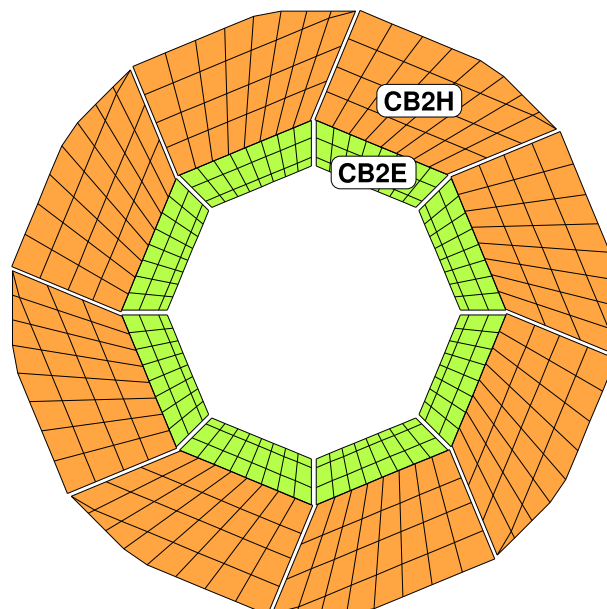


Figure 3.12: Transverse cross section of a central barrel (CB2) wheel of the LAr calorimeter, viewed along the proton beam direction.

ward part and becomes finer towards the forward direction (cf. bottom part of figure 3.11). As viewed from the ep interaction point, the number of layers increases from three to six in the electromagnetic section, and from four to six in the hadronic section. In terms of the Moliere radius⁶, R_M , which is a measure of the transverse extension of electromagnetic showers, the typical size of the cells varies between $2.5 R_M$ in the backward region and $1.0 R_M$ in the forward part. The fine granularity allows for both a precise position measurement of electromagnetically interacting particles and a clean separation of electromagnetic and hadronic showers. The latter provides the basis for an efficient electron identification.

Energy Measurement in the LAr Calorimeter

The energies deposited by incident particles in the electromagnetic and hadronic cells are reconstructed in several steps by the LAr reconstruction software.

Input to LAr calorimeter reconstruction are charges collected with charge sensitive amplifiers from the read-out pads. During data taking, depending on the cell location only cells with absolute value of the collected charge above 2-3 sigmas of the electronic noise are recorded (so-called “*zero suppression*”). The calorimeter reconstruction program converts charges to energies in the calorimeter for both hadronic and electromagnetic showers, corrected for the effects of dead material, eliminates electronic noise and forms clusters from groups of cells.

The conversion from charge to energy (electromagnetic scale) involves a charge to energy calibration factor (determined for each stack geometry in calibration runs at CERN [104]), a correction for the charge collection efficiency for operating at 1 500 V (derived from HV curves obtained with cosmic muons) and correction factors for local variations of gap and absorber thickness (measured during stack construction). The calibration of electronics is performed during special pulse runs [65], which are taken once every few weeks.

An important first step of the reconstruction program is *noise suppression*. The electronic noise is measured for each channel during electronic calibration [65]. It varies between 15 and 30 MeV equivalent energy depending on the calorimeter region. In events recorded with a random trigger, 1100 cells out of a total 45000 cells pass a $+2\sigma$ noise threshold on average. Adding up this energy of the full calorimeter yields an average value of 48 GeV with a standard deviation of 3 GeV [65, 68]. The basic idea of the noise suppression algorithm is to keep a *localised* energy deposit several standard deviations above the noise level together with all neighbouring cells. This rejects single noisy cells as well as noise adding up from small contributions of a large number of cells. If to keep cells with energy above $+2\sigma$ and below -2σ , the residual noise contribution after noise suppression is 0.1 GeV with a $\sigma = 0.5$ GeV.

For Monte Carlo simulations (see chapter 4), noise is included for each cell by using events recorded with random triggers in special runs with no zero suppression. This noise is added on top of the simulated energy deposit and than the full noise sup-

⁶The Moliere radius, R_M , is a characteristic constant of a material describing its electromagnetic properties, and is related to the radiation length by $R_M = X_0 E_s / E_c$, with the radiation length X_0 , a scale energy $E_s \approx 21$ MeV, and the critical energy E_c [67].

pression procedure is applied as for the data.

Neighbouring cells which have not been rejected as noise are associated to *clusters*, i.e. groups of cells which are likely to contain the shower of the same incident particle. The clustering algorithm works quite well for compact showers induced by electrons and photons. It was found [69], that 95-97% (depending on the energy of the incident particle) of electromagnetic showers in the LAr are reconstructed as a single cluster, while simultaneously resolving pairs of electrons into two separate clusters down to opening angles of about 2° (IF) - 5° (FB, CB) between the two electromagnetic showers [69]. The clustering algorithm does not work so well for hadronic showers, however. As a result of the broader and more fluctuating shower shape, hadronic showers induced by single hadrons are often reconstructed as several clusters.

The clusters found are then classified as either belonging to electromagnetic or hadronic showers, depending on the compactness of the cluster and on the position at which the shower started [64, 68]. An early shower start in the first electromagnetic layer of the calorimeter indicates that the shower is induced by a photon or electron. Additionally, the cell energies are corrected for energy loss in the cracks and the dead-material in front of the calorimeter (between 1-2 X_0 , varying with polar angle [65]).

Identified hadronic objects are subjected to an *energy weighting* algorithm [62, 70], which has been developed to equalise the response of the LAr calorimeter to electromagnetic and hadronic showers. The fine granularity of the LAr makes it possible to detect the electromagnetic components of hadronic showers, which are induced by neutral pions and indicated by high local energy densities. Note that the energy contained in the electromagnetic components of showers need no correction. By applying individual energy correction factors only to those cells in the hadronic shower which are not associated with electromagnetic subshowers, the influence of the reconstructed energy on variations in the number of neutral pions in the hadronic shower is reduced.

Final corrections to the reconstructed energies are applied by a *calibration* on the particle level. Both the *electromagnetic energy scale* and the *hadronic energy scale* are calibrated using neutral current DIS events (see sections 6.6 and 6.7). The energy resolution of the LAr calorimeter has been determined in CERN tests to be

$$\frac{\sigma_E^{em}}{E} = \frac{0.12}{\sqrt{E} [\text{GeV}]},$$

for electrons [65] and

$$\frac{\sigma_E^{had}}{E} = \frac{0.50}{\sqrt{E} [\text{GeV}]},$$

for charged pions [66].

3.6.2 The “Spaghetti” Calorimeter

The “Spaghetti” calorimeter (SpaCal) is installed in the backward region of the H1 detector and covers the polar angular range $153^\circ < \theta < 174^\circ$. The primary goal of

SpaCal is the detection of electrons scattered through small angles. Additionally, it allows for the measurement of backward scattered hadrons.

Like the LAr calorimeter, the SpaCal is a sampling calorimeter and consists of an electromagnetic and a hadronic section. Both sections are constructed of long thin scintillating fibres (giving rise to the name ‘‘Spaghetti’’ calorimeter), aligned parallel to the beam direction and embedded in a lead matrix. In the lead, incident particles induce electromagnetic and hadronic showers which are detected by the scintillation light emitted by the fibres when charged shower particles excite molecules in the scintillator material. The scintillation light is collected at the backward end of the fibres and guided to *photomultiplier* tubes (PMT), which amplify the light and convert it to electric signals. The electric signals provided by the photomultiplier are then read-out to reconstruct the energy of the incident particles.

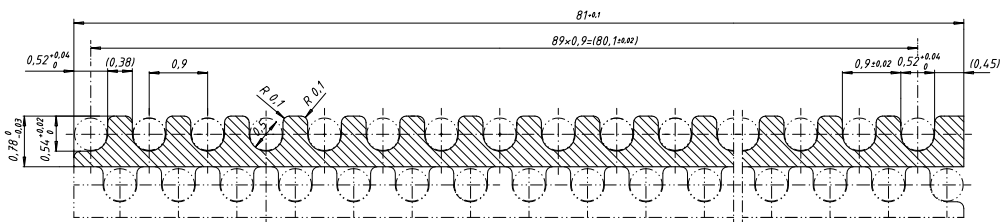


Figure 3.13: The profile of lead sheets (electromagnetic SpaCal).

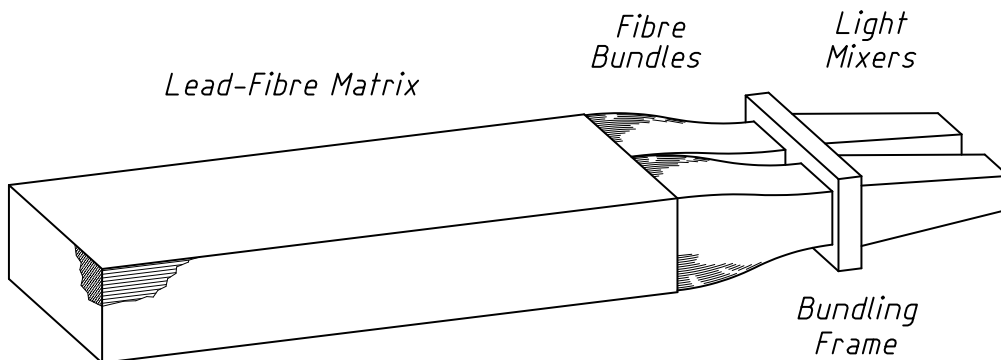


Figure 3.14: The module of the electromagnetic SpaCal calorimeter.

The electromagnetic section of SpaCal consists of 1172 cells [73] with an active volume $40.5 \times 40.5 \times 250 \text{ mm}^3$ each. The cells consist of lead sheets with grooves into which the scintillating fibres are laid. The profile of a lead sheet is shown in figure 3.13. The lead/fibre volume ratio is 2.27:1. A 2-cell-unit, see figure 3.14, consists of 52 stacked lead plates with 4680 fibres each. Eight of these pairs are held together to form a so-called supermodule.

The hadronic section consists of 128 cells with size $120 \times 120 \times 250 \text{ mm}^3$. The fibres are of the same type as in the electromagnetic section but have a larger diameter of

1.0 mm. The construction of the hadronic section is similar but the cells are assembled individually.

The hadronic section as well as the electromagnetic one provide an equivalent of one nuclear interaction length.

The PMTs have to operate in the 1.15 T magnetic field of the main solenoid. The chosen PMTs (Hamamatsu meshdynode type) provide a typical gain of 10^4 , a factor of 100 smaller than in the case of no field [71]. Each supermodule is furnished with a high-voltage (HV) distribution module which provides the high-voltage for the PMTs. A calibration module (CAM) is attached to the rear of each supermodule. A CAM contains control electronics and two pulsed LEDs which feed light through fibres into light mixers and PMTs. Potential instabilities of the light output of each LED are monitored by photodiodes. The LEDs are typically pulsed at a rate of 1 Hz, synchronised to empty HERA bunches. LED pulses are used to monitor the stability of the photomultiplier gains over time and are therefore important for the calibration of the SpaCal calorimeter [72].

3.7 Tracking

The tracking system of H1 provides simultaneous triggering, track reconstruction and particle identification. The tracking detectors are located in the innermost part of the H1 detector, so that the momenta of particles produced in the primary ep interaction may be measured before the particles lose energy in secondary interactions with the calorimeter material.

The H1 tracking system is based on three different detector technologies: drift chambers, multi-wire proportional chambers and silicon detectors. The drift chambers provide accurate track reconstruction, while the multi-wire proportional chambers (MWPCs) allow for a fast (but less precise) estimate of the track parameters for trigger purposes. The silicon detectors improve the track reconstruction of the drift chambers by providing a precise measurement of track parameters close the beam pipe.

Drift chambers consists of anode and cathode wires arranged to create a nearly uniform electric field. Ionisation left by the passage of a charged particle drift to the anode wire plane at nearly constant velocity. A precise spatial measurement is possible in the drift volume through measurement of the electron (and ion) drift time. The third space coordinate can be reconstructed by comparing the current read out at both ends of the wire, with a resolution of approximately 1% of the wire length. Also, the event timing can be reconstructed from the drift times to the wires.

The multi-wire proportional chambers at H1 consist of many closely spaced anode wires placed between cathode plates. The charged particle ionises the gas as it passes through the chamber. The ionised electrons accelerate towards the closest anode wire, leading to further ionisation and causing an avalanche of secondary ions. The resulting signal is proportional to the initial ionisation. The signals are collected promptly enough for use in triggering and give a spatial precision of the wire spacing

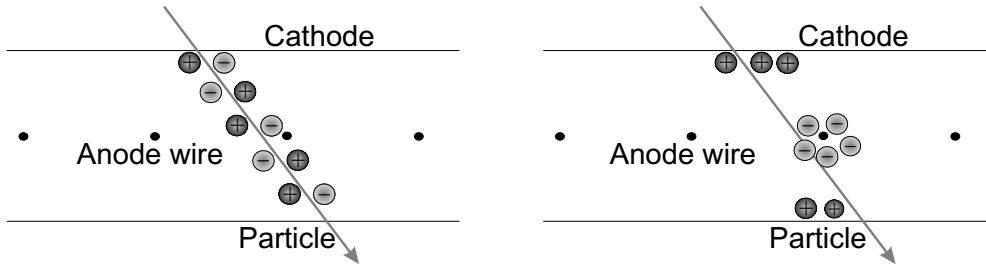


Figure 3.15: Principle of drift and multiwire proportional chambers: Charged particles interact with the gas molecules and produce positive ions and electrons. With HV applied between the anode wires and the cathode plane the ionised electrons are accelerated towards the anode wire and positive ions drift to the cathode.

(approximately 10 mm).

Silicon trackers are placed close to the beam pipe in order to precisely measure the ep vertex and to detect secondary vertices created by the decay particles of long-lived hadrons. The silicon strip detectors at H1 consist of n-type silicon wafers, etched on one side with thin parallel strips of p-type silicon. A charged particle passing through the wafer creates electron-hole pairs which drift towards the surfaces on application of a voltage. Since the energy needed to create an electron-hole pair, 3.6 eV, is approximately an order of magnitude smaller than the ionisation energy of a liquid or gas, an adequate signal can be collected in thin silicon wafers (typically a few 100μ). The low threshold means that low noise readout electronics is needed.

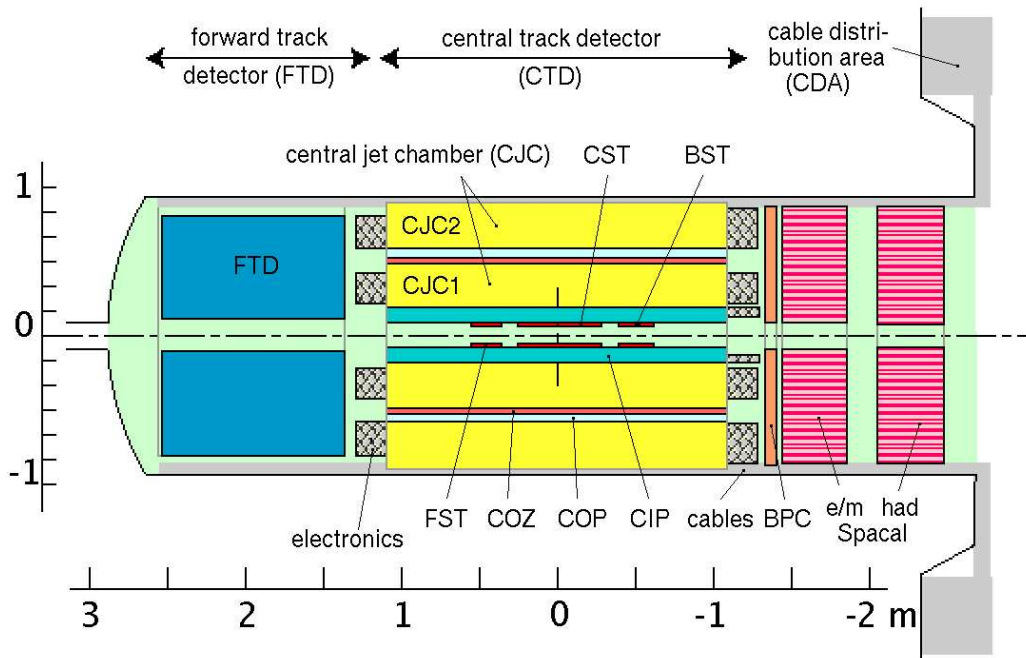


Figure 3.16: The side view of the tracking system.

The different tracking detectors of the H1 tracking system are displayed in figure 3.16. In the forward region drift chambers are employed for track reconstruction in the *For-*

ward *Track Detector* (FTD). In the central region, drift chambers are employed in the *Central Jet Chamber* (CJC) and the *Central Outer Z-Chamber* (COZ) of the Central Tracking Detector. Trigger signals are provided in the central region by the *Central Inner* and *Central Outer Proportional Chambers* (CIP and COP). In the backward region, tracks are reconstructed in the *Backward Proportional Chamber* (BPC). Inside CTD, directly surrounding the beam-pipe, the *Forward Silicon Tracker* (FST), *Central Silicon Tracker* (CST) and *Backward Silicon Tracker* (BST) are installed to improve the track measurements provided by the drift chambers.

Detector	θ_{min}	θ_{max}
FST	8°	16°
FTD (planar and radial chambers)	5°	25°
CST	$\sim 30^\circ$	$\sim 150^\circ$
CIP	9°	172°
CJC	15°	165°
COP	25°	156°
COZ	25°	156°
BST	162°	176°
BPC	153°	176°

Table 3.2: Geometrical acceptances of the individual tracking detectors in the forward, central and backward regions of the H1 detector; the minimum and maximum polar angles of charged particles within the detector acceptances are referring to the nominal interaction point.

In combination, the different tracking detectors allow the direction and momentum of charged particles to be measured in the angular range $5^\circ \lesssim \theta \lesssim 176^\circ$; the geometrical acceptances of the individual detectors are listed in table 3.2.

3.7.1 Central Tracking Detector

The central tracking detector (CTD) consists of five coaxial tracking chambers (see figure 3.17), with an angular coverage of $15^\circ \lesssim \theta \lesssim 165^\circ$. The main components of CTD are the central jet chambers, CJC1 and CJC2, which provide an accurate reconstruction of the transverse momentum and azimuthal angle of charged particles. For a precise reconstruction of the polar angle, the central jet chambers are supplemented by the COZ, which provides a complementary measurement of the z -coordinate. Last but not least, the CTD includes the COP and CIP, which provides a fast reconstruction of the event vertex for trigger purposes.

The CJC1 and CJC2 [74] are two larger cylindrical drift chambers. The CJC1 consists of 30 cells with 24 sense wires parallel to the z axis, the CJC2 consists of 60 cells with 32 wires. From the drift-time measured by the anode wires, single hits are reconstructed with a spatial resolution in the $r - \phi$ plane of $\sigma_{r-\phi}$ about $170 \mu\text{m}$. Along the anode wires a resolution of σ_z of about 22 mm, of the order of 1% of the wire length, is obtained by charge division. The event timing can be determined with a precision of about 1 ns from the drift times. The CJC allows measuring the transverse momentum, p_T of a charged particles, with a resolution

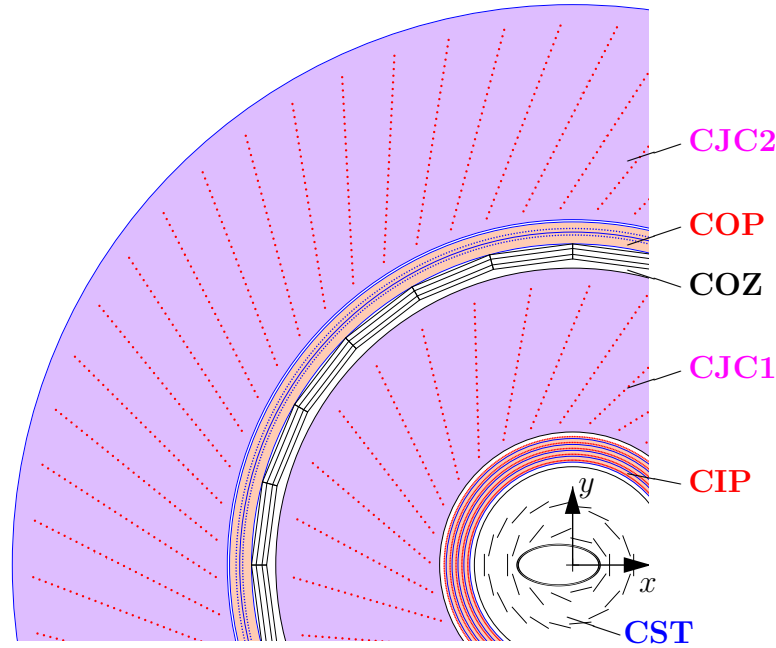


Figure 3.17: Cross-section view of the central track detector.

$$\frac{\sigma(p_T)}{p_T} = 0.01 \cdot p_T[\text{GeV}], \quad (3.17)$$

and a measurement of dE/dx with a resolution of about 10%.

The jet chamber cells are tilted by about 30° such that in the presence of the magnetic field the ionisation electrons drift approximately perpendicular to stiff, high momentum tracks originating from the centre. This not only gives optimum track resolution, but also leads to additional advantages: The usual drift chamber ambiguity is easily resolved by connecting track segments of different cells. The wrong mirror track segments do not match, as demonstrated in 3.18. They also do not point to the event vertex and therefore obstruct only small parts of a real track in the opposite half cell. Each stiff track crosses the sense wire plane at least once in CJC1 and in CJC2. From the fine match at crossing, the passing time of a particle can be determined to an accuracy of about 0.5 ns. This allows an easy separation of tracks coming from a different bunch crossing.

The central outer z -chamber (COZ) are located between CJC1 and CJC2 and complements the measurement of charged track momenta. This chamber delivers track elements with typically $300 \mu\text{m}$ resolution in z , which can be linked to those obtained from the jet chamber for the final accuracy on both the longitudinal as well as the transverse momentum components. The polar angle covered by COZ is $25^\circ < \theta < 156^\circ$.

The *Central Inner Proportional* chamber (CIP) is designed as a five layer multiwire proportional chamber with cathode pad readout.

In figure 3.19 a side view of the CIP chamber is shown in the rz -plane. A strong elec-

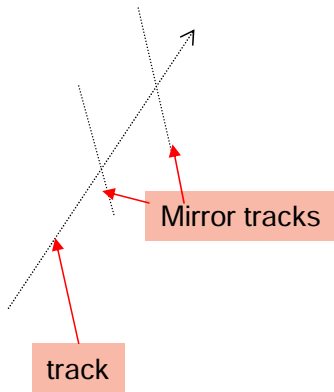
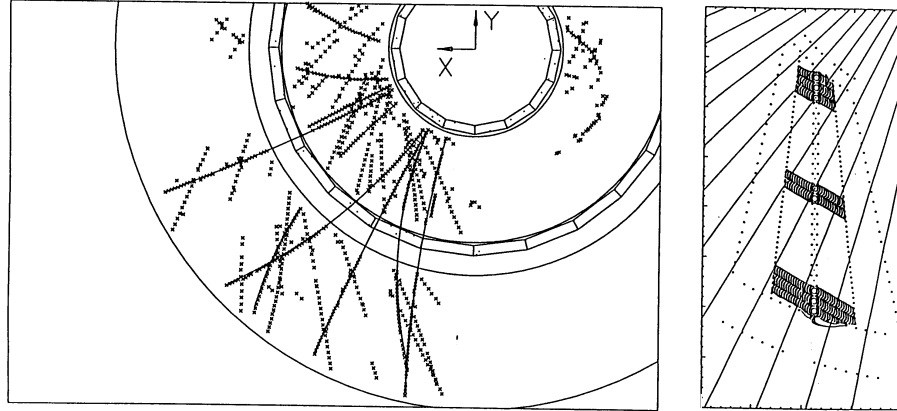


Figure 3.18: Illustration of mirror tracks in the central track detector, resulting from the left-right ambiguity in drift chambers. The tilted anode wire planes cause mirror track segments to neither link with track segments in neighbouring drift cells nor to point to the event vertex, allowing for mirror tracks to be easily identified.

tric field of about 2kV is applied between the wires and ground. On the inner side, the cathode plane is made of aluminium. On the outer side, a capton layer, coated with carbon, is used as cathode. The carbon has a finite resistivity (550-600 k Ω m), thus the positive charge does not immediately discharge and an electric potential between ground and the location of the charge accumulates. On the lower right side of figure 3.19, the equivalent circuit diagram of the cathode pad readout is shown. The signal of a charged particle is separated into negative charge at the anode wire (negative pulse form) and a positive induced charge on the carbon ground plane. A capacitor, consisting of the carbon layer and the readout pad with capton-foil as dielectric, transports the charge to the readout electronics. The induced charge of every single pad is fed into a charge-sensitive amplifier and then to a discriminator for digitisation [76].

The cathode pad readout leads to a precise and fast detection of the position of the particle in the rz -plane.

The *Central Outer Proportional* chamber (COP) is two layer multi wire proportional chamber located between the inner and the outer central jet chamber (CJC1, CJC2). The CIP and the COP together can reconstruct the z vertex position with a resolution of about 5 cm in a region within 44 cm of the nominal interaction point.

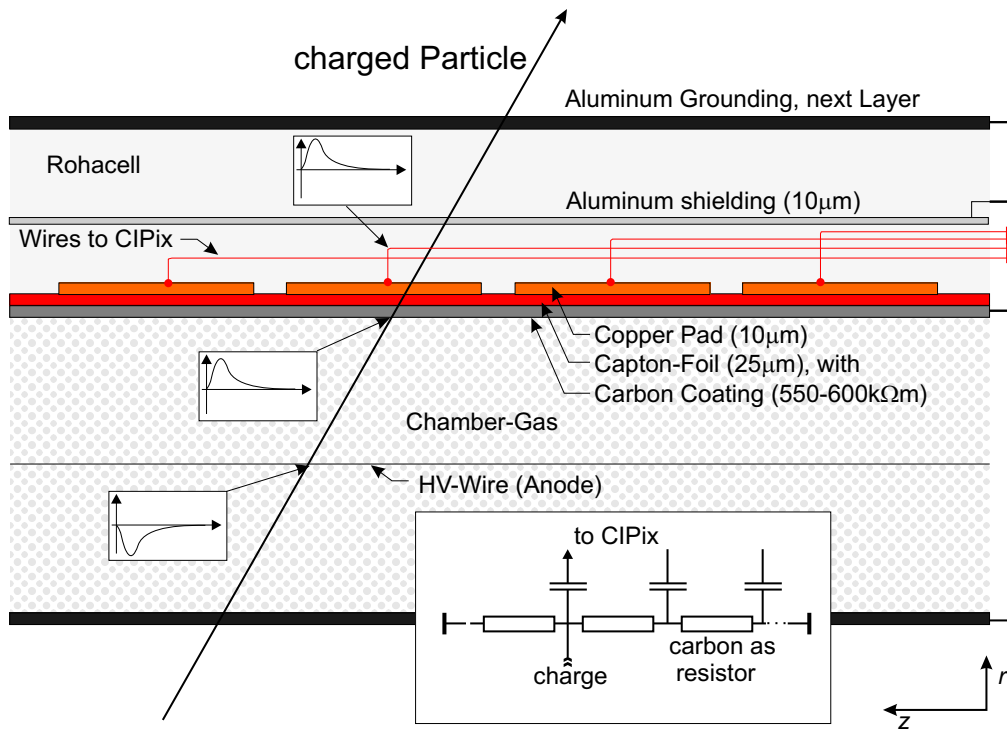


Figure 3.19: Side view of the CIP chamber in the rz -plane: The charged particle deposits charge, that cannot discharge immediately due to the high resistance of the carbon coating. Thus, a current is induced on the cathode pad near the accumulation of the charge.

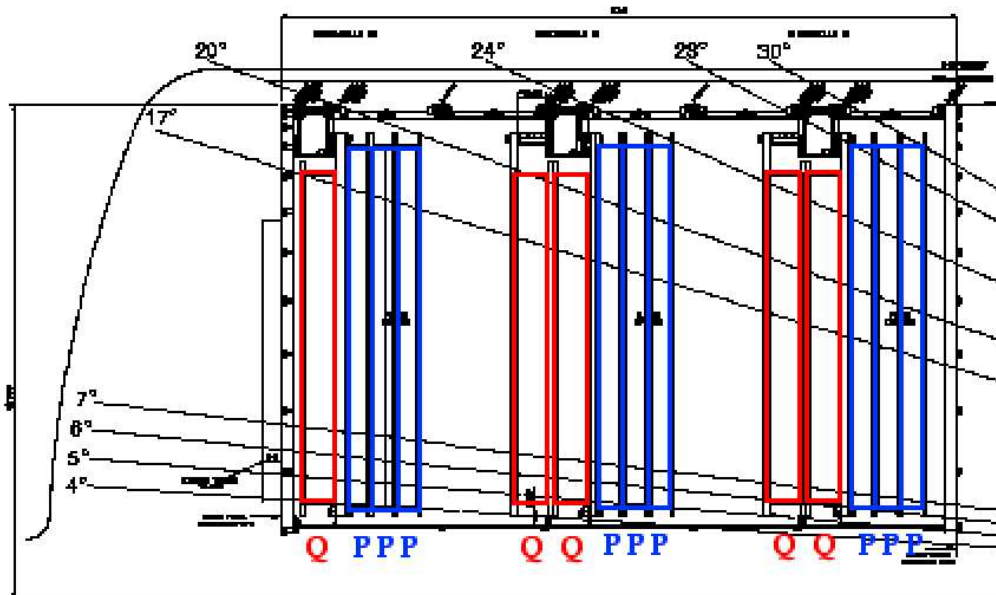


Figure 3.20: The Forward Tracking Detector.

3.7.2 The Forward Tracking Detector

The Forward Tracking Detector (FTD) extends the tracking coverage of the H1 detector in the forward region, providing a polar angle measurement in the range

$5^\circ < \theta < 25^\circ$. The FTD consists of nine planar drift “P” chambers and five “Q” chambers collected into three “supermodules”, as illustrated in figure 3.20.

Each supermodule consists of three P chambers, oriented at 0° , 60° and -60° in azimuth, and two Q chambers (one in the most forward supermodule), oriented at 30° and 90° . The P chambers consists of four layers of wires, each strung in the xy plane, and the Q chambers have eight layers of wires.

3.8 The Muon System

The muon system is mounted outside the superconducting solenoid magnet. The *Central Muon Detector* (CMD) is integrated into the iron yoke. Ten iron layers, each 7.5 cm thick, are instrumented with limited steamer tubes. The detector covers the angular region $4^\circ \leq \theta \leq 171^\circ$ and allows to detect muons with an energy greater than 1.5 GeV. The CMD is subdivided into four subdetectors (forward end cap, forward and backward barrel and backward end cap, see figure 3.21).

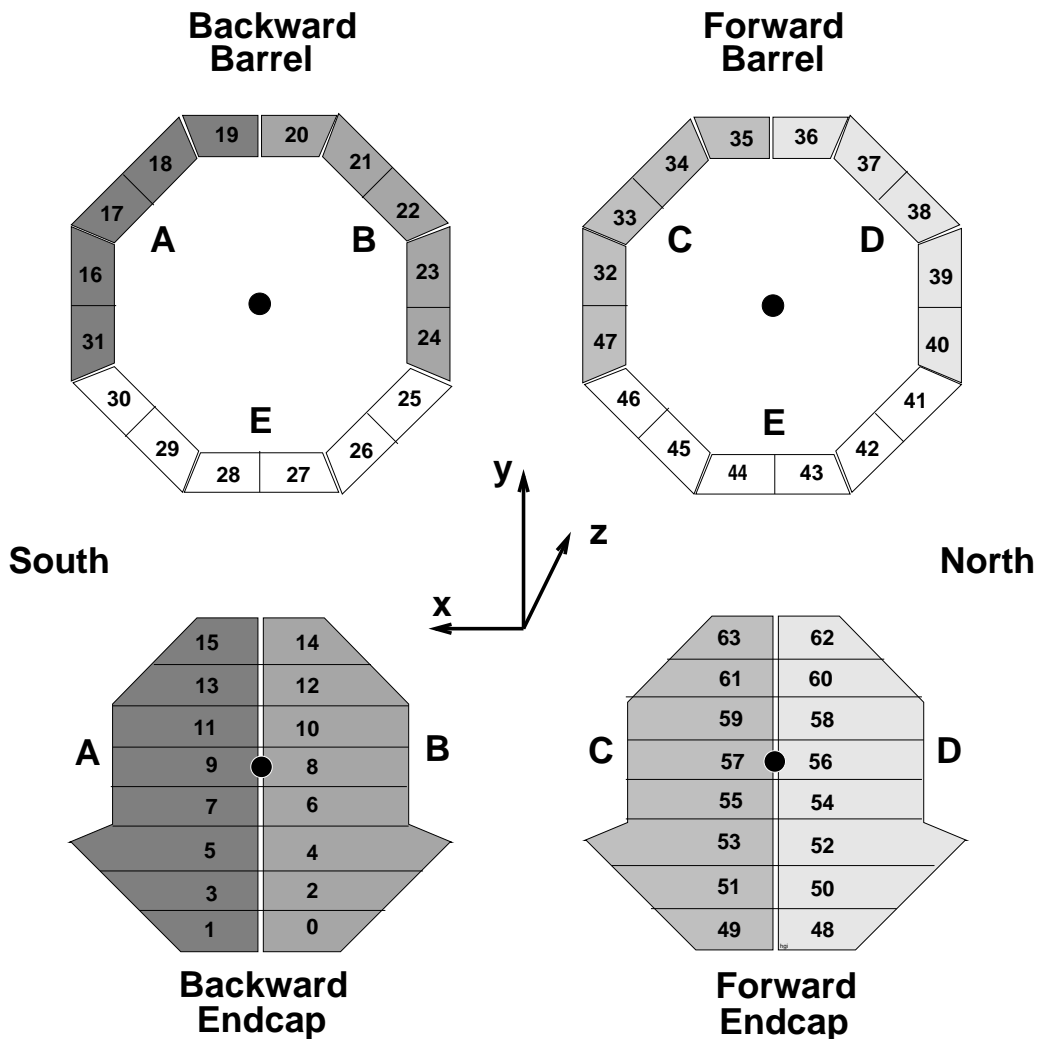


Figure 3.21: Division of the central muon system into modules.

The *Forward Muon Detector* (FMD). The FMD is situated between 6.4 m and 9.4 m forward of the nominal ep interaction vertex and detects muons in a polar angle range $3^\circ \leq \theta \leq 17^\circ$. It consists of six double layers of drift chambers, three on either side of a toroid magnet. The toroid provides a field varying with radius, from 1.75 T at a radius of 0.65 m to 1.5 T at a radius of 2.90 m. Only muons with momenta of at least 5 GeV will pass through this detector. The FMD is also used to detect highly energetic forward jets.

High energy muons from ep interactions are not absorbed in the calorimeters but penetrate into the muon system. Due to the large amount of material in front of and inside the muon detectors, the muons suffer significant multiple scattering, which allows only a rough measurement of the muon momentum in the toroid field of the FMD.

3.9 Time-of-Flight Counters

Fast scintillation detectors at H1 are used to distinguish real ep interactions from beam-induced background. The particles produced from ep interaction will arrive at a different time than particles produced from the background interactions relative to the nominal time of the bunch crossing. This is caused by different path lengths and different times of interactions. Background events produced near the nominal vertex cannot be distinguished from genuine ep interactions in this way. The scintillation counters, however, give a significant reduction of the background with vertices far away from IP.

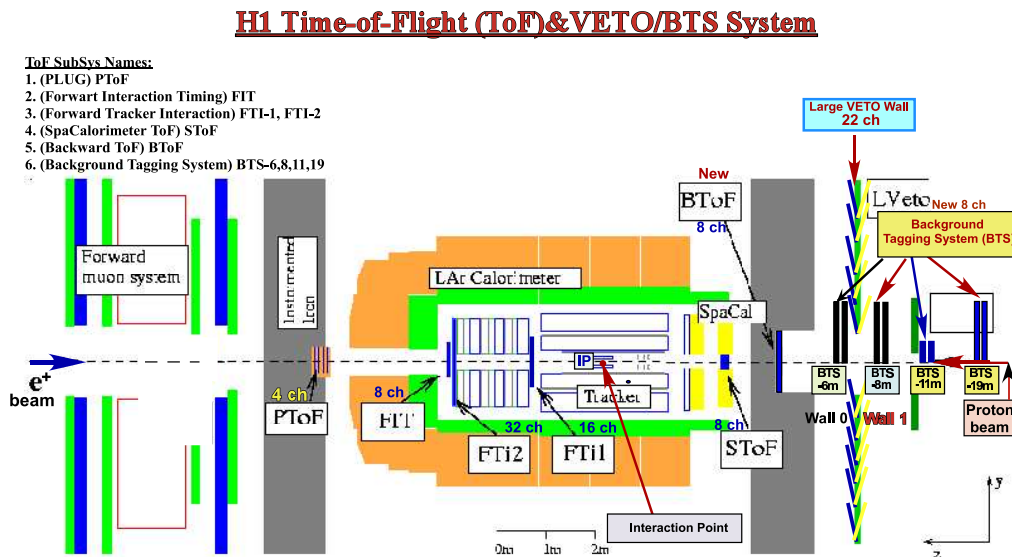


Figure 3.22: The ToF system.

The Time-of-Flight (ToF) system consists of a number of components. The ToF devices are placed close to the beam-pipe, as illustrated in figure 3.22: the PToF is located within the unused gaps of the PLUG absorber; the SToF is integrated inside

the SpaCal calorimeter; the BToF is behind the backward end-cap of the instrumented iron. The FTi system was added during the HERA II upgrade. FTi2 (FTi1) sits in front (behind) the Forward Tracker at $z = 2.65$ m (1.45 m). The FIT, which has been installed in 1998, can be found just downstream of FTi2. Finally, the Large Veto Wall (LVeto) at $z = -6.5$ m is used to detect particles from the proton beam halo as well as upstream proton background.

3.10 Luminosity System

The luminosity is determined from the rate of *Bethe-Heitler* [75] events $ep \rightarrow ep\gamma$ having a large and precisely calculable cross section (known with an accuracy of about 0.5%). The main source of background is bremsstrahlung from the residual gas in the beam pipe, $eA \rightarrow eA\gamma$, with an even a larger cross section and the same experimental signature. The rate of these events at design luminosity for the pressure in the beam pipe is at the level of 10% of the $ep \rightarrow ep\gamma$ rate. This background is measured experimentally using the electron pilot bunches. Then the luminosity is calculated as

$$L = \frac{R_{tot} - (I_{tot}/I_0)R_0}{\sigma_{vis}}, \quad (3.18)$$

where R_{tot} is the total rate of the bremsstrahlung events, R_0 is the rate in the electron pilot bunches, I_{tot} , I_0 are the corresponding electron beam currents and σ_{vis} is a visible part of the $ep \rightarrow ep\gamma$ cross section, taking into account the acceptance and the trigger efficiency of the luminosity detector.

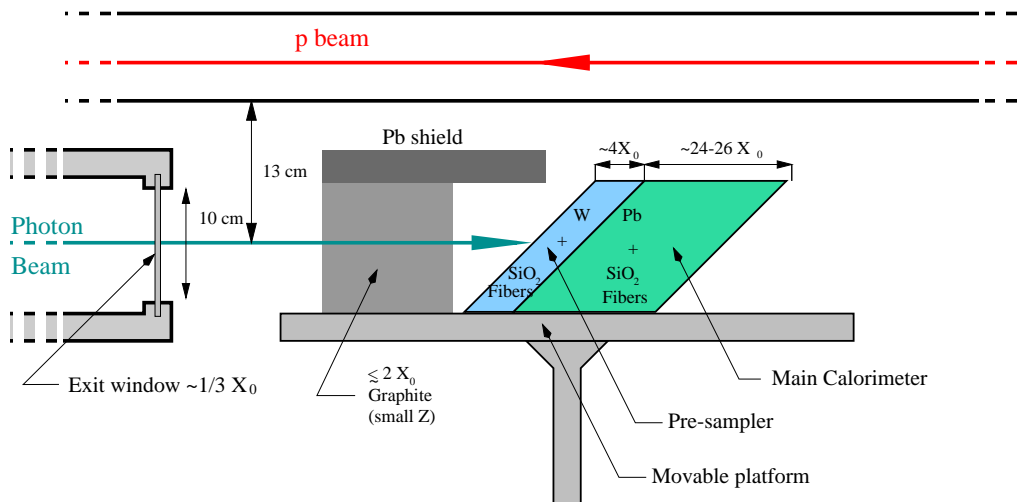


Figure 3.23: Layout of the Photon Detector in the tunnel: the γ beam axis is 13 cm below the proton beam pipe. An absorber of roughly $2X_0$ reduces the amount of synchrotron radiation (and the produced heat) directly hitting the presampler and the main calorimeter. All the detectors are mounted on a vertically movable table.

The main components of luminosity system are three small angle calorimeters the Photon Detector (PD) and Electron Taggers (ET6, ET40). The luminosity system has following functions:

- Continuous online measurement of the luminosity and monitoring of the electron beam at the interaction point, for feedback to HERA.
- High precision off-line measurement of the integrated luminosity.
- Tagging of $Q^2 < 0.01 \text{ GeV}^2$ photoproduction events, and energy measurement of the electron, scattered at very small angles.
- Measure “hard” photons from the initial state QED radiation in DIS.

The luminosity system has been substantially modified to deal with the challenges of HERA II [113,114]. The strong focusing and bending (see section 3.4) of the electron beams leads to a significantly higher rate of synchrotron radiation compared to HERA I. The Photon Detector (PD) must be sufficiently radiation-hard to function in this hostile environment. The PD is now protected by two interaction lengths of absorber with a low atomic number, Z , in order to strongly attenuate the synchrotron radiation while limiting the degradation of the Bethe-Heitler photon energy spectrum. Multiple photons may be produced per bunch crossing at the increased design luminosities at HERA II. For this reason, upgraded electronics is necessary to control photon pileup effects. Finally, the additional focusing magnets close to the beam-pipe, near the H1 Interaction Point, restrict the possible position of electron taggers in the backward region.

The bremsstrahlung photons are measured by the *Photon Detector*, installed next to the beam-pipe in the upstream direction at $z_{PD} = -101.8 \text{ m}$ (see figure 3.23). The Photon Detector is a Cherenkov sampling fibre calorimeter consisting of optical quartz fibres (24 channels) sandwiched between layers of tungsten radiator plates. It has length of $25X_0$ and transverse size of $12 \times 12 \text{ cm}^2$. The PD is preceded by $2X_0$ of Beryllium absorber, which attenuates the synchrotron radiation by almost five orders of magnitude. The photon detector provides a luminosity measurement by counting the photons above an energy threshold and comparing to the predicted Bethe-Heitler cross section to determine the instantaneous luminosity (see equation 3.3). It also measures the x and y position of the photon in order to provide feedback on the beam tilt to HERA. The water Cherenkov detector installed in front of the photon detector is used as a *Veto Counter* (VC) to have an independent way to measure the bremsstrahlung process. The Cherenkov detector is read out by two photomultipliers giving two channels: a spectrometric channel (nominal HV) and a veto channel (increased HV). It has a length of 5 cm ($0.15X_0$) along the beam.

A compact *Electron Tagger*, ET6, is installed at -5.4 m , where scattered electrons are directed into its acceptance by the beam optics. The ET6 is a lead/tungsten 12 channels (6×2 cells) SpaCal type calorimeter (see section 3.6.2) with a transverse size of $75.6 \times 25 \text{ mm}^2$ and a depth of 20 cm ($22 X_0$). The electron tagger is used to measure the energies of the scattered electron from low Q^2 photoproduction processes. Another electron tagger, the ET40, is installed at -40.0 m . It is a six channel (2×3 crystals) total absorption Cherenkov calorimeter, made of $2 \times 2 \text{ cm}^2$ KRS15 crystals, with a hodoscopic structure.

The luminosity is measured online at 10 second intervals. The luminosity is determined offline with a high level of accuracy. The photon detector energy is calibrated and corrections are made for energy losses in the Beryllium absorber. Corrections are

applied for pileup from multiple photons and for the acceptance of the PD. Finally, the luminosity is corrected for so-called “satellites bunches” which precede and follow the main proton bunches at ± 70 cm.

3.11 Trigger System

The HERA bunch crossing interval is 96 ns (corresponding to a BC frequency of ~ 10 MHz) and is about four orders of magnitude smaller than the time needed by the H1 detector to write out information from its various components. However, the majority of events detected by H1 are background, mostly caused by synchrotron radiation, cosmic muons and muons from proton halos and proton induced background (proton-beam wall interactions, and proton-gas particle interactions, referred to as “beam-wall” and “beam-gas” interaction, respectively). Since the background processes have a rate about 10^4 times higher than the electron-proton collisions, it is essential to trigger on interesting collisions in a manner that minimises dead-time, in which the detector is not sensitive to new events. For this purpose, the H1 detector uses a pipelined, multi-layered trigger system, illustrated in figure 3.24.

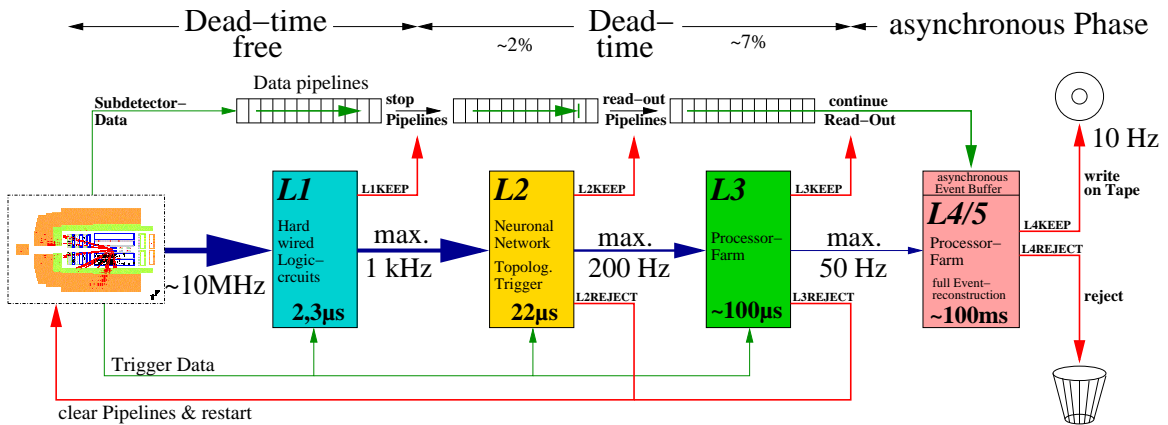


Figure 3.24: Illustration of the four-level trigger system of the H1 experiment. The status of the pipelines buffering the event information is shown as well as the dead-time generated by the different trigger levels during nominal operation of the H1 experiment.

3.11.1 Trigger Level One

The first trigger level selects candidate events for interesting ep interactions with a trigger rate of about 1 kHz. The processing time available to reach a trigger decision on L1 is 24 BC, during which time the information of subdetectors is buffered in circular pipelines. To meet these time constraints, the first trigger level is constructed of fast hardwired logics. The L1 trigger decision is based on a maximum of 256 *trigger elements* (L1TE), which are sent from the various subdetectors to the trigger system and describe the particle activity in the respective subdetectors. Since the generation of trigger elements needs a variable period of time in different subdetectors (depending on their response time, cable delays, and the time needed for processing), the trigger elements have to be synchronised by the central trigger logic. The 256 trigger elements

are logically combined to a maximum of 128 *raw subtriggers* (L1RAW). Many of the 128 available subtriggers are defined as *physics triggers*, which are configured to trigger efficiently the signatures of the different *ep* processes under study. The physics triggers are complemented by several *monitor triggers*, which are used to check the performance of individual subdetectors and to determine the efficiency of the physics triggers. As not all fulfilled physics or monitor trigger conditions are intended to initiate an event read-out due to excessive rate, each L1RAW may be individually *prescaled*. A prescale factor of n means that the respective raw subtrigger is set in only one out of n times, corresponding to an *actual subtrigger* (L1AC). The L1 trigger decision is determined by the actual subtriggers. An *L1keep* signal is issued by the central trigger logic for a certain BC, if at least one actual subtrigger fires in that BC:

$$L1keep = OR(L1_i^{ac}).$$

The *L1keep* signal stops the circular pipelines buffering the event information. As long as the pipelines remain stopped, the H1 detector is insensitive to further *ep* interactions. Accordingly, the *L1keep* signal starts the dead-time of the detector. Otherwise, in case none of the actual subtriggers is set, the event information in the pipelines is simply overwritten by the data of succeeding bunch-crossings and no dead-time is generated.

The LAr Calorimeter Trigger

Overview: The liquid argon calorimeter trigger is one of H1's central triggering devices. The trigger is processing the information of approximately 45000 *Geometric Pads* (GP) which are the basis of all LAr calorimeter energy measurements. In order to reduce the number of signals to a manageable level for the trigger electronics, the analog signals of the GPs are added up in a parallel electronic chain to 4846 so-called *Trigger Cells* (TC) (for the readout chain of the calorimeter the GPs remain separated). From these trigger cells, 688 *Trigger Towers* (TT) and, after further analog summing, 256 *Big Towers* (BT) are built, each of them split in an electromagnetic (EM) and a hadronic (HA) section. The resulting 512 analog signals are digitised in fast ADCs (FADC). Further processing delivers, after so-called *AdderTree* (AT) hardware, quantities like energy sums or BT counters, i.e. the numbers of BT containing energies above a certain threshold. From these quantities the LAr Trigger Elements (TE) are derived, which are then fed to H1's central trigger decision logic (CTL).

The LAr Trigger Hardware: The LAr trigger electronics is divided into an analog and a digital part. The task of the analog part is to reorder and to combine the analog signals from the 45000 geometric read out pads into 256 geometrically motivated projective objects, *Big Towers* (BT), which are divided into EM and HA sections. These 2×256 BTs are digitised with fast analog to digital converters (FADC, 10.4 MHz frequency) and fed into digital summing electronics yielding various energy sums. These sums are finally discriminated using programmable threshold functions, providing the TEs for the CTL. A general overview of the electronics of the LAr trigger is presented in figure 3.25.

Besides the fast determination of the TEs the trigger has to deliver the exact time or bunch crossing of the corresponding energy deposition (the so-called " T_0 signal").

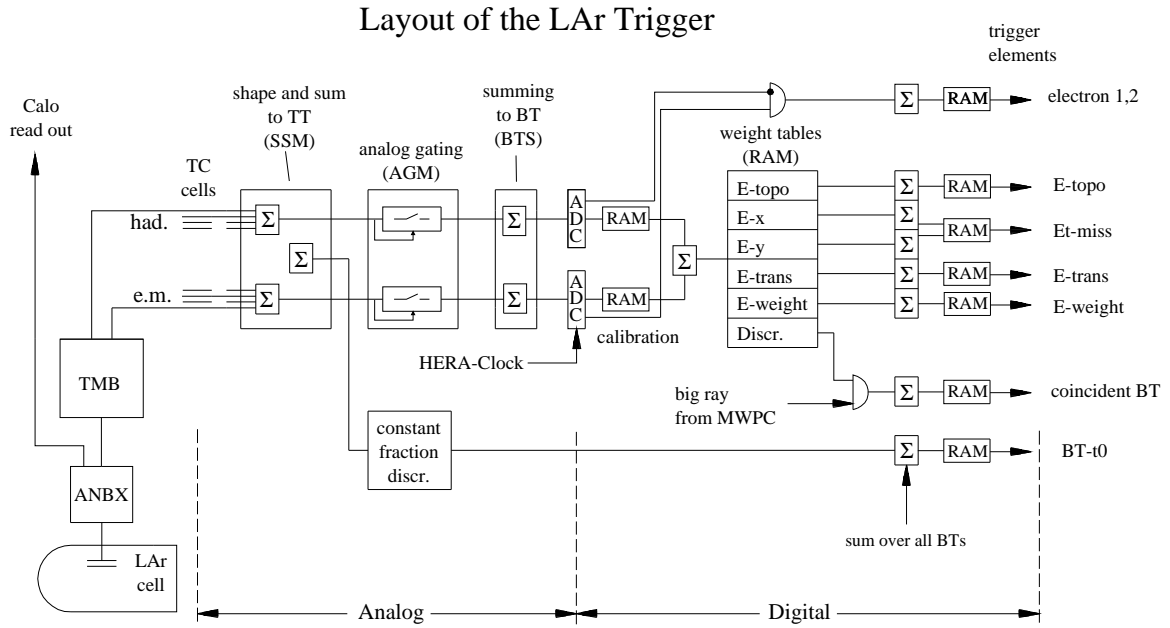


Figure 3.25: Schematic overview of the H1 LAr trigger. See text for details.

This is done in a separate data stream in the analog part by means of a pulse delay and crossing technique at the TT level. The gated T_0 signals are then synchronised with the HERA clock signal, logically *OR*'ed and sent to the CTL as a single logical pulse of one BC length.

The analog signals have their origin in the deposition of ionisation charges produced by particle showers. The ionisation charges are collected on the GPs; the resulting signals are fed into the front-end *Analog Cards* (ANCD) which are situated in the *Analog Boxes* (ANBX) mounted on the LAr cryostat. On these cards, the GP signals are amplified by preamplifier hybrids. This amplification is common to the trigger and to the calorimeter read-out data streams. The GP signals, used for energy measurement, are stored for later readout on so-called “sample-and-hold electronics”.

Still on the ANCDs, a first reduction of the data volume for the trigger is achieved by summing the GP signals to TC signals: in the EM part of the trigger 16 neighbouring geometric pads of the calorimeter are summed to give a TC; for the hadronic case 4 pads are summed into one TC. Only pads of one layer are summed into one TC to minimise smearing of the signals' amplitudes due to timing variations caused by different pad capacities contributing to the TC.

The TC signals are then transferred from the ANCDs to the H1 electronic trailer. On the *Trigger Merging Board* (TMB) the trigger cells are re-arranged to projective⁷ TTs. In this way the HERA event kinematics can be taken into account. The actual summing of TCs to TTs is done in the *Summing-and-Shaping Modules* (SSM), where the TC signals are also individually adjusted in amplitude and synchronised in time. Up to 4 EM cells give one EM tower, up to 6 HA cells one HA tower. In case of problems (for example noise) it is possible to exclude single cells from the summation via *switches* on the SSM; these switches are computer controlled. At this stage, the EM and HA trigger tower signals are still separate. In addition, the sum of the two

⁷“Projective” means “pointing to the nominal interaction vertex”.

is available to derive a T_0 signal for the TT.

After the SSM, the TT signals are discriminated in the *Analog Gating Modules* (AGM). Both the EM and the HA part of the TT signal are compared to separate thresholds, adjustable for each TT independently. Signals below the threshold are suppressed. The height of the AGM threshold is of crucial importance for the efficiency of the LAr trigger as it determines how well low energy signals can be triggered.

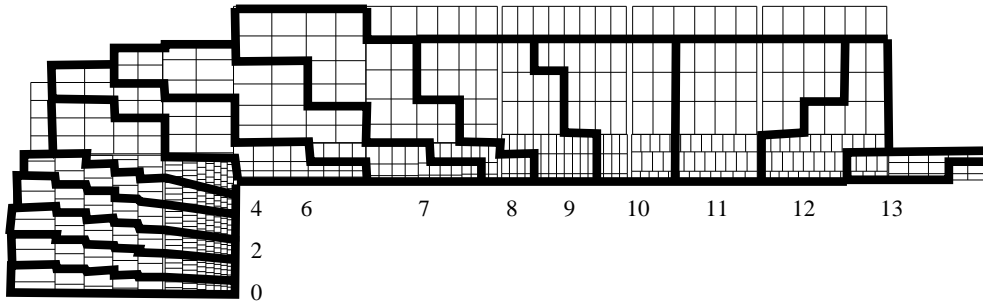


Figure 3.26: Arrangement of Big Towers in the LAr calorimeter. Each tower points toward the nominal interaction vertex.

In the last step of the analog signal path, the BT signals are built in the *Big Tower Summing Units* (BTS). The EM and HA signals of up to 4 TT are summed separately to give the EM and HA BT energies. The BTs thus show a coarser granularity than the TTs, but as these they are pointing to the nominal interaction vertex. In the polar angle θ the calorimeter is divided in 14 BTs, in φ up to 32 BTs are found, depending on the position in θ . The finest granularity is realised in the forward direction where strongly collimated jets due to the Lorentz boost are expected. The spatial arrangement of the BTs as a function of θ is shown in figure 3.26. The BT signals are finally fed into the fast ADC's and are digitised with 8 bit precision.

As mentioned above, the analog sums of the EM and HA parts of the TT signals are used to derive the T_0 for a given TT. To do this, the signal, which has a width of about $1 \mu\text{s}$, is delayed by 500 ns and the original and the delayed signal are overlaid. The intersection of the two curves defines the time (the “asynchronous T_0 ”) for the given TT, if the signals are above a given θ -dependent threshold. Note that the crossing point is independent of the signal amplitude. Synchronising this T_0 with the HERA clock gives the synchronous TT- T_0 . The logical OR of all TT belonging to a certain BT defines the T_0 for this BT. The number of BT T_0 signals are summed up in the digital adder tree.

Digitised by FADCs, the electromagnetic and hadronic signals from each BT are used to identify electron candidates; Big Towers are also used to from global energy sums and topological quantities.

The LAr Calorimeter Trigger Elements: The LAr trigger elements important for this analysis are:

- **LAr_electron_1:** The LAr_electron_1 Trigger Element is set if the electromagnetic energy deposited in a BT exceeds a given threshold value and the energy in the associated hadronic big tower is lower than a certain threshold value. The thresholds for the LAr_electron_1 TE range from 5 GeV in the backward region to 25 GeV in the IF.

$$\text{LAr_electron_1} = \sum_{BT} \text{BT_electron_1}$$

- **LAr_T0:** The LAr_T0 (“event T0”) is set when the number of all BTs giving a T0 signal exceeds a certain value. For the actual HERA running one BT T0 signal is sufficient to fire the LAr_T0.
- **LAr_Etmiss:** The LAr_Etmiss TE is the total missing transverse momentum measured in the calorimeter. It is calculated from the BT energies and angles:

$$\text{LAr_Etmiss} = \sqrt{\left(\sum_{BT} P_{BT,x}\right)^2 + \left(\sum_{BT} P_{BT,y}\right)^2},$$

with

$$P_{BT,x} = E_{BT} \sin \theta_{BT} \cos \varphi_{BT},$$

$$P_{BT,y} = E_{BT} \sin \theta_{BT} \sin \varphi_{BT},$$

where θ_{BT} , φ_{BT} and E_{BT} are Big Tower’s angles and energy. The Big Tower energy must exceed a θ -dependent threshold to be accepted in the adder tree. The two Big Towers θ bins at the lowest angles (closest to the beam-pipe) are not included in the sum since they are very sensitive to background from beam-gas and beam-wall interactions.

The CIP Trigger

The Central Inner Proportional chamber provides the z vertex trigger for the H1 experiment [76]. The CIP provides fast trigger information on the origin of tracks along the z (beam) axis. The track finding performed by the CIP trigger is demonstrated in figure 3.27. Tracks are formed by a combination of hits from at least three layers of the CIP and are extended to the beam axis. The z origins of the tracks are filled into a histogram with 22 bins. This allows the reconstruction of bins in a range of about 380 cm along the z axis (compared to the active length of the CIP of 220 cm). The z resolution of about 20 cm is sufficient to identify and reject beam related background originating far from the interaction point.

The bins of the z vertex histogram are grouped into a forward region, a central region and a backward region. In the ep data taking, the backward tracks are defined as those originating from close to the C5A and C5B collimators and are identified as background.

- **T0 information (CIP_T0, CIP_T0_next_BC):** An important function of the CIP trigger is to provide a T0 signal, which is used as a timing reference. The T0 is set to 1, if at least one track is seen in the central region. Additionally, the same T0 signal is given exactly one bunch crossing earlier in the second bit

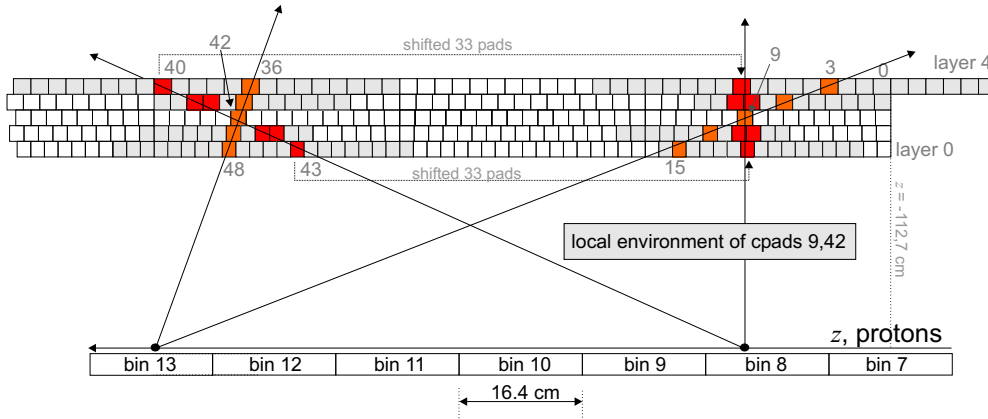


Figure 3.27: The projective geometry of the CIP is shown. The event vertex is reconstructed by building a histogram of the possible z origins of tracks and identifying the event vertex as lying in the bin with the highest population.

of the 16-bin trigger element word. This signal is called `T0_next_BC`. If a trigger comes at the same time as the `T0_next_BC`, it has most likely the wrong timing and can be rejected.

- **Significance of tracks from the central region (`CIP_sig`):** Two trigger elements (4 possible states) are used to give the ratio between the number of central tracks versus the number of background (backward + forward) tracks:

$$N(\text{central}) > S \cdot (N(\text{backward}) + N(\text{forward})). \quad (3.19)$$

If $S = 0$, there are more or the same number of background tracks than central tracks. On other hand, if $S > 0$, there are S times more central tracks than background tracks, as shown in table 3.3.

<code>CIP_sig</code>	0	1	2	3
S	0	1	2	4

Table 3.3: The significance is set to the given value if the number of tracks in the central region is S times higher than the number of backward and forward tracks.

- **Multiplicity information (`CIP_mul`):** Three trigger elements are reserved for an event multiplicity information. This means, that the total number of tracks, counted in the CIP trigger, are added:

$$N(\text{central}) + N(\text{forward}) + N(\text{backward}) > M. \quad (3.20)$$

The value M is correlated with the number of tracks given to the central trigger control in the 3-bit decoded multiplicity as described in table 3.4.

Veto Triggers

Veto conditions are applied to a large number of subtriggers in H1. They mainly reject background from beam-gas and beam-wall interactions.

CIP_mul	1	2	3	4	5	6	7
M	0	2	6	10	20	30	100

Table 3.4: The multiplicity is set to the described values if the number of tracks (M) is higher than the presented threshold.

- **ToF-Veto:** Scintillators with excellent time resolution (better than 2 ns) are able to place events in either an interaction (IA) or background (BG) time window. The ToF-Veto is based on the VETO_BG, BToF_BG, STof_BG and FIT trigger elements of the ToF system described in section 3.9.
- **CIP-Veto:** The CIP can be used to veto background coming from collimators close to the H1 interaction region. The requirement (CIP_mul==7 && CIP_sig==0) efficiently rejects background by tagging events with a high (> 100) track multiplicity and a majority of background tracks.

3.11.2 Trigger Level Two

The L1 trigger decision is validated by the *second level trigger* (L2). The L2 consists of two independent trigger systems, the *neural net trigger* (L2NN) and the *topological trigger* (L2TT). L2NN and L2TT have to decide within 20 μ s whether the event should be kept. Otherwise it will be rejected and the central trigger restarts the pipelines (*L2 Reject* signal). The L2 trigger gets L2-information from the subdetectors. Some trigger systems generate dedicated information for the L2 trigger. This information is used to validate or reject the L1 trigger decision.

The results of the L2 trigger are given to the central trigger L2 decision logic (CTL2).

L2NN: This trigger is based on neural networks (NN). The networks have to be trained with samples of *ep* and background events. For the neural network trigger, parallel processors are used. The L2NN trigger is described in detail in [77].

L2TT: The topological trigger (TT) is based on a matrix which represents the geometry of the detector in the (θ, φ) -matrix. A “distance to background” is calculated to find a trigger decision [78].

Following a positive L2 decision (*L2keep* signal), the readout of the about 270 000 channels of the H1 detector components begins. A detailed description of the L2 trigger can be found at [79].

3.11.3 Trigger Level Three

A third level of triggering is envisaged, employing a farm of RISC based processors, taking 50 μ s, employing the *Fast Track Trigger* and making more use of correlation between detector subsystems. An “L3 Reject” signal can stop the readout and restart the pipeline, thus terminating the dead-time.

The Fast Track Trigger (FTT) [80], commissioned as part of the H1 upgrade program, performs a fast reconstruction of CJC tracks. The FTT provides some trigger

elements for use at L1 and L2 and will be able to perform particle identification at L3.

3.11.4 L45 Processing

The final trigger level (L45, for level four and five) performs a complete reconstruction and classification of the event. It is an asynchronous trigger level, implemented by software algorithms running on a dedicated PC farm. The processing of the event information on the farm system starts once the central event builder of the data-acquisition system has finished collecting the raw event data provided by the subdetectors. At this moment, the pipelines are also started again, terminating the dead-time of the detector. The event filtering is achieved by making a full reconstruction of the event and classifying it into categories of potential interest. The L45 reconstruction software, H1REC, is described in [96]. Events which cannot be allocated to any *ep* physics class are rejected, apart from 1% which are kept for monitoring purposes. Furthermore, high rate soft scale processes are downscaled, in favour of more “interesting” events. The events surviving all trigger requirements are written to tape at a rate of approximately 5-10 Hz. The raw event information is stored along with the reconstructed data on “Production Output Tapes” (POTs) and the reconstructed information is also written to the more compact “Data Summary Tapes” (DSTs). DSTs are used as a starting point for analysis at H1.

3.11.5 The NC Stubtriggers

The triggering of NC events is based on the signature of high Q^2 NC events in the detector, i.e. a highly energetic scattered electron in the LAr calorimeter. The trigger element LAr_electron_1 is based on this condition. This trigger element is combined with the timing information from the LAr calorimeter and the central proportional chamber CIP. The subtriggers used in this analysis are ST67, ST77 ⁸:

ST67:	(LAr_electron_1) && (CIP_T0 (LAr_T0 && !CIP_T0_next_BC)) && (!VETO_BG && !BToF_BG && !SToF_BG) && (FIT_IA !FIT_BG) && (!(CIP_mul==7 && CIP_sig==0))	energy requirement time requirement ToF veto ToF veto CIP veto
ST77:	(LAr_Etmiss > 1) && (CIP_T0) && (FIT_IA !FIT_BG) && (!BToF_BG && !SToF_BG) && (!(CIP_mul==7 && CIP_sig==0))	energy requirement time requirement ToF veto CIP veto
ST57:	(LAr_electron_1) && (CIP_T0 (LAr_T0 && !CIP_T0_next_BC))	energy requirement time requirement

The majority of NC events is triggered by ST67. The decision of subtrigger ST67 is based on the recognition of a local energy deposit through the LAr_electron_1 trigger element. Having a high energy threshold (above 5 GeV) the rate of this trigger element is low. Since the CIP have a better time resolution than the LAr calorimeter the

⁸Here “&&“ denotes a logical AND, “||“ a logical OR, “!” a logical NOT.

timing requirement of LAr calorimeter is valid only if the central inner proportional chamber do not recognise the event in the next bunch-crossing.

Although ST77 is based on a missing energy requirement via $LAr_E_{miss} > 1$ it can be used to trigger NC events. Apparent missing transverse energy may arise when a highly energetic electron exceeds the dynamic range of the corresponding FADC. ST77 uses the timing requirement coming from CIP only.

The veto conditions added to ST67 and ST77 subtriggers are used to reject beam-wall and beam-gas background (see section 3.11.1).

The monitor ST57 trigger is a copy of ST67 without the veto conditions⁹ applied. It is prescaled to keep the rate manageable. ST57 is used to study the efficiencies of the ToF and CIP veto conditions.

3.12 Offline Analysis and H100

A complete new software environment for analysis, H100, has been developed, to complement the hardware upgrades for HERA II. The new software environment based on ROOT [109], written in C++ and utilising object oriented programming techniques, was designed and implemented over the course of the HERA luminosity upgrade project. A summary of the H100 project can be found in [110].

Data Storage

The physics data scheme consists of three layers of storage. At the lowest level is the *Object Data Store* (ODS), which is completely equivalent to the DST. The ODS stores the same track, cluster and other detector-level information as the DST, albeit represented as C++ objects. These are the classes H1Track, H1Cluster and H1Cell. In practice, to avoid duplication of information on disk, the ODS layer is usually created “on the fly” when accessing the DST. The DST contents are read and the ODS information for the event is created in memory. This has only a small performance penalty compared to accessing persistently stored ODS files. In this way, the transient ODS storage layer functions as an interface from the DST tapes to the H100 software. The second level, the *micro-ODS* (μ ODS), allows fast access to particle level information. The μ ODS stores identified particle four vectors (for example electromagnetic particles, hadronic particle hypotheses) and associated information. The third event layer, known as the *H1 Analysis Tag* (HAT), contains event level information such as the reconstructed vertex position, trigger information or kinematic quantities. The HAT is a flat tree, storing only simple variable types rather than collections of objects. This allows a fast pre-selection of events. At each state, the storage space needed per event decreases and the size of an event on the HAT is significantly smaller than on the ODS. The data storage levels are represented

⁹For most of the 2003-04 e^+p period ST57 had ToF veto requirements, as well. therefore it was used to monitor the *CIP_veto* condition only during that time. For the last part of the 2004 e^+p and whole 2005 e^-p part of running ST57 was loosened so that it contained no veto conditions, as given in the table above.

schematically in figure 3.28.

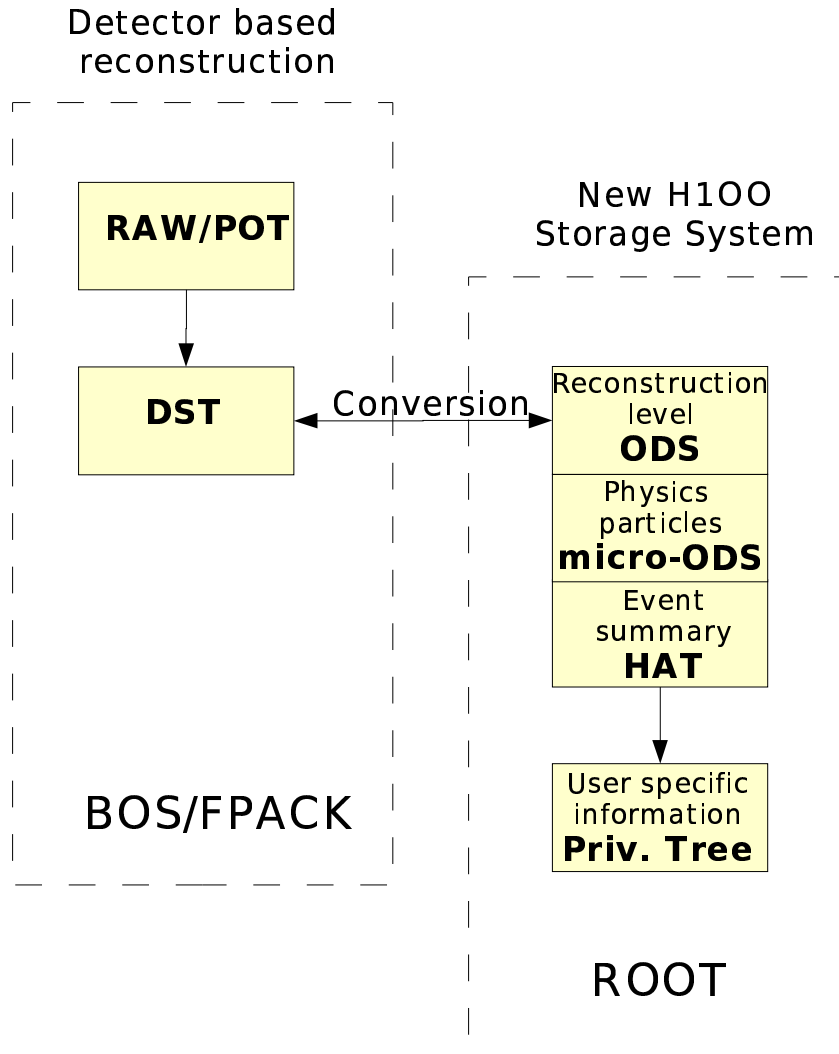


Figure 3.28: A schematic overview of the data storage levels used by the H100 Project.

Finally, the H100 environment allows for further data layers to be added. The “normal” layers of storage described above can be extended by specially filled trees containing user-defined information. These *User Trees* allow persistent storage of specialised information. Reading User Trees is faster than reading and processing ODS (or POT raw data) information. User Trees allow for experimental extensions of basic H100 objects, filling of detector level information found only on DST (or in raw data) or more sophisticated physics finders used only for a small subset of analysis.

In this analysis, detailed information on the LAr trigger is used to evaluate the efficiency of the principal trigger element for high Q^2 neutral current, *LAr_electron_1*. The list of big towers that fired for each selected NC event is stored in a User Tree for convenient offline analysis (see section section 6.8.1 for discussion of the results of this study).

Generic Analysis

While the H100 project provides a common basis for analysis, with expert knowledge available to all users and the ready availability of all quantities suitable for analysis, there still remains a need to standardise common analysis tasks. Hence the need for a generic analysis framework to complement the H100 software with high level analysis tools. Tasks like event selection book-keeping, histogramming, determination of event weights and binning of kinematic variables are common to all kinds of physics analysis. The H100 generic analysis framework, described in further detail in [111], provides tools to accomplish all these tasks. The steps required for analysis are further formalised with dynamically steerable¹⁰ analysis objects. This allows users to quickly build in a simple way, or extend, an analysis code base comprised of objects representing the tasks necessary in the analysis.

The “Calculator” package is an important part of the generic analysis framework, which interfaces to the H100 data. The Calculator is essentially a transient event layer, lying between the data storage and the high level analysis tools. As well as providing further information calculated from μ ODS/HAT variables, the Calculator allows the determination and combination of event weights for data and simulation. It also provides a mechanism for the propagation of systematic uncertainties, e.g. in the scattered electron energy, through the re-calculation of the event kinematics. The effect of possible systematic mis-measurements can be accounted for by propagating a shift of these quantities by $\pm\sigma$ up to the final result. This is effective, and much less expensive in terms of CPU time and storage space than re-creating data files for each systematic shift.

The analysis presented in this document has been performed in the H100 analysis framework using the generic analysis tools.

¹⁰The H100 framework provides a steering mechanism, allowing run time behaviour to be set by text files.

Chapter 4

Monte Carlo Simulation

To make a well controlled physics measurement, a detailed simulation of the physics processes and detector response is needed. For these purposes, stochastic techniques are commonly used. These techniques, which use random numbers and probability distributions to simulate physical processes are termed Monte Carlo (MC) methods. In order to ensure that the statistical error of the simulated sample can be, to a good approximation, ignored, the simulated event samples are generally required to be several times the size of the data samples.

A cross section measurement requires corrections for acceptance, and an understanding of the influence of the resolution of the detector components on the final result. These are difficult to determine directly from data due to the complex interplay of different detector effects.

Monte Carlo event simulations are also used in developing the data selection criteria. The Monte Carlo programs can help to determine which variables are particularly useful for separating signal from background. In developing the selection criteria and determining the acceptance corrections, it is necessary that the Monte Carlo simulations accurately describe the data. In addition, many different Monte Carlo generator programs must be used, each describing a specific class of process. It also means that detailed simulations of the detector response to particles must be performed, in active as well as in inactive materials.

When the discrepancy of simulation from data is observed the MC simulation is adjusted to model the data behaviour. The Monte Carlo is also used to model an inevitable smearing of reconstructed variables due to finite detector resolutions. The efficiency of the selection criteria, the detector calibration and the resolution are determined directly from data and are implemented in MC.

4.1 Generation of DIS Events

Deep inelastic scattering processes are generated using the *DJANGO* Monte Carlo simulation program [88], which is based on *LEPTO* [90] for the hard interaction and *HERACLES* [87] for single photon emission off the lepton line and virtual EW corrections. *LEPTO* combines $\mathcal{O}(\alpha_s)$ matrix elements with higher order QCD effects using the colour dipole model as implemented in *ARIADNE* [91]. The *JETSET* program is

used to simulate the hadronisation process [92].

The events are generated using the MRSH [81] PDFs as input. The simulated events are then re-weighted by the ratio of the DIS cross section using the NLO QCD fit of the HERA I data (H1 2000 PDF [85]) and the MRSH fit. This is equivalent to the usage of the H1 2000 PDF parameterization for the generated MC events.

4.2 Generation of Background Events

For the measurement of DIS cross sections it is important to estimate the contribution from non-DIS events which can have signatures in the detector similar to those of DIS events. The main background contribution to DIS arises from the following processes:

- **Photoproduction** ($e \rightarrow e\gamma$): Photoproduction is the dominant background process for NC DIS. At very low four-momentum transfer squared ($Q^2 \approx 0 \text{ GeV}^2$), the proton interacts with a quasi-real photon and the cross section is large. Generally, the electron scattered through a small angle is not detected in the central part of the H1 Detector. However, a particle from the hadronic final state may be mis-identified as the scattered electron.

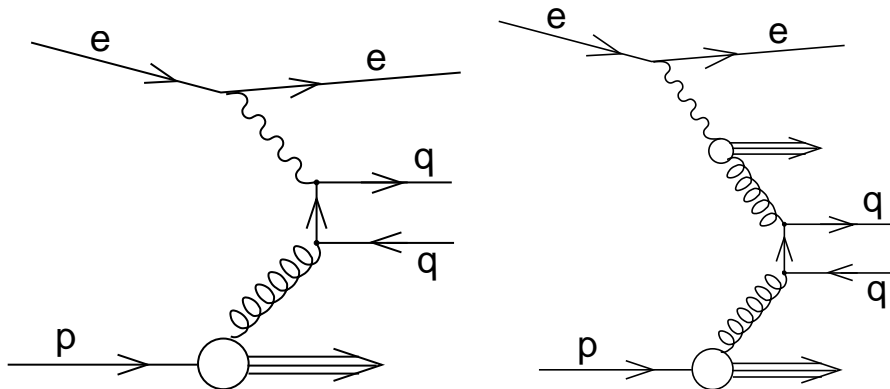


Figure 4.1: Examples of leading order diagrams for direct (left) and resolved (right) photoproduction, contributing to NC DIS background.

In the description of photoproduction processes, *direct* and *resolved* interactions of the photon are distinguished. In direct processes, the photon is absorbed by a quark line, the dominant process being *boson-gluon fusion* $\gamma g \rightarrow q\bar{q}$, shown on the left of figure 4.1. In resolved processes, the photon fluctuates to a quark anti-quark pair plus gluons, i.e. is “resolved”, and one of these photonic partons interacts with a parton emitted by the proton. An example of such a process is shown on the right in figure 4.1.

Photoproduction is modelled by the PYTHIA [89] event generator. PYTHIA is a Lund type Monte Carlo program. It allows for both resolved as well as direct photon reactions. The program also includes both initial and final state QCD radiation, and uses the JETSET package for hadronization. The partonic “hard” scattering cross sections are calculated in LO.

- **Elastic QED-Compton scattering ($ep \rightarrow ep\gamma$):** The QED-Compton events may contribute to the background when the exchanged photon has a very small Q^2 . Both the electron and photon can be scattered into the central part of the detector when the virtuality of the intermediate electron is large. For the simulation of the QED-Compton process the MC generator **WABGEN** [95] is used.
- **Lepton-pair (e, μ, τ) production:** Lepton-pair production processes may contribute to the background in cases when one of the paired leptons escapes detection. At HERA, the dominant production process for lepton-pair events is the *photon-photon interaction* illustrated in figure 4.2.

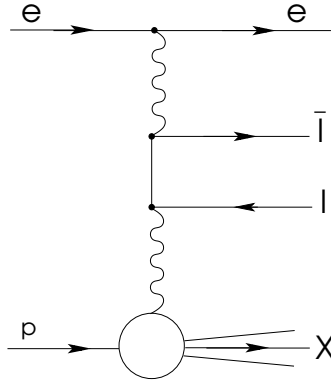


Figure 4.2: Leading order diagram for lepton-pair production.

Direct production of lepton-pairs is simulated by the event generator **GRAPE** [59]. **GRAPE** includes the contributions from the full set of leading order electro-weak processes and approximates next-to-leading order effects by simulating initial and final state radiation.

- **W production:** At HERA, real W bosons may be produced in photoproduction processes $\gamma p \rightarrow WX$. The cross-section of such process is small, $\sigma \approx 1$ pb. If the boson decays leptonically the event may be misidentified as a NC event, and is therefore treated as a background source. The dominant contribution to the W production cross-section is due to the processes shown in figure 4.3.

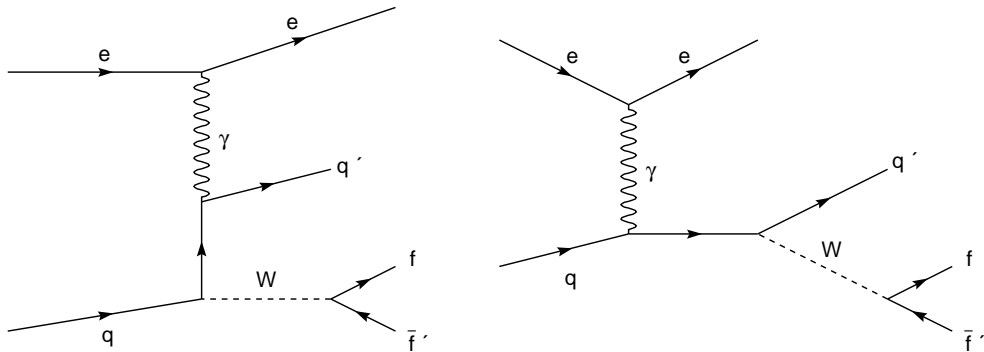


Figure 4.3: Leading order diagrams for the production of real W bosons via neutral current $ep \rightarrow eWX$ processes at HERA and the subsequent decay $W \rightarrow f\bar{f}'$.

The production of real W bosons in ep collisions is implemented to leading order in the EPVEC [93] Monte Carlo generator.

Besides these ep induced background processes a significant background contribution arises from non- ep induced background. The main sources of non- ep background are:

- Interaction of the proton beam with gas particles or the beam pipe wall, called “*beam-gas*” and “*beam-wall*” background, respectively.
- “Beam-halo muons” originating far up-stream from the H1 Interaction Point, and passing through the calorimeters parallel to the proton beam direction.
- Muons from cosmic rays.

Some of these events can be rejected by timing and vertex requirements. The remaining background events are identified by topological filters designed for this purpose (see section 6.10) and rejected, leaving a negligible contamination. Non- ep background events therefore need no simulation.

4.3 Simulation of the H1 Detector

The detector response to the particles generated in an event is simulated in detail by the H1SIM-package [99] which is based on the GEANT-program [100]. The parameters used by this program were determined in test beam measurements and optimised during the ep data taking. For the simulation of the energy response of the calorimeters a fast parameterization is used for the development of electromagnetic showers and the electromagnetic component of the hadronic showers as implemented in H1FAST [101, 102]. For the hadronic component of the shower developing the “full simulation” (GEANT) is used. Both data and simulated events are subject to the same reconstruction program H1REC [96].

Chapter 5

Kinematics Reconstruction and Coverage of the Phase Space

5.1 Reconstruction of Kinematic Variables

In neutral current ep scattering at HERA, both the scattered electron and the hadronic system can be measured. The properties of the scattered electron are usually described by its energy E'_e and scattering angle θ_e . Since part of the hadronic final state is moving in the incident proton direction and escapes unobserved through the beam pipe, the following variables are chosen to describe the hadronic final state:

$$\Sigma = \sum_i (E_i - P_{z,i}), \quad (5.1)$$

$$P_{T,h} = \sqrt{\left(\sum_i P_{x,i}\right)^2 + \left(\sum_i P_{y,i}\right)^2}. \quad (5.2)$$

Here, E_i and $P_{z,i}$ are the energy of particle i and the corresponding momentum component along the beam direction. $P_{x,i}$ and $P_{y,i}$ are the transverse components of the particle momentum. The summation is performed over all measured particles in the hadronic final state¹. By construction, these variables are relatively insensitive to losses in the beam pipe in the positive z direction. Combining the variables Σ and $P_{T,h}$, the inclusive hadron angle γ_h is defined as:

$$\tan \frac{\gamma_h}{2} = \frac{\Sigma}{P_{T,h}}. \quad (5.3)$$

In QPM, γ_h corresponds to the polar angle of the struck quark.

For a perfect detector, energy-momentum conservation requires that $E - P_z \equiv \Sigma + E'_e(1 - \cos \theta_e)$ and $|\vec{P}_{T,tot}|$, summing up the scattered electron and the hadronic final state, to be equal to the initial values of these variables before the ep interaction:

$$E - P_z = 2 \cdot E_e \approx 55 \text{ GeV}, \quad (5.4)$$

$$|\vec{P}_{T,tot}| = 0. \quad (5.5)$$

In a real detector, resolution effects and losses due to detector acceptance could lead to deviations from these relations.

¹All measured particles except of the scattered electron are attributed to the hadronic final state.

The kinematics of DIS events is defined by three variables, as described in section 2.1.1. There are many possible choices for these variables, e.g. x, y, Q^2, W or s . For the structure function measurements, the results are quoted in terms of x and Q^2 . The natural variables for the total γ^*p cross section measurement are Q^2 and W . In this analysis Q^2, x and y are used and all other variables can be calculated from these three². There are several ways to use the energy E'_e and polar angle θ_e of the scattered electron, and the longitudinal ($P_{z,h}$) and transverse momentum of the hadronic final state ($P_{T,h}$) for the reconstruction of the kinematic variables.

• The Electron Method

In the electron method [105] the kinematic variables are reconstructed using the energy E'_e and the polar angle θ_e of the scattered electron:

$$Q_e^2 = 4E_e E'_e \cos^2\left(\frac{\theta_e}{2}\right), \quad (5.6)$$

$$y_e = 1 - \frac{E'_e}{E_e} \sin^2\left(\frac{\theta_e}{2}\right), \quad (5.7)$$

$$x_e = \frac{Q_e^2}{s y_e}. \quad (5.8)$$

It is a very simple and powerful method, since it only requires the measurement of one particle. The Q^2 and x measurement errors are given as³:

$$\frac{\delta Q_e^2}{Q_e^2} = \frac{\delta E'_e}{E_e} \oplus \tan \frac{\theta_e}{2} \delta \theta_e, \quad (5.9)$$

$$\frac{\delta x_e}{x_e} = \frac{1}{y_e} \frac{\delta E'_e}{E'_e} \oplus \tan \frac{\theta_e}{2} \left(x \frac{E_p}{E_e} - 1\right) \delta \theta_e. \quad (5.10)$$

$$(5.11)$$

The electron method is the best method for measuring Q^2 . The shortcoming of the electron method is a degradation of the x resolution at small values of y due to the $1/y$ dependence of $\frac{\delta x_e}{x_e}$. The x resolution, however, is very good at large y . This method is sensitive to radiative effects.

• The Hadron Method

The hadron method relies entirely on the hadronic system, and was introduced by Jacquet and Blondel [106]. It uses the hadronic final state variables defined by the equations (5.1)-(5.2):

$$Q_h^2 = \frac{P_{T,h}^2}{1 - y_h}, \quad y_h = \frac{\Sigma}{2E_e}, \quad x_h = \frac{Q_h^2}{s y_h}. \quad (5.12)$$

² $Q^2 = xys$ and at HERA, at fixed s , only two variables are independent.

³ $A \oplus B \equiv \sqrt{A^2 + B^2}$.

In practice, the final state hadrons are represented by calorimeter energy deposits or tracks. The hadron method is stable against energy losses in the forward direction through the beam pipe since these losses contribute very little to Σ or P_T^2 . However, it is sensitive to calorimeter noise at very small y , and is sensitive to energy losses in the backward direction, i.e. at higher values of y . It requires a good understanding of the hadronic energy scale and is therefore sensitive to resolution effects. On the other hand, the hadron method is rather insensitive to radiative corrections, which mainly affect the kinematics derived using the properties of the scattered electron.

The hadron method is the only one available for the reconstruction of the charged current DIS kinematics. For the measurement of NC DIS it is not used because of the degradation of the resolution at high y :

$$\left. \frac{\delta Q_h^2}{Q_h^2} \right|_{P_{T,h}} \propto \frac{\delta P_{T,h}}{P_{T,h}}, \quad \left. \frac{\delta Q_h^2}{Q_h^2} \right|_{\Sigma} \propto \frac{\delta \Sigma}{1-y}, \quad (5.13)$$

where the term $1/(1-y)$ becomes increasingly important and severely degrades the resolution in Q^2 and, consequently, in x .

- **The Sigma (Σ) Method**

The Σ -method [107] makes use of the longitudinal momentum conservation relation $E - P_z = 2E_e$ (see equation (5.4)), and in such a way accounts for a potential reduction of the electron beam energy due to initial state radiation which usually escapes detection since the radiated photons are emitted into the beam pipe in the negative z direction:

$$Q_{\Sigma}^2 = \frac{E_e'^2 \sin^2 \theta_e}{1 - y_{\Sigma}}, \quad y_{\Sigma} = \frac{\Sigma}{E - P_z}, \quad x_{\Sigma} = \frac{Q_{\Sigma}^2}{s y_{\Sigma}}. \quad (5.14)$$

Here, $E - P_z$ is used for estimation of the lepton beam energy after radiation of a photon with energy $E_{\gamma} = E_e - \frac{1}{2}(E - P_z)$. This changes the centre-of-mass energy available for the hard ep interaction to $s' = 2(E_e - E_{\gamma})E_p = \frac{E - P_z}{2E_e} \cdot s$. Since x is calculated using the full centre-of-mass energy, the Σ -method retains some sensitivity to initial state radiation.

Compared to the electron method, the Σ -method provides a better resolution in x and y at low and moderate values of y (see figure 5.1).

- **The eSigma ($e\Sigma$) Method**

The $e\Sigma$ -method [108] combines the Q^2 reconstruction from the electron method and x reconstruction from the Σ method:

$$Q_{e\Sigma}^2 = Q_e^2, \quad x_{e\Sigma} = x_{\Sigma} \quad (5.15)$$

and y is calculated according to

$$y_{e\Sigma} = \frac{Q_e^2}{x_{\Sigma}s}. \quad (5.16)$$

The $e\Sigma$ method has the best resolution both in x and Q^2 over the full kinematic range accessible at HERA and is relatively insensitive to radiation. This method is used to determine the kinematic variables for NC events in this analysis.

- **The Double Angle (DA) method**

The Double Angle method [105] uses the electron polar angle θ_e and the inclusive hadronic polar angle γ_h which is the polar angle of the struck quark, assuming that the quark forms a single massless jet:

$$y_{DA} = \frac{\sin\theta_e(1 - \cos\gamma_h)}{\sin\gamma_h + \sin\theta_e - \sin(\theta_e + \gamma_h)}, \quad (5.17)$$

$$Q_{DA}^2 = \frac{4E_e^2 \sin\gamma_h(1 + \cos\theta_e)}{\sin\gamma_h + \sin\theta_e - \sin(\theta_e + \gamma_h)}, \quad (5.18)$$

$$x_{DA} = \frac{Q_{DA}^2}{sy_{DA}}. \quad (5.19)$$

The DA method is also sensitive to photon emission from the primary electron. On the other hand it is, to a good approximation, insensitive to the energy scales. Thus, it has been used to check and improve the energy calibration for the scattered electron (see section 6.6.1) and for the hadronic system (section 6.7.2).

The energy of the scattered electron determined using the DA method is given by:

$$E_{DA} = \frac{2E_e \sin\gamma_h}{\sin\gamma_h + \sin\theta_e - \sin(\gamma_h + \theta_e)}. \quad (5.20)$$

The transverse momentum using the double angle method $P_{T,DA}$ is:

$$P_{T,DA} = \frac{2E_e}{\tan \frac{\gamma_h}{2} + \tan \frac{\theta_e}{2}}. \quad (5.21)$$

The y dependences of the Q^2 and x resolution for the different kinematic reconstruction methods are compared in figure 5.1, obtained using the DJANGO MC with the neutral current selection described in section 7.3. One can see that the best reconstruction of Q^2 is provided by the electron method, and of x by the sigma method (except at very low y , where the hadron method is superior). The hadron method is very poor for the Q^2 measurements, and the electron method is poor for the x measurements at low y . The $e\Sigma$ method used in the analysis combines the advantages of the electron and sigma methods with respect to resolution, and is insensitive to radiative effects.

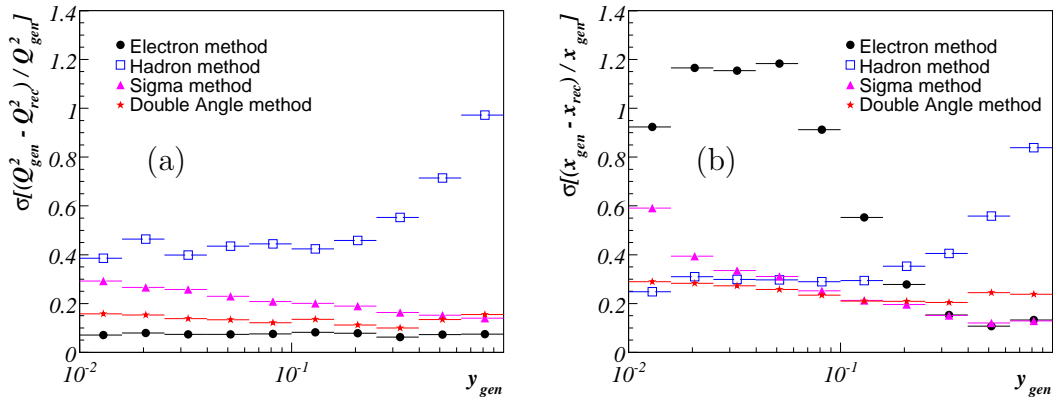


Figure 5.1: The resolution of reconstructed Q^2 (a) and x (b) as a function of y for different reconstruction methods. Q_{rec}^2 (Q_{gen}^2) and x_{rec} (x_{gen}) refer to the reconstructed (generated) values of Q^2 and x respectively.

5.2 Coverage of the Kinematic Phase Space

The structure functions describing the electron-proton scattering processes depend on the two kinematic variables x and Q^2 . The *kinematic plane* covered by HERA is shown in figure 5.2 in comparison with the range covered by fixed-target experiments.

Since the HERA centre-of-mass energy of $\sqrt{s} = 318$ GeV is large compared to fixed target experiments, HERA provides extensive access to both the extremely low x and the very high Q^2 kinematic regions. The HERA DIS data of H1 and ZEUS cover roughly the range of $1 \lesssim Q^2 < 5 \cdot 10^4$ GeV² and $10^{-5} < x < 0.65$. The measurements of the fixed target experiments populate the kinematic plane at the lower right corner, providing valuable data with high statistics at large x .

This analysis covers the kinematic range of high $Q^2 \gtrsim 200$ GeV² and $0.05 < y < 0.9$.

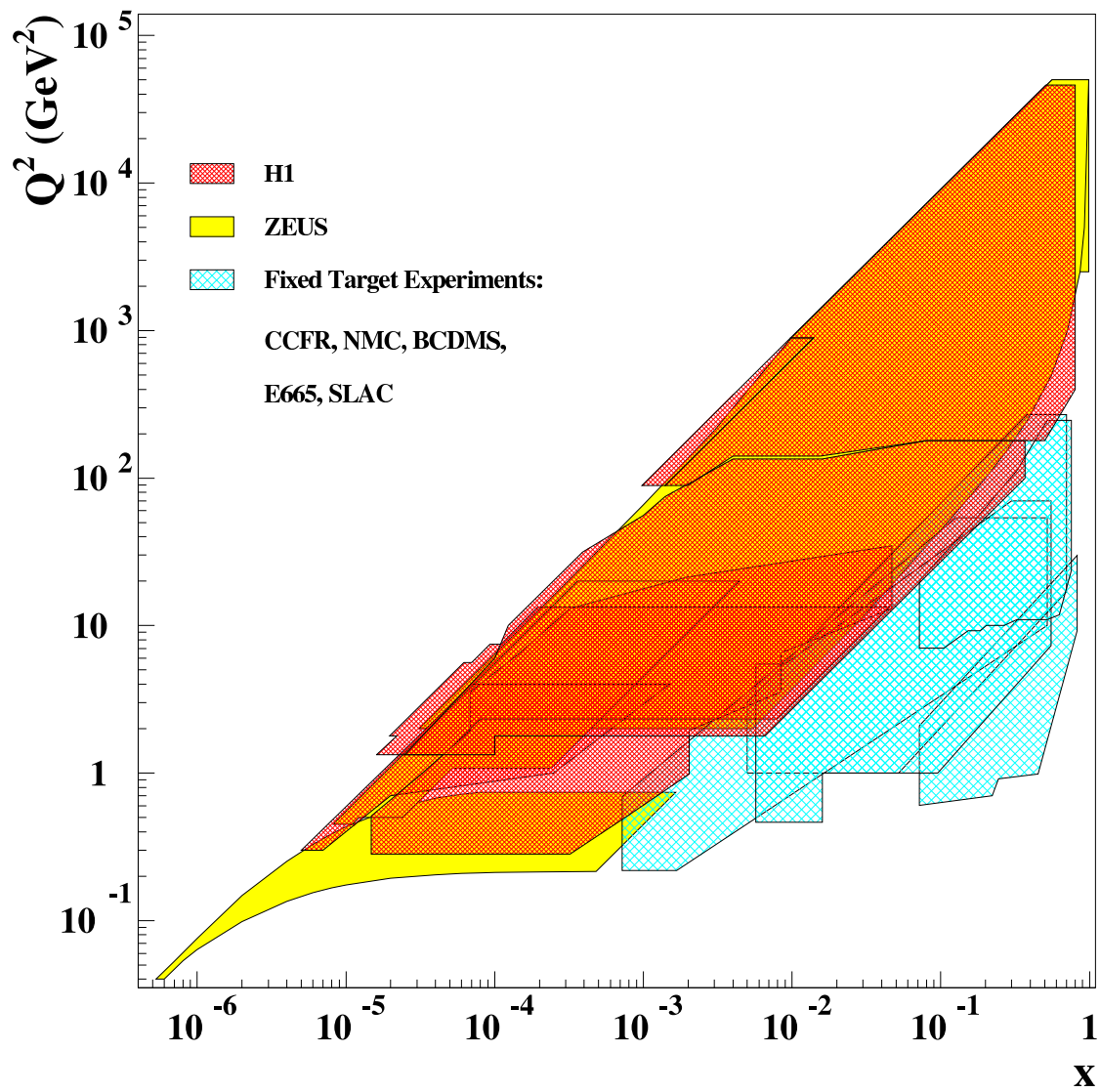


Figure 5.2: The HERA coverage of the kinematic plane in comparison to previous fixed-target experiments.

Chapter 6

Data Treatment

Precise measurements of the NC inclusive cross section require a careful treatment of the data. In this chapter the scattered electron identification, measurement of the electron energy and angle, measurement of the hadronic final state properties and the position measurement of the primary interaction vertex are discussed. All these quantities are needed for an accurate reconstruction of the DIS kinematics. In addition, the ep and non- ep background rejection procedures are described.

Performance and efficiencies of the different detector components are determined directly from the data. This information is used to adjust the simulation such that MC describes the data behaviour in any respect essential for the analysis, including the time dependences of the detector response during the whole running period.

6.1 Electron Identification

In the neutral current events with large momentum transfer $Q^2 \gtrsim 130 \text{ GeV}^2$, the incoming electrons are scattered into the LAr calorimeter. The electron identification is based solely on calorimeter information and benefits from the fine granularity of the LAr calorimeter. Electron candidates are identified as isolated and compact energy depositions of the well defined electromagnetic shower shape. The electron finding procedure applied in this analysis [110] uses the QESCAT algorithm [112].

An initial electron candidate is defined by a cone of 7.5° around the centre of gravity (CoG) of any prominent energy cluster in the electromagnetic part of the calorimeter. The cone extends from the interaction vertex to the first layer of the hadronic section. Any cluster within this envelope is merged with the initial “seed” cluster. Electron candidates are then identified on the basis of estimator variables, which quantify the shape and the size of the shower. These seven estimator variables are described below, and summarised in table 6.1.

Electron candidate clusters are required to contain a prominent energy deposition in the calorimeter (estimators ETOT, NCEL) to separate them from random noise and low energetic hadrons, which usually deposit low energy clusters of a few cells.

- **EATOT** is true if the electron candidate cluster energy, E_{tot} , is above 5 GeV and the transverse momentum, p_T , is above 3 GeV.

- **NCEL** is the number of cells in the cluster. The cluster must consist of at least four calorimeter cells.

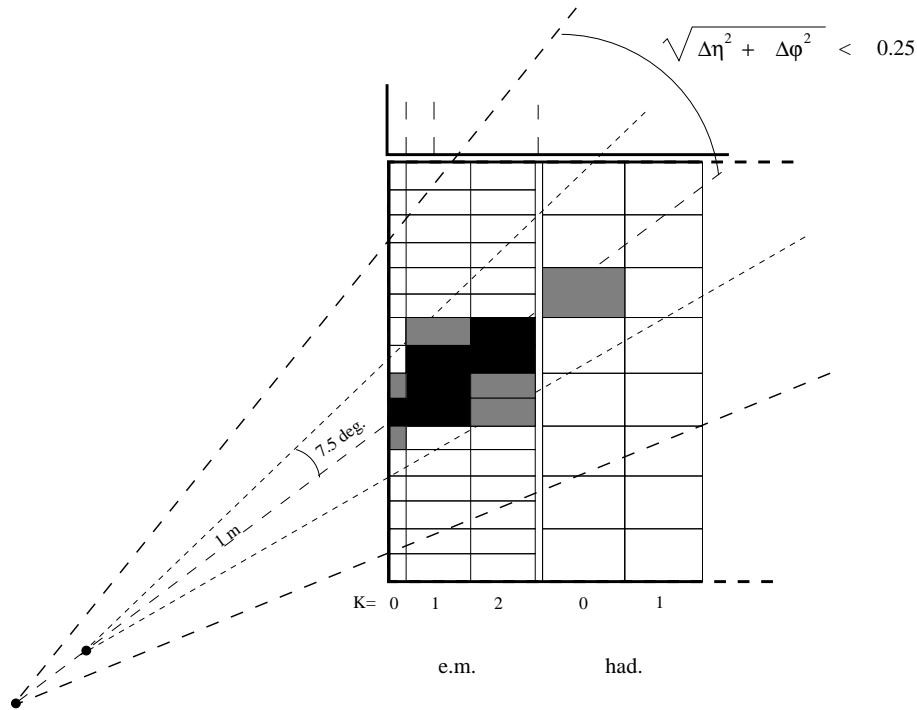


Figure 6.1: Schematic view of the electron identification envelope cone.

For electromagnetically interacting particles, the shower has to develop early in the calorimeter and deposits most of its energy in the electromagnetic section (EAEM). The cluster has to be compact both in the longitudinal and transverse directions (EAHN, EATR).

- **EAEM** is the electromagnetic energy fraction of the cluster, defined as E_{em}/E_{tot} . Here, E_{em} is the electromagnetic energy deposited in the first two (three in the forward region) layers of the electromagnetic part of the LAr. The minimum value for EAEM is θ dependent.
- **EAHN** is the energy fraction deposited in the N hottest neighbouring cells, E_{hot}^N/E_{em} . The value of N varies through the LAr and is 4 in BBE, 8 in CB3 and FB, and 12 in the IF wheel. EAHN is required to be greater than 0.8 (0.4) in the backward (forward) region.
- **EATR** is the transverse dispersion of the electron candidate cluster, a measure of the cluster radius. $\sigma(R) = \sqrt{\langle r^2 \rangle - \langle r \rangle^2}$, is calculated from the energy-weighted transverse distances, r_i , of all cells in the cluster.

Finally, the electron candidate is tested for isolation from the hadronic final state within the LAr calorimeter. An isolation cone is defined in $\eta - \phi$ space¹, with the radius

$$R_{\eta-\phi} = \sqrt{(\Delta\eta)^2 + (\Delta\phi)^2} = 0.25. \quad (6.1)$$

¹ $\eta = -\ln(\tan(\frac{\theta}{2}))$ is the pseudo-rapidity.

- **EAI**F is the fraction of deposited energy in the isolation cone, E_{iso} , that is associated with the electron candidate: E_{tot}/E_{iso} . EAIF must be at least 0.98.
- **E**AHD is the total energy deposited in the hadronic section of the isolation cone. The EAIF cut can be decreased to 0.95 if EAHD is below 300 MeV.

The chance for the electron finder to misidentify a hadron as an electron is smaller than 1% [60]. However, an electron in a jet may still fake the scattered electron. The isolation of identified electromagnetic particles against other calorimeter deposits is tested by examining the total calorimetric energy not belonging to the electron, E_{cone} , in a cone of radius $R_{\eta-\phi} = 0.5$. Electrons are flagged as isolated if $E_{cone}/E_{tot} < 5\%$. In case of multiple electron candidates, an “isolated” electron with highest p_T is regarded as the scattered electron.

Estimator	Description	Cut
EATOT	Energetic cluster	$E_{tot} > 5 \text{ GeV}$ and $p_T > 3 \text{ GeV}$
NCEL	Cells assigned to electron candidate	> 3
EAEM	Electromagnetic fraction	$> 0.94 + 0.05 \cos(2\theta)$
EAHN	Energy fraction in the hot core	$> 0.8(0.4)$ in bwd (fwd) region
EATR	Cluster radius	θ dependent
EAIF	Energy fraction in isolation cone carried by electron candidate	EAIF > 0.98 or
EAHD	Hadronic energy in isolation cone	(> 0.95 if EAHD $< 300 \text{ MeV}$)

Table 6.1: The estimator variables used by the electron finding algorithm. Each estimator is briefly described and the cut values are noted (see text).

6.2 Electron Finding Efficiency

The electron identification is based on shower shape estimators to distinguish an electromagnetic particle from hadronic activity. To study the efficiency of this electron finding algorithm, an independent track-based electron finder [61] is used.

The track-based electron finder is looking for isolated tracks within an isolation cone of radius $R_{\eta-\phi} = 0.5$ with a track transverse momentum $P_T > 1.5 \text{ GeV}$. The main part of the calorimetric energy inside the cone is required to be compactly deposited in the electromagnetic part of the calorimeter. In addition, a momentum-energy match between the track and the associated cluster is required.

The track based electron finder has a reduced efficiency. Therefore in this analysis it is used only for monitoring purposes, although it could be useful for the identification of the electrons with very low transverse momentum.

The electron finding efficiency for data and simulation are displayed in figure 6.2 as a function of the impact position of the electron on the surface of the LAr calorimeter in z and φ . In general, the efficiency is very high, approximately 100% in the central barrel region. In the vicinity of the z and φ cracks of the LAr calorimeter, the electron identification is less efficient. In these regions, the electron has to pass

inactive material including the support structures of the calorimeter. Furthermore, in the φ cracks and in the z crack between the CB2 and CB3 wheels, the electron may enter the hadronic section without prior interactions. The coarse granularity of the hadronic part of the LAr calorimeter does not allow an efficient separation of electromagnetic particles from hadrons. Therefore, the z and φ crack regions are excluded for the measurement of the cross sections.

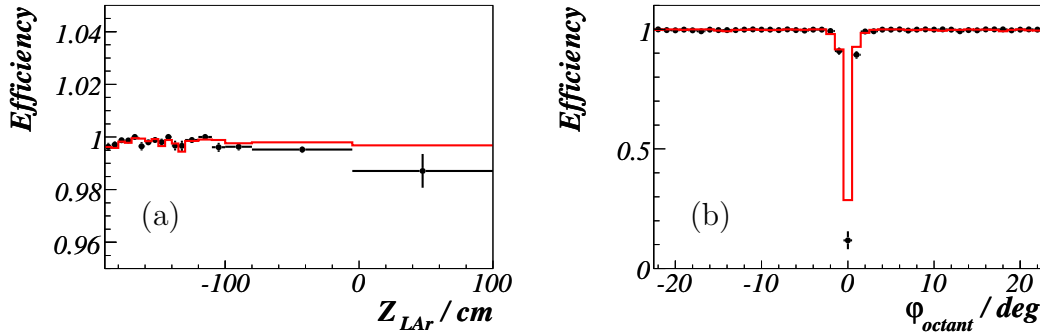


Figure 6.2: Electron finding efficiency for data (full points) and simulation (histogram) as a function of the electron z impact (a) and φ angle between the electron impact point and the closest φ -crack (b).

In the remaining fiducial volume, the electron identification efficiency observed for the data is described by the simulation within the statistical uncertainty. However, for $z > 0$ cm, the data tend to lie systematically below the Monte Carlo prediction, due to imperfect description of the behaviour of the estimators in the simulation. This difference is taken into account in the systematic errors.

The track electron finder can be used to monitor the original electron finder only in the angular range covered by the central tracking device. For the more forward region, with the electron impact position $z_{imp} > 100$ cm, the electron identification efficiency is assumed to be described in the simulation. The systematic uncertainty due to this assumption is estimated to be 2% [85].

The systematic uncertainty on the electron identification is taken to be 0.5% for $z_{imp} < 0$ cm and 2% for $z_{imp} > 0$ cm.

6.3 Interaction Vertex

For an accurate reconstruction of the event kinematics a precise knowledge of the ep interaction position is needed. In particular, the position of the vertex is directly used in the measurement of the polar angle of the scattered electron θ_e based on the LAr information. It is important that the vertex position properties are well modeled in MC.

6.3.1 Vertex Re-weighting in MC

The primary interaction vertex is spread out in z around the nominal interaction point due to the longitudinal size of the proton bunches ($\sigma_z(p) \approx 13$ cm, the electron bunches are much shorter, $\sigma_z(e) \approx 2$ cm). The mean z vertex position depends on the beam settings of the accelerator and, in general, is different for each machine fill. For fixed beams parameters, the z vertex distribution is approximately Gaussian.

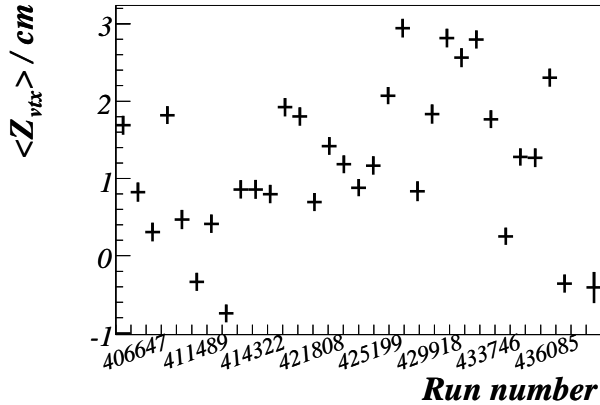


Figure 6.3: Mean z_{vtx} as a function of run number in bins of equal luminosity.

For practical reasons, the Monte Carlo events are simulated with a fixed z vertex distribution corresponding to a Gaussian function with a mean $z_{vtx}^{mc} = 0$ and a width $\sigma^{mc} = 13$ cm. To model the real z vertex distribution corresponding to the selected data sample, the simulated events are re-weighted in z preserving the overall normalisation of the Monte Carlo simulation. A 11th order polynomial function with parameters β_i is used for re-weighting of MC events as a function of the generated z position, z_{vtx}^{gen} . The weight applied to the MC event is calculated as:

$$w_{z_{vtx}} = \frac{\sum_{i=0}^{10} \beta_i \cdot z_{vtx}^{gen}}{\beta_{11}}, \quad (6.2)$$

where β_{11} is the normalisation parameter.

The parameters β_i are extracted using a sub-sample of the inclusive neutral current selection given in section 7.3. Additional criteria are applied to ensure good quality of the selected sample:

- The polar angle of the scattered electron is required to be $\theta_e < 145^\circ$ to avoid biases due to the geometrical acceptance of the LAr.
- $y_h > 0.1$ is applied to ensure good measurement of the hadronic final state and therefore good measurement of the event vertex.

The z vertex distribution of the data and Monte Carlo events before and after the MC re-weighting is shown in figure 6.4. To account for correlations with other time dependent detector effects, the simulated events were splitted in sub-samples corresponding to the data subsets and the re-weighting is performed separately for each subset (see chapter 7 for details).

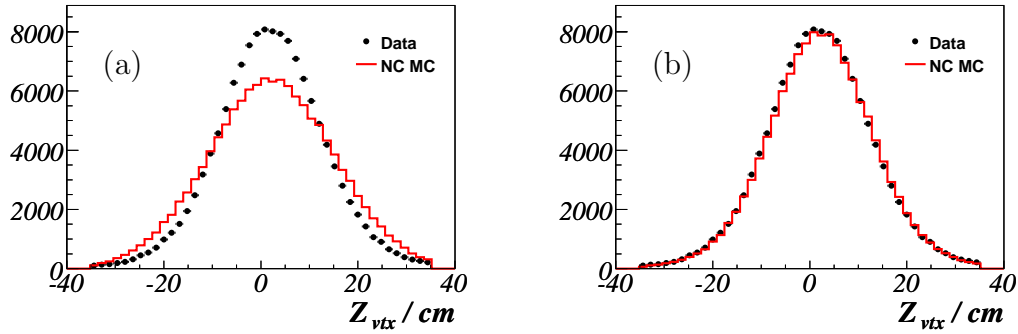


Figure 6.4: The z_{vtx} distribution for data and Monte Carlo events before (a) and after reweighting of the MC (b). The simulation is normalised to the luminosity of the data.

6.4 Vertex and Track Link Requirements

A reconstruction of the primary interaction vertex is required in the NC events selection. This requirement reduces non- ep -collision background substantially and enables the precise measurement of the event kinematics. At large polar angles $\theta_e > 30^\circ$ a track matching to the electromagnetic cluster is required to reduce further the contamination to the NC sample due to misidentified photons and hadrons from background processes.

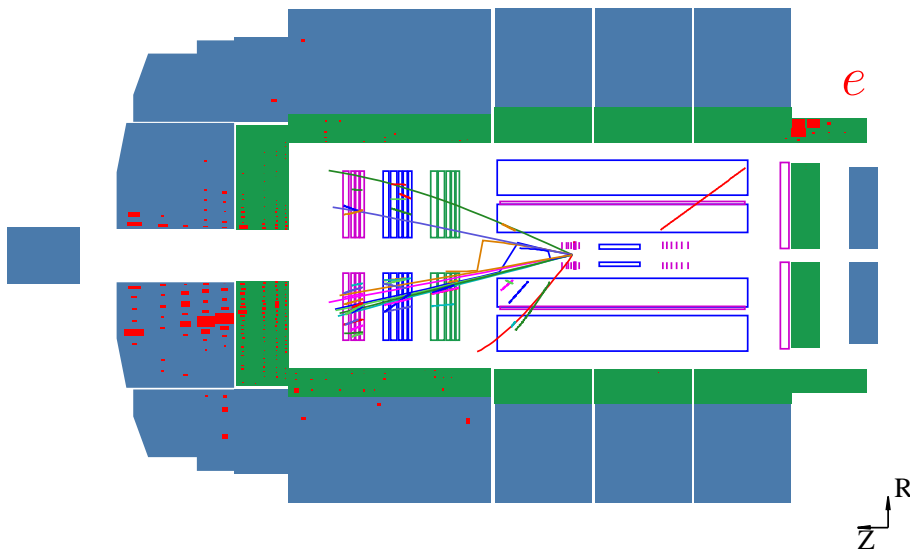


Figure 6.5: An NC event with a nuclear interaction in the beam pipe by the hadronic final state. Tracks from the hadronic final state point to the vertex of the nuclear interaction. The electron track is originating from the primary ep interaction vertex.

The reconstruction of charged particle tracks is described in [63]. Briefly, track segments are found by fitting a helical path to the hits in space, determined in the CJC. The track fitting can be improved by introducing the vertex as a constraint. The ep interaction region extends over a few tens of μm in the xy -plane with a mean value

that typically stays constant over several runs. The known x and y position of the interaction vertex can then be used to improve the track fit by providing an extra constraint. The z position of the vertex is obtained from these vertex fitted tracks. The tracks that can be fitted to the interaction vertex are known as DTRA tracks. Non-vertex-fitted tracks are known as DTNV tracks.

A track is associated to the electron if the distance between the extrapolated track trajectory into the LAr calorimeter and the centre of gravity of the electron cluster in the calorimeter (DCA_{tr-cl}) is smaller than 12 cm.

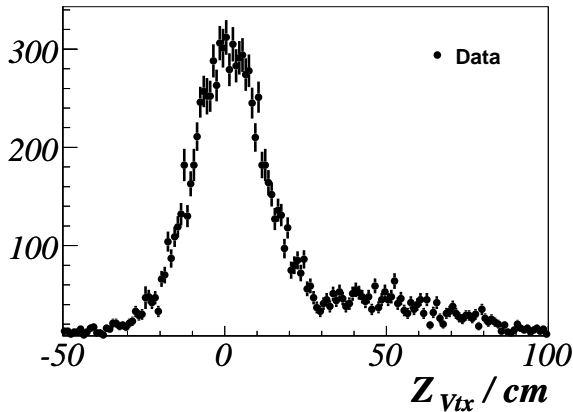


Figure 6.6: Distribution of the z vertex for NC events with no DTRA electron track. The vertices determined from the hadronic final state give rise to the right tail of the z_{vtx} distribution caused by nuclear interactions in the beam pipe.

For this analysis, the vertex is required to be reconstructed using CJC tracks with a z_{vtx} position within 35 cm around zero in the H1 coordinate system. The requirement $|z_{vtx}| < 35$ cm corresponds approximately to 3σ of the gaussian z_{vtx} distribution, expected for the ep physics events.

A hadronic final state particle can participate in a nuclear interaction in the beam pipe, producing tracks originating from the secondary vertex. The reconstruction program considers all tracks as originating from a primary vertex, therefore the vertex fit in this case will give wrong result.

The particles from interactions in the beam pipe have a $T0$ from the CJC of about 3 ns later than the scattered electron and will distort the event $T0$. This wrong event $T0$ deteriorates the reconstruction of the electron track. An example of such an event one can see in figure 6.5. The electron track is not fitted to the vertex from the hadronic final state, which is wrongly taken as the primary vertex by the reconstruction. Such vertices give long tails to the vertex distribution and spoil the kinematics measurement. In figure 6.6 the z -vertex distribution is plotted for events where no DTRA electron track was found.

In order to exclude events with wrong vertex due to nuclear interactions in the beam pipe, the electron track is required to be fitted to the primary vertex (DTRA track).

The track and vertex requirements are closely related since the track segments are constrained to originate from a common vertex during the vertex fitting procedure. Therefore, efficiencies due to both requirements, to have a primary vertex reconstructed using CJC tracks and to find a DTRA track associated with the scattered

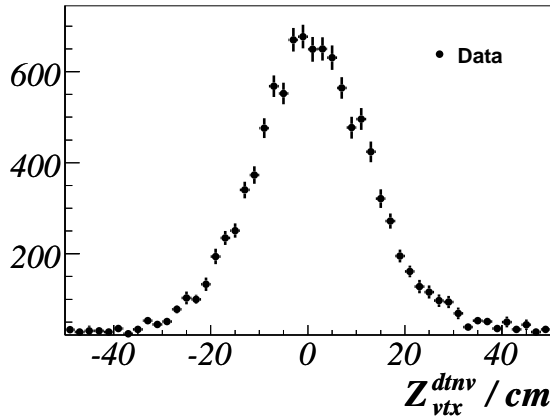


Figure 6.7: Distribution of the z “DTNV vertex”. The “DTNV vertex” is calculated from the extrapolation of the scattered electron DTNV track to the run average vertex. This vertex does not depend on nuclear interactions with the beam pipe by hadronic final state and is used for the vertex and electron track link efficiency studies.

electron, are considered together. The term “*vertex and electron track link*” efficiencies is used further in the text for these efficiencies.

Although the efficiency for finding an interaction vertex and an electron track is quite high, there are several sources for inefficiency. It could be nuclear interactions with the beam pipe or dead material between CJC1 and CJC2. The dead material is also a reason for radiation of the electron. After the radiation the scattered electron bends more in the magnetic field and then the track does not extrapolate to the average run vertex anymore and therefore is not considered during the vertex fitting procedure.

To study vertex and electron track link efficiencies a “clean NC sample” is used. This sample is selected applying all analysis selection requirements (see chapter 7) apart from the vertex and track requirements. Instead, the events are required to be well balanced in longitudinal ($45 < E - p_z < 65$ GeV) and transverse momentum ($0.5 < p_{T,h}/p_{T,e} < 1.4$) to suppress non- $e p$ -collision and photoproduction background. Also a set of additional background finders that does not contain track or vertex requirements is applied.

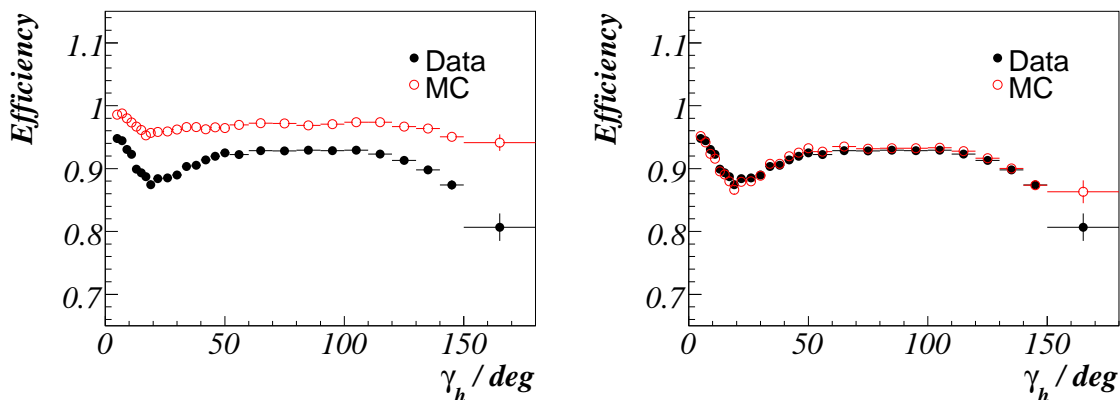


Figure 6.8: Vertex and track link efficiency as a function of γ_h before (left) and after (right) MC correction. The data are shown by full points and simulation by open points.

When no electron DTRA track is found within the CJC acceptance ($\theta_e > 30^\circ$), the

electron DTNV track information is used to reconstruct the position of the primary vertex. If the electron DTNV track does not exit or the scattered electron is outside of the acceptance of the CJC ($\theta_e < 30^\circ$) z_{vtx} is assumed to be zero. The DTNV electron track trajectory is extrapolated back to the beamline. The closest point of the track trajectory to the run average vertex provides the z position of the “DTNV vertex”, z_{vtx}^{DTNV} (see figure 6.7). The distance of closest approach (DCA) is required to be smaller than 2 cm to ensure good quality of the DTNV vertex. For larger DCAs, the z vertex position is taken to be zero.

The DTNV vertex, determined in the way described above, is independent from the biases due to nuclear interactions of the hadronic final state with the beam pipe. In case of absence of the electron DTRA track this vertex is used to reconstruct all necessary kinematic variables.

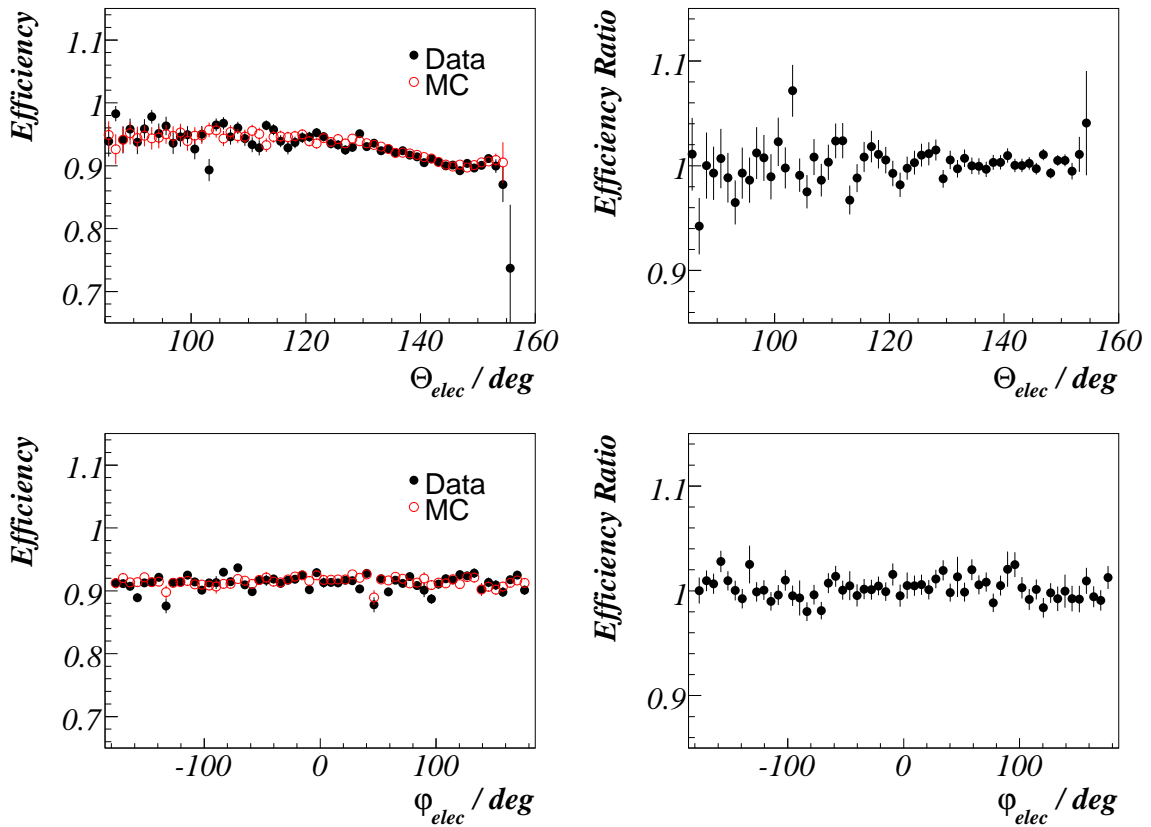


Figure 6.9: Vertex and track link efficiency (left) and efficiency ratio of data to MC (right) as a function of polar, θ_{elec} , (top) and azimuthal, φ_{elec} , (bottom) angles of the scattered electron for data (full points) and simulation after correction (open points).

The efficiency of the vertex and track link requirements is defined as

$$\varepsilon_{tr-vtx} = \frac{\text{Events with central vertex and } (DCA_{tr-cl}^{DTRA} < 12.0 \text{ cm or } \theta_e > 30^\circ)}{\text{All monitor events}}, \quad (6.3)$$

where the monitor sample is defined above.

The efficiency is studied for both data and MC. The MC events are then weighted in the following way to describe the data:

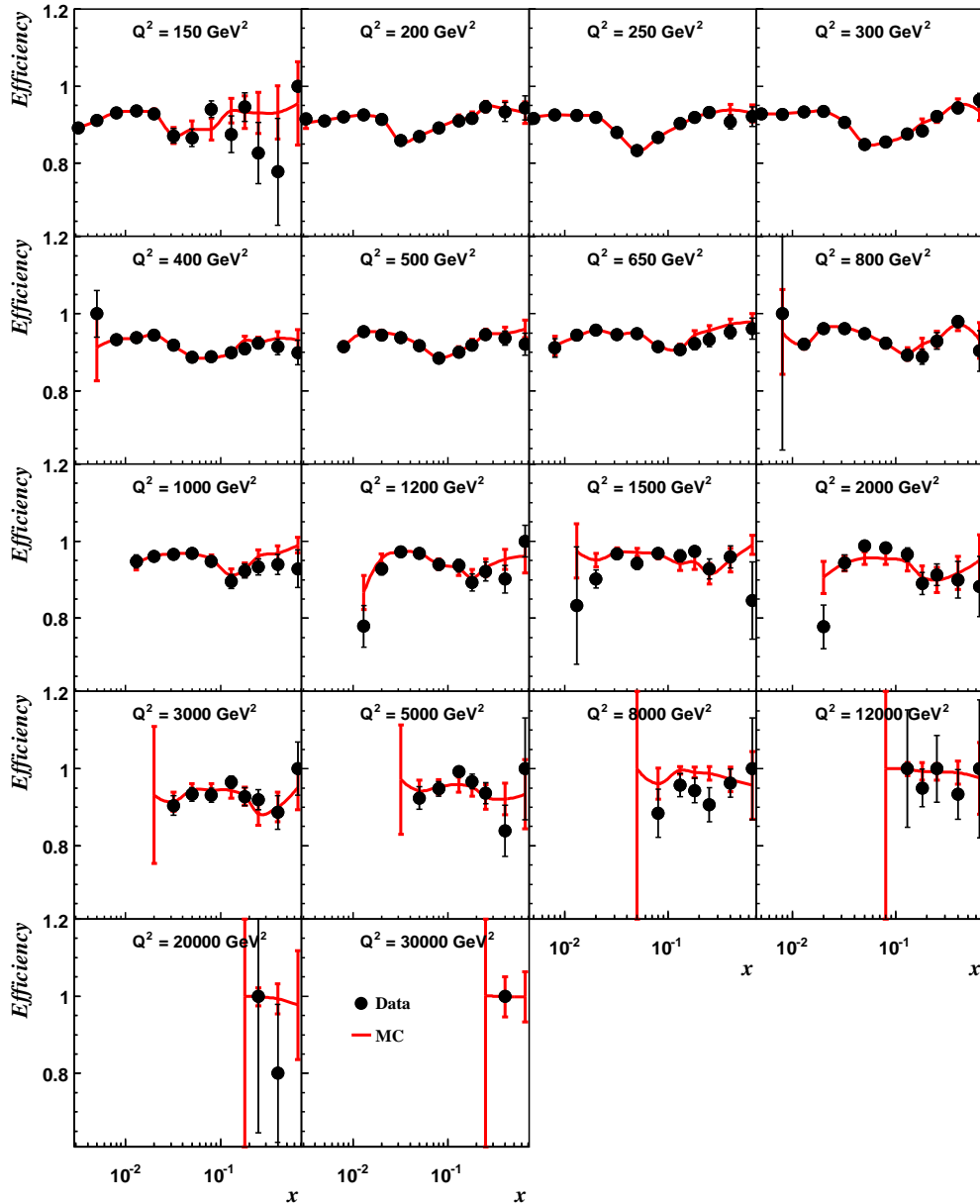


Figure 6.10: Vertex and track link finding efficiency in (Q^2, x) bins for the data (points) and for the MC after correction (curve).

- for $\log Q_e^2 > 3.25$: – use correction as a function of Q^2 .
- for $\log Q_e^2 \leq 3.25$: – first, correct as a function of γ_h , and then apply additional 2-dimensional corrections in Q^2 and x bins.

The inefficiency due to nuclear interactions of the hadronic final state with the beam pipe depends strongly on the struck quark angle γ_h . In the central region, where the struck quark is emitted at angles close to 90° , the efficiency is quite high (see figure 6.8), since the vertex fitting procedure gives more precise results. The efficiency decreases in the forward ($\gamma_h \sim 25^\circ$) and backward ($\gamma_h \sim 140^\circ$) regions due to the nuclear interactions. In the very forward region ($\gamma_h < 20^\circ$) the hadronic final

state is out of CJC acceptance and the vertex is defined by the electron track alone. Therefore the efficiency in this region rises.

The efficiency of the vertex and track link requirement is about 92%. It is shown in figure 6.9 for data and MC after correction as a function of the polar (θ_{elec}) and azimuthal (ϕ_{elec}) angles of the scattered electron, and in the (Q^2, x) bins used for the cross section measurement in figure 6.10. The efficiency corrections are determined and applied to MC separately for each helicity sub-period of the data taking to account for small time dependent effects. An uncorrelated uncertainty due to the vertex and track finding is assigned to be 3% for 2003-04 e^+p and 2% for 2005 e^-p data set.

The knowledge of the primary z vertex distribution is also needed for the luminosity determination. The luminosity is calculated in the same region in z_{vtx} , $|z_{vtx}| < 35$ cm, as is required for the analysis event selection. For the luminosity determination it is assumed that the primary z vertex distribution is gaussian, accompanied by two satellites of gaussian form, located at $z = \pm 70$ cm. Effects like nuclear interactions or imperfections of the beam optics add non-gaussian tails. Also an event occurring within ± 35 cm could be wrongly reconstructed outside ± 35 cm. The uncorrelated systematic uncertainty due to imperfect knowledge of the z_{vtx} distribution is conservatively estimated to be 0.5%. It appears as an additional normalisation error. This error was estimated studying migrations of events in the tails of the z vertex distribution.

6.5 Electron Angle Measurement

The polar (θ_e) and azimuthal (ϕ_e) angles of the scattered electron can be derived from the parameters of the track associated with the electron (if the track exists) or can be calculated from the position of the electron cluster in the LAr calorimeter and the position of the primary vertex. For the latter case the LAr calorimeter has to be aligned with the tracking system which defines the H1 coordinates and the position of the primary interaction point.

6.5.1 Track Extrapolation

Charged particles follow a helical trajectory in the H1 detector due to the 1.15 T solenoidal magnetic field. The determination of the impact position of the track in the LAr calorimeter is necessary in order to compare the track measurements with the energy deposits in the calorimeter. The track extrapolation method used in this analysis is briefly described below and is documented in [110].

The track trajectory is described by five parameters: the x , y , z coordinates of the track starting point, the polar (θ) and initial azimuthal (φ) angles of the track vector, and the curvature of the track which determines the trajectory in x and y (projection in the $r - \varphi$ plane) as the track moves outwards.

The track is extrapolated to the reference surface of the octagon (in the BBE 16-fold

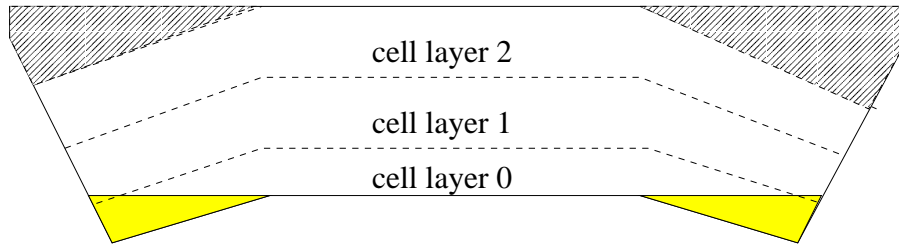


Figure 6.11: Schematic view of the BBE octant. The filled areas indicate the regions where there is no overlap with the CB1 wheel viewed along the z axis. The hatched areas in the plot corresponds to the non-instrumented part of the BBE.

polygon) structure with an inner radius of 105 cm. The z coordinate of the intersection of the extrapolated track and the reference surface is called z *impact* position. The well defined reference surface has the advantage, in contrast to the cluster position, to be independent of the longitudinal shower development of the electron cluster.

In case, the electrons enters the BBE through the front face of the BBE wheel, in a region where there is no overlap with the CB1 wheel (these regions are shown in figure 6.11), the z impact position corresponds to the front face of the BBE at $z = -152.5$ cm.

6.5.2 Alignment of the LAr Calorimeter

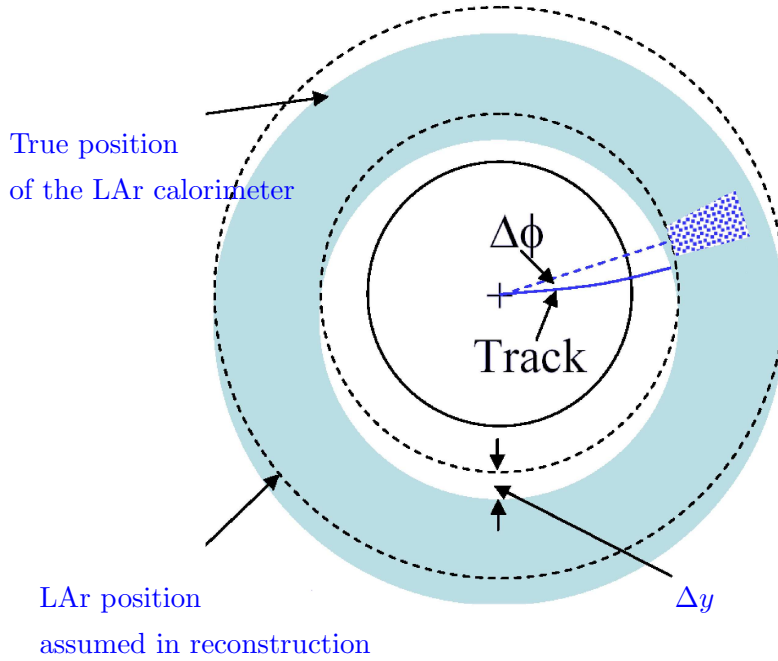
The precise reconstruction of the event kinematics requires the exact relative alignment of the different detector components. Therefore, the knowledge of the relative position of the LAr calorimeter and the central tracking system is crucial. The latter measures the interaction vertex for each event and defines the H1 coordinate system.

During the assembly of the LAr calorimeter, the wheels were pushed successively into the cryostat where they reside on supporting rails without a fixed connection among each other. The cool down to LAr temperature at about 72 K causes shrinkage of the LAr calorimeter wheels, in particular, in the z direction. Since the dimensions of the LAr calorimeter have been determined at room temperature, the change of the LAr calorimeter dimensions due to the low temperatures of the liquid argon should be corrected for [103]:

$$z_{cold} = 23.67 \text{ cm} + (z_{warm} - 23.67 \text{ cm}) \cdot (1 - 0.0027)$$

It corresponds to a 0.7 cm shift in z in the IF region ($z = 292$ cm).

An alignment of the LAr calorimeter relative to the tracking system is performed using the scattered electrons in the neutral current events. The procedure is based on the comparison of the position of the scattered electron measured in the LAr calorimeter with an associated CJC track extrapolated to the electron cluster. The alignment is performed for the data only since in MC the detectors are aligned by construction.

Figure 6.12: Illustration of the $\Delta\phi$ method.

The LAr calorimeter is aligned to the central tracking system by three rotations and three translations, defined in equations 6.4-6.6 and 6.7 respectively:

Rotations

$$x_1 = x_0 \quad y_1 = y_0 \cos \alpha - z_0 \sin \alpha \quad z_1 = z_0 \cos \alpha + y_0 \sin \alpha \quad (6.4)$$

$$x_2 = x_1 \cos \beta + z_1 \sin \beta \quad y_2 = y_1 \quad z_2 = z_1 \cos \beta - x_1 \sin \beta \quad (6.5)$$

$$x_3 = x_2 \cos \gamma - y_2 \sin \gamma \quad y_3 = y_2 \cos \gamma + x_2 \sin \gamma \quad z_3 = z_2 \quad (6.6)$$

where the subscript 0 refers to the point position in the unaligned coordinate system, and the subscripts 1, 2 and 3 refers to the coordinates of the point after a rotation of the coordinate system around the x , y and z axes respectively. Here, α , β and γ are the angles of rotation around the x , y and z axes, respectively.

Translations

$$x_f = x_3 - \Delta x, \quad y_f = y_3 - \Delta y, \quad z_f = z_3 - \Delta z, \quad (6.7)$$

where Δx , Δy and Δz are translations in x , y and z directions.

In the x and y direction these three rotations and translations of the LAr calorimeter with respect to the CJC are seen as z dependent shifts in φ of the cluster position with respect to the expected position defined from the tracker, as shown in figure 6.12. These shifts are studied by looking at $\Delta\phi = \varphi_{track} - \varphi_{cluster}$ as function of φ in slices of z_{LAr} (so-called “ $\Delta\phi$ -method”), which in case of misalignment has a sinusoidal form, as it is illustrated at the figure 6.13. The $\Delta\phi$ distributions for the slices are then simultaneously fitted and the alignment constants are extracted.

The $\Delta\phi$ -method is not sensitive to translations in the z direction. Therefore such translations are studied looking at $\Delta\theta = \theta_{track} - \theta_{cluster}$ (“ $\Delta\theta$ -method”) as function

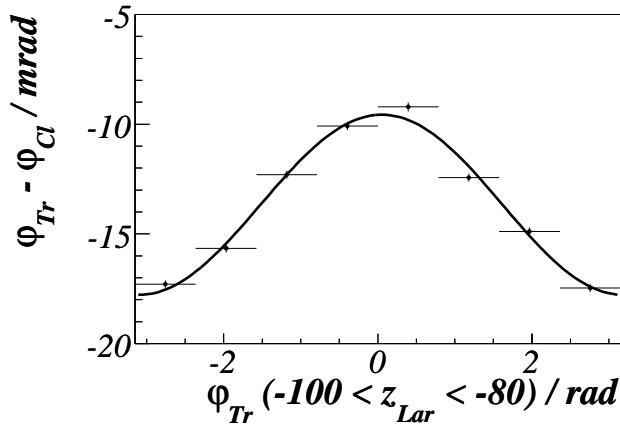


Figure 6.13: Illustration of the $\Delta\varphi$ -method. $\Delta\varphi = \varphi_{track} - \varphi_{cluster}$, as a function of φ of the track for the z slice $-100 \text{ cm} < z_{LAr} < -80 \text{ cm}$, shown for data (full points). The curve represents results of the alignment fit.

of φ in slices of z_{LAr} in a similar way as for the $\Delta\phi$ -method.

The applied alignment constants are listed in table 6.2.

rotations:	
$\alpha = +0.0 \text{ mrad}$	around x
$\beta = -0.9 \text{ mrad}$	around y
$\gamma = +0.0 \text{ mrad}$	around z
translations:	
$\Delta x = -0.14 \text{ cm}$	in x
$\Delta y = +0.40 \text{ cm}$	in y
$\Delta z = +0.00 \text{ cm}$	in z

Table 6.2: The alignment parameters of the LAr calorimeter.

In figure 6.14 the effect of the alignment of the LAr calorimeter is shown. The figure shows that after alignment the Δx , Δy and Δz differences between the position of the cluster and the entrance of the track to the LAr are very close to zero, and well described by MC which is intrinsically aligned.

The CJC and LAr measurements of the scattered electron polar angle θ_e are compared after alignment in figure 6.15, as a function of φ and the electron z impact position in the LAr calorimeter. They are in reasonable agreement. The remaining differences of the LAr to the CTD angle measurements are described by MC well within the quoted systematic uncertainty of 3 mrad. These differences may be attributed to the lack of precise z measurement from CJC. CIP and COZ are presently unable to improve the precision of the θ determination.

6.5.3 Azimuthal and Polar Electron Angles

The most accurate measurement of the azimuthal angle φ_e is provided by the CJC which is optimised for $r - \varphi$ measurements. Therefore, if a DTRA track is matched with the scattered electron, φ_e is taken from the track. When no track is associated to the scattered electron, the azimuthal angle is determined using the position of the

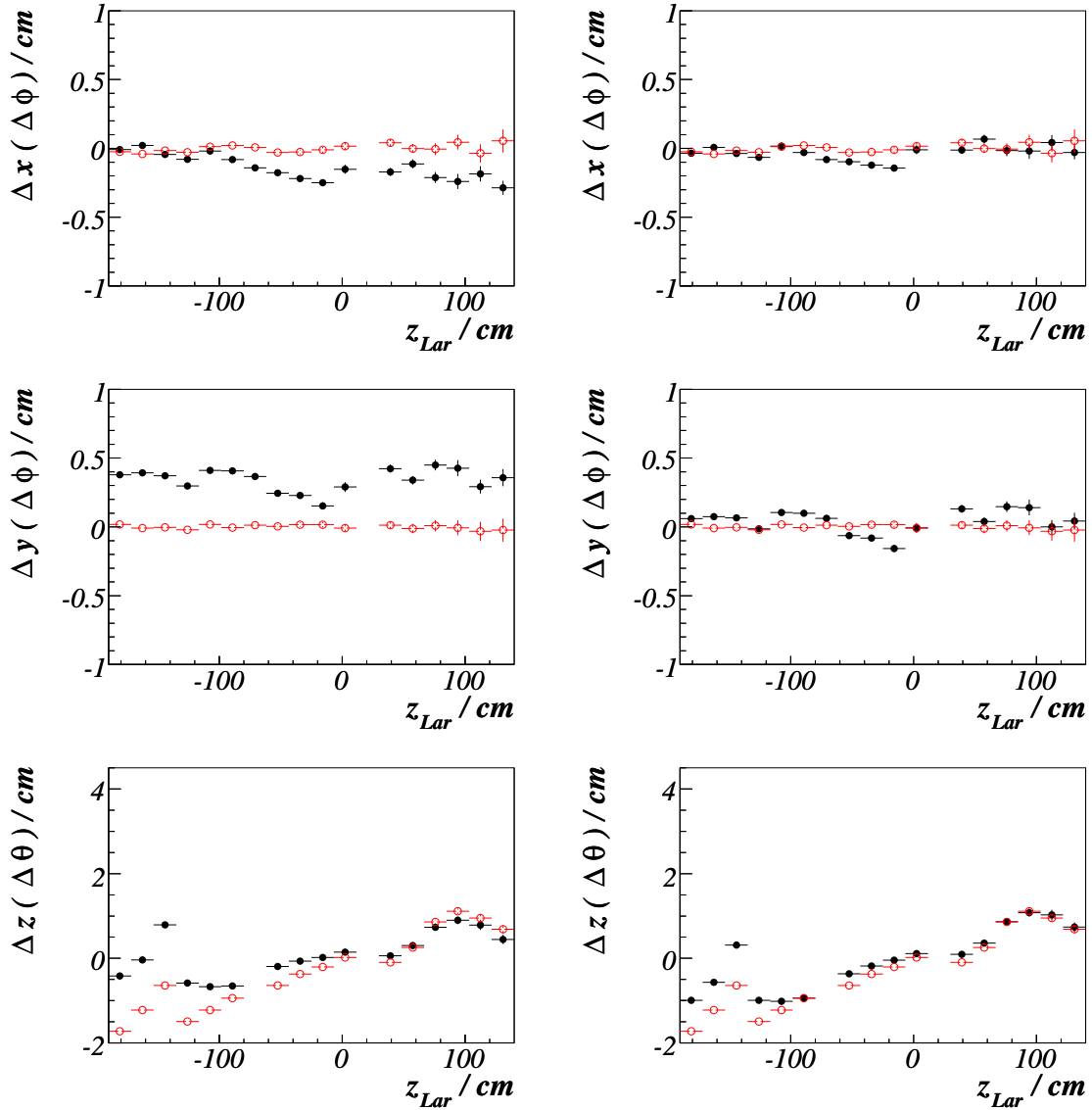


Figure 6.14: Track cluster matching before (left) and after (right) alignment for data (full points), compared to the simulation (open points). The shifts Δx and Δy , determined using the $\Delta\phi$ -method, and Δz , using the $\Delta\theta$ -method, are shown as function of the z impact position of the scattered electron in the LAr calorimeter.

cluster in the LAr calorimeter and the interaction vertex.

The z information provided by the CJC is poor due to the inferior z resolution. Therefore, the polar angle measurement θ_e is taken from the LAr clusters.

Electron tracks entering the Forward Track Detector are difficult to control. Electrons tend to shower in the dead material between CJC and FTD. Therefore, in the forward region, $\theta_e < 30^\circ$, the calorimeter cluster is used both for the azimuthal and polar angle measurements.

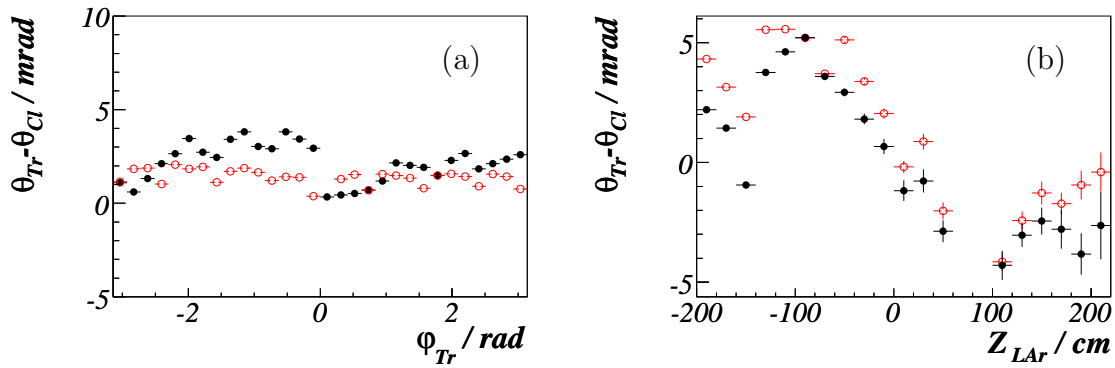


Figure 6.15: The track-cluster θ_e difference as a function of φ_e (a) and as a function of z impact position (b), shown for data (full points) and simulation (open) points.

Beam Tilt Correction

The ep beam axis does not exactly coincide with the z -axis of the H1 coordinate system. The beam has a small inclination in the x and y directions (see figure 6.16), the so-called “beam tilt”.

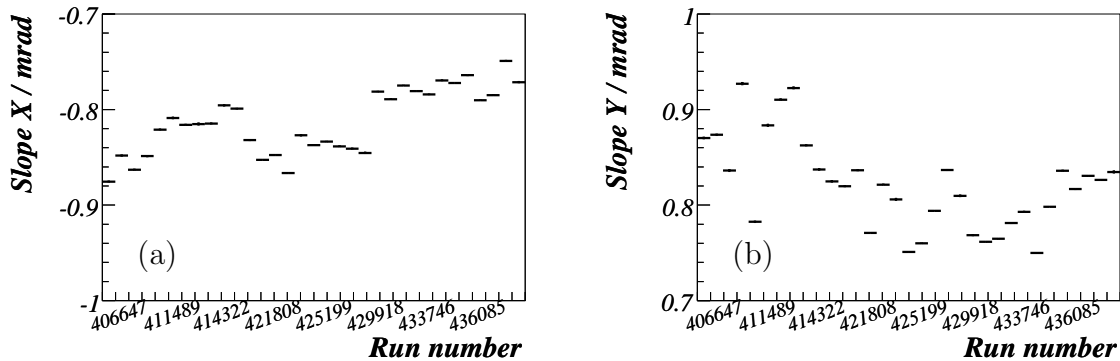


Figure 6.16: Beam tilt: the inclination of the beam with respect to the H1 coordinate system in the $x - z$ (a) and the $y - z$ (b) plane.

For the final calculation of the polar and azimuthal angles of the electron this difference between beam axis and the H1 coordinate system is taken into account. For this purpose a tilted coordinate system (x', y', z') is defined with the z' -axis in the direction of beam. The position of the electron cluster (x_e, y_e, z_e) in the original (X, Y, Z) coordinate system is then projected into tilted coordinate system (x'_e, y'_e, z'_e) and the final angles are determined as $\theta_e = \arctg\left(\frac{z'_e}{\sqrt{x_e'^2 + y_e'^2}}\right)$ and $\varphi_e = \arctg\left(\frac{y'_e}{x'_e}\right)$.

6.6 Electron Energy Measurement

In NC interactions both the scattered electron and the hadronic final state are measured in the H1 detector. This means that the system is over-constrained and different methods can be used for the reconstruction of the event kinematics (see section 5.1). The DA method does not rely on the energy measurement. Therefore the measured

angles of the scattered electron and of the hadronic final state, together with the precisely known beam energies, can be used to predict the energy of the scattered electron, using equation (5.20), and to perform a calibration of the calorimeter response.

The absolute calibration of the electron energy measurement is done separately for the data and MC in order to account for possible biases in the reconstruction.

6.6.1 Electron Energy Calibration

For the electron calibration the cluster energy in the LAr calorimeter is compared to the electron energy calculated using the double angle method (equation (5.20)). The energy calibration is studied using a sub-sample of the inclusive selection given in section 7.3. Additional criteria are applied to ensure sufficient precision of the DA method:

- $E'_e > 14$ GeV.
- $y_\Sigma < 0.3$ (0.5) for $z_{\text{impact}} \leq 20$ cm ($20 < z_{\text{impact}} < 100$ cm) ensures an accurate estimation of the E_{DA} (hadronic final state is well measured).
- $44 < E - P_z < 66$ GeV reduces effects of initial state radiation.
- $\gamma_h > 10^\circ$ ensures that the hadronic final state is contained in the detector acceptance and therefore well measured.
- The regions near the φ and z cracks, where the electrons are poorly measured, are excluded from the analysis.

The calibration is performed comparing the calorimetric energy with the DA-prediction as a function of the z impact position of the electron in the calorimeter. The main geometrical structures of the LAr calorimeter are z -dependent wheel and the φ -dependent octant structures (see section 3.6.1).

Calibration factors are obtained from the mean of the ratio E_e/E_{DA} . In order to reduce the influence of tails in the distributions only events with $0.85 < E_e/E_{DA} < 1.15$ are considered in the averaging. The calibration is done iteratively in a two stage process:

- **The wheel- and octant-wise calibration.** The first calibration step is performed octant-wise for each of the BBE, CB1, CB2 and CB3 wheels. The regions are enumerated by $N_{\text{stack}} = 8 \cdot N_{\text{wheel}} + N_{\text{octant}}$. Here, $N_{\text{octant}} = 0 - 7$ for $\varphi = 0 - 360^\circ$, and the wheels are enumerated by $N_{\text{wheel}} = 0 - 3$ for BBE, CB1, CB2, CB3. Because of the limited statistics, for the wheels FB1 and FB2 only one calibration factor per wheel is determined. Figure 6.17 shows the inverse calibration factors as a function of the stack number.
- **The z-wise calibration.** Further calibration factors are determined as function of the z position of the electron impact point in the LAr calorimeter

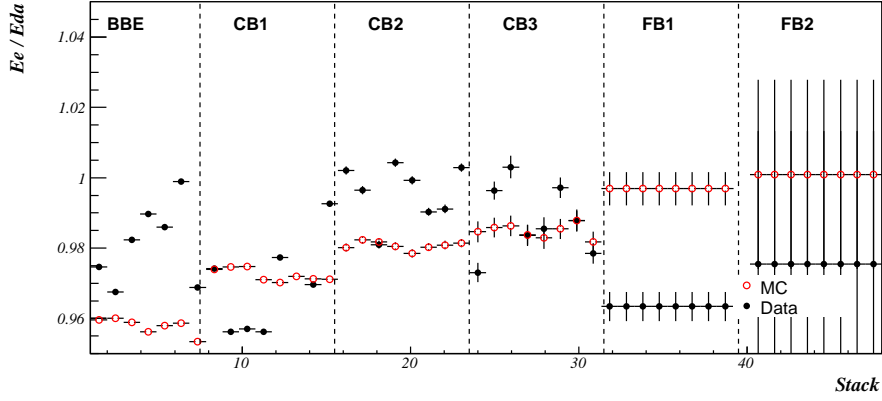


Figure 6.17: Mean values of the ratio E_e/E_{DA} as a function of the stack number for data (full circles) and MC (open circles) before calibration.

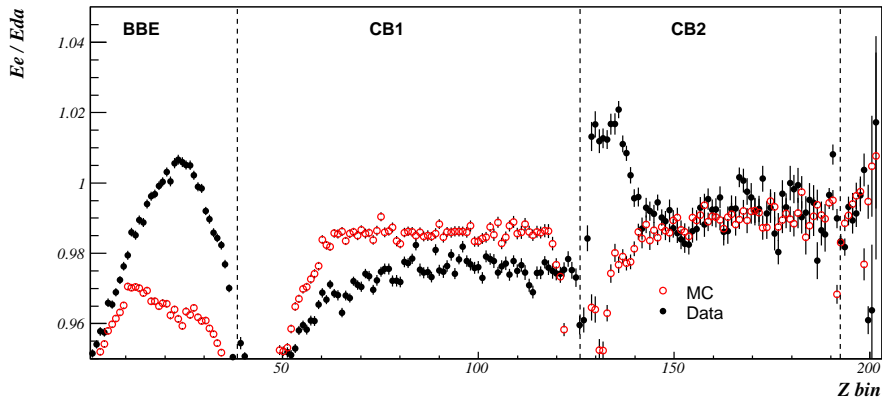


Figure 6.18: Mean values of the ratio E_e/E_{DA} as a function of the z position of the electron impact point for data (full circles) and MC (open circles) before calibration. Bin zero corresponds to $z = -190$ cm.

z_{LAr} . The factors are determined in 1 cm bins for $z_{LAr} < 0$, 10 cm bins for $0 \leq z_{LAr} < 90$ cm, 20 cm bins for $90 \leq z_{LAr} < 110$ cm and 50 cm bins for $z_{LAr} \geq 110$ cm. The increasing bin size is related to the decreasing statistics of the NC events (increasing Q^2). The calibration factors are shown as a function of z_{bin} in figure 6.18.

- The two steps procedure is iteratively repeated with narrowing of the averaging window for E_e/E_{DA} to $0.9 < E_e/E_{DA} < 1.1$.

After applying these calibration factors, the ratio E_e/E_{DA} is shown in figure 6.19. The ratio is everywhere close to unity, with only small deviations (less than 1%) near the cracks and in BBE. A good agreement, well within 1%, between data and simulation is observed.

The total uncertainty on the electron energy scale is estimated to be:

- for $z_{LAr} \leq 20$ cm 1%;
- for $20 \text{ cm} < z_{LAr} \leq 110$ cm 2%;
- for $z_{LAr} > 110$ cm 3%;

The correlated part of the total uncertainty comes mainly from possible biases of the calibration method and is estimated to be 0.5% throughout the LAr calorimeter.

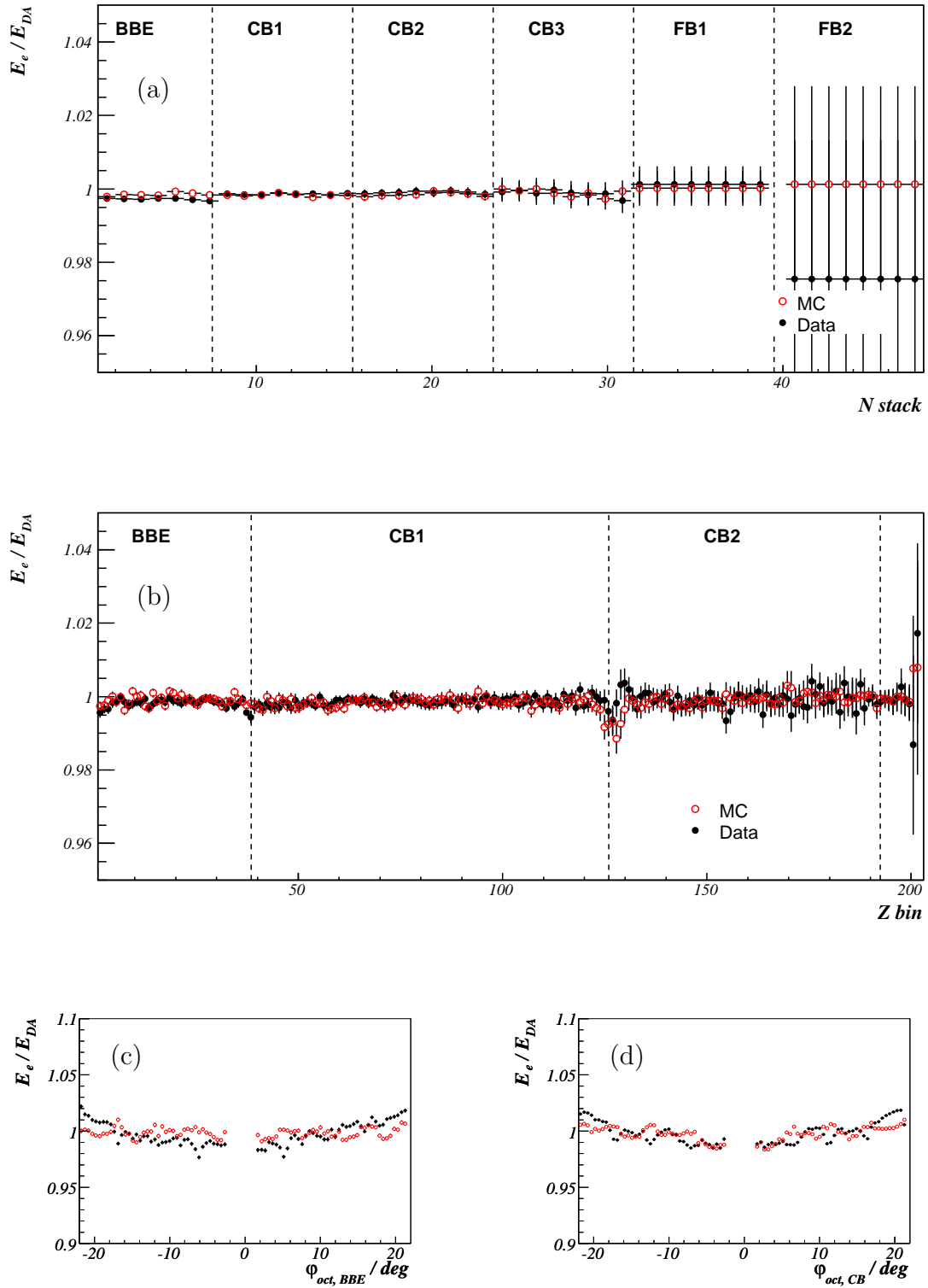


Figure 6.19: Electron energy measurement after calibration for the data from 2004-05. The mean values of the ratio E_e/E_{DA} as a function of the stack number (see text) (a) and the z position of electron impact point (b). The ratio E_e/E_{DA} as a function of the φ angle between the electron impact point and closest φ -crack for BBE (c) and CB1-CB3 (d).

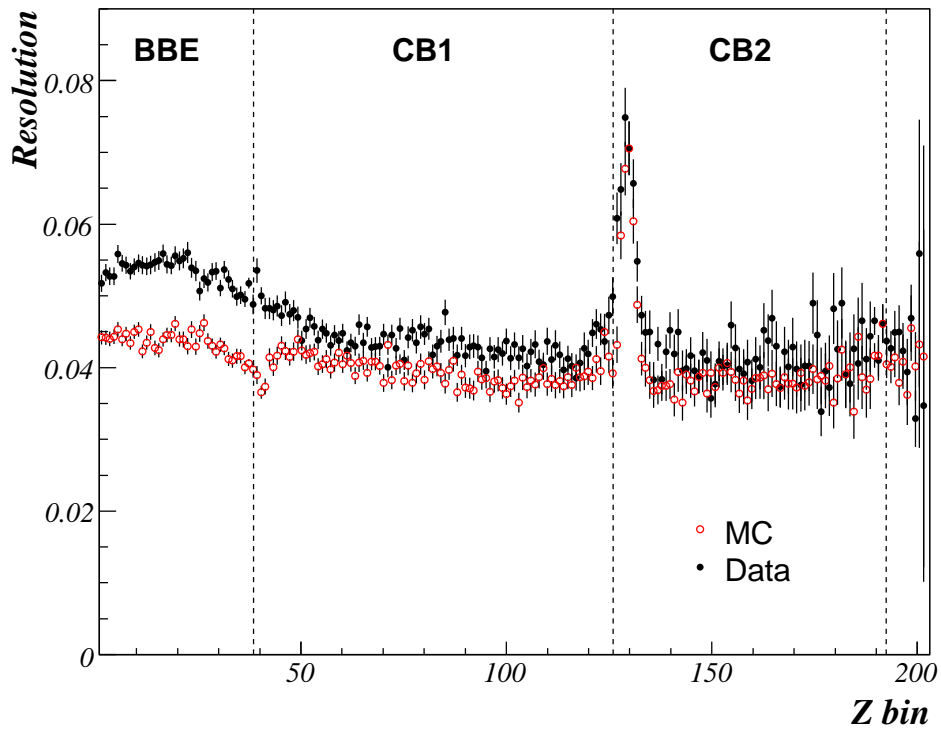


Figure 6.20: The resolution of the electron energy measurement as a function of the z -position of the impact point before calibration for data (full circles) and MC (open circles).

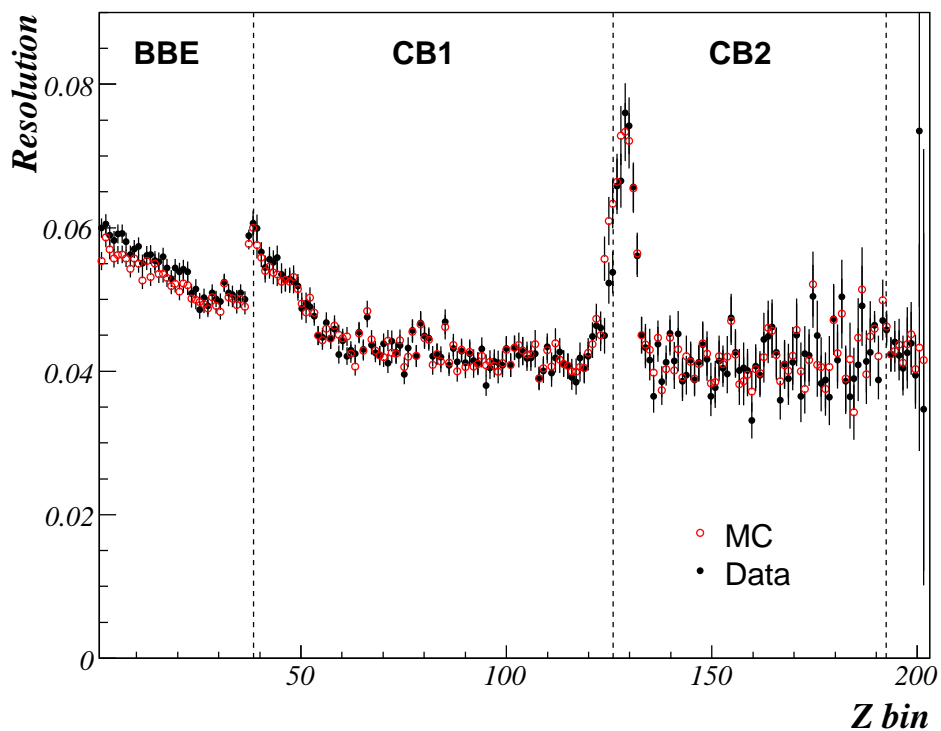


Figure 6.21: The resolution of the electron energy measurement as a function of the z -position of the impact point after calibration and a Gaussian smearing of the energy in simulation.

6.6.2 Electron Energy Resolution

The energy resolution of the LAr for electromagnetic deposits has been studied with the test beams at CERN [104] and was found to be

$$\sigma(E)/E = 12\%/\sqrt{E/\text{GeV}} \otimes 1\%.$$

The electron energy resolution in the LAr calorimeter as function of z impact determined using a root mean square of the ratio E_e/E_{DA} is shown in figure 6.20. For the given event selection it is typically between four and six percent. The resolution is significantly worse near the z -cracks, at $z \simeq -65$ cm and $z \simeq -150$ cm. To improve the description of the resolution by the simulation, additional energy smearing in MC is applied using a Gaussian function with $\sigma_{smear} = \sqrt{\sigma_{Data}^2 - \sigma_{MC}^2}$. This difference is determined for each z bin used in the z -wise calibration. Figure 6.21 shows that, after this additional smearing the MC describes the data almost perfectly.

6.7 Hadronic Energy Measurement

For the reconstruction of the DIS event kinematics the following hadronic variables are used: $E - P_z$, $P_{T,h}$ and γ_h (see chapter 5). These variables are calculated summing over all particles in the hadronic final state as they are measured in the LAr calorimeter and SpaCal together with the central tracker. In order to provide a good measurement of these variables, a precise knowledge of the hadronic energy scale is needed.

The hadronic energy measurement in the calorimeter can be strongly affected by the noise originating from the preamplifier electronics (see section 3.6.1). Therefore the noise suppression is particularly important in the analysis. The noise in the calorimeter can bias the measurement of $y_h = \sum_h (E^h - P_z^h)/2E_0$. At low y_h , when $E^h \sim P_z^h$ most of the hadrons are produced in the forward direction. Even relatively low energy noisy clusters in the barrel part of the LAr will strongly bias the y_h measurement.

Figure 6.22 shows the relative contributions of the LAr calorimeter, SpaCal and tracks to y_h as function of the inelasticity y . The main contribution is coming from the LAr calorimeter. SpaCal is contributing only at high y . A sharing of y_h between the different components is well described by the simulation. The figure shows also the suppressed noise contribution relative to the measured y_h . For the remaining difference of the suppressed noise, a systematic uncertainty of 10% is assigned to the energy identified as noise in the LAr calorimeter.

The reconstruction of the *hadronic final state* (HFS) is performed by the HFS finder within the H100 framework, using the HADROO2 algorithm [97], combining measurements from different sub-detectors. The inputs to the HADROO2 algorithm are *clusters* reconstructed in the LAr and SpaCal calorimeters and *tracks* measured by the Central Tracker. The tracks must satisfy certain quality criteria, as described in [97].

The treatment of tracks and clusters in the HADROO2 algorithm is briefly reviewed below. Then the jet calibration is discussed and the tests of the hadronic energy

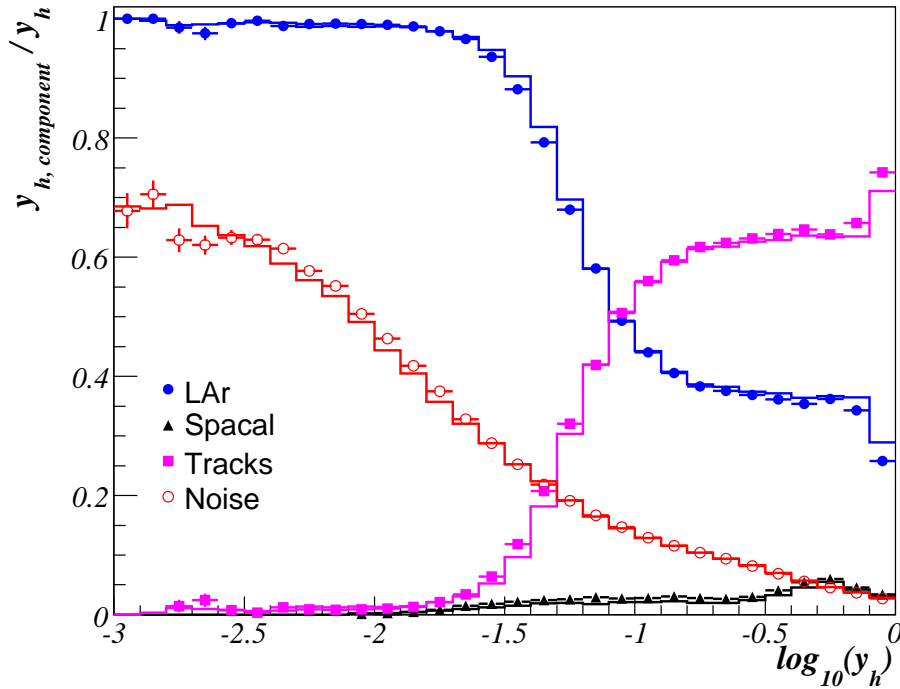


Figure 6.22: Relative contributions from LAr calorimeter, tracks and SpaCal to the total y_h and the suppressed noise contribution relative to the measured y_h .

calibration are presented.

6.7.1 The HADROO2 Algorithm

The HADROO2 algorithm realises the treatment of the HFS particles candidates. If there are identified electrons or muons which are not flagged as isolated², they are considered as being part of the hadronic final state. These leptons with their corresponding four vectors are taken as particle candidates into HFS and their associated tracks and clusters are excluded from any additional treatment.

The algorithm starts with the previously described list of selected tracks and clusters. The algorithm aims to combine track and cluster measurements, both of which may exist for a charged particle, in order to obtain an optimal measurement of the HFS. The relative resolution of each charged track is compared to the expected resolution for a calorimeter deposit of the same energy, and is used to form a decision on the choice of which measurement is taken. No attempt is made of combining the measurements.

²A muon is isolated if the calorimeter energy in a cylinder (cylinder radius of 35 cm in the electromagnetic, 75 cm in the hadronic LAr section) around the extrapolated muon track is below 5 GeV and if there is no other selected track in a cone of $R_{\eta-\varphi} = 0.5$. The isolation criteria of the LAr electrons against clusters are defined in section 6.1. All SpaCal electrons are considered as isolated.

Comparison of Tracker and Calorimeter Resolutions

Each track in the HFS is supposed to originate from a pion, with energy

$$E_{track}^2 = P_{track}^2 + m_\pi^2 = P_{T,track}^2 / \sin^2\theta + m_\pi^2. \quad (6.8)$$

The error on this energy is obtained by standard error propagation:

$$\frac{\sigma_{E_{track}}}{E_{track}} = \frac{1}{E_{track}} \sqrt{\frac{P_{T,track}^2}{\sin^4\theta} \cos^2\theta \sigma_\theta^2 + \frac{\sigma_{P_T}^2}{\sin^2\theta}}, \quad (6.9)$$

where σ_{P_T} and σ_θ are the corresponding errors on P_T and θ , neglecting their correlations. The corresponding error on the LAr measurement of the same energy, $\sigma_{E,LAr\ expect}$, is given by the hadronic energy resolution as

$$\left(\frac{\sigma_E}{E}\right)_{LAr\ expectation} = \frac{\sigma_{E,LAr\ expect}}{E_{track}} = \frac{0.5}{\sqrt{E_{track}}}. \quad (6.10)$$

The relative resolutions defined by equations (6.9) and (6.10) are compared to determine which component, the tracker or the calorimeter, provides a better measurement.

Track Measurement

If the following relation holds

$$\frac{\sigma_{E_{track}}}{E_{track}} < \frac{\sigma_{E,LAr\ expect}}{E_{track}}, \quad (6.11)$$

then the track measurement is used to make a particle candidate. In this case the calorimetric energy is suppressed to avoid double counting. Each track is extrapolated up to the surface of the calorimeter as a helix, and inside LAr as a straight line. The calorimetric energy $E_{cylinder}$ is computed as the sum of all clusters in the overlapping volume of a 67.4° cone and two cylinders of radius 25 cm in the electromagnetic part of LAr and 50 cm in the hadronic part. This volume will be referred hereafter as the ‘‘cylinder’’.

Then the track energy E_{track} is compared to the calorimetric energy inside the cylinder $E_{cylinder}$, taking into account possible fluctuations of both measurements within their standard errors. The well-measured E_{track} provides a constraint on the energy deposited by charged particles; so the calorimeter measurement is discarded unless $E_{cylinder}$ fluctuates more than 1.96σ (the 95% Confidence Level) above E_{track} . In this case, the discrepancy is attributed to neutral particles with energy $E_{cylinder} - E_{track}$. This means that the calorimetric energy is reduced by energy of the track.

Calorimetric Measurement

If equation (6.11) is not fulfilled then the energies $E_{cylinder}$ and E_{track} are compared and:

- if $E_{track} \in [E_{cylinder} - 1.96\sigma_{E_{cylinder}}, E_{cylinder} + 1.96\sigma_{E_{cylinder}}]$, with $\sigma_{E_{cylinder}} = 0.5\sqrt{E_{cylinder}}$, the track is considered to be compatible with the calorimetric deposit and the calorimetric measurement is used to define a particle candidate.

- if $E_{track} < E_{cylinder} - 1.96\sigma_{E_{cylinder}}$, the track measurement is used and the calorimetric energy is reduced by the energy of the track.
- if $E_{track} > E_{cylinder} + 1.96\sigma_{E_{cylinder}}$, the track is suppressed and a hadron is defined using the calorimetric clusters only.

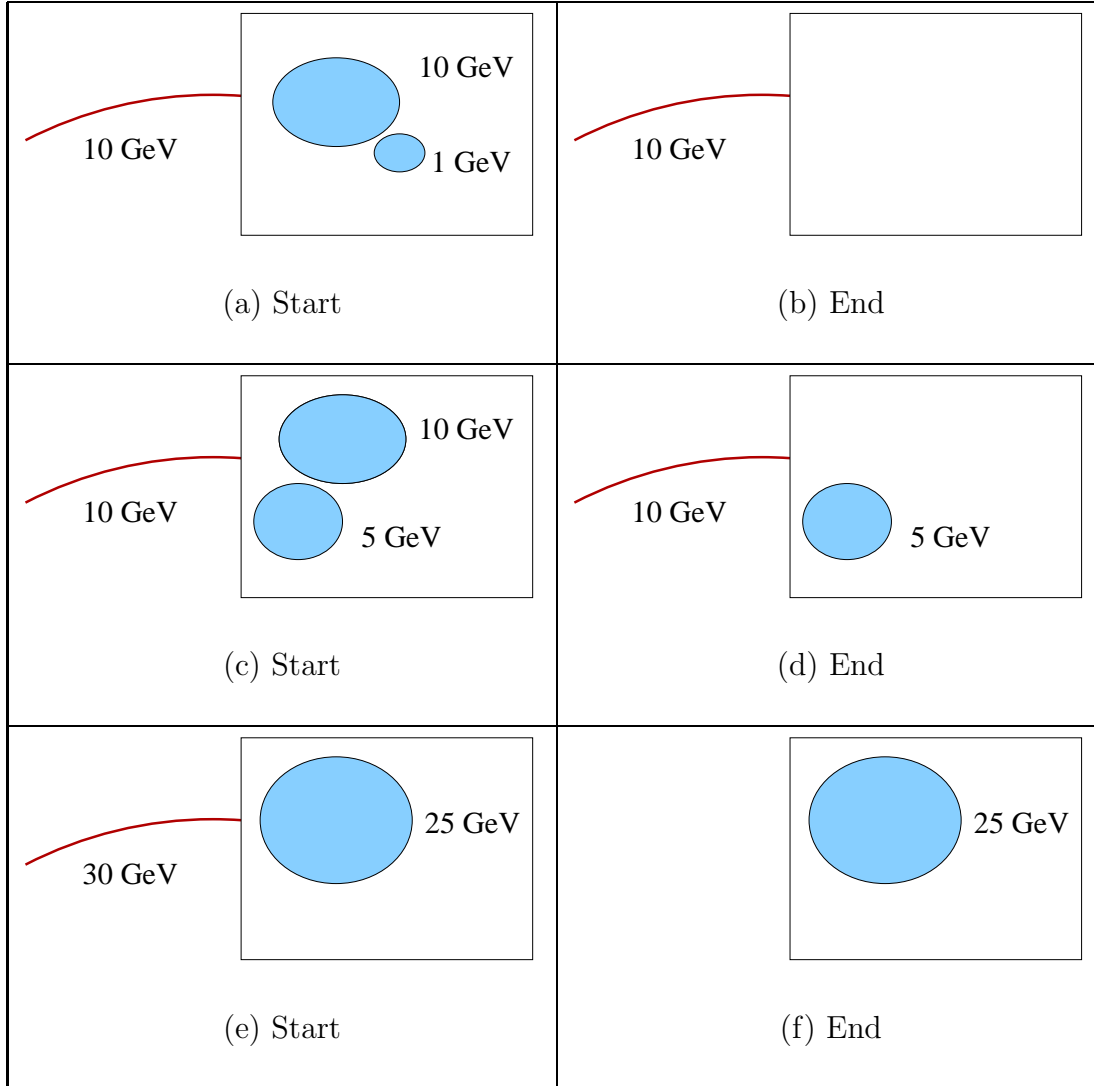


Figure 6.23: Examples: The behaviour of the HADROO2 algorithm, given three starting situations involving tracks and clusters. On the first line, a 10 GeV track measured with a 4 % accuracy is kept and all the calorimetric information is removed. In the second line the track information is still kept, however the cylinder energy of 15 GeV is determined to contain a neutral component and it is reduced by the track energy. In the third line the track is not well measured (15 % accuracy) and the calorimetric information is used.

Treatment of residual clusters

Once all tracks have been considered, the remaining particle candidates are made out of clusters. These particles correspond to either neutral particles with no associated track or to charged particles with a badly measured or non-reconstructed track.

6.7.2 Calibration of Hadronic Energy

Once the hadron finding algorithm has been fully specified, a suitable calibration procedure can be applied. The selected tracks are considered as calibrated and the calibration procedure for the hadrons must not change their energy. The aim is therefore to perform a jet calibration, but only changing the energy of calorimeter clusters. The double angle method is used to calibrate the hadronic energy on the basis of reconstructed jets. The calibration has been performed separately for data and simulated events.

The implementation of the jet calibration is described in [97]. Briefly, the double angle kinematics (see equation (5.20)) determines the reference scale, $p_T^{DA} = E_{DA} \sin \gamma_h$, in an analogous way to the electron calibration discussed in section 6.6.1. The calibration factors are determined using DIS NC events in which the hadronic final state is formed by one jet.

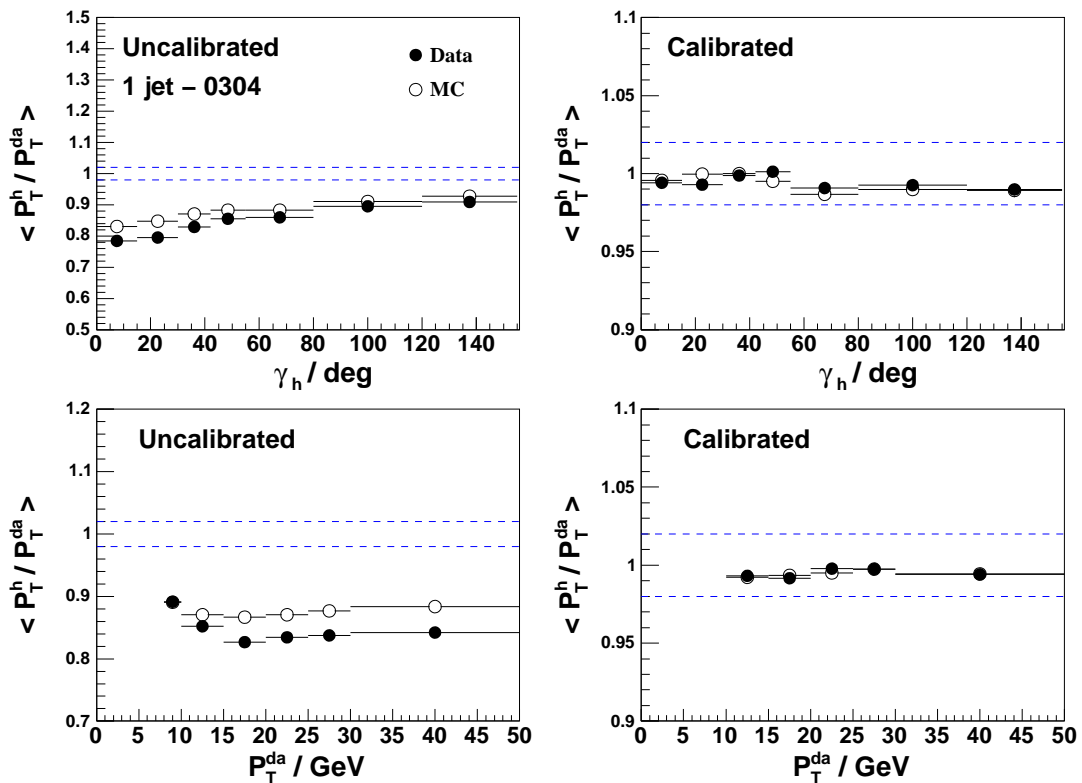


Figure 6.24: Distribution of p_T^{bal} for data and Monte Carlo events as function of the hadronic polar angle γ_h (upper two plots) and p_T^{DA} (bottom two plots) before (left) and after (right) the jet calibration. The dotted lines represent a $\pm 2\%$ uncertainty around unity.

The evolution of mean values of the momentum balance, $p_{T,Bal} = p_T^h / p_T^{DA}$, is fitted

separately for individual γ_h regions. The functional form used for the fit is

$$F_{p_T, Bal}^{\gamma_h}(p_T^{DA}) = A_{\gamma_h}(1 - \exp^{-B_{\gamma_h} - C_{\gamma_h} p_T^{DA}}). \quad (6.12)$$

This provides an absolute calibration factors.

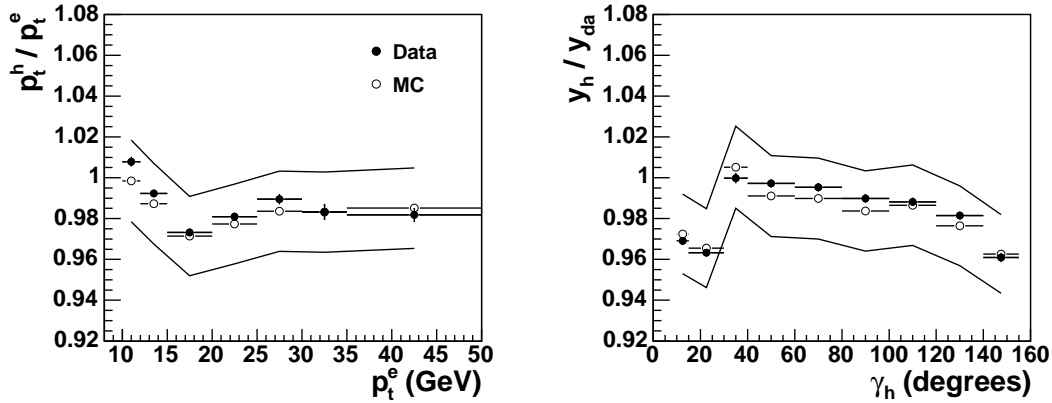


Figure 6.25: The mean values of the transverse momentum balance, p_t^h/p_t^e , as a function of the transverse momentum of the scattered electron, p_t^e , (left) and y balance with respect to the double angle reference, y_h/y_{da} , as a function of γ_h . The error bands correspond to a 2% systematic uncertainty.

For each jet the fraction of P_T^{jet} carried by clusters before calibration C_{cls} is defined as

$$C_{cls} = \frac{P_T \text{ uncalibrated clusters}}{P_T \text{ tracks} + P_T \text{ uncalibrated clusters}}. \quad (6.13)$$

Both data and MC are calibrated in an iterative procedure by multiplying the energy of all clusters in the jet by the following factor

$$f = \frac{1 - F_{p_T, Bal}^{\gamma_h} \cdot (1 - C_{cls})}{F_{p_T, Bal}^{\gamma_h} \cdot C_{cls}}. \quad (6.14)$$

However parameterization given in equation (6.12) does not completely describe data of low p_T jets [97]. Therefore only jets with $p_T^{jet} > 4$ GeV are calibrated with this method. In the very forward region, $\gamma_h < 7^\circ$, affected by leakage in the beam-pipe no absolute calibration can be reasonably applied, too. Jets reconstructed in the SpaCal calorimeter ($\gamma_h > 155^\circ$) are not calibrated either.

In order to also calibrate the remaining hadrons which are not part of a jet, or in jets not calibrated using $F_{p_T, Bal}^{\gamma_h}$, the dependence of the calibration coefficients is determined using p_t^h/p_T^{DA} in γ_h bins. These coefficients are applied to all remaining hadrons, separately for data and MC, to perform an absolute calibration, except in the region $\gamma_h < 7^\circ$ where a relative calibration is applied. Here, only data events are calibrated, to bring the response of the LAr calorimeter in data to the one in the MC simulation.

The hadronic energy scale before and after calibration is demonstrated by figure 6.24. The hadronic final state transverse momentum is compared to the double angle reference scale, showing good agreement between data and MC after calibration.

The comparison of the mean values of the transverse momentum balance and the y balance with respect to the double angle reference is shown for the data and MC simulation in figure 6.25. The agreement of data and MC in both distributions is well within 2%, taken as the hadronic calibration uncertainty.

6.8 Determination of the Trigger Efficiency

During data taking the decision whether to record an event for further analysis or not is done through a multi-level trigger system. Since in the high Q^2 NC DIS events the electron is scattered into the LAr calorimeter the most important trigger component for this analysis is the LAr trigger.

The efficiency of a trigger element TE, or a combination of trigger elements, is defined as follows:

$$\varepsilon_{TE} = \frac{\text{number of events triggered by MT and TE}}{\text{number of events triggered by MT}} \quad (6.15)$$

where MT is an independent monitor trigger or trigger element. The selection of monitor triggers is given in table 6.3

LAr trigger elements	monitor trigger
LAr_electron_1	PSNC
LAr_T0	CIP_T0
CIP_T0	LAr_T0
ToF Veto	ST57 and special runs
CIP Veto	ST57 and special runs

Table 6.3: NC trigger elements and their monitor triggers

Two mutually independent trigger efficiencies, condition A and condition B, can be combined to form the efficiency of (A OR B):

$$\varepsilon_{AB} = \varepsilon(A|B) = \varepsilon(A) + [1 - \varepsilon(A)] \cdot \varepsilon(B). \quad (6.16)$$

6.8.1 *LAr_electron_1* TE Efficiency

The trigger level information on the calorimeter Big Towers (see section 3.11.1 for an overview of the LAr trigger system) is exploited to study the *LAr_electron_1* TE efficiency. The *LAr_electron_1* TE can be fired by both the scattered electron and the hadronic final state. The efficiency of the LAr triggering on an electron deposit is evaluated using those neutral current events in which the hadronic final state caused the *LAr_electron_1* TE to fire. In turn, the efficiency for triggering on the hadronic final state is calculated with events in which an electron deposit causes the

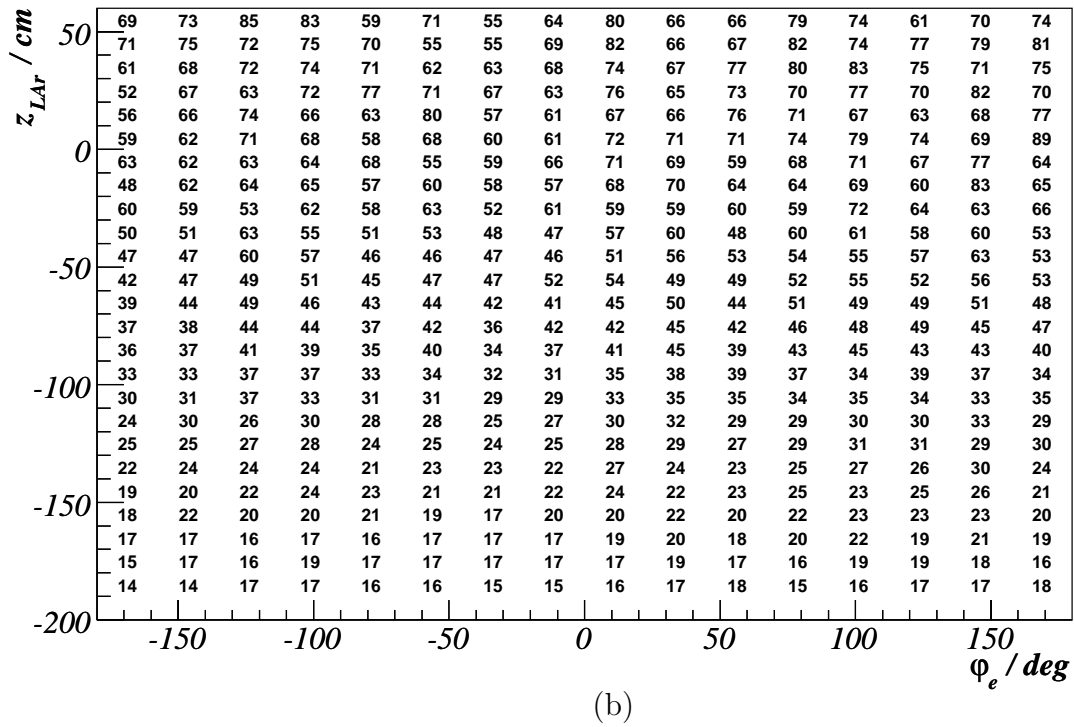
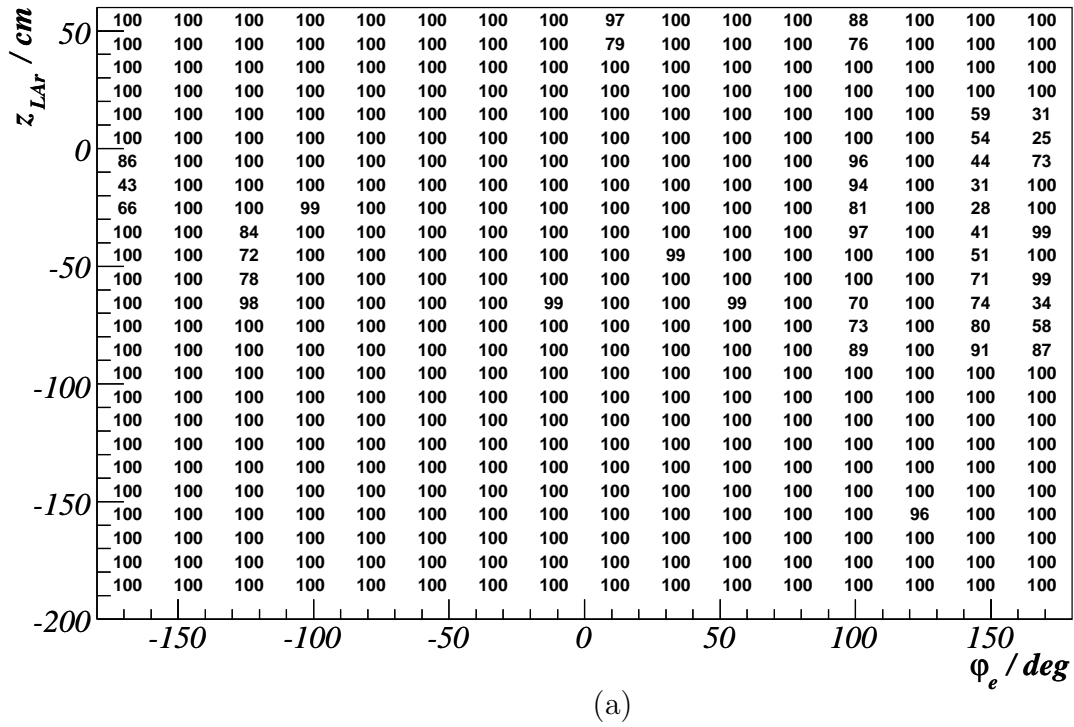


Figure 6.26: The efficiency to fire the *LAr_electron_1* TE by the scattered electron (a) and by the hadronic final state (b), presented in a $z - \varphi$ grid, using the 2005 e^-p data.

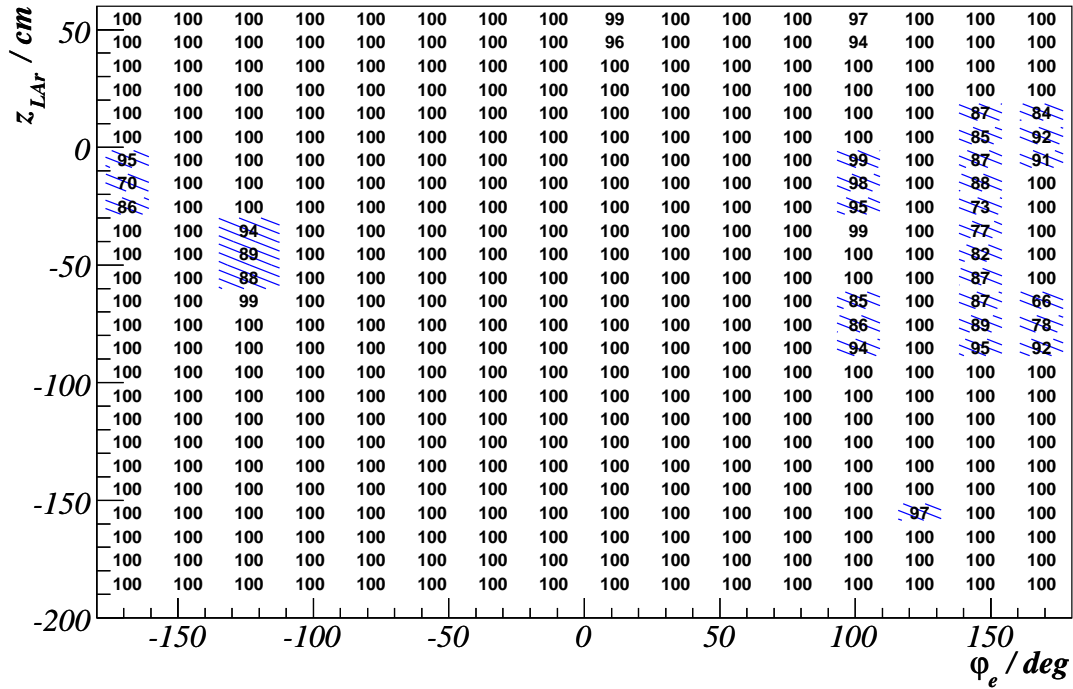


Figure 6.27: The efficiency of the trigger element *LAr_electron_1*, presented in a $z-\varphi$ grid using the 2005 e^-p data. The hatched areas indicate regions which are excluded because of low efficiency of the *LAr_electron_1* TE.

LAr_electron_1 to fire.

The efficiency to fire the *LAr_electron_1* TE by the scattered electron is 100% except in some local regions (see figure 6.26 (a)). These regions are attributed to areas where trigger cells have been switched off due to high noise or malfunctioning hardware. The efficiency to fire the *LAr_electron_1* TE by the hadronic final state is shown in figure 6.26 (b). It is low, about 17%, in BBE ($-190 < z_{LAr} < 151$ cm) and rises up to $\simeq 70\%$ for $z_{LAr} > 0$ cm. The reason for this is that the density of the energy deposit in the LAr calorimeter by the hadronic final state is higher (Lorentz boost) in the central and forward regions compared to the one in the backward region. Having more energy deposited in a single Big Tower, the probability to exceed a threshold value and to fire the *LAr_electron_1* TE is higher.

The efficiency for triggering on hadrons is independent of the efficiency for triggering on electrons, so that the combined trigger efficiency can be estimated using equation 6.16. As an example, this combined efficiency is shown in figure 6.27 for the 2005 e^-p data set. The efficiency is found to be very high over the bulk of the detector volume. Inefficient regions (marked as hatched areas in figure 6.27) are excluded from the analysis. After these fiducial cuts, the *LAr_electron_1* efficiency is essentially 100%.

In order to account for small time dependent effects the *LAr_electron_1* TE efficiency is studied in a way it is discussed above and inefficient regions are excluded for each of the helicity sub-periods of the 2003-04 e^+p and 2005 e^-p data taking.

6.8.2 Timing Condition

The T0 trigger elements allow the determination of the bunch crossing time. In the subtriggers the T0 requirements from the LAr calorimeter and CIP chamber are used. The efficiency of T0 trigger elements as function of φ_e and z impact position of the scattered electron are shown for the 2003-04 e^+p (figure 6.28) and for the 2005 e^-p (figure 6.29) data periods. The combined LAr T0 CIP T0 efficiency is close to 100%.

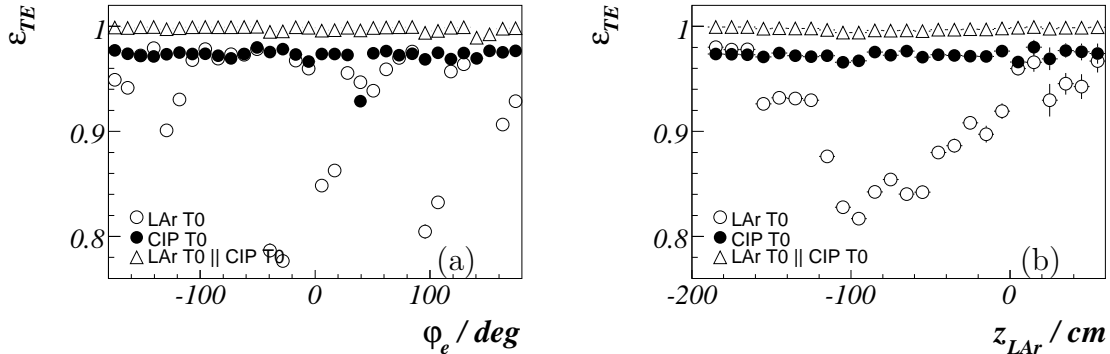


Figure 6.28: T0 trigger efficiencies as a function of (a) φ_e and (b) z_{LAr} for the 2003-04 e^+p data period.

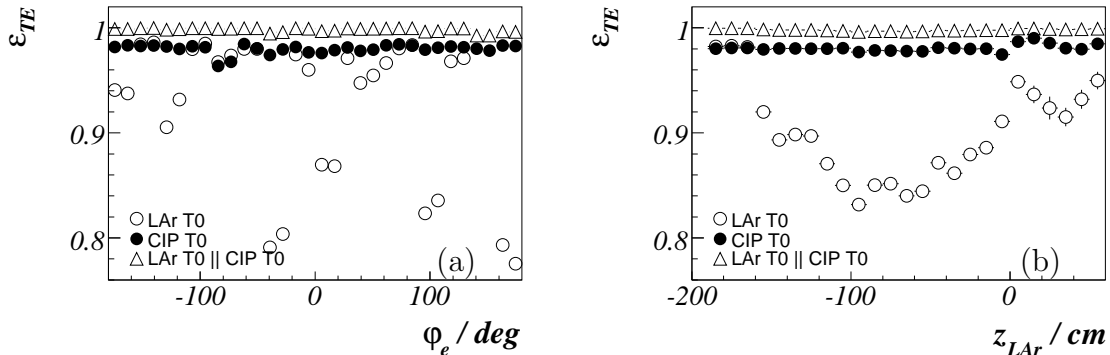


Figure 6.29: T0 trigger efficiencies as a function of (a) φ_e and (b) z_{LAr} for the 2004-05 e^-p data period.

6.8.3 Veto Conditions

The veto conditions in subtriggers ST67 and ST77 are described in section 3.11.1. The veto conditions use time-of-flight (ToF) information to reject out of time background events. In addition, the CIP is able to veto background from interactions in the collimators located in the beam pipe on the basis of the z vertex origin of tracks.

The signal inefficiency due to these veto conditions, i.e. the chance of rejecting good ep events, is continuously monitored with the subtrigger ST57. This monitor trigger is a copy of ST67 without the veto conditions applied. It is prescaled to keep the rate manageable. For most of the 2003-04 e^+p period, ST57 monitors only the *CIP_veto* condition. For the last part of the e^+p and the whole 2005 e^-p part of the

running, ST57 was loosened so that it contained neither CIP nor ToF veto conditions. Figure 6.30 shows inefficiency of the veto conditions, determined by the monitoring subtrigger ST57.

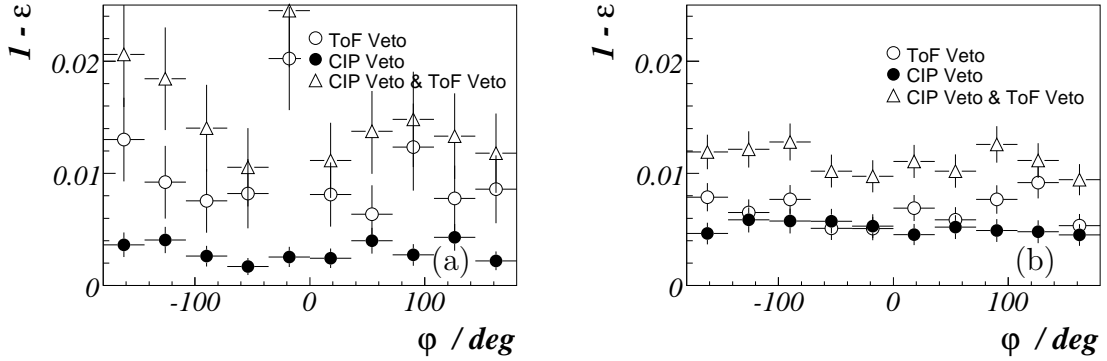


Figure 6.30: Veto trigger efficiencies as a function of φ_e for (a) e^+p 2003-04 and (b) for e^-p 2005.

To estimate the inefficiency of the *ToF_veto* conditions for the 2003-04 e^+p period, special runs without veto requirements were used:

- 367976-367979 (67.2 nb⁻¹)
- 368015-368016 (3.9 nb⁻¹)
- 368957-368990 (113.3 nb⁻¹)

Since these samples have limited statistics and the ToF rejection does not depend on the type of ep process, low Q^2 NC events were used with the following selection:

- Scattered electron in SpaCal ³.
- Electron energy $E_{elec} > 14$ GeV.
- Distance R_{clus} of the electron cluster from the z axis in $r - \varphi$ -plane:
 $R_{clus} > 20$ cm.
- $Q_e^2 > 4$ GeV².
- $y_e < 0.9$.
- Longitudinal momentum balance: $35 \text{ GeV} < E - p_z < 65 \text{ GeV}$.
- “Central” vertex with $|z_{vtx}| < 35$ cm.

The obtained value for the *ToF_veto* inefficiency, $(0.46 \pm 0.06)\%$, for the 2003-04 e^+p data, is then averaged with the value estimated for the last part of e^+p period, using ST57.

The efficiencies of the *CIP_veto* and *ToF_veto* requirements as well as their corresponding errors are listed in table 6.4 for the 2003-04 e^+p and the 2005 e^-p data sets. Each helicity sub-period is corrected for the corresponding veto inefficiency values.

³A description of the SpaCal electron finder can be found in [13].

Year	Period	CIP veto eff., %	ToF veto eff., %	Total veto eff., %
0304 $e + p$	RH	99.79 ± 0.03	99.30 ± 0.25	99.09 ± 0.25
	LH	99.56 ± 0.07	99.30 ± 0.25	98.86 ± 0.26
2005 $e - p$	RH	99.44 ± 0.07	99.09 ± 0.09	98.54 ± 0.11
	LH	99.49 ± 0.04	99.44 ± 0.04	98.93 ± 0.06

Table 6.4: Veto efficiencies.

6.8.4 Trigger Efficiency

The *LAr_electron_1* TE and timing conditions are the core of the high Q^2 NC trigger used in this analysis. It is required that the trigger is fully efficient for the selected data. The regions in which this is not the case are excluded as indicated on the figure 6.31.

The efficiency of the veto conditions, which are introduced in the trigger to reject non- ep background, does not depend on the ep physics process. The small inefficiencies observed due to these requirements are corrected for.

An uncorrelated systematic uncertainty of 0.5% is attributed to the trigger efficiency.

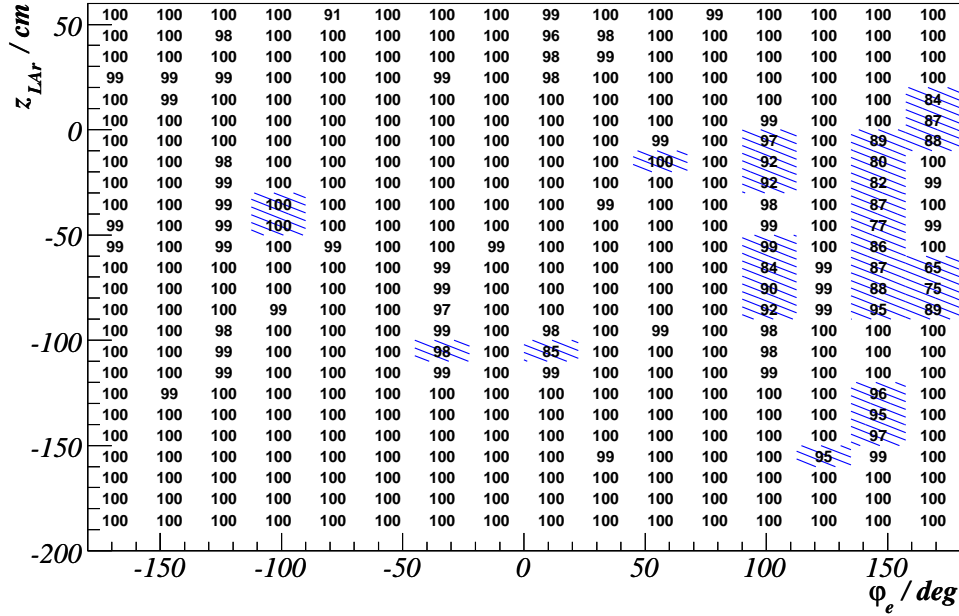
6.9 Fiducial Volume Definition

The fiducial volume cuts ensure the precise measurement of the scattered electron of NC high Q^2 events. The φ and z crack regions are excluded to obtain a reliable electron identification (cf. section 6.1), a precise determination of the cluster position (cf. section 6.5), and good resolution of the electron energy measurement (cf. section 6.6). In addition, regions of inefficient LAr trigger cells and CIP trigger pads are excluded from the analysis, taking into account their time variation (cf. section 6.8). The fiducial volume definition is applied using the impact position (see section 6.5.1) of the scattered electron.

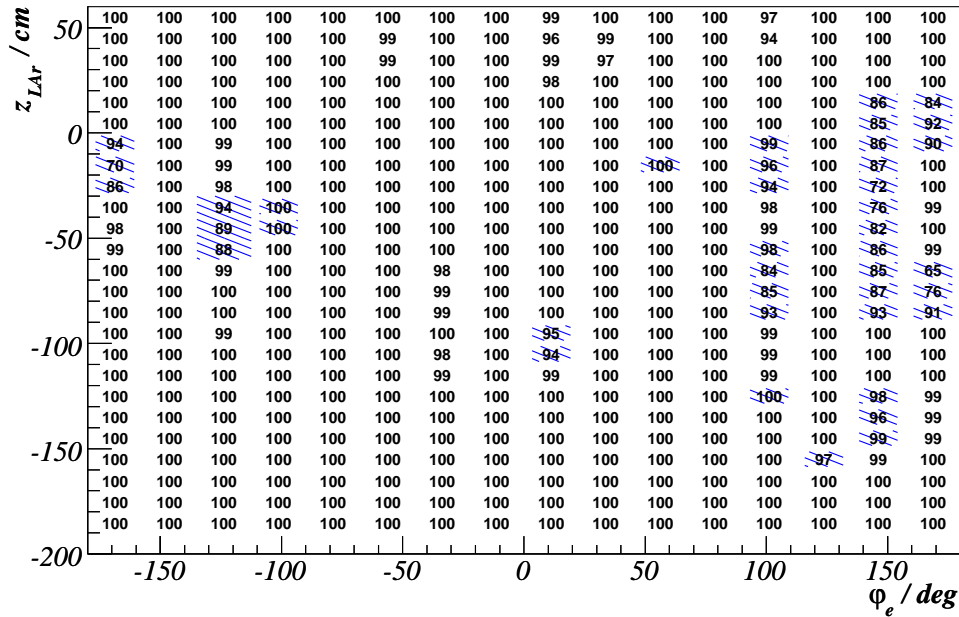
6.10 Rejection of Non- ep Background

Apart from events produced by interactions of the electron and proton beams, a small fraction of events containing cosmic muons or originating from collisions of the proton beam with the beam-pipe wall or residual gas molecules in the beam-pipe are still triggered and recorded by the H1 experiment. These *cosmic muon*, *beam-halo muon* and *beam-gas* events constitute the non- ep background to physics analyses at HERA and need to be rejected, in order to make measurements and to be able to compare the data with theory predictions. The three different types of non- ep background events are rejected on the basis of their characteristic signatures in the detector:

- Cosmic muons are produced by decaying hadrons from collisions of high energetic cosmic particles with gas molecules in the earth's atmosphere. Correspondingly, cosmic muons penetrate the H1 detector typically with incident angles around $\theta \approx 90^\circ$, $|\varphi| \approx 90^\circ$. The experimental signature of the cosmic



(a)



(b)

Figure 6.31: Trigger efficiency in the $z - \phi$ plane of the electron impact position, shown for the 2003-04 e^+p (a) and for the 2005 e^-p (b) data taking periods. The hatched areas indicate regions which are excluded because of low trigger efficiency.

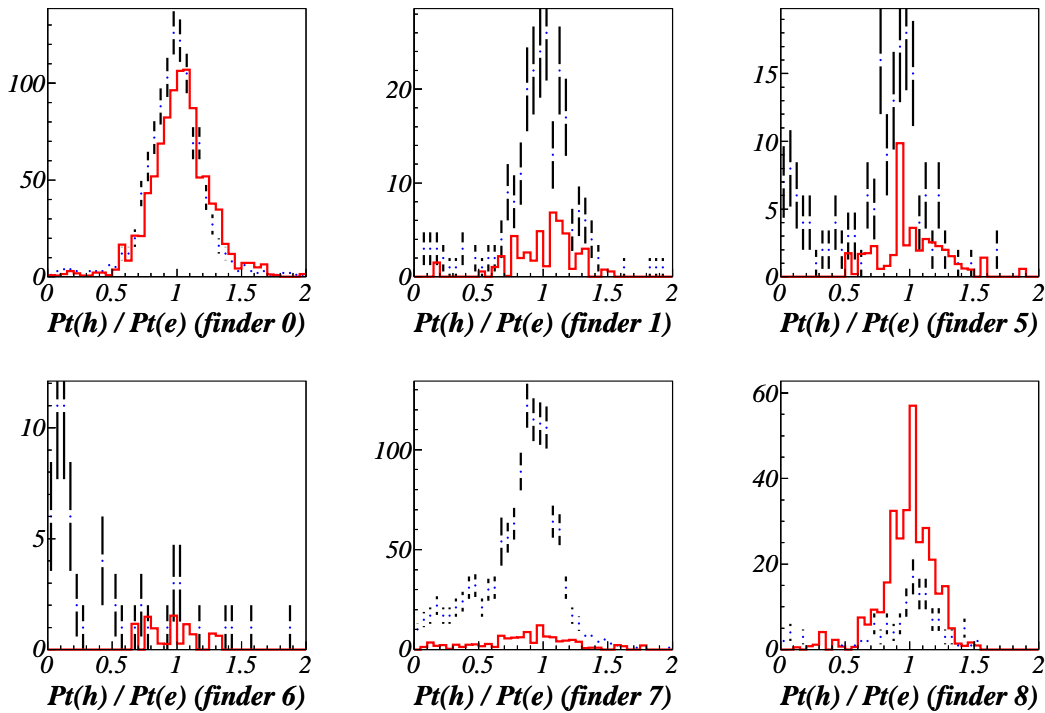


Figure 6.32: Distribution of p_T balance for events found by the background finders 0-8 (points). The line corresponds to genuine NC events from MC (see text).

muon events are two isolated muon tracks in the instrumented iron, the liquid argon calorimeter and the central tracking detector which are “back-to-back” in polar and azimuthal angle, and with a timing difference of a few ns between the tracks measured in the central jet chamber.

- Beam-halo particles are produced in collisions of stray protons in the tails of the transverse beam profile with the beam-pipe walls. The produced hadronic component is absorbed quickly, so that mainly muons are observed in beam-halo events in the H1 detector. The experimental signature of beam-halo events is a muon track in the backward iron endcap, the liquid argon calorimeter and the forward iron endcap, parallel to the beam-pipe.
- Beam-gas events originate from collisions of the proton beam with residual gas molecules in the beam-pipe. As a result of the high proton beam energy, the particles produced in beam-gas interactions are strongly boosted in the forward direction. The experimental signature of beam-gas events are many low p_T tracks isotropically distributed in azimuth.

The majority of the beam-halo, beam-gas and cosmic muon background may be suppressed by algorithms (“non- ep background finders” [98]) that reject the non- ep background on the basis of topological criteria, exploiting information about tracks and clusters in different sub-detectors that are characteristic for beam-halo, beam-gas and cosmic muon events.

Finder	Algorithm	Description
0	HALAR	Longitudinal energy pattern in the LAr calorimeter.
1	HAMULAR	Longitudinal energy pattern in the LAr calorimeter with energy deposit inside the backward iron endcup.
5	COSMUMU	Two opposite muon tracks matching in directions.
6	COSMULAR	At least one muon with 90% energy deposited in a matching LAr cluster.
7	COSTALAR	Two opposite clusters in the Tail Catcher with 85% energy deposited in matching LAr clusters.
8	COSTRACK	Two CJC tracks with opposite directions in space.

Table 6.5: Background finding algorithms [98] for halo-muons and cosmic muons.

Distribution of the p_T balance for events found by different background finding algorithms are shown in 6.32. The NC events, as expected, have $P_T^h/P_T^e \simeq 1$. Therefore an event is rejected if it is found:

- by one of the finders 5, 6 for $P_T^h/P_T^e < 0.5$,
- by finder 7 for $P_T^h/P_T^e < 0.1$,
- by finder 0 and 1 or by two finders out of 5-7 for $P_T^h/P_T^e > 0.1$.

Distribution of the p_T balance for events found by pair of the background finders as described above are shown in figure 6.33.

Figures 6.32 and 6.33 demonstrate that the background finders allow for an efficient rejection of the non-ep background while keeping all ep NC events shown by the line. After applying the background finders the selected sample is essentially free from non-ep background events. This was also confirmed by visual scanning of events with $Q^2 > 5\,000\text{ GeV}^2$.

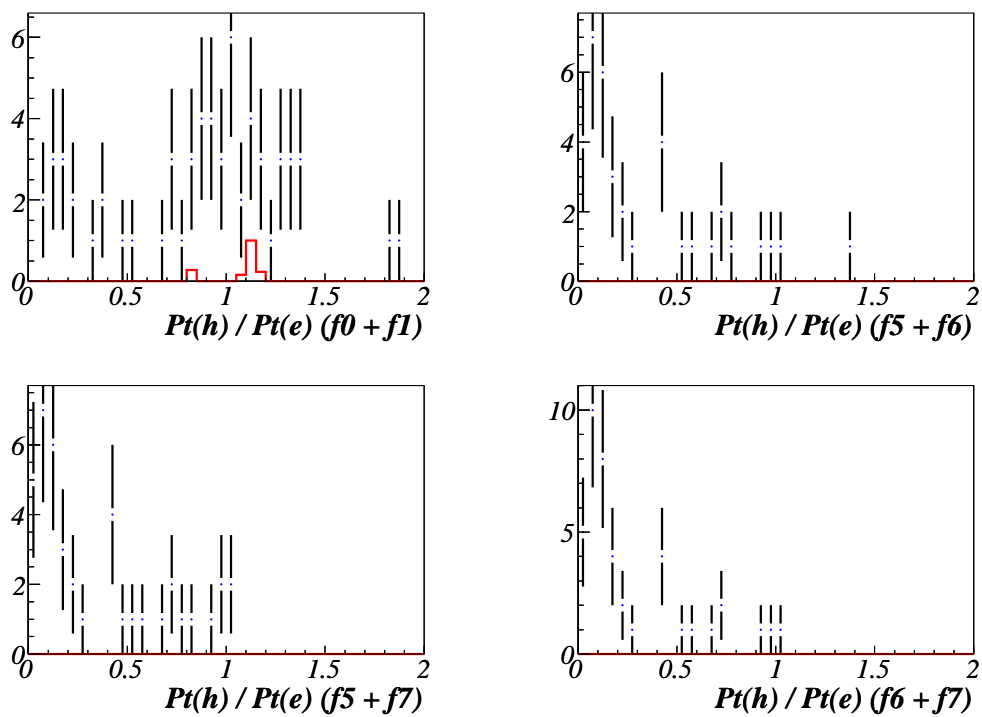


Figure 6.33: Distribution of p_T balance for events found by background finders which are rejected by a pair of background finders (see text). The line corresponds to genuine NC events from MC.

Chapter 7

Selection of NC Events

This chapter presents the data selection applied for the inclusive neutral current cross section measurement. The run selection including the polarisation requirements and the luminosity measurement are explained and the data samples used in the analysis are introduced. Finally, the NC selection is summarised and the Monte Carlo simulation is compared to the data.

7.1 Run Selection

During data taking, events are collected in time intervals (up to two hours), called *runs*, with nominally stable accelerator and detector conditions. Depending on the overall detector performance, background situation, problems with readout and so on, the runs are classified as “good”, “medium” or “poor”. For this analysis only “good” and “medium” runs are selected. Furthermore, for each run it is required that all important components are fully operational (supplied by *high voltage*, HV) and included in the readout. These components are the LAr calorimeter and the LAr trigger, the central drift chambers (CJC1 and CJC2) and the proportional chamber (CIP), the luminosity system and the ToF system¹. The information about the high voltage status of each hardware component during data taking is stored in a database every ten seconds. A run is rejected if any of the relevant detector components was “off” for a large fraction of time. An event in the run is accepted only during time periods when the relevant (see above) HV settings were “on”. Correspondingly, the luminosity associated with the run is calculated only for these time periods. The luminosity measurement procedure was discussed in section 3.10.

Runs with luminosity less than 0.2 nb^{-1} are rejected to ensure a certain level of stability during data taking.

7.1.1 Polarisation Selection

The technical aspects of the polarisation measurement were discussed in section 3.3. The polarisation is taken as measured by the LPOL polarimeter. If there is no LPOL

¹Some HV requirements are already included in the definition of a “good” or “medium” run. Since a run can be classified as “medium” when CIP or ToF is off, or just only one of the central drift chambers is operational, explicit HV requirements are applied.

measurement available, then the TPOL is used. If neither polarimeter is operational at the time when an event is recorded, the event is rejected. This requirement was put in order to reduce the systematic error on the polarisation measurement. The luminosity is calculated only for the time periods when the polarisation measurement is available, in a similar manner as for the HV requirement.

Runs with polarisation $-20\% < P_e < 0\%$ for 2003-04 e^+p and $0\% < P_e < 15\%$ for 2005 e^-p were excluded from the analysis. The fraction of luminosity for these runs is small compared to the main sample.

The luminosity weighted profiles of the measured e^+ and e^- polarisations are shown in figure 7.1.

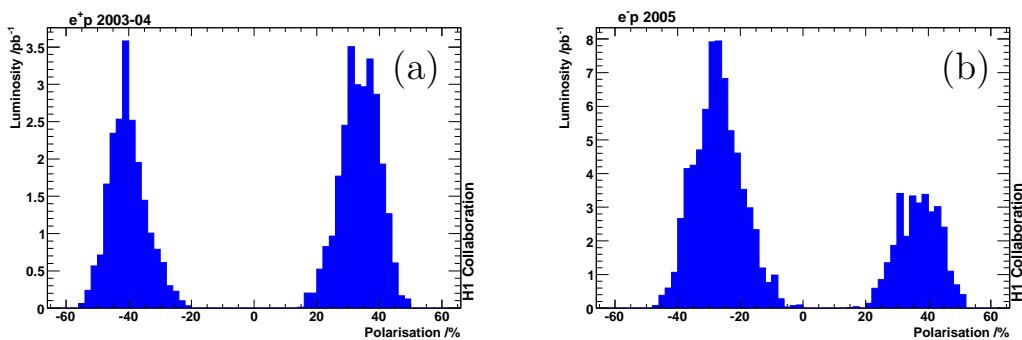


Figure 7.1: The luminosity weighted polarisation profile for the 2003-04 e^+p (a) and the 2005 e^-p (b) data.

Both 2003-04 e^+p and 2005 e^-p data sets are subdivided into samples with positive (“RH”) and negative (“LH”) average longitudinal polarisations. The corresponding luminosities and average longitudinal lepton beam polarisations are given in table 7.1.

Data sample	Luminosity	Polarisation	Time period
e^+p RH	26.9 pb^{-1}	$(+33.6 \pm 0.6)\%$	17.10.03-01.04.04, 02.07.04-12.08.04
e^+p LH	20.7 pb^{-1}	$(-40.2 \pm 1.1)\%$	03.04.04-19.06.04
e^-p RH	29.6 pb^{-1}	$(+37.0 \pm 1.3)\%$	25.05.05-06.09.05
e^-p LH	68.6 pb^{-1}	$(-27.0 \pm 1.8)\%$	03.02.05-18.05.05, 09.09.05-11.11.05

Table 7.1: Table of luminosities and luminosity weighted average longitudinal polarisations, for the data sets presented in this analysis.

A global uncertainty of 1.3% and 2.0% on the luminosity measurement is assigned for e^+p and e^-p data respectively, of which 0.5% is common to both [119]. For the e^+p data the uncertainty in the measurement of the lepton beam polarisation is taken to be 1.6% for the LPOL and 3.5% for the TPOL [120], yielding a total relative polarisation uncertainty of 1.8% for RH data set and 2.7% for the LH data set. For the e^-p data a global uncertainty of 5% is considered [119].

The run selection criteria used in this analysis are summarised in table 7.2.

Run quality	“good” or “medium”. Runs with “problems” are excluded (see text).
High voltage on and in read-out	LAr and LAr trigger, CJC1 and CJC2, Lumi, CIP, ToF
Run duration	$L_{run} > 0.2 \text{ nb}^{-1}$
Polarisation	Polarimeter measurements are available and $P_e < -20\%$ for 2003-04 e^+p LH $P_e > +15\%$ for 2005 e^-p RH

Table 7.2: Run selection requirements related to data taking conditions and operational status of the detector systems.

7.2 Event Yield

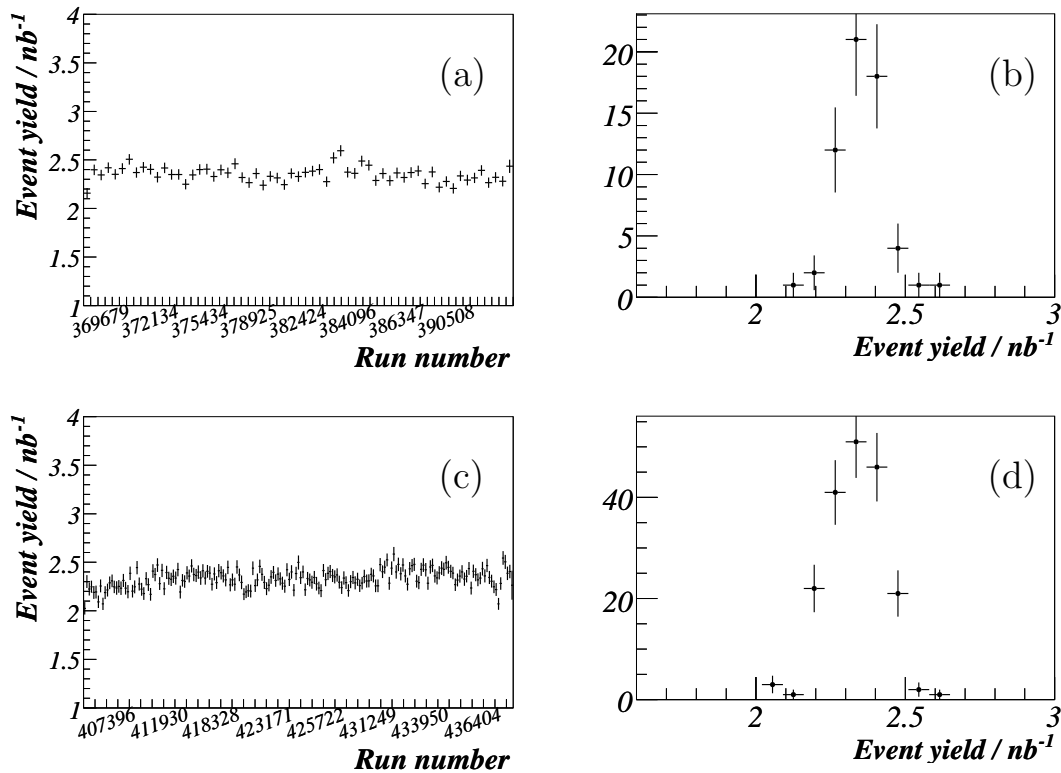


Figure 7.2: The event yield per nb^{-1} , shown as a function of the run number (a) for the 2003-04 e^+p and (c) for the 2005 e^-p data, and the event yield projection (b) for the 2003-04 e^+p and (d) for the 2005 e^-p .

The event yield is defined as the number of observed events per unit of integrated luminosity (nb^{-1}) after the run and event selection described in section 7.3 below. The event yield is shown in figure 7.2 in bins of equal luminosity as function of the run number. The projections of the event yield are shown in the figure 7.2 as well. The runs with an event yield smaller than the average by more than six standard deviations are investigated for the cause of this behaviour and are finally excluded. Low yield is usually a sign for problems with the data logging during this run. For both the 2003-04 e^+p and 2005 e^-p data periods the event yields are stable over the

whole running period.

7.3 Neutral Current Selection Criteria

The criteria used for the selection of the NC events are summarised below:

- Runs selection.
- Event triggered by the subtriggers ST67 or ST77.
- Electron identified by the electron finding algorithm.
- Electron validated by a DTRA track for $\theta_e > 35^\circ$.
- Electron energy $E'_e > 11$ GeV.
- “Central” vertex with $|z_{vtx}| < 35$ cm.
- Very backward part of BBE ($z_{LAR} > -190$ cm) excluded.
- Time dependent trigger fiducial volume and exclusion of z and φ cracks:
 $|\varphi_e - n \cdot 45^\circ| < 2^\circ$, $n = 0, 1, \dots, 7$; $25 < z_{LAR} < 15$ cm.
- Rejection of cosmic and halo-muon events identified by background finding algorithms (see section 6.10).
- Longitudinal momentum balance: $E - P_z > 35$ GeV.
- $0.05 < y_e < 0.9$.
- $Q_e^2 > 133$ GeV².
- At least one of polarimeters TPOL or LPOL on.

7.4 Neutral Current Data Samples

The general characteristics of the neutral current event samples are presented in the following to demonstrate that the simulation provides a good description of the data. Thus, the Monte Carlo simulation is suitable to be used for the acceptance correction of the data in the cross section determination which will be presented in the following chapter 8.

In all distributions shown below, the simulated of neutral current and background events are normalised to the luminosity of the data. The error bars represent statistical errors only.

The z vertex distributions of the data and the simulation have already been shown in figure 6.4, verifying that the simulation reproduces the behaviour of the data.

The variables of the scattered electron are presented in figure 7.3. The energy distribution has a sharp maximum for the region of the *kinematic peak* ($E'_e \approx E_e$) and extends up to values of a few hundred GeV. The spectrum of the polar angle falls

rapidly towards small angles reflecting the $1/Q^4$ dependence of the cross section. The data are well described by the simulation.

The contribution from ep background, dominated by photoproduction, is illustrated in figure 7.4. The contamination by mis-identified electrons is very small and appears mainly at low electron energies.

Figure 7.5(a) show the azimuthal angle of the scattered electron. The structure in φ_e arises from regions of the detector removed from the sample due to energy leakage in cracks or trigger inefficiencies (see sections 6.9). The z impact position of the scattered electron in the calorimeter is displayed in the figure 7.5(b) for the range $-200 < z_{LAR} < 0$ cm and 7.5(c) for $0 < z_{LAR} < 200$ cm and is well modelled in the MC. The z crack at $15 < z_{LAR} < 25$ cm can be distinctly seen, as can the forward edge of the BBE at $z_{LAR} = -152.5$ cm. The BBE has a different structure in the $r - \varphi$ plane compared to the central barrel wheels. Thus it is not always possible to make an unambiguous assignment of the electron position (further details can be found in section 6.5.1).

The good understanding of the hadronic final state is demonstrated in figure 7.6. Both the $P_{T,h}/P_{T,e}$ distribution and the $E - P_z$ distribution are well described by the MC. The $P_{T,h}/P_{T,e}$ demonstrate the consistency of the absolute electromagnetic and hadronic energy scales.

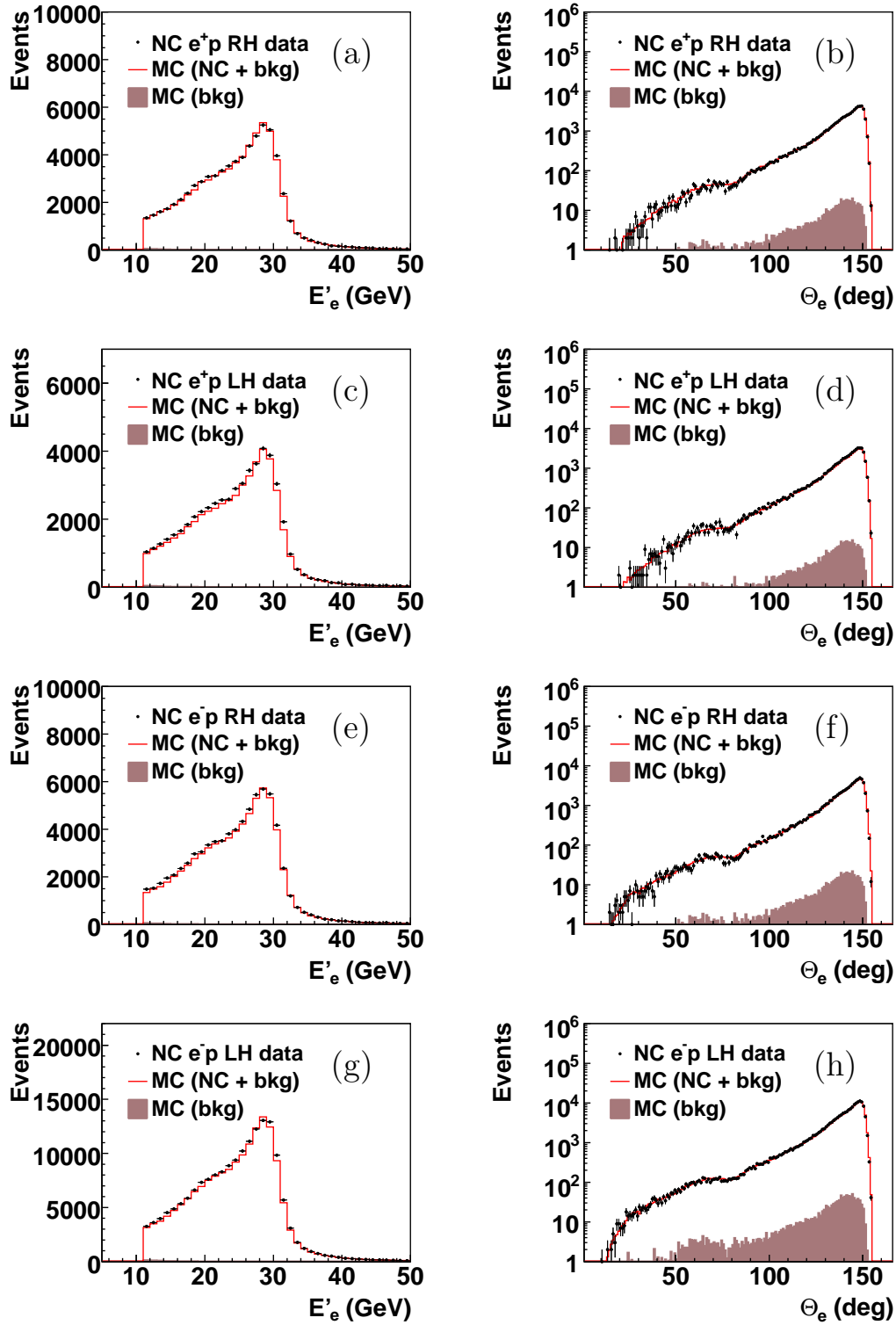


Figure 7.3: Distributions of the electron energy E'_e (left) and the polar angle θ_e (right) shown for selected events in the RH (a,b) and LH (c,d) e^+p data sets, and in the RH (e,f) and LH (g,h) e^-p data sets. The Monte Carlo (MC) contributions from the neutral current (NC) process and the ep background (bkg) processes are shown as open histograms with the latter contribution alone being shown as shaded histograms.

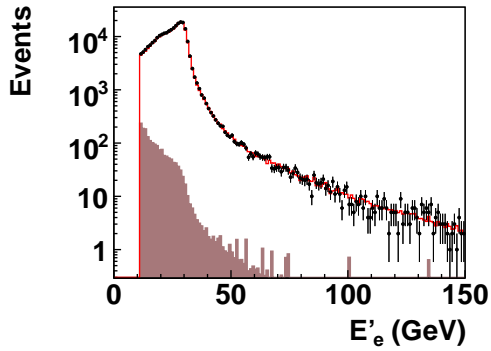


Figure 7.4: Distribution of electron energy E'_e in logarithmic scale. The contribution of the ep background, shown as shaded histogram, is very small and appears mainly at low electron energies.

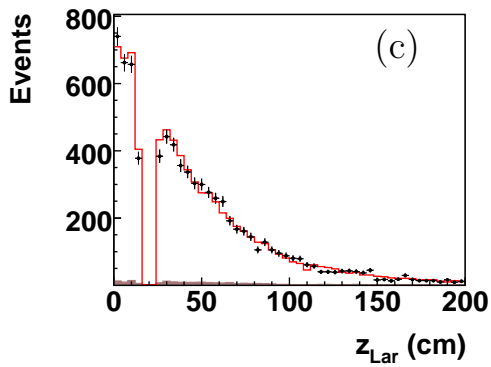
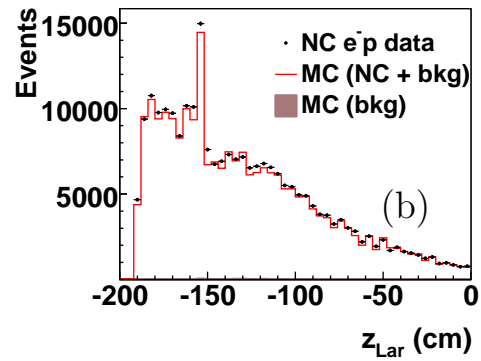
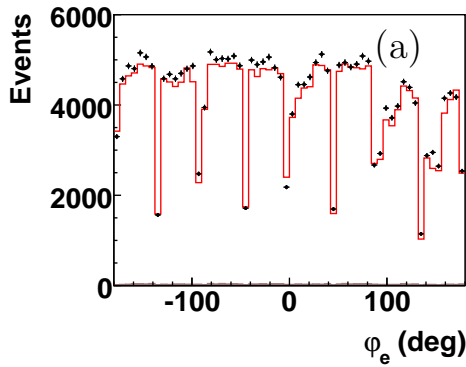


Figure 7.5: Distribution of the electron azimuthal angle φ_e (a). The z impact position of the scattered electron in the LAr calorimeter shown in the ranges $-200 < z_{LAr} < 0$ cm (b), and $0 < z_{LAr} < 200$ cm (c).

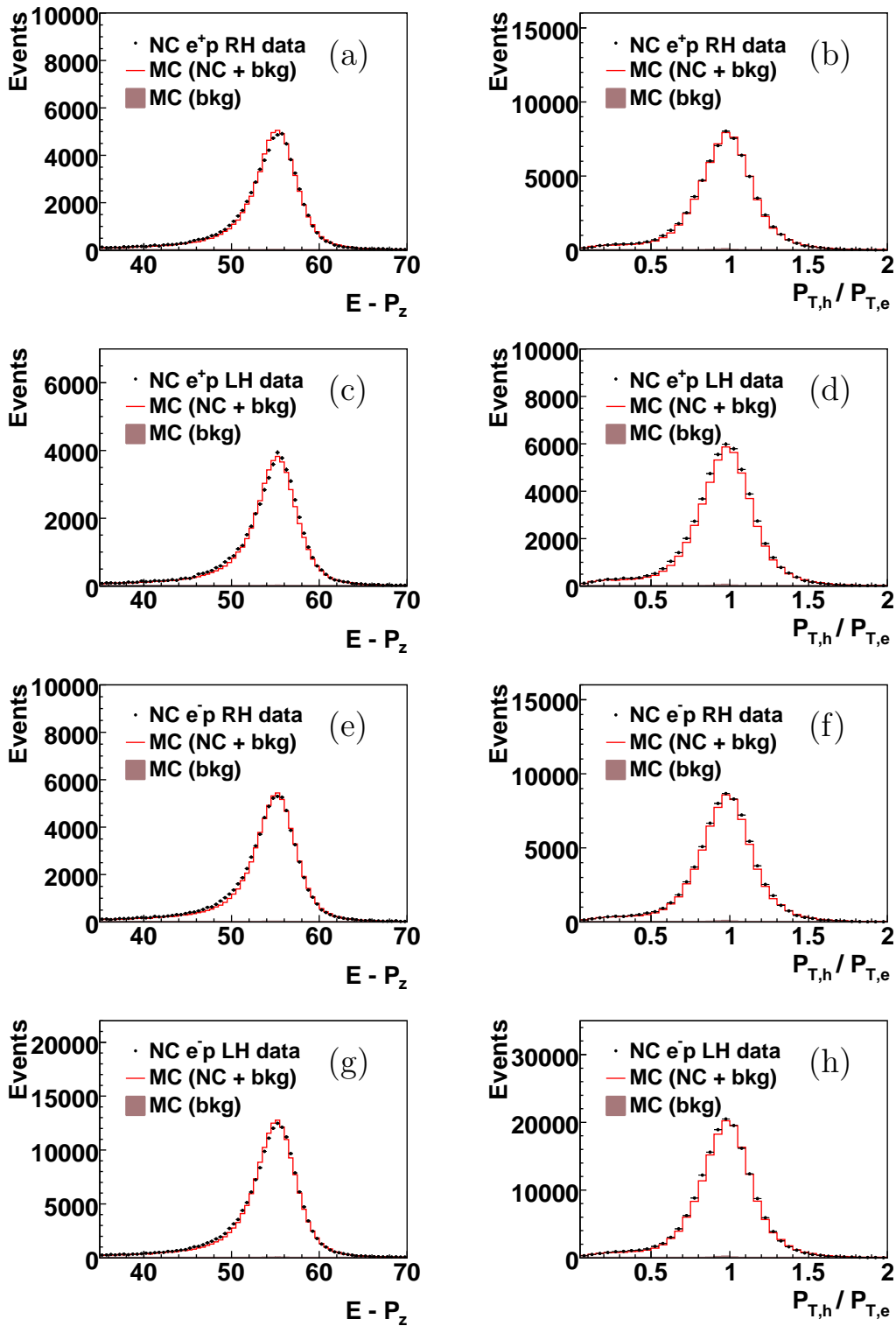


Figure 7.6: Distributions of the longitudinal momentum balance $E - P_z$ (left) and the transverse momentum balance $P_{T,h}/P_{T,e}$ (right), shown for selected events in the RH (a,b) and LH (c,d) e^+p data sets, and in the RH (e,f) and LH (g,h) e^-p data sets. The Monte Carlo (MC) contributions from the neutral current (NC) process and the ep background (bkg) processes are shown as open histograms, with the latter contribution alone being shown as shaded histograms.

Chapter 8

Cross Section Measurement Procedure

8.1 Bin Definitions in $x - Q^2$ Plane

The cross section measurement in this analysis is performed in bins of x and Q^2 . The binning used was developed in NC analyses at HERA I [82–85]. The bin centres and bin boundaries are given in table 8.1. There are ten bins per decade in Q^2 and five bins per decade in x . For $Q^2 \geq 3000 \text{ GeV}^2$ the bin size is doubled due to limited statistics. The resolution is always better than the bin width [103].

Q^2 (GeV ²) centre	Q^2 (GeV ²) limits	$\log Q^2$ limits	x centre	x limits	$\log x$ limits
100	89.12	1.95			
120	112.2	2.05			
150	141.2	2.15			
200	177.8	2.25	0.0013	0.0010	-3.00
250	223.9	2.35	0.0020	0.0016	-2.80
300	281.8	2.45	0.0032	0.0025	-2.60
400	354.8	2.55	0.0050	0.0040	-2.40
500	446.7	2.65	0.0080	0.0063	-2.20
650	562.3	2.75	0.0130	0.0100	-2.00
800	707.9	2.85	0.0200	0.0158	-1.80
1000	891.2	2.95	0.0320	0.0251	-1.60
1200	1122	3.05	0.0500	0.0398	-1.40
1500	1412	3.15	0.0800	0.0631	-1.20
2000	1778	3.25	0.1300	0.1000	-1.00
3000	2239	3.35	0.1800	0.1445	-0.84
5000	3548	3.55	0.2500	0.2089	-0.68
8000	6000	3.78	0.4000	0.3162	-0.50
12000	10000	4.000	0.6500	0.5012	-0.30
20000	16680	4.222		1.0000	0.00
30000	27778	4.444			
	46334	4.666			

Table 8.1: Binning in x and Q^2 .

8.2 Purity, Stability and Acceptance

In order to obtain precise measurements from the data, various effects of the detector need to be corrected for, i.e. the finite detector resolutions, efficiencies and geometric acceptances. To do this, events from a MC generator, DJANGO [88] in the case of this analysis, are compared before and after they are passed through the detector simulation, labelled generator (GEN) level and reconstructed (REC) level, respectively. If the REC level events describe the data in every detail, then it is possible to correct the data for the detector effects. If deficiencies are found in the simulation, for example the resolution of a particular detector is not modelled correctly, then the simulated resolution is tuned to the data in order to obtain a better description. The remaining differences between data and simulation are accounted for by systematic uncertainties.

The effects of the detector are studied by looking into the relationships between the GEN level events and the REC level events. The event selection is applied on simulated events at both the GEN and REC levels. This leaves four scenarios which can be described by four independent variables, illustrated in figure 8.1.

The four independent variables are defined as:

- N_{STAY} = The number of events which have the same GEN and REC bin number (i) (events are generated and reconstructed in the same bin).
- N_{LOST} = The number of events with a GEN bin (j) but no REC bin (not selected at the reconstructed level).
- $N_{SMEARIN}$ = The number of events which smeared into a REC bin (j) (not originated from GEN bin (j)).
- $N_{SMEAROUT}$ = The number of events which smeared out of a GEN bin (i) (selected in REC bin (j) with $j \neq i$).

The total number of GEN and REC events are then defined as:

- $N_{REC} = N_{STAY} + N_{SMEARIN}$
- $N_{GEN} = N_{STAY} + N_{SMEAROUT} + N_{LOST}$

These definitions can be used to define the variables purity \mathcal{P} , stability \mathcal{S} , and acceptance \mathcal{A} , which are defined by the relationship between the events in generated and reconstructed bins and quantify the effects of the detector resolution and efficiency:

$$\mathcal{A} = \frac{N_{REC}}{N_{GEN}} \quad (8.1)$$

$$\mathcal{P} = \frac{N_{STAY}}{N_{REC}} \quad (8.2)$$

$$\mathcal{S} = \frac{N_{STAY}}{N_{GEN} - N_{LOST}} \quad (8.3)$$

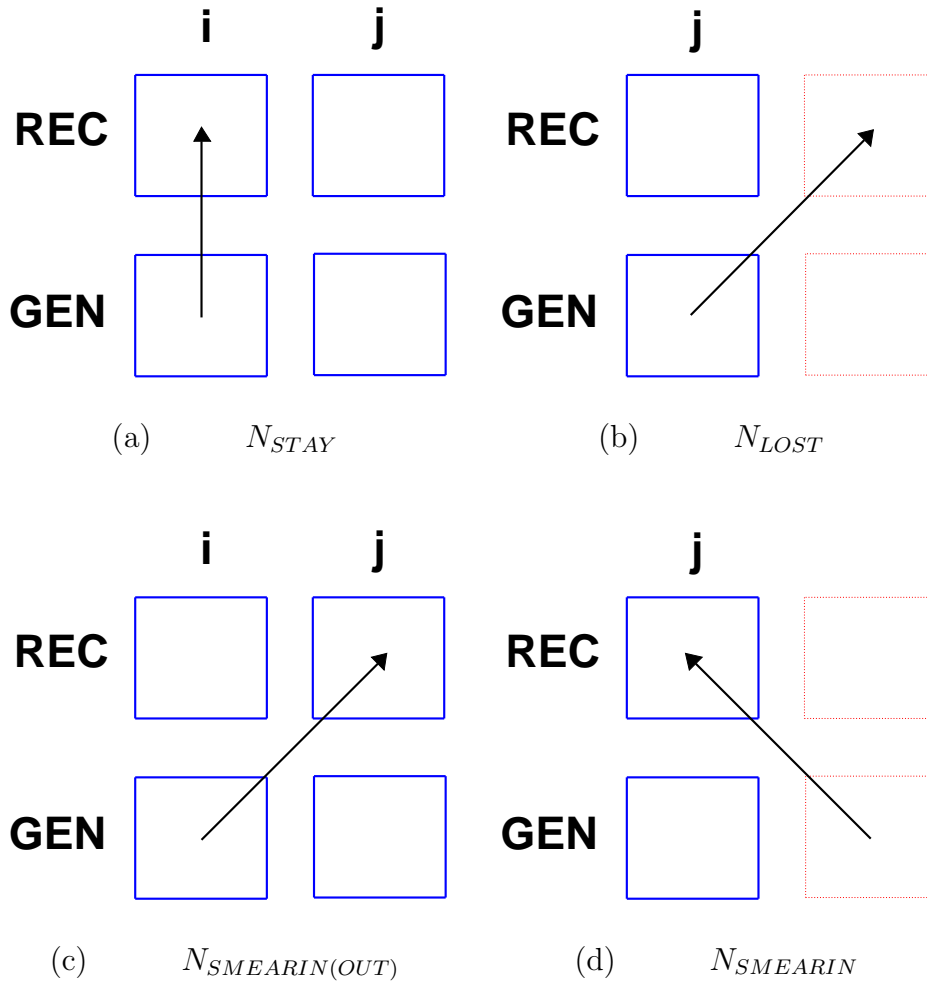


Figure 8.1: Schematic view of the migrations dynamics. The arrows show the path of an event from the GEN level to the REC level, thick squares are bins inside the measured phase-space, dotted squares are bins outside the measured phase-space; (a) is an illustration of the situation where an event has the same GEN and REC bin; (b) shows a GEN event being lost from the REC sample by being reconstructed outside of the measured phase-space; (c) illustrates an event smearing out of a GEN bin into a different REC bin; finally, (d) shows an event smearing into a REC bin from outside of the GEN phase-space, i.e. the generated quantities do not satisfy the x, Q^2 cut applied.

The acceptance of a bin quantifies the overall correction which must be made for detector effects. The true number, N_{True} of events after correcting the data for detector effects is recovered by applying the acceptance correction:

$$N_{True} = N_{Data} \times \frac{N_{GEN}}{N_{REC}} = \frac{N_{Data}}{\mathcal{A}}. \quad (8.4)$$

The effects of smearing are quantified by the purity and stability of the bin. Purity quantifies the fraction of reconstructed events in bin i , which originate from the same bin on the generator level. The stability quantifies the fraction of generated events which do not change the bin after the detector simulation, i.e do not migrate out of a bin due to resolution effects. Stability does not take into account events that are lost to smearing outside of the binning scheme.

The values of acceptance, purity and stability for each bin used in this measurement are required to satisfy:

$$\begin{aligned}\mathcal{A} &> 20\% \\ \mathcal{P} &> 30\% \\ \mathcal{S} &> 30\%\end{aligned}$$

in order to guarantee that the contents of the bin are well understood [85]. As an example, purity, stability and acceptance for the 2003-04 e^+p NC selected event sample are shown in figure 8.2. The other samples have similar features.

8.3 Extraction of Cross Section

The cross section measured in a specific bin in x and Q^2 is given by:

$$\frac{d^2\sigma}{dx dQ^2}(x_c, Q_c^2) = \frac{N^{data} - N^{bg}}{\mathcal{L} \cdot \mathcal{A}} \cdot \delta^{bc}, \quad (8.5)$$

where

- N^{data} is the number of selected events in the bin.
- N^{bg} is the number of background events in the bin.
- \mathcal{L} is the total integrated luminosity.
- \mathcal{A} is the detector acceptance, as defined in equation 8.1, determined from MC which includes radiative corrections.
- δ^{bc} , is the relation factor between cross section in the bin centre (x_c, Q_c^2) and cross section integrated over a bin of finite size $\Delta x = x_{max} - x_{min}$ and $\Delta Q^2 = Q_{max}^2 - Q_{min}^2$:

$$\delta^{bc} = \frac{\frac{d^2\sigma}{dx dQ^2} \Big|_{x=x_c, Q^2=Q_c^2}}{\int_{x,min}^{x,max} \int_{Q^2,min}^{Q^2,max} \frac{d^2\sigma}{dx dQ^2} dx dQ^2}.$$

The acceptance and the δ^{bc} are obtained from the MC simulation which includes the radiative corrections calculated using the program **HERACLES** [87] as implemented in **DJANGO**. In this case formula 8.5 can be simplified to:

$$\frac{d^2\sigma}{dx dQ^2}(x_c, Q_c^2) = \frac{N^{data} - N^{bg}}{N_{rec}^{MC}} \cdot \frac{\mathcal{L}_{MC}}{\mathcal{L}} \frac{d\sigma^{MC}}{dx dQ^2}(x_c, Q_c^2). \quad (8.6)$$

Here, \mathcal{L}_{MC} is the luminosity of the MC sample and N_{rec}^{MC} the number of MC events reconstructed in the bin with center in (x_c, Q_c^2) .

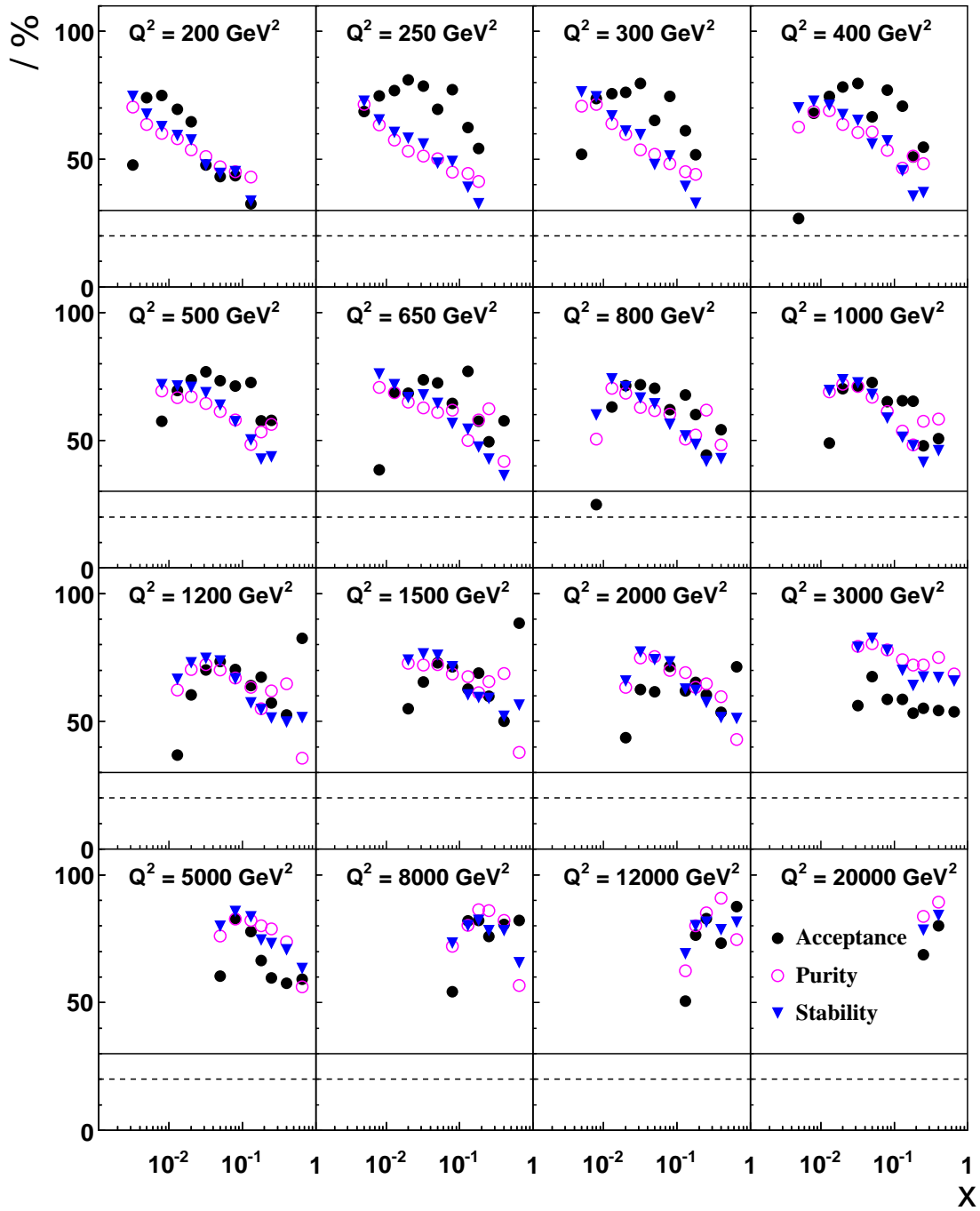


Figure 8.2: Acceptance (solid points), purity (open points) and stability (triangles) as function of x in bins of Q^2 . The solid lines indicate the minimum purity and stability of 30% and the dashed lines the required 20% for the acceptance.

8.4 Systematic Uncertainties

The uncertainties related to the performance of the detector lead to systematic errors on the cross section measurement. A distinction to errors which are correlated between all bins (bin-to-bin correlated errors) and errors which are uncorrelated from bin to bin is made. For instance, a correlated error on the hadronic energy measurement of 1% means that it is possible for the hadronic energy scale to differ from the “true” hadronic energy scale by 1%. The uncorrelated errors are assumed to be due to local fluctuations or deficiencies. The trigger efficiency can be different by 0.5% at low Q^2 in a certain calorimeter region, but this has no impact on the efficiency at high Q^2 . Some sources of errors are treated to be partially correlated and partially uncorrelated. All systematic errors are found to be symmetric to a good approximation and are assumed so in the following. The total systematic error is formed by adding the individual errors in quadrature.

The systematic uncertainties on the measurement are listed below, and the resulting relative error on the cross section is given where appropriate. Further detail on the studies related to each source of systematic uncertainty can be found in the noted sections.

- **The electron energy measurement – §6.6**

The total uncertainty on the electron energy scale is

- for $z_{LAr} \leq 20$ cm 1%;
- for $20 \text{ cm} < z_{LAr} \leq 110$ cm 2%;
- for $z_{LAr} > 110$ cm 3%;

The correlated part of the total uncertainty comes mainly from the possible bias of the calibration method and is estimated to be 0.5% throughout the LAr calorimeter.

- **The polar angle of the scattered electron – §6.5**

The correlated uncertainty on the polar angle is 3 mrad. This leads to a typical uncertainty on the NC reduced cross section of less than 1%, increasing up to $\sim 5\%$ at high x .

- **The efficiency of the electron identification – §6.1**

The uncorrelated error originates from the uncertainty of the electron identification efficiency:

- for $z_{LAr} < -5$ cm: 0.5%
- for $z_{LAr} > -5$ cm: 2.0%

It is estimated using an independent, track-based electron identification algorithm, limited to $z_{LAr} > -5$ cm by statistics.

- **Uncertainty on vertex-track finding efficiency – §6.4**

An uncorrelated uncertainty due to the vertex and track finding is assigned to be 3% for 2003-04 e^+p and 2% for 2005 e^-p data set.

- **Uncertainty due to the vertex requirement ($|z_{vtx}| < 35$ cm) is assigned to be 0.5% (see section 6.4). This appears as an additional normalisation error.**

- **Hadronic energy measurement – §6.7**

A 1% correlated and a 1.7% uncorrelated uncertainty is assigned. This yields

a total uncertainty of 2%. The corresponding error on the NC cross sections is typically $\lesssim 1\%$.

- **Noise subtraction in the LAr calorimeter** – §6.7

A 10% uncertainty on the amount of energy in the LAr calorimeter attributed to noise, which gives rise to a sizeable correlated systematic error at low y , reaching $\simeq 15\%$ in the bins with lowest y .

- **Photoproduction background** – §4.2 and §7.4

The photoproduction background is estimated from the simulation. A 30% uncertainty on the subtracted photoproduction background is considered. This results in a correlated systematic error of typically $\lesssim 1\%$ for a phase space region dominated by photoproduction background.

- **Trigger efficiency** – §6.8

An uncorrelated error of 0.5% is considered on the trigger efficiency.

- **QED radiative corrections**

An uncorrelated error of 1% is estimated on the QED radiative corrections by comparing the radiative corrections used in the Monte Carlo program (DJANGO) with those calculated from HECTOR and EPRC [94]. The error also includes small missing corrections in DJANGO due to the exchange of two or more photons between the lepton and the quark lines.

In addition, there is a global uncertainty of 1.3% and 2.0% on the luminosity measurement for the e^+p and e^-p data, respectively, of which 0.5% is common to both. For the e^+p data the uncertainty in the measurement of the lepton beam polarisation is taken to be 1.6% for the LPOL and 3.5% for the TPOL [120], yielding a total relative polarisation uncertainty of 1.8% for RH data set and 2.7% for the LH data set (see chapter 7). For the e^-p data a global uncertainty of 5% is considered [119] (see chapter 7).

The measured cross section should be independent of the method used for determination of the event kinematics. Therefore, the cross section measurement is cross checked by comparison of the measurements in which different methods for their determination are used. For example, in figure 8.3 the results obtained using the $e\Sigma$ method and DA methods are compared. These two methods are to a large extent independent since the DA is independent of the energy scales while the $e\Sigma$ method largely relies on them. The comparison between these two methods shows no systematic deviations, giving confidence to the final results obtained using $e\Sigma$ method, which is chosen on the bases of optimal resolution in x and Q^2 .

8.5 Q^2 Bins Combination of $e^\pm p$ Cross Sections for Determination of $x\tilde{F}_3$

Because of limited statistics in the region of sensitivity to $x\tilde{F}_3$ the cross section measurements in the neighbouring Q^2 bins are combined. The combination is done using the following formula:

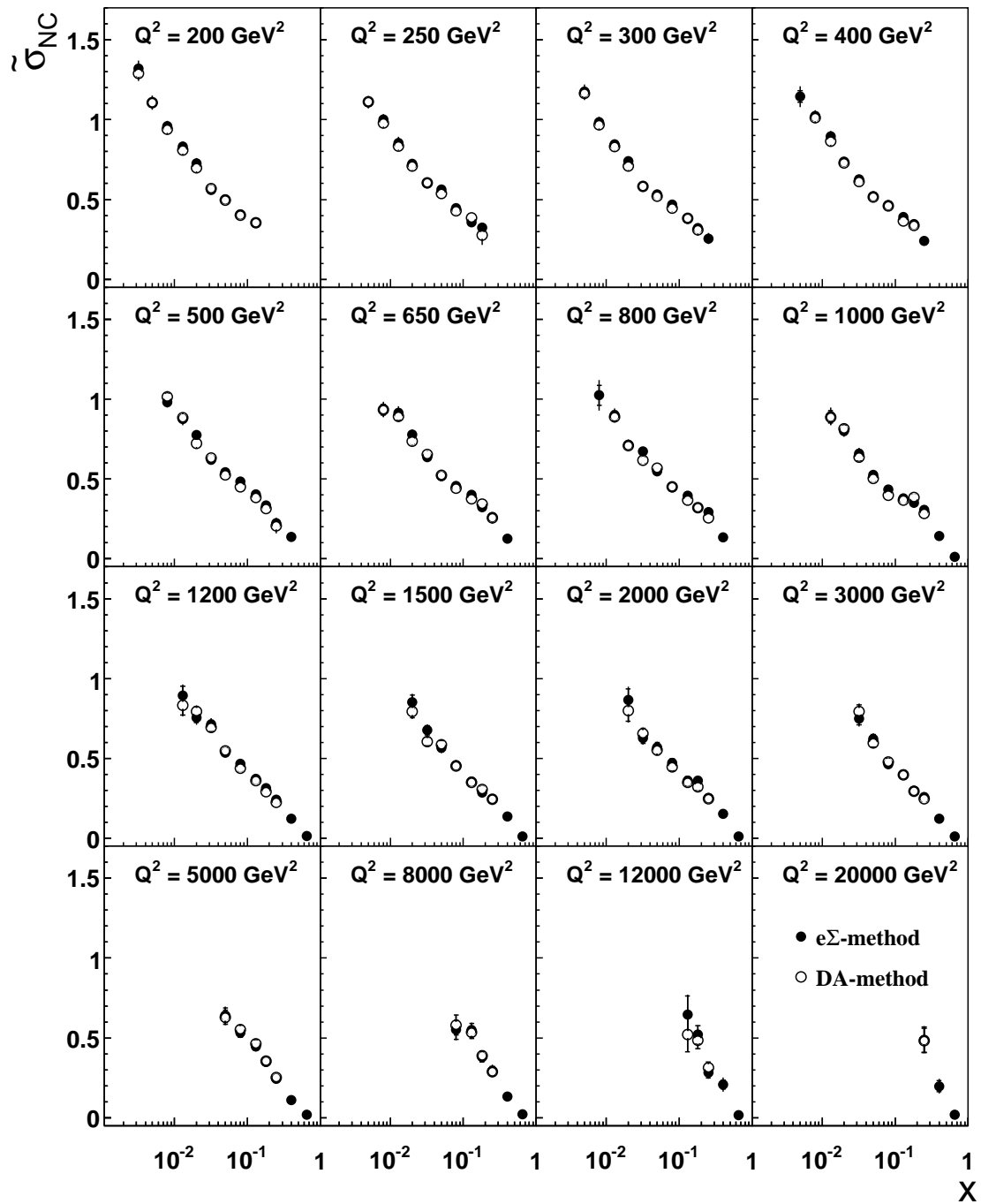


Figure 8.3: Comparison of the reduced cross section measurements $\tilde{\sigma}(x, Q^2)$ using the $e\Sigma$ method (solid points) and DA method (open points) for the reconstruction of the kinematic variables method.

Q_1^2 GeV ²	Q_2^2 GeV ²	Q_3^2 GeV ²	Q_c^2 GeV ²	x
1200	1500		1500	0.020
1200	1500	2000	1500	0.032
1200	1500	2000	1500	0.050
1200	1500	2000	1500	0.080
3000			5000	0.050
3000	5000	8000	5000	0.080
3000	5000	8000	5000	0.130
3000	5000	8000	5000	0.180
3000	5000	8000	5000	0.250
3000	5000	8000	5000	0.400
3000	5000	8000	5000	0.650
12000			12000	0.180
12000	20000		12000	0.250
12000	20000	30000	12000	0.400
12000	20000	30000	12000	0.650

Table 8.2: The combination of the Q^2 bins for the extraction of the structure function xF_3 . Given are the Q^2 bin centres of the initial bins, Q_1^2, Q_2^2 and Q_3^2 , and the bin centres of the combined bins Q_c^2 . The last column lists the bin centres in x .

$$\tilde{\sigma}_c = \frac{\sum_i \frac{\int \sigma_i^{th}}{\tilde{\sigma}_i^{th}} \cdot \tilde{\sigma}_i^{data}}{\frac{1}{\tilde{\sigma}_c^{th}}} \quad \text{with} \quad \int \sigma_i^{th} = \int_{bin_i} \frac{d^2 \sigma^{th}}{dx dQ^2} dx dQ^2, \quad (8.7)$$

where $\tilde{\sigma}_c = \tilde{\sigma}(x_c, Q_c^2)$ are the reduced cross sections in the combined bin; $\tilde{\sigma}_i = \tilde{\sigma}(x_i, Q^2)$ is the reduced cross section in the original bins; $\sigma^{th} = \sigma^{th}(x, Q^2)$ is the NC cross section and $\tilde{\sigma}_i^{th} = \tilde{\sigma}^{th}(x_i, Q_i^2)$ the reduced cross section calculated using the H1 2000 PDF fit. The integration over the (x, Q^2) bins is done taking into account the event selection requirement applied on y ($0.05 < y < 0.9$). The summation in the formula goes over the bins which are combined. For the determination of the xF_3 structure function, three Q^2 bins are combined (table 8.2).

The absolute statistical and systematic errors are combined in the following way:

$$\delta_c^{stat} = \frac{\sqrt{\sum_i \left(\frac{\int \sigma_i^{th}}{\tilde{\sigma}_i^{th}} \cdot \delta_i^{stat} \right)^2}}{\frac{1}{\tilde{\sigma}_c^{th}} \sum_i \int \sigma_i^{th}} \quad \delta_c^{syst} = \frac{\sum_i \frac{\int \sigma_i^{th}}{\tilde{\sigma}_i^{th}} \cdot \delta_i^{syst}}{\frac{1}{\tilde{\sigma}_c^{th}} \sum_i \int \sigma_i^{th}} \quad (8.8)$$

Since the cross section integrated over the bin i is proportional to the number of events measured in the bin, this method of combining cross sections is very close to the direct measurement of the cross section in the combined bin. However, the influence of the different cuts, e.g. trigger fiducial cuts, may cause the number of events in a bin not being proportional to the integrated cross section. It was checked that this effect is negligible by performing the measurement directly in the combined bins and by comparing the cross sections combined using equation 8.7 and the cross sections combined according to the number of events:

$$\tilde{\sigma}_c = \frac{N_1 \tilde{\sigma}_1^{data} + N_2 \tilde{\sigma}_2^{data}}{N_1 + N_2} \quad (8.9)$$

8.6 Combination of Cross Sections From Different Measurements

In order to improve the statistical precision the cross section data presented here can be combined with the previously published H1 measurement [85] from HERA I. Using a luminosity weighted combination of two cross section measurements σ_1 and σ_2 , the combined cross section, σ_{comb} , can be expressed as

$$\sigma_{comb} = \frac{L_1 \sigma_1 + L_2 \sigma_2}{L_1 + L_2} \quad (8.10)$$

$$\delta_{comb}^{stat} = \sqrt{\left(\frac{\delta_1^{stat} \cdot L_1}{L_1 + L_2}\right)^2 + \left(\frac{\delta_2^{stat} \cdot L_2}{L_1 + L_2}\right)^2}, \quad (8.11)$$

where L_1 is the luminosity value of the first measurement and L_2 is luminosity value of the second one. δ_1^{stat} , δ_2^{stat} and δ_{comb}^{stat} are statistical uncertainties of the first, second and combined measurements respectively.

To a good approximation the correlated systematic uncertainty is considered to be 100% correlated and uncorrelated uncertainties of two measurements are uncorrelated

$$\delta_{comb}^{corr} = \frac{\delta_1^{corr} \cdot L_1}{L_1 + L_2} + \frac{\delta_2^{corr} \cdot L_2}{L_1 + L_2} \quad (8.12)$$

$$\delta_{comb}^{unc} = \sqrt{\left(\frac{\delta_1^{unc} \cdot L_1}{L_1 + L_2}\right)^2 + \left(\frac{\delta_2^{unc} \cdot L_2}{L_1 + L_2}\right)^2}, \quad (8.13)$$

where δ_1^{corr} , δ_2^{corr} and δ_{comb}^{corr} are correlated systematic uncertainties, and δ_1^{unc} , δ_2^{unc} and δ_{comb}^{unc} to be uncorrelated systematic uncertainties:

Chapter 9

NC Cross Section Results

In this section the results of this analysis are presented. The measurements are based on the 2003-04 e^+p and the 2005 e^-p data. The inclusive single differential cross section $d\sigma/dQ^2$ and the double differential cross section $d^2\sigma/dxdQ^2$ are presented for the neutral current process $e^\pm p \rightarrow e^\pm X$ in interactions with longitudinally polarised lepton beams. The cross sections are measured in the region of large negative four-momentum transfer squared $Q^2 \geq 200 \text{ GeV}^2$ and inelasticity $y < 0.9$.

The HERA II data are combined together with previously published data from HERA I [85] to determine the structure function $x\tilde{F}_3$ with improved precision. This measurement is combined with the corresponding ZUES measurement to provide the most accurate measurement of the interference structure function $xF_3^{\gamma Z}$, which is sensitive to the valence quark distributions down to low values of Bjorken x .

The data on polarised cross section asymmetries, A^\pm , are presented showing the first observation of parity violation in neutral current $e^\pm p$ scattering at high Q^2 .

9.1 The e^+p and e^-p Double Differential Cross Sections $d^2\sigma/dxdQ^2$

The measured double differential NC cross sections in their reduced form, $\tilde{\sigma}_{NC}$ (defined in equation 2.45), are shown in figure 9.1 for e^+p and 9.2 for e^-p processes for RH (solid points) and LH (open points) leptons. The measurements cover the range of $200 \text{ GeV}^2 \leq Q^2 \leq 20\,000 \text{ GeV}^2$ and $0.0032 < x < 0.65$. The results are presented as a function of x and Q^2 . The data with both helicities exhibit similar features and are well described by the predictions of the SM using the H1 2000 PDF fit.

The measured cross sections are listed in tables C.1-C.4. The tables contain also the statistical, systematic and total errors. The uncorrelated and correlated parts of the systematic errors together with the contributions from electromagnetic and hadronic energy scales, polar angle measurement, noise and background subtraction are given as well. In the bulk of the kinematic region the statistical error is about 2-3% and the total error is about 4-5%. The errors are increasing towards low y . At high Q^2 , $Q^2 > 1000 \text{ GeV}^2$, the statistical error becomes larger than the systematic error.

The reduced cross section exhibits a strong rise with decreasing x . This behaviour

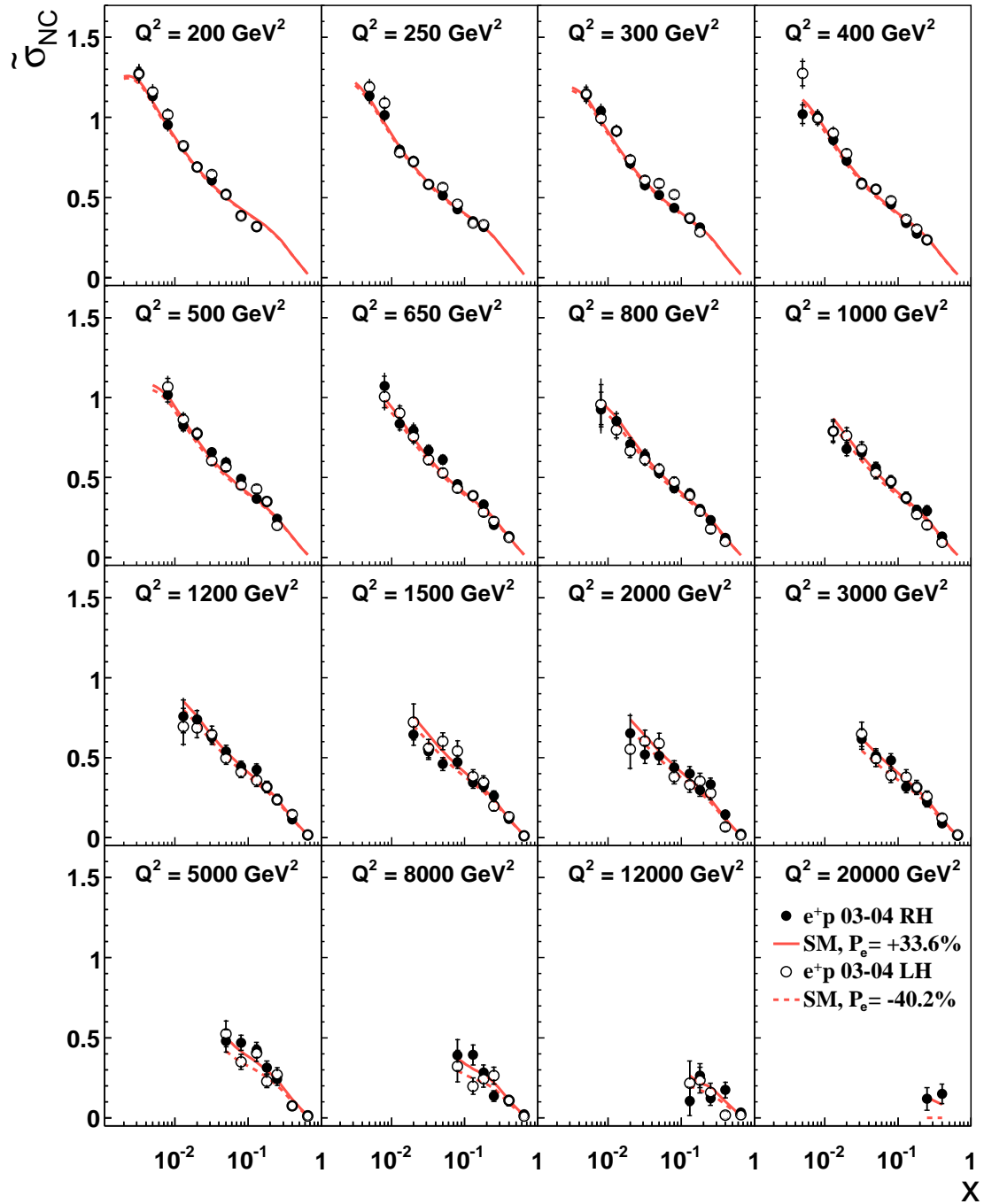


Figure 9.1: The NC reduced cross section $\tilde{\sigma}_{NC}(x, Q^2)$ for e^+p scattering with positive (full points) and negative (open points) longitudinal positron polarisation (data from years 2003-04). The inner and outer error bars represent the statistical and total errors, respectively. The 1.4% normalisation uncertainty is not included in the error bars. The curves show the predictions from the H1 2000 PDF fit.

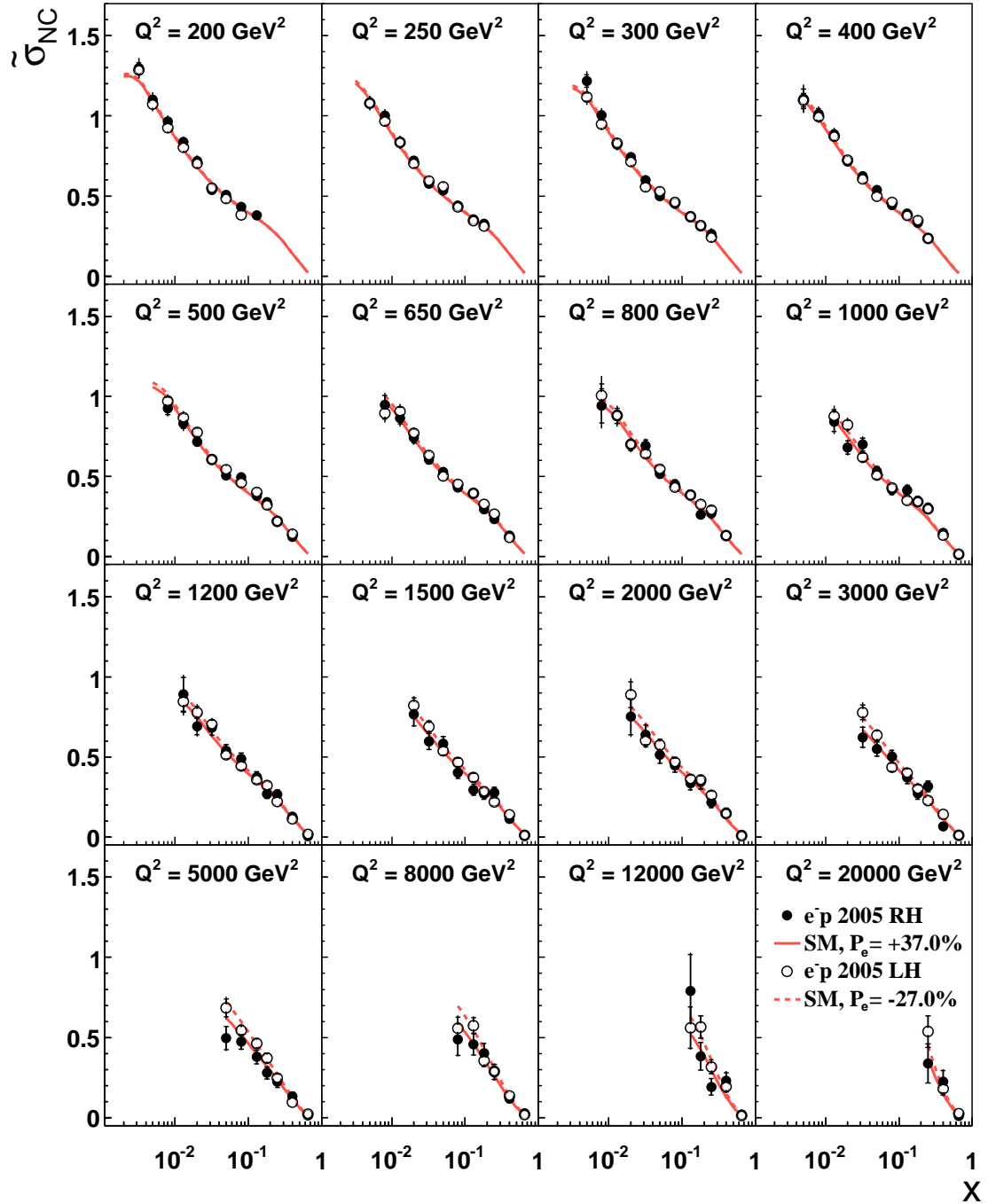


Figure 9.2: The NC reduced cross section $\tilde{\sigma}_{NC}(x, Q^2)$ for e^-p scattering with positive (full points) and negative (open points) longitudinal electron polarisation (data from year 2005). The inner and outer error bars represent the statistical and total errors, respectively. The 2.1% normalisation uncertainty is not included in the error bars. The curves show the predictions from the H1 2000 PDF fit.

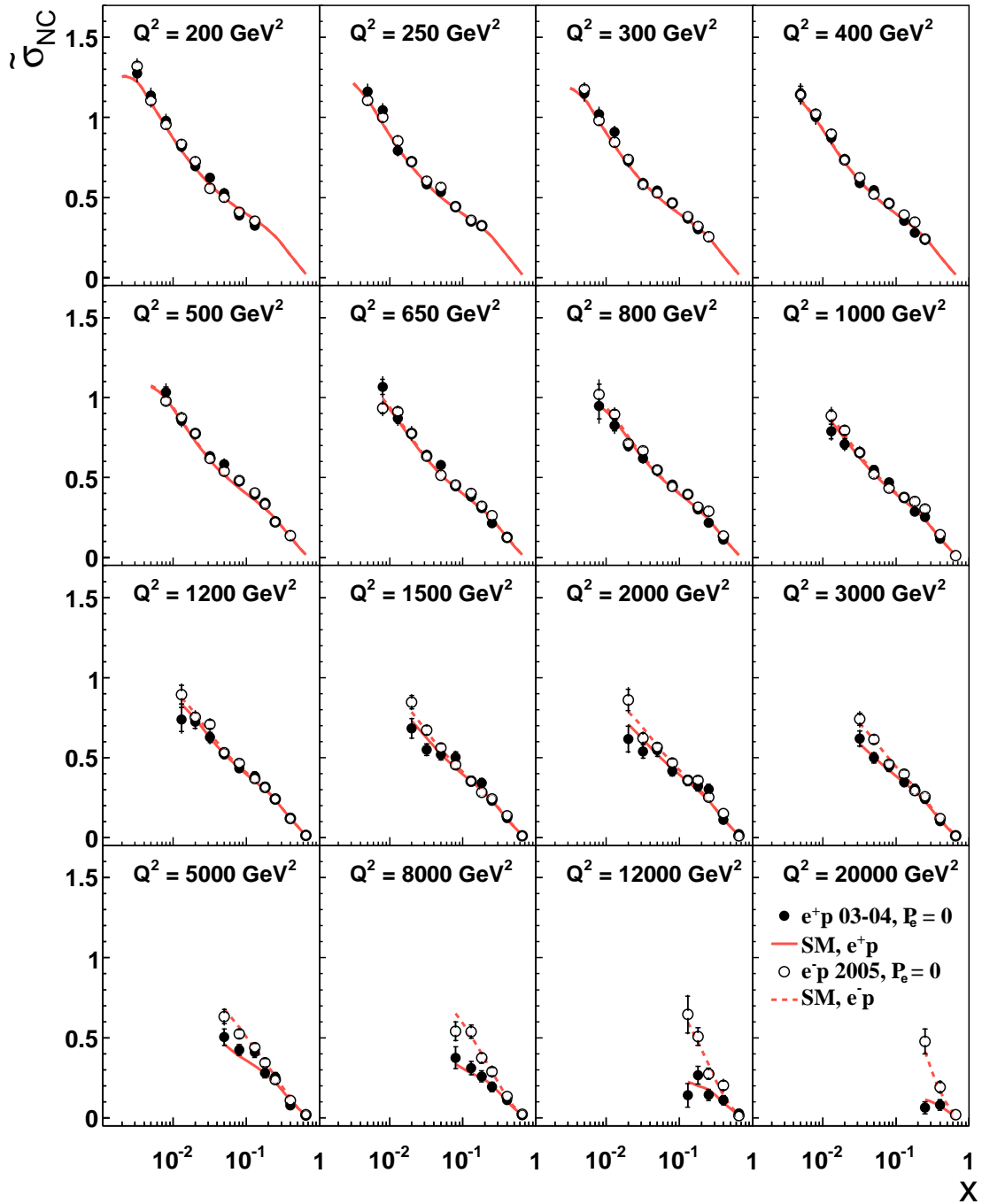


Figure 9.3: The unpolarised reduced cross sections $\tilde{\sigma}^{\pm}(x, Q^2)$ shown for the HERA II data (open/solid points) compared to the Standard Model (solid/dashed curves). The inner error bars represent the statistical uncertainties and the outer error bars represent the total errors. The normalisation uncertainties of 1.4% for e^+p data and 2.1% for e^-p data respectively are not included in the error bars.

can be interpreted as originating from the rise of the sea quark distribution which is dominating the proton structure function \tilde{F}_2 at low x (see equations 2.41 and 2.48). This rising sea quark distribution is in turn driven by the dominant gluon density at low x . The rise with decreasing x becomes stronger as Q^2 increases.

The behaviour of the cross section at lowest x (highest y) departs from the monotonic rise of \tilde{F}_2 indicating a contribution of the longitudinal structure function \tilde{F}_L to the cross section (see, e.g. the theoretical expectations in the bin $Q^2 = 200 \text{ GeV}^2$).

At very high Q^2 the e^+p cross section for right handed polarised positrons is higher than for the left handed ones (figure 9.1), and the e^-p cross section for left handed polarised electrons is higher than for the right handed (figure 9.2). The effect, however, is very small. It is visible more clearly if the cross sections are integrated over x and presented as function of Q^2 ($d\sigma/dQ^2$). This effect (polarisation asymmetry) on the cross section is discussed in chapter 9.4.

The LH and RH data can be combined together and then corrected for the small residual polarisation, providing an unpolarised cross section measurement. The unpolarised reduced cross sections are shown for $e^\pm p$ scattering in figure 9.3 and demonstrate a clear suppression of the e^+p cross section with respect to the e^-p data. The data compare well to the Standard Model prediction from the H1 PDF 2000 fit in which the observed difference arises from the generalised structure function $x\tilde{F}_3$ (see equation 2.37). The difference between e^+p and e^-p cross sections is basically unnoticeable at low Q^2 ($Q^2 \lesssim 1000 \text{ GeV}^2$, i.e. far away from the mass squared of the Z^0 boson) and increases with rising Q^2 .

9.2 The e^+p and e^-p Single Differential Cross Sections $d\sigma/dQ^2$

The single differential cross section $d\sigma/dQ^2$ (see equation 2.46) for $y < 0.9$ as well as the ratio of the $d\sigma/dQ^2$ measurements to the SM expectation are shown for RH (figure 9.4) and LH (figure 9.5) e^+p and for RH (figure 9.6) and LH (figure 9.7) e^-p . The cross sections are measured in the range from $Q^2 = 200 \text{ GeV}^2$ up to $Q^2 \simeq 20000 \text{ GeV}^2$. The cross sections fall by almost six orders of magnitude with increasing Q^2 , following the $1/Q^4$ dependence (see equation 2.36), due to the dominating photon exchange. The data with both lepton charges and polarisations are well described by the predictions of the SM using H1 2000 PDF fit.

The measured cross sections have a total error about 4% in the lower Q^2 bins, dominated by the systematic error. The contribution from the statistical errors increases with increasing Q^2 and dominates the total error above $Q^2 \simeq 1000 \text{ GeV}^2$.

9.3 Electroweak Effects at High Q^2

The NC 2003-04 e^+p and 2005 e^-p cross sections presented here together with the corresponding $e^\pm p$ CC measurements provide a test of the electroweak part of the Stan-

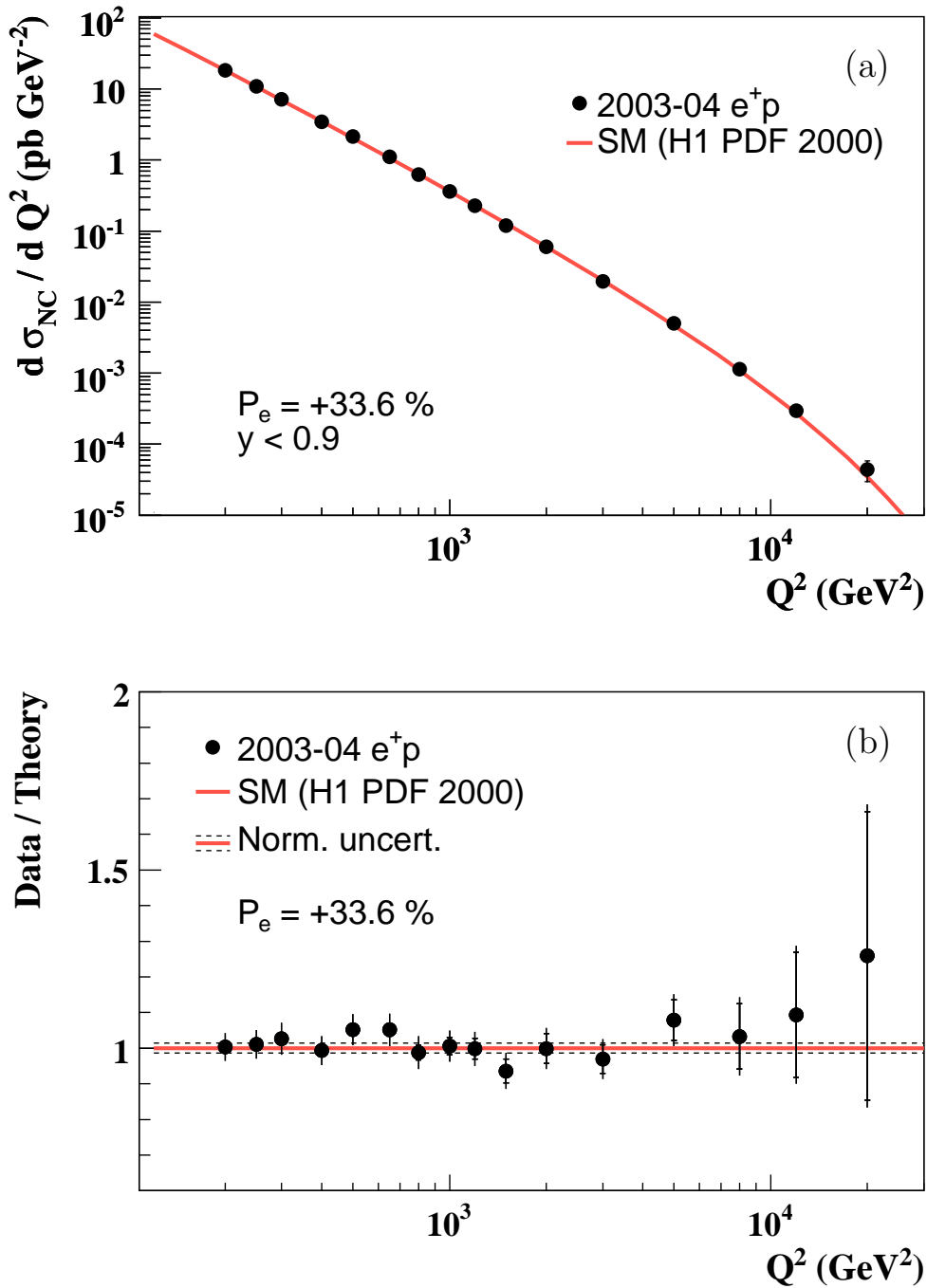


Figure 9.4: The Q^2 dependence of the NC cross sections $d\sigma/dQ^2$ cross sections for e^+p scattering with positive longitudinal positron polarisation (a). The ratio of cross sections for data and theory is shown in (b). The data (full points) are compared to the predictions from the H1 2000 PDF fit (solid curve). The inner and outer error bars represent the statistical and total errors, respectively. The 1.4% normalisation uncertainty is not included in the error bars and indicated by the dashed lines in (b).

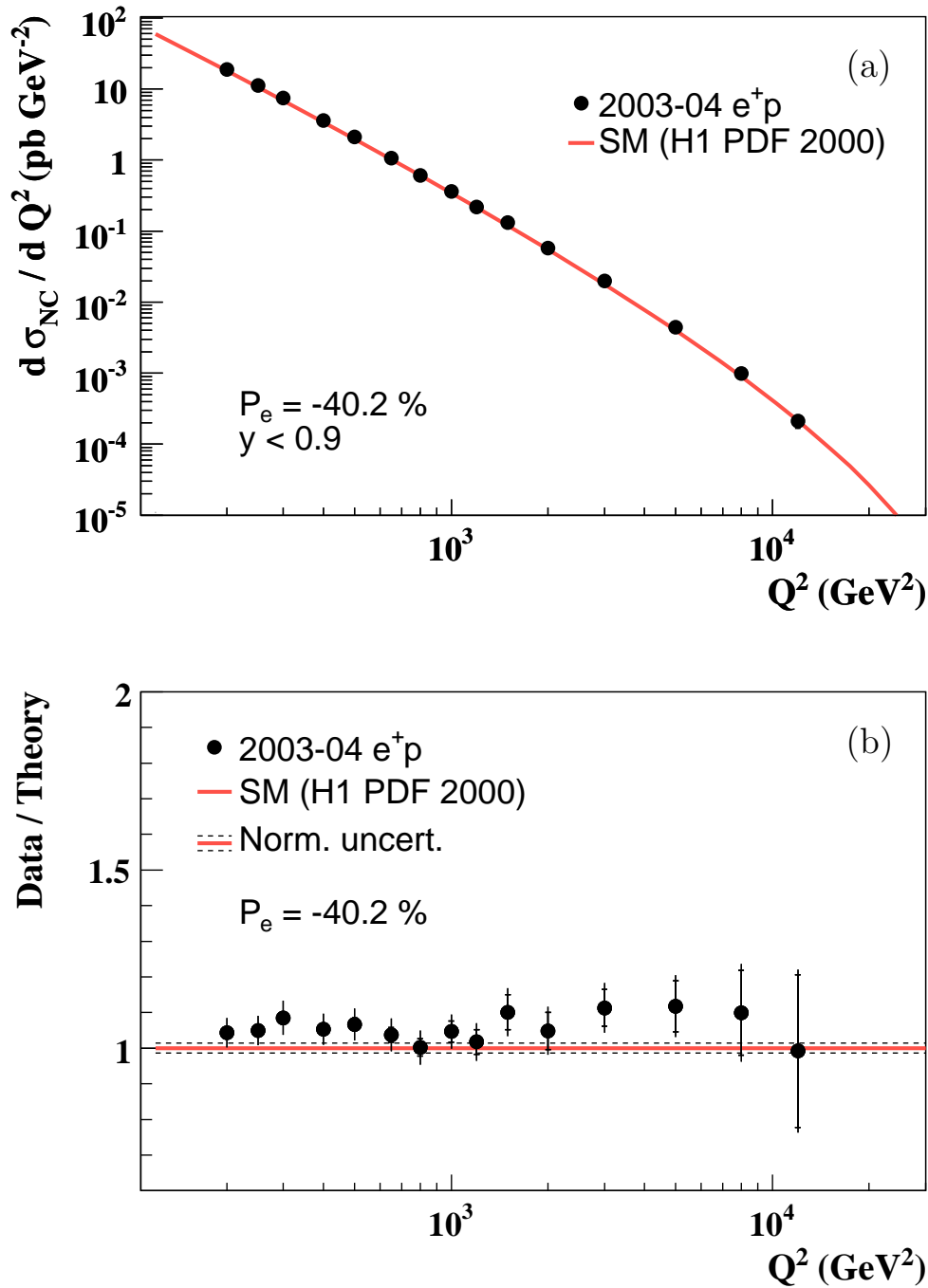


Figure 9.5: The Q^2 dependence of the NC cross sections $d\sigma/dQ^2$ cross sections for e^+p scattering with negative longitudinal positron polarisation (a). The ratio of cross sections for data and theory is shown in (b). The data (full points) are compared to the predictions from the H1 2000 PDF fit (solid curve). The inner and outer error bars represent the statistical and total errors, respectively. The 1.4% normalisation uncertainty is not included in the error bars and indicated by the dashed lines in (b).

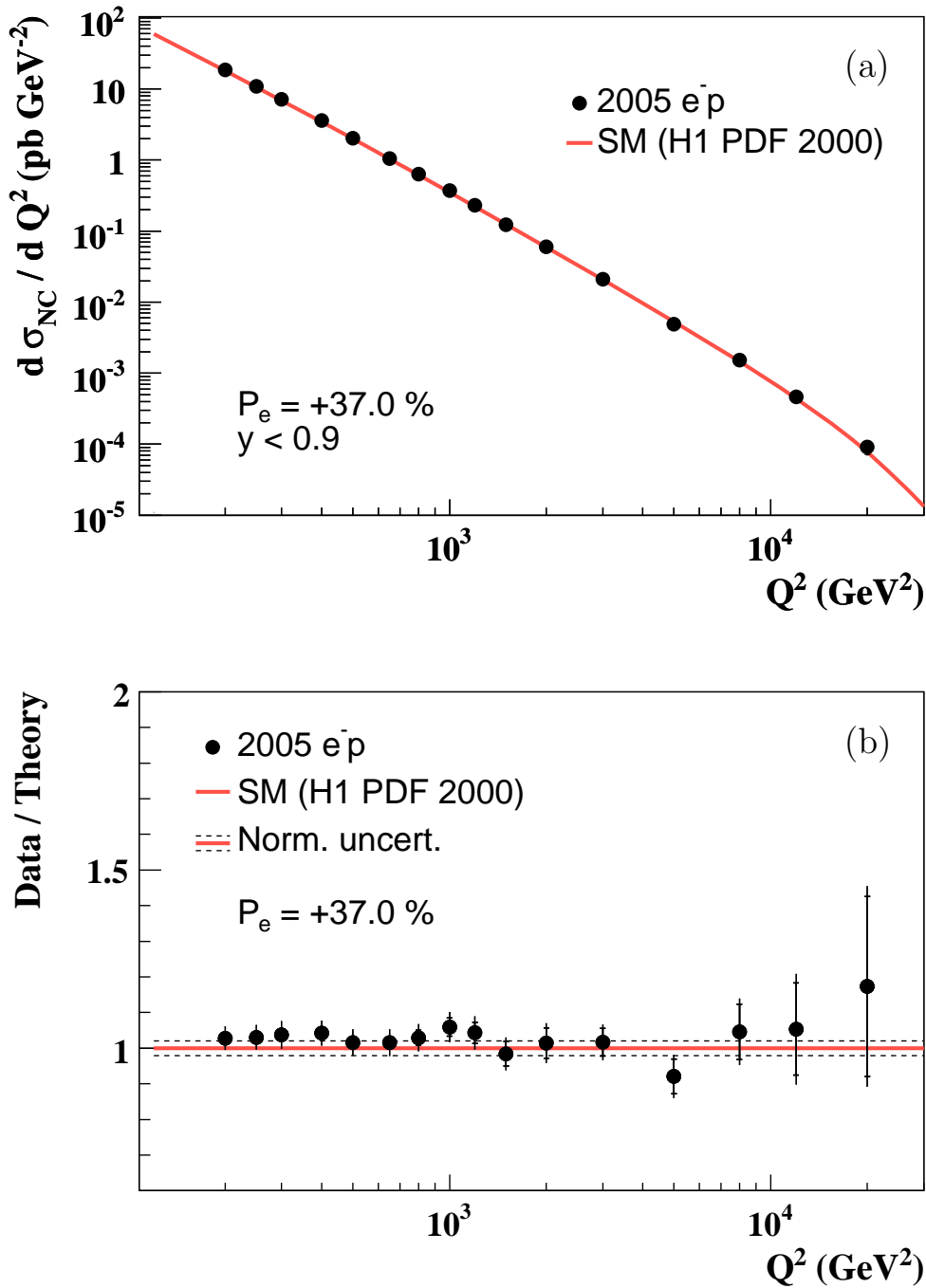


Figure 9.6: The Q^2 dependence of the NC cross sections $d\sigma/dQ^2$ cross sections for e^-p scattering with positive longitudinal electron polarisation. The ratio of cross sections for data and theory is shown in (b). The data (full points) are compared to the predictions from the H1 2000 PDF fit (solid curve). The inner and outer error bars represent the statistical and total errors, respectively. The 2.1% normalisation uncertainty is not included in the error bars and indicated by the dashed lines in (b).

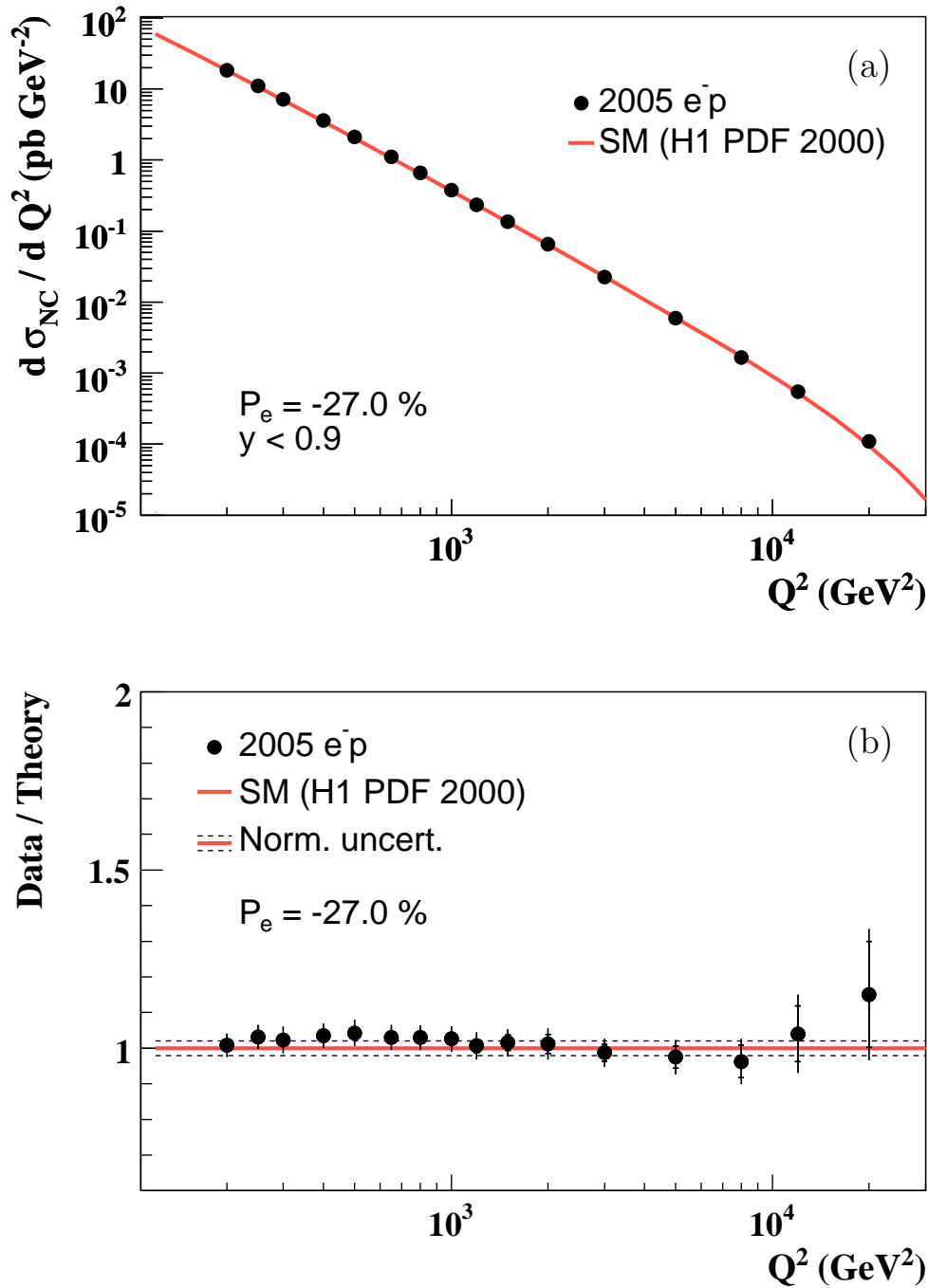


Figure 9.7: The Q^2 dependence of the NC cross sections $d\sigma/dQ^2$ cross sections for e^-p scattering with negative longitudinal electron polarisation (a). The ratio of cross sections for data and theory is shown in (b). The data (full points) are compared to the predictions from the H1 2000 PDF fit (solid curve). The inner and outer error bars represent the statistical and total errors, respectively. The 2.1% normalisation uncertainty is not included in the error bars and indicated by the dashed lines in (b).

Standard Model. Figure 9.8 shows unpolarised single differential cross section, $d\sigma/dQ^2$, for the NC and CC [116,117] processes in e^+p and e^-p scattering.

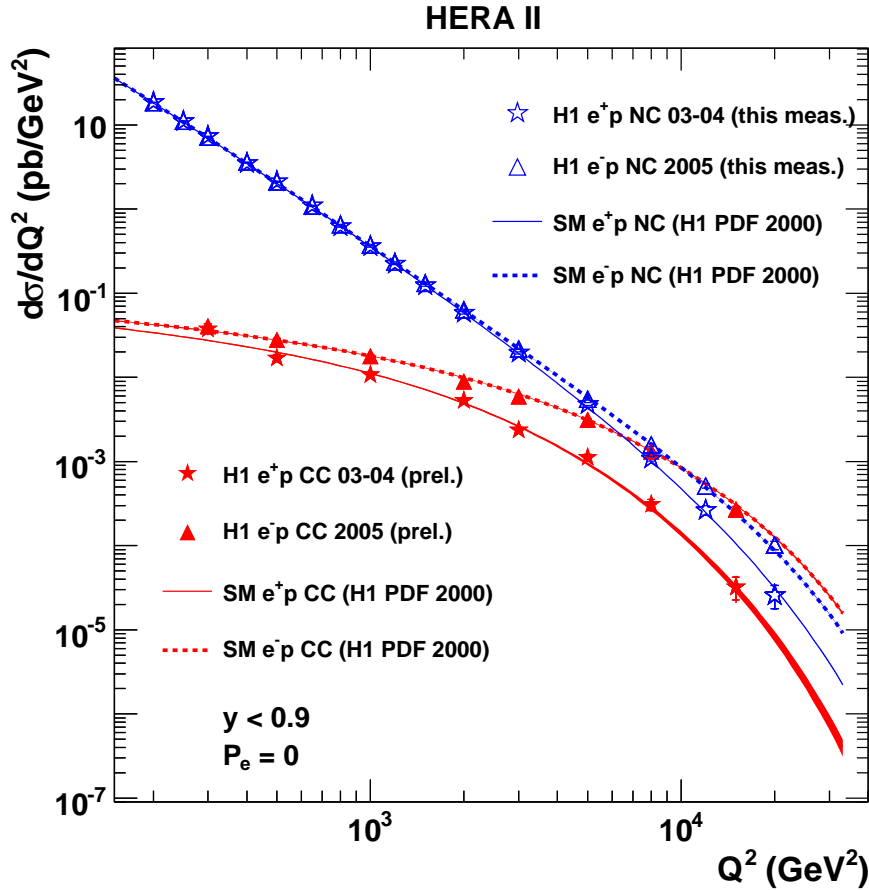


Figure 9.8: The Q^2 dependence of the NC (open symbols) and CC (solid symbols) unpolarised cross sections $d\sigma/dQ^2$ are shown for the 2003-04 e^+p (stars) and 2005 e^-p (triangles) measurements. The data are compared to the Standard Model expectations determined from the H1 PDF 2000 fit. The normalisation uncertainties of 1.4% for e^+p data and 2.1% for e^-p data respectively are not included in the error bars.

The NC cross section measurements span six orders in magnitude and more than two orders in Q^2 . At low Q^2 the NC cross section is larger than the CC cross section by more than two orders of magnitude. The strong increase of the NC cross section with decreasing Q^2 is due to the dominating photon exchange cross section $\propto 1/Q^4$. In contrast, the CC cross section is proportional to $[M_W^2/(Q^2 + M_W^2)]^2$ and therefore flattens at low Q^2 . The CC and NC cross sections are of comparable size at $Q^2 \gtrsim 10^4$ GeV². These measurements thus demonstrate the unification of the electromagnetic and the weak interactions in deep inelastic scattering.

The Standard Model provides an accurate description of all details of the NC and CC data behaviour up to the highest Q^2 , i.e. $Q^2 = 20\,000$ GeV².

9.4 Polarisation Asymmetry

The Standard Model predicts a difference in the cross section for leptons with different helicity states arising from the chiral structure of the neutral electroweak exchange. In figure 9.9 the ratio of cross sections with positive lepton beam polarisation to negative one is shown separately for the e^+p and e^-p scattering data. In both cases the ratio is found to be consistent, within the experimental uncertainty, with unity at low Q^2 , indicating little dependence of the cross section on the beam polarisation. It is assumed that the correlated uncertainties and uncertainty on QED radiative correction cancel in the ratio. The normalisation uncertainties of the measurements are not included in the errors bars, but are indicated by the dashed lines in the figure. At higher Q^2 , the data have a tendency to deviate from unity. For positron scattering the data indicate that right handed positrons yield a larger cross section than left handed positrons, whereas for electron scattering the data indicate the opposite behaviour. This behaviour is consistent with the Standard Model expectation shown as the solid curve in figure 9.9.

The influence of the lepton beam polarisation on the measured cross sections can be presented by combining the e^+p and e^-p scattering data in the ratio R , defined as

$$R = \frac{d\sigma/dQ^2(e^+p, P_e > 0) + d\sigma/dQ^2(e^-p, P_e < 0)}{d\sigma/dQ^2(e^+p, P_e < 0) + d\sigma/dQ^2(e^-p, P_e > 0)}. \quad (9.1)$$

For fixed polarisation and at fixed x and Q^2 this ratio is approximately given by

$$R \simeq \frac{F_2 - (v_e + P_e a_e) \kappa \frac{Q^2}{Q^2 + M_Z^2} F_2^{\gamma Z}}{F_2 - (v_e - P_e a_e) \kappa \frac{Q^2}{Q^2 + M_Z^2} F_2^{\gamma Z}}. \quad (9.2)$$

The ratio R is shown in figure 9.10. At low Q^2 , R is found to be consistent with unity and deviations from this behaviour are observed with increasing Q^2 . The data are consistent with the Standard Model expectation shown as the solid curve albeit the precision of this data is still moderate.

Another direct measure for the electroweak effects are the charge dependent polarisation asymmetries of the neutral current cross sections. The cross section asymmetries, defined as

$$A^\pm = \frac{2}{P_R - P_L} \cdot \frac{\sigma^\pm(P_R) - \sigma^\pm(P_L)}{\sigma^\pm(P_R) + \sigma^\pm(P_L)}, \quad (9.3)$$

to a very good approximation measure the structure function ratio

$$A^\pm \simeq \mp k a_e \frac{F_2^{\gamma Z}}{F_2}, \quad (9.4)$$

which is proportional to combinations $a_e v_q$ (see equation 2.48) and thus a direct measure of parity violation. One also finds that A^+ is expected to be positive (since $a_e = -1/2$) and about equal to $-A^-$ in the Standard Model. At large x the asymmetries measure the d/u ratio of the valence quark distributions according to [115]

$$A^\pm \simeq \pm k \frac{1 + d_v/u_v}{4 + d_v/u_v}. \quad (9.5)$$

The asymmetries A^\pm measured in this analysis are shown in figure 9.11 (a). It is assumed that the correlated uncertainties cancel in the asymmetry calculation. The

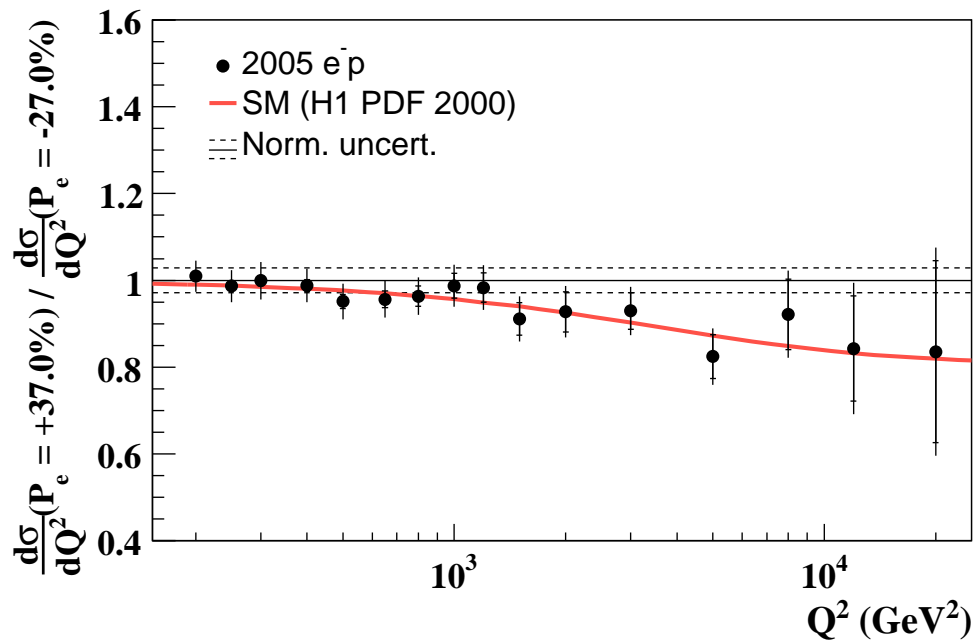
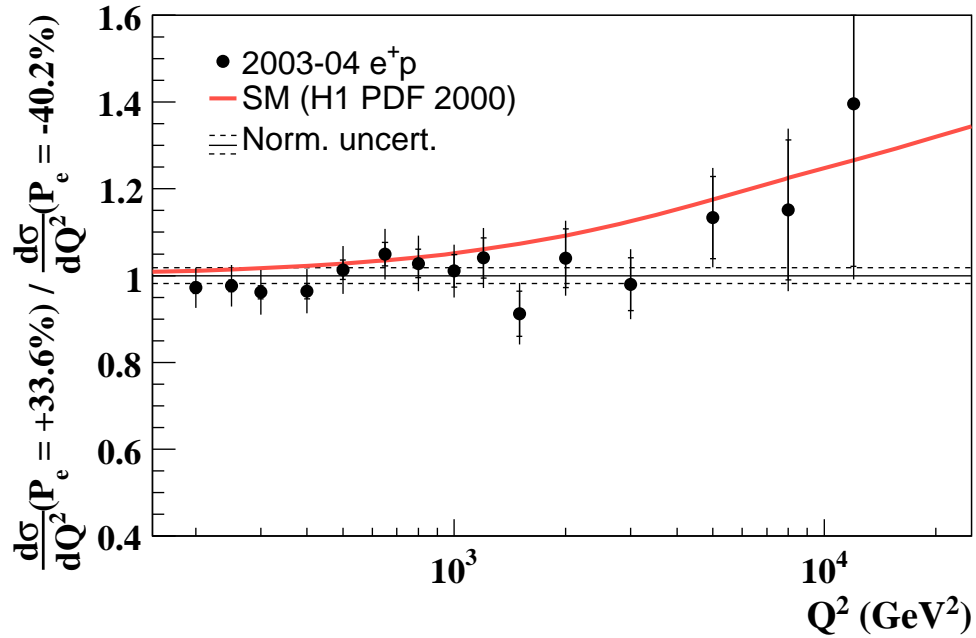


Figure 9.9: The Q^2 dependence of the NC cross section ratio $\frac{d\sigma}{dQ^2}$ (RH) / $\frac{d\sigma}{dQ^2}$ (LH) for the (a) e^+p scattering and (b) e^-p scattering. The inner error bars represent the statistical uncertainties and the outer error bars represent the total errors. The normalisation uncertainty is not included in the error bars and is instead shown as dashed lines. The data (solid points) are compared to the Standard Model prediction (solid curve).

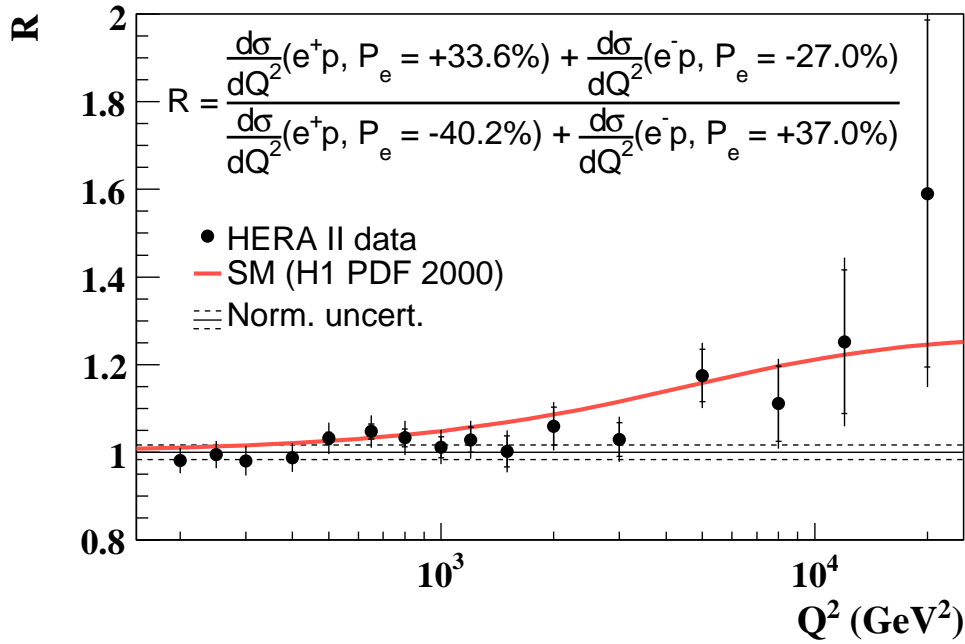


Figure 9.10: The Q^2 dependence of the combined $e^\pm p$ LH and RH NC cross section ratio R . The inner error bars represent the statistical uncertainties and the outer error bars represent the total errors. The normalisation uncertainty is not included in the error bars and is instead shown as dashed lines. The data (solid points) are compared to the Standard Model prediction.

data are consistent with the Standard Model expectation.

The statistical precision could be improved when the data from the two experiments, H1 and ZEUS, are combined. The results of this analysis are combined with the ZEUS measurement [115] and are shown in the figure 9.11 (b). A combination of the H1 and ZEUS data is performed by correcting the ZEUS data to $y < 0.9$ and then taking a weighted average in the common Q^2 intervals using the total uncorrelated errors. For a few Q^2 values no counterpart exists and then either the H1 or the ZEUS asymmetry value enters the combined asymmetry alone. The asymmetries are well described by the SM predictions. By definition these are rather insensitive to the details of the parton distributions as in the ratio $F_2^{\gamma Z}/F_2$ the x dependencies cancel to a large extent. The asymmetries A^\pm are thus a direct measure of electroweak interaction effects.

The asymmetries A^\pm are clearly observed to be of opposite sign. The difference $\delta A = A^+ - A^-$ can be seen to be significantly larger than zero. This is quantified by calculating the χ^2 for δA with respect to zero, based on the total uncorrelated uncertainty, and the corresponding probability of δA to be zero as a function of the minimum Q^2 considered. The behaviour of this function is as expected: At very large Q^2 the interference effects are large but hidden by the limited statistics. At low Q^2 they are small and not readily seen given the present uncertainties of the measurement. An optimum Q_{min}^2 of about 5000 GeV^2 exhibits a χ^2/dof of 4.0 corresponding to a probability of $3.1 \cdot 10^{-3}$ of δA to be zero.

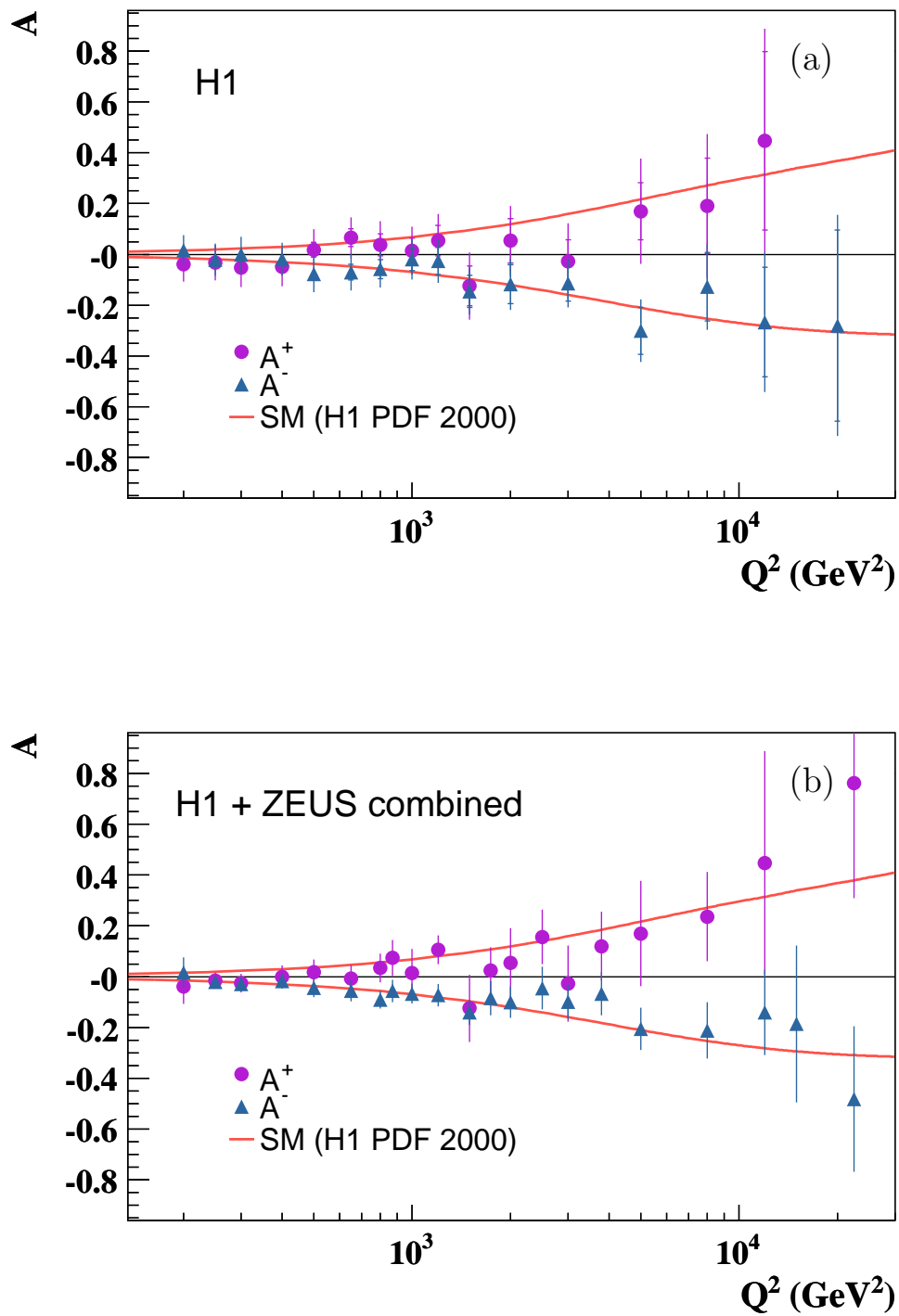


Figure 9.11: Measurements of the polarisation asymmetries A^\pm by this analysis (a) and combined with ZEUS (b). The error bars denote the total uncertainty which is dominated by the uncorrelated error contributions. The curves describe the theoretical prediction using the H1 PDF 2000 fit.

9.5 Structure Function $x\tilde{F}_3$

Combining the cross sections for different lepton charges allows the structure function $x\tilde{F}_3$ to be measured. In order to remove charge dependent terms in the \tilde{F}_2 part of the cross section the net unpolarised data from HERA II are used. The cross section difference between positron and electron data determines the generalised structure function $x\tilde{F}_3$

$$x\tilde{F}_3 = \frac{Y_+}{2Y_-} [\tilde{\sigma}^-(x, Q^2) - \tilde{\sigma}^+(x, Q^2)]. \quad (9.6)$$

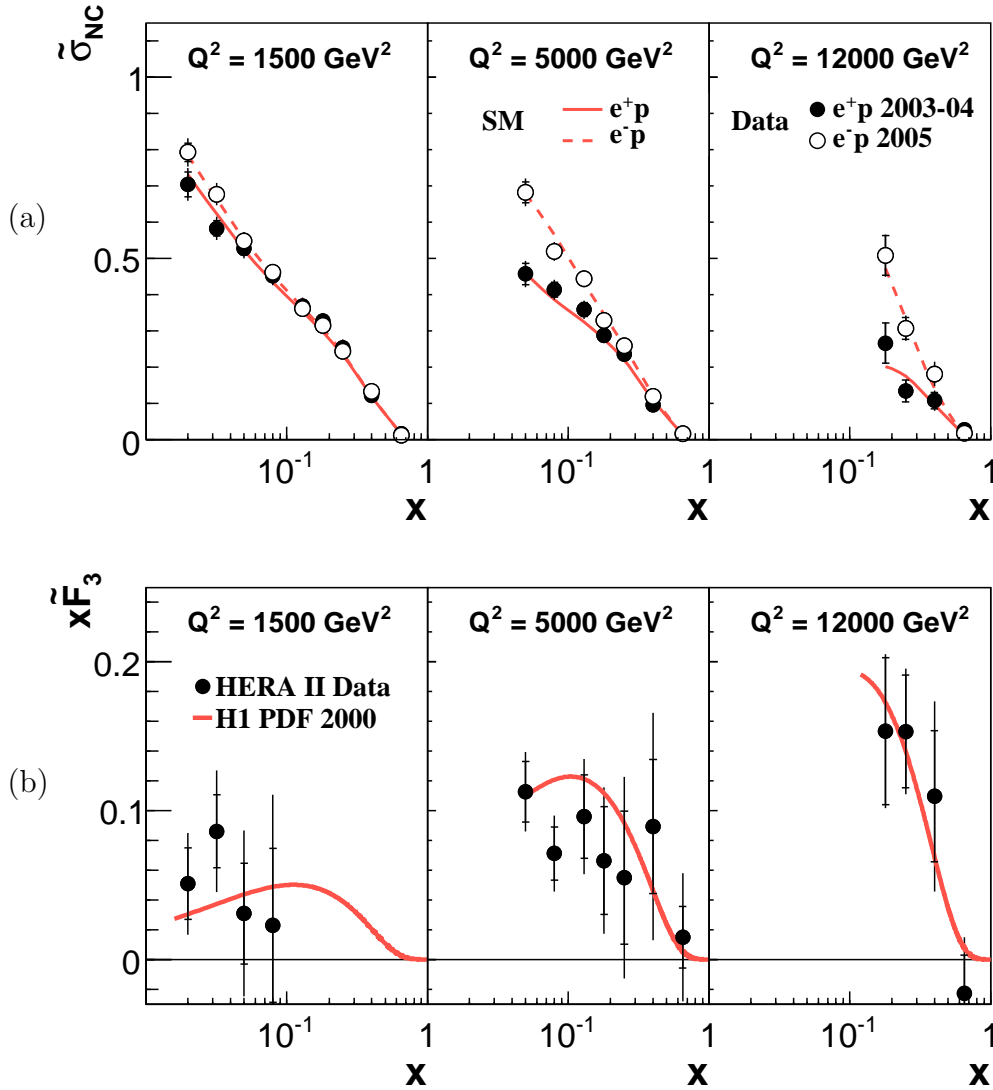


Figure 9.12: Unpolarised reduced cross sections $\tilde{\sigma}^\pm(x, Q^2)$ function of x for various values of Q^2 are shown in (a) for the HERA II data (open/solid points) compared to the Standard Model (solid/dashed curves). The structure function $x\tilde{F}_3$ evaluated using the HERA II data is shown in (b) (solid points) compared to the Standard Model (solid curve). The inner error bars represent the statistical uncertainties and the outer error bars represent the total errors. The normalisation uncertainty is included in the error bars for (b) only.

In order to optimise the sensitivity to $x\tilde{F}_3$, both the e^+p and the e^-p cross section

results are rebinned into three Q^2 bins as explained in section 8.5. The reduced cross sections $\tilde{\sigma}_{NC}^\pm$ measured in these bins together with expectations determined from the H1 PDF 2000 fit are shown in figure 9.12 (a). The resulting generalised structure function $x\tilde{F}_3$ is shown in figure 9.12 (b). As expected, $x\tilde{F}_3$ rises with Q^2 for fixed values of x due to the Z^0 propagator.

In the context of the Standard Model it can be seen from equation 2.42 that the dominant contribution to $x\tilde{F}_3$ arises from the γZ interference term, since the pure Z exchange term is suppressed by an additional factor of $Q^2/(Q^2 + M_Z^2)$ and, in the case of unpolarised scattering, the small vector coupling v_e . Thus $xF_3^{\gamma Z}$ may be determined by

$$xF_3^{\gamma Z} \simeq x\tilde{F}_3 \frac{(Q^2 + M_Z^2)}{a_e \kappa Q^2} \quad (9.7)$$

neglecting terms proportional to v_e .

The structure function $xF_3^{\gamma Z}$ is shown in figure 9.13 (a) for three Q^2 values and compared to the expectation. The weak Q^2 dependence of this non-singlet structure function is expected from the H1 PDF 2000 fit. Since the dependence is weak, the data are transformed to one Q^2 value at 1500 GeV² and then combined by weighted averaging using the full uncertainty. The combination of the extracted $xF_3^{\gamma Z}$ data for all Q^2 values is shown in figure 9.13 (b). Note that, $xF_3^{\gamma Z}$ is directly sensitive to the valence quark distributions (see equation 2.49). The Standard Model prediction is also shown and found to be in excellent agreement in both shape and magnitude with the data.

In order to improve the statistical precision the cross section data presented here are combined with the previously published [85] unpolarised NC reduced cross sections from HERA I in order to determine $x\tilde{F}_3$. The combination procedure is described in section 8.6. The resulting generalised structure function $x\tilde{F}_3$, listed in table C.9, is shown in the figure 9.14 (a) for the three Q^2 values. The corresponding $xF_3^{\gamma Z}$ is shown in figure 9.14 (b).

Figure 9.15 (a) shows the comparison of the structure function $xF_3^{\gamma Z}$ measured by ZEUS [115] and by H1 where the HERA I and HERA II data have been combined, as described above. The two measurements agree within the quoted uncertainties. In order to study x dependence of $xF_3^{\gamma Z}$ more accurately, a weighted average of these data is determined using the full uncertainty of either measurement. The averaged result for the interference structure function $xF_3^{\gamma Z}$ is shown in figure 9.15 (b) and listed in table C.9. The measurement is well described by the prediction of the SM using the H1 PDF 2000 NLO QCD fit.

In leading order pQCD “interference structure function” $xF_3^{\gamma Z}$ can be written as

$$xF_3^{\gamma Z} = 2x[e_u a_u (U - \bar{U}) + e_d a_d (D - \bar{D})], \quad (9.8)$$

with $U = u + c$ and $D = d + s$ for four flavours. The $xF_3^{\gamma Z}$ structure function thus provides information about the light quark axial vector couplings (a_u, a_d) and the sign of the electric quark charges (e_u, e_d). Equivalently one can write

$$xF_3^{\gamma Z} = 2x[e_u a_u (u_v + \Delta_u) + e_d a_d (d_v + \Delta_d)]. \quad (9.9)$$

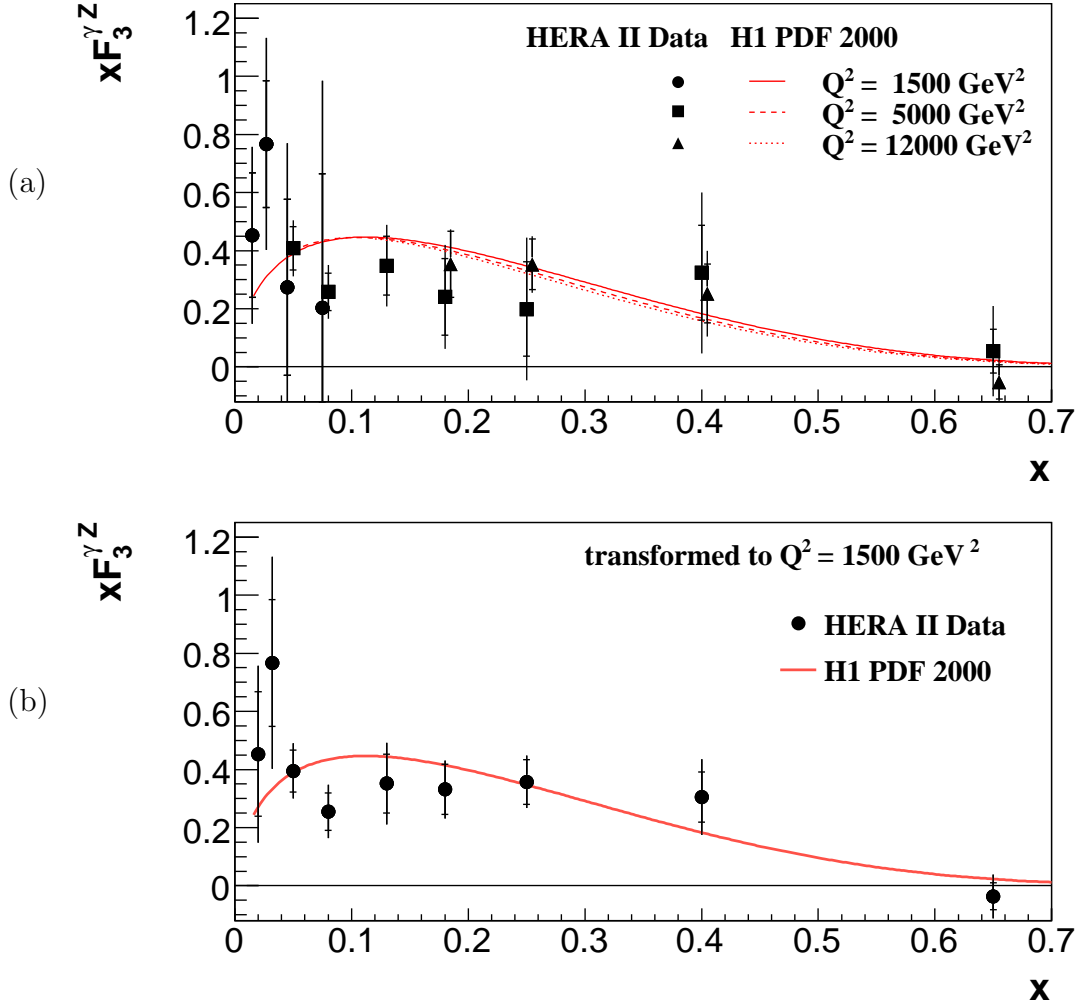


Figure 9.13: The structure function $x F_3^{\gamma Z}$ extracted from HERA II data (solid and open points) is shown in (a) for three Q^2 bins together with the Standard Model expectation (full, dashed and dotted curves). In (b) the data are transformed to $Q^2 = 1500 \text{ GeV}^2$ and combined in each x bin. The inner error bars represent the statistical uncertainties and the outer error bars represent the total errors. The normalisation uncertainty is included in the error bars.

In the naive parton model as in conventional perturbative QCD it is expected that the differences $\Delta_u = (u_{sea} - \bar{u} + c - \bar{c})$ and $\Delta_d = (d_{sea} - \bar{d} + s - \bar{s})$ are zero. However, in non-perturbative QCD differences may occur, for example between the strange and antistrange quark distributions, for which there are some hints in DIS neutrino nucleon di-muon data [121]. Inserting the standard charge and axial coupling values one finds

$$x F_3^{\gamma Z} = \frac{x}{3} (2u_v + d_v + \Delta) \quad (9.10)$$

with $\Delta = 2\Delta_u + \Delta_d$. Neglecting Δ leads to a sum rule [122] which in leading order is

$$\int_0^1 x F_3^{\gamma Z} \frac{dx}{x} = \frac{1}{3} \int_0^1 (2u_v + d_v) dx = \frac{5}{3}. \quad (9.11)$$

The structure function $x F_3^{\gamma Z}$ thus is determined by the valence quark distributions

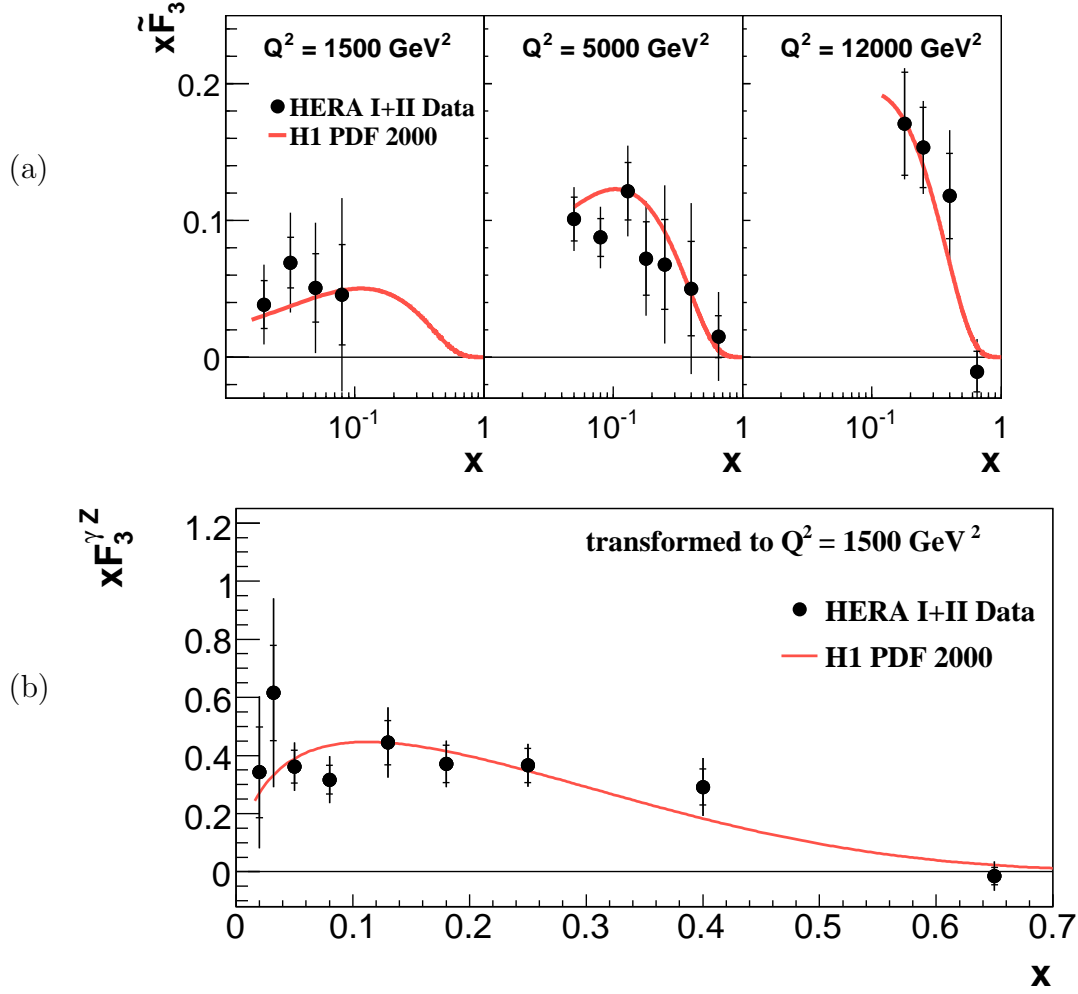


Figure 9.14: The structure function $x\tilde{F}_3$ evaluated using combined HERA I and HERA II data is shown in (a) (solid points) compared to the Standard Model (solid curve). The structure function $x F_3^{\gamma Z}$ extracted from HERA I and HERA II data (solid and open points) is shown in (b) together with the Standard Model expectation (solid curve). The inner error bars represent the statistical uncertainties and the outer error bars represent the total errors. The normalisation uncertainty is included in the error bars.

and is therefore predicted to be only very weakly depending on Q^2 .

In the range of acceptance the integral of $F_3^{\gamma Z}$ is measured to be

$$\int_{0.02}^{0.65} F_3^{\gamma Z} dx = 1.21 \pm 0.09(\text{stat}) \pm 0.08(\text{syst}) \quad (9.12)$$

Using the H1 2000 PDF fit prediction to subtract the valence quark contribution to the sum rule, a constraint is obtained for the difference term

$$\int_{0.02}^{0.65} \Delta dx = 0.09 \pm 0.09(\text{stat}) \pm 0.08(\text{syst}) \quad (9.13)$$

in the quoted kinematic range which is consistent with zero.

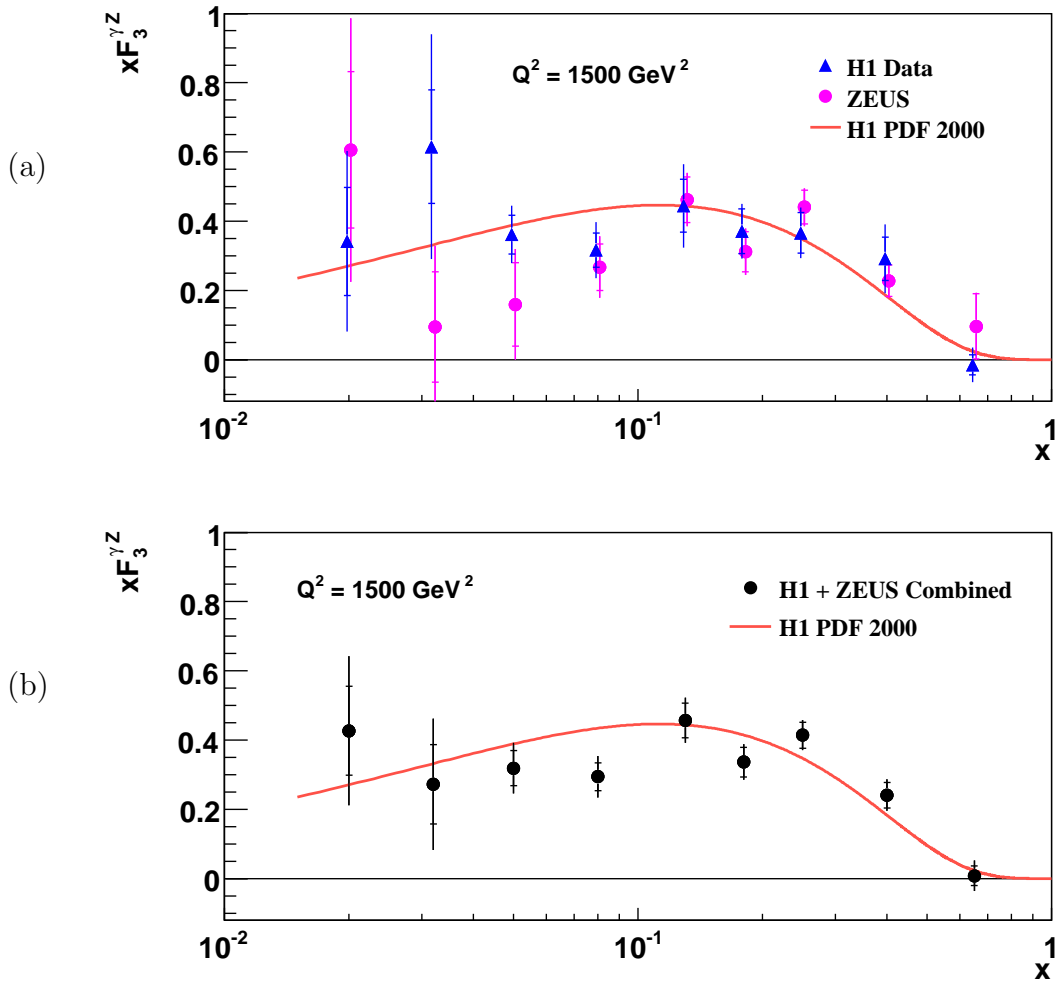


Figure 9.15: The structure function $x F_3^{\gamma Z}$ extracted from all HERA I and the HERA II H1 and ZEUS data (solid and open points) is shown in (a) for three Q^2 bins together with the Standard Model expectation (full, dashed and dotted curves). In (b) the data are transformed to $Q^2 = 1500 \text{ GeV}^2$ and combined in each x bin. The inner error bars represent the statistical uncertainties and the outer error bars represent the total errors. The normalisation uncertainty is included in the error bars.

Chapter 10

Summary and Outlook

10.1 Summary of the Analysis

In this thesis measurements of inclusive $e^\pm p$ neutral current deep inelastic scattering, using the H1 detector at HERA, have been presented. The data come from interactions of longitudinally polarised leptons with unpolarised protons. Single and double differential cross sections in the four-momentum transfer squared Q^2 and Bjorken variable x are measured. The measurements were performed in the domain up to the highest Q^2 , comparable with the square of the Z^0 boson mass, making tests possible of both components of the Standard Model, QCD and the electroweak theory.

The data were taken with an incident lepton beam energy of 27.5 GeV, while the unpolarised proton beam energy was 920 GeV, yielding a centre-of-mass energy of $\sqrt{s} = 318$ GeV. In the year 2003-04, 26.9 pb⁻¹ of e^+p data have been taken with positive longitudinal lepton beam polarisation ($P_e = 33.6\%$) and 20.7 pb⁻¹ with negative longitudinal polarisation ($P_e = -40.2\%$). In the year 2005, 29.6 pb⁻¹ of e^-p data have been taken with positive longitudinal lepton beam polarisation ($P_e = 37.0\%$) and 68.6 pb⁻¹ with negative longitudinal polarisation ($P_e = -27.0\%$).

Double and single differential cross sections are measured in x and Q^2 :

- **Double differential cross sections $d^2\sigma/dxdQ^2$**

The e^+p and e^-p double differential cross sections for neutral current processes in collisions with positive and negative longitudinally polarised leptons are measured for $200 < Q^2 < 20\,000$ GeV² and $0.0032 < x < 0.65$. The precision of the measurement is at the level of a few per cent at low Q^2 , where the systematic error dominates, and is limited by the statistical precision of the data at very high Q^2 .

- **Single differential cross sections $d\sigma/dQ^2$**

The measured cross sections cover a range of two orders of magnitude in Q^2 , $200 < Q^2 < 20\,000$ GeV² and fall by about six orders of magnitude with increasing Q^2 due to the propagator of the exchanged particle. At highest Q^2 , comparable with the W^\pm and Z^0 boson masses squared, the NC cross section is of similar size as the CC cross section, illustrating the unification of the electromagnetic and weak forces in deep inelastic scattering.

The measured cross sections are used to determine:

- **Polarisation asymmetries A^\pm**

The inclusive cross section measurements from this analysis for different lepton beam charge (\pm) and beam polarisation states are used to measure the parity violating asymmetries A^\pm . These asymmetries measure the product of vector and axial-vector couplings of the leptons and quarks. They demonstrate parity violation at very small distances, down to about 10^{-18} m.

- **Proton structure function $x\tilde{F}_3$**

The difference of the e^+p and the e^-p cross sections in the region of very high Q^2 is explored for the extraction of the structure function $x\tilde{F}_3$ in the region of $1500 < Q^2 < 12000$ GeV² and $0.02 < x < 0.65$. This structure function is dominated by the γZ^0 interference term $xF_3^{\gamma Z}$. The structure function $x\tilde{F}_3$, being a sensitive probe of the valence quarks in the proton, is explicitly derived from the measurement.

The results obtained in this analysis are also combined with previously published H1 data from HERA I and ZEUS data from HERA I and HERA II to provide the most accurate HERA measurements.

The Standard Model predictions based on the parton distribution functions, as determined from the H1 PDF 2000 NLO QCD fit, provide a consistent description of all data presented, including the measured cross sections, the polarisation asymmetries and the $x\tilde{F}_3$ structure function.

10.2 Outlook

In 2006 HERA continued its operation with electrons, followed by e^+p operation, which will go until the HERA shut down in the middle of 2007. During 2006 H1 has accumulated 69.7 pb⁻¹ which corresponds to an increase of e^-p statistics by a factor of 1.4. The final HERA II e^+p data sample is expected to increase by factor of 2-2.5.

Sizable effect of the polarisation and charge asymmetries appears only at very high Q^2 region, where data are limited by the statistical precision. Therefore, an increase of statistics is important. In addition, there are several areas where the systematic errors on the measurement could be improved in future:

- An increase of statistics will allow to improve the understanding of some of the systematic errors on the measurement. In particular higher statistics will allow the electron energy scale to be studied in greater detail in the forward region (high Q^2).
- Better understanding of the z measurement in the Central Tracking detector would allow a significant reduction of the systematics on the polar angle measurement. This may be coupled to a better measurement of central vertices and a better modelling of the vertex and track finding efficiencies by the simulation.
- Further development in the understanding of the forward tracking detector at HERA II is needed. The inclusion of forward vertices would improve

the efficiency at low y and the use of forward tracks may improve the scattered electron measurement at the highest Q^2 .

The measured cross sections may be used to extract the axial ($a_{u,d}$) and vector ($v_{u,d}$) couplings of the light quarks, the u and the d , to the Z^0 boson. With a sizeable HERA dataset it may be possible to determine $a_{u,d}$ and $v_{u,d}$ with a precision that rivals the measurement of the heavy quark couplings from LEP [49].

A precise knowledge of parton distribution functions, provided by HERA is essential for future studies in the field of particle physics, for example, in studies of pp collisions at the Large Hadron Collider (LHC). There, the understanding of the proton structure is important, e.g. to control background processes in the search for Higgs boson production, “missing item“ of the Standard Model.

Appendix A

Trigger Fiducial Cuts

Here, in table A.1 a run (time) dependent trigger fiducial requirements are given. The listed regions are excluded from the analysis due to low trigger efficiency (see section 6.8 for more details).

φ_{min}	φ_{max}	z_{min}	z_{max}
For run ≥ 356241 :			
135.0°	157.5°	−90.0 cm	0.0 cm
157.5°	180.0°	−90.0 cm	−60.0 cm
90.0°	112.5°	−90.0 cm	−60.0 cm
90.0°	112.5°	−30.0 cm	0.0 cm
157.5°	180.0°	−10.0 cm	20.0 cm
135.0°	157.5°	−150.0 cm	−120.0 cm
0.0°	22.5°	−110.0 cm	−100.0 cm
112.5°	135.0°	−160.0 cm	−150.0 cm
45.0°	67.5°	−20.0 cm	−10.0 cm
−112.5°	−90.0°	−50.0 cm	−30.0 cm
90.0°	112.5°	−50.0 cm	−30.0 cm
For $356241 \leq \text{run} < 395000$:			
−45.0°	−22.5°	−110.0 cm	−100.0 cm
For run ≥ 395000 :			
−135.0°	−112.5°	−60.0 cm	−30.0 cm
−180.0°	−157.5°	−30.0 cm	0.0 cm
0.0°	22.5°	−100.0 cm	−90.0 cm
90.0°	112.5°	−130.0 cm	−120.0 cm
135.0°	157.5°	0.0 cm	20.0 cm

Table A.1: Regions excluded from the analysis due to low trigger efficiency.

Appendix B

Events in the H1 Detector

The following figures show examples of events in the H1 Detector from the 2003-05 data taking. High Q^2 NC and CC event are shown in figures B.1 and B.2, respectively (see chapter 2 and 3 for more details).

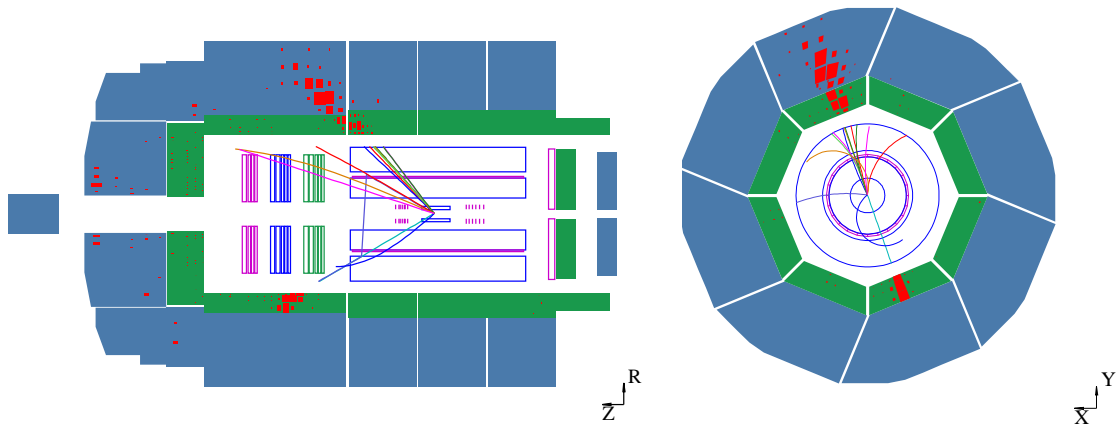


Figure B.1: Example of a NC event with high Q^2 in the H1 Detector from 2003-05 data taking.

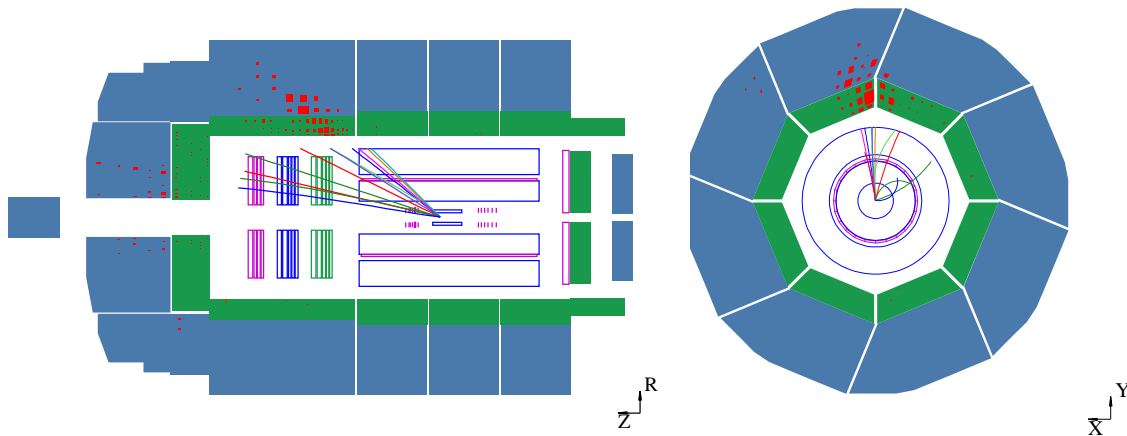


Figure B.2: Example of a CC event with high Q^2 in the H1 detector from 2003-05 data taking.

Examples of events from non- ep background processes are shown in figure B.3 (halo-muon and cosmic muon events) and figure B.4 (beam-gas interaction). Such events are taken out by dedicated background finders and their remaining contamination to the NC sample is essentially zero (see section 6.10).

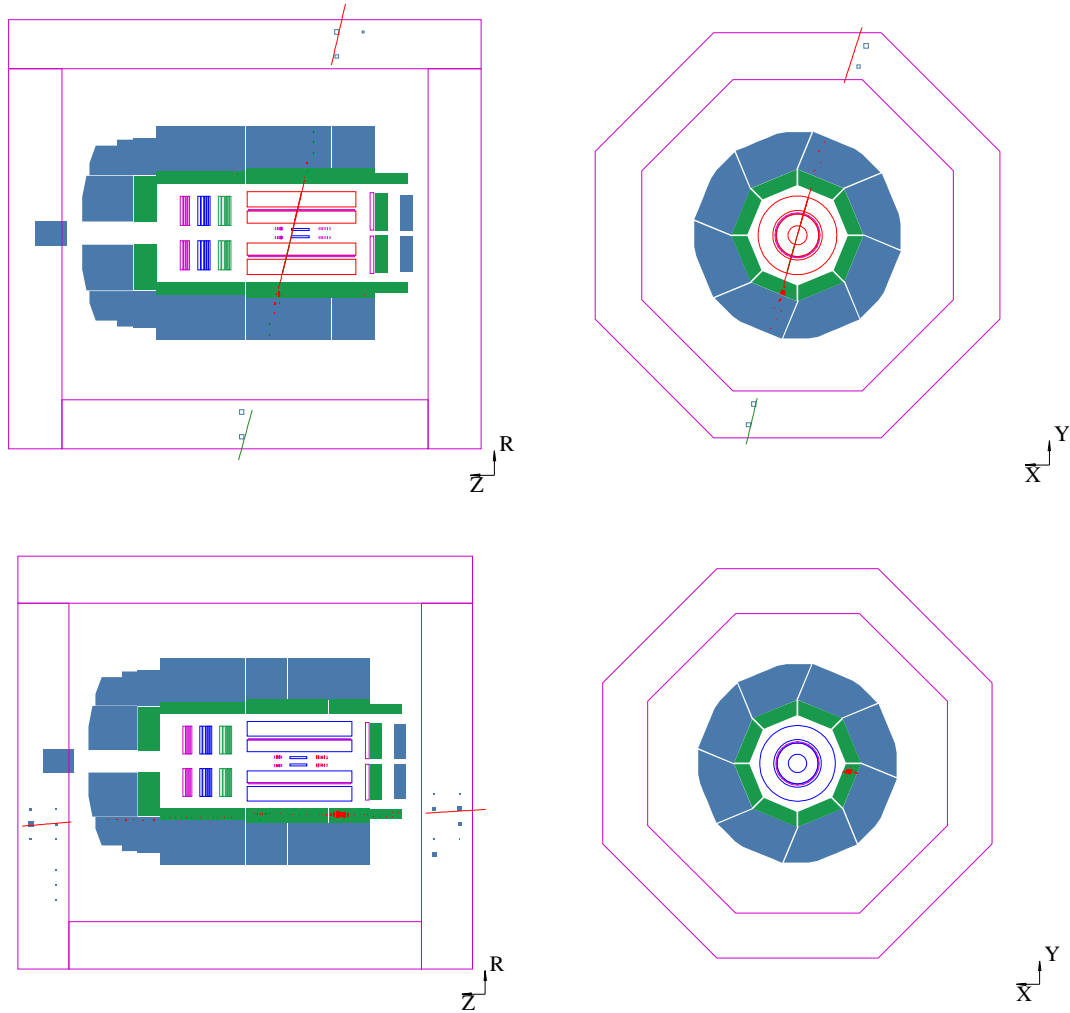


Figure B.3: Cosmic (top) and halo-muon (bottom) events in the H1 detector.

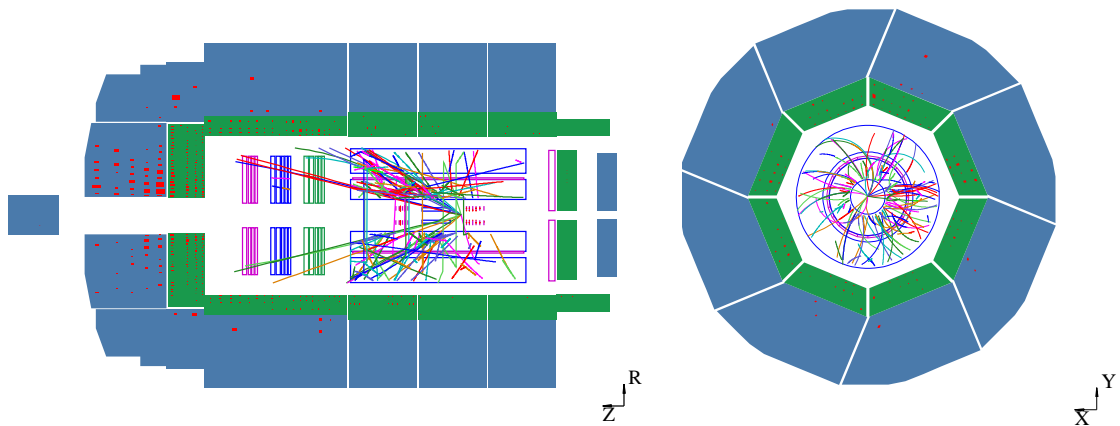


Figure B.4: Beam-gas event in the H1 detector.

Appendix C

Tables of Results

Cross sections measured in this thesis are tabulated on the following pages. The effect of possible systematic mis-measurements is calculated by propagating a shift of the corresponding quantity by $\pm\sigma$ up to the final result. The statistical and systematic error contributions are shown separately for each bin. The systematic error is separated into uncorrelated and correlated contributions. The complete list of systematic uncertainties is given section 8.4. The total systematic error is formed by adding the individual errors in quadrature (see chapters 8 and 9 for more details).

Table C.9 shows the results of measurement of the generalised structure function $x\tilde{F}_3$ and the interference structure function $xF_3^{\gamma Z}$ (see section 9.5).

Q^2 (GeV ²)	x	y	$\tilde{\sigma}_{NC}$	δ_{stat} (%)	δ_{sys} (%)	δ_{tot} (%)	δ_{unc} (%)	δ_{unc}^E (%)	δ_{unc}^h (%)	δ_{cor} (%)	δ_{cor}^{E+} (%)	$\delta_{cor}^{\theta+}$ (%)	δ_{cor}^{h+} (%)	δ_{cor}^{N+} (%)	δ_{cor}^{B+} (%)
200	0.0032	0.6176	1.275	2.6	4.0	4.7	3.7	0.8	0.9	1.5	-0.6	-1.0	0.5	0.4	0.8
200	0.0050	0.3953	1.131	2.1	5.0	5.4	4.0	1.0	1.0	3.0	-1.2	-1.7	-1.3	-1.6	0.3
200	0.0080	0.2470	0.952	2.1	4.1	4.6	3.5	0.1	1.0	2.1	0.5	-1.7	0.4	1.2	0.1
200	0.0130	0.1520	0.816	2.2	4.2	4.7	3.5	0.2	0.3	2.3	-0.8	-1.7	0.3	1.2	0.1
200	0.0200	0.0988	0.695	2.4	5.6	6.0	4.2	1.5	1.8	3.7	-0.5	-2.1	-1.9	-2.3	0.1
200	0.0320	0.0618	0.605	2.9	4.9	5.7	4.3	0.7	1.9	2.3	-1.2	-1.4	0.7	1.1	0.0
200	0.0500	0.0395	0.524	3.4	10.1	10.6	6.5	3.8	3.2	7.7	4.3	3.6	3.5	3.9	0.0
200	0.0800	0.0247	0.389	3.8	5.5	6.7	4.0	1.9	0.5	3.8	-1.3	-3.0	-1.0	-1.6	0.0
200	0.1300	0.0152	0.316	5.3	7.3	9.0	4.4	1.5	2.2	5.8	-4.2	-3.1	2.2	-0.9	0.0
250	0.0050	0.4941	1.133	2.5	4.1	4.8	3.8	0.7	1.7	1.5	-0.4	-0.9	0.8	0.6	0.5
250	0.0080	0.3088	1.011	2.4	4.1	4.7	3.7	0.7	1.2	1.8	-0.7	-0.8	0.8	-1.2	0.2
250	0.0130	0.1900	0.799	2.4	5.4	5.9	4.5	1.7	1.5	3.0	1.2	-1.7	1.2	1.8	0.1
250	0.0200	0.1235	0.730	2.4	4.1	4.8	3.7	0.8	1.2	1.9	-0.7	-1.6	-0.2	0.6	0.1
250	0.0320	0.0772	0.584	2.7	4.2	5.0	3.8	0.9	1.0	1.8	1.3	-0.8	-0.4	-0.8	0.0
250	0.0500	0.0494	0.513	3.0	5.2	6.0	3.6	1.1	0.3	3.8	-1.5	-1.7	-1.3	2.7	0.0
250	0.0800	0.0309	0.426	3.2	5.1	6.0	4.0	1.9	1.2	3.1	0.7	-1.6	-1.3	-2.1	0.0
250	0.1300	0.0190	0.352	4.1	5.9	7.2	5.1	3.2	1.4	3.0	1.1	2.5	-0.8	0.8	0.0
250	0.1800	0.0137	0.315	5.3	6.9	8.7	5.4	1.8	1.6	4.4	2.1	-1.8	-2.6	2.1	0.0
300	0.0050	0.5929	1.139	3.3	4.0	5.2	3.6	0.8	1.0	1.7	-0.6	-1.4	-0.5	-0.1	0.7

Table C.1: The NC e^+p double differential cross section $d^2\sigma_{NC}/dQ^2dx$ for RH polarised positrons ($P_e = 33.6\%$) with the statistical (δ_{stat}), systematic (δ_{sys}) and total (δ_{tot}) errors. Also shown are the total uncorrelated systematic (δ_{unc}) errors and two of its contributions: the electron energy error (δ_{unc}^E) and the hadronic energy error (δ_{unc}^h). The effect of the other uncorrelated systematic errors is included in (δ_{unc}). The table also provides the correlated systematic error (δ_{cor}) and its contributions from a positive variation of one standard deviation of the error on the electron energy (δ_{cor}^{E+}) and polar angle ($\delta_{cor}^{\theta+}$), of the hadronic energy error (δ_{cor}^{h+}), of the error due to noise subtraction (δ_{cor}^{N+}) and background subtraction (δ_{cor}^{B+}) (δ_{unc}^h). The effect of the other correlated systematic errors is included in (δ_{cor}). The normalisation uncertainty of 1.4% is not included in the errors. The table continues on the next 4 pages.

Q^2 (GeV ²)	x	y	$\tilde{\sigma}_{NC}$	δ_{stat} (%)	δ_{sys} (%)	δ_{tot} (%)	δ_{unc} (%)	δ_{unc}^E (%)	δ_{unc}^h (%)	δ_{cor} (%)	$\delta_{cor}^{E^+}$ (%)	$\delta_{cor}^{\theta^+}$ (%)	$\delta_{cor}^{h^+}$ (%)	$\delta_{cor}^{N^+}$ (%)	$\delta_{cor}^{B^+}$ (%)
300	0.0080	0.3706	1.040	2.7	4.1	4.9	3.7	0.3	1.6	1.6	0.3	-1.2	0.6	0.8	0.2
300	0.0130	0.2280	0.906	2.6	4.0	4.8	3.6	1.0	0.7	1.7	0.5	-1.0	1.1	0.5	0.1
300	0.0200	0.1482	0.711	2.8	4.9	5.6	3.7	1.3	0.4	3.2	1.1	-2.6	0.6	1.3	0.1
300	0.0320	0.0926	0.577	3.0	5.3	6.1	4.0	2.2	0.6	3.5	1.7	-2.6	-0.7	1.5	0.0
300	0.0500	0.0593	0.516	3.5	4.8	5.9	4.1	2.3	0.5	2.4	0.9	-1.6	-0.2	1.5	0.0
300	0.0800	0.0371	0.436	3.5	4.8	6.0	3.8	1.3	0.9	3.0	-1.0	-1.3	-1.0	2.3	0.0
300	0.1300	0.0228	0.365	4.5	9.1	10.2	6.9	4.9	3.0	6.0	3.4	3.0	3.1	2.4	0.0
300	0.1800	0.0165	0.312	5.5	6.9	8.8	5.4	2.9	1.5	4.3	-2.7	-2.4	-1.2	-2.0	0.0
400	0.0050	0.7905	1.024	5.8	5.1	7.7	4.0	1.6	1.1	3.1	1.9	1.6	0.8	1.2	1.1
400	0.0080	0.4941	1.002	3.3	4.2	5.4	3.8	0.4	1.6	1.9	-0.4	-0.9	1.5	0.3	0.4
400	0.0130	0.3040	0.860	3.1	4.1	5.1	3.8	1.4	1.2	1.4	0.2	-1.1	-0.3	0.7	0.2
400	0.0200	0.1976	0.721	3.2	3.7	4.9	3.5	0.6	0.6	1.1	-0.1	-0.9	-0.2	0.6	0.1
400	0.0320	0.1235	0.594	3.3	4.4	5.6	3.9	1.8	0.2	2.2	1.4	-1.5	0.6	0.6	0.1
400	0.0500	0.0791	0.548	3.7	5.0	6.2	4.2	2.0	0.8	2.8	1.1	1.3	1.0	2.0	0.1
400	0.0800	0.0494	0.458	3.8	5.3	6.5	4.3	1.8	1.5	3.2	-1.5	-1.7	-0.9	-2.0	0.0
400	0.1300	0.0304	0.341	5.0	6.5	8.2	5.2	3.4	1.9	3.9	3.3	-1.4	-1.1	0.9	0.0
400	0.1800	0.0220	0.272	6.5	6.1	8.9	5.2	3.6	1.7	3.2	2.2	-1.8	-0.2	-1.6	0.0
400	0.2500	0.0158	0.232	6.7	8.0	10.4	4.7	2.9	1.3	6.4	1.1	-2.5	-1.7	-5.6	0.0
500	0.0080	0.6176	1.013	4.2	4.7	6.3	4.2	1.2	1.5	2.2	-0.7	-1.5	-0.8	-0.9	0.7
500	0.0130	0.3801	0.824	3.8	4.2	5.7	3.8	0.7	1.2	1.8	0.5	-0.9	0.7	1.3	0.2
500	0.0200	0.2470	0.771	3.9	3.9	5.5	3.6	0.9	1.1	1.5	0.5	-1.0	0.5	0.8	0.1
500	0.0320	0.1544	0.658	3.7	3.8	5.3	3.7	1.4	0.5	1.2	-0.8	-0.6	-0.6	0.3	0.1
500	0.0500	0.0988	0.595	4.2	5.6	7.0	4.8	3.1	1.0	2.9	1.9	-1.5	0.5	1.4	0.0
500	0.0800	0.0618	0.492	4.3	4.7	6.4	3.7	0.6	0.6	2.9	-1.1	-1.1	-0.4	2.4	0.0
500	0.1300	0.0380	0.367	5.3	5.1	7.4	4.6	3.0	0.3	2.3	1.2	-1.4	-0.6	-1.2	0.0
500	0.1800	0.0274	0.349	6.3	8.4	10.6	6.8	5.4	2.2	5.0	3.2	-2.1	-2.2	-2.4	0.0
500	0.2500	0.0198	0.240	7.4	5.5	9.2	4.2	1.4	1.4	3.5	-1.9	-2.1	-1.1	1.7	0.0
650	0.0080	0.8029	1.078	5.9	5.0	7.7	4.1	2.0	1.2	2.8	-1.3	-1.5	-0.5	1.4	1.1

Q^2 (GeV ²)	x	y	$\tilde{\sigma}_{NC}$	δ_{stat} (%)	δ_{sys} (%)	δ_{tot} (%)	δ_{unc} (%)	δ_{unc}^E (%)	δ_{unc}^h (%)	δ_{cor} (%)	δ_{cor}^{E+} (%)	$\delta_{cor}^{\theta+}$ (%)	δ_{cor}^{h+} (%)	δ_{cor}^{N+} (%)	δ_{cor}^{B+} (%)
650	0.0130	0.4941	0.836	4.4	4.4	6.2	3.6	0.6	1.3	2.4	1.4	-1.5	1.3	0.2	0.4
650	0.0200	0.3211	0.797	4.2	4.9	6.5	4.5	1.0	2.7	2.0	1.3	-0.9	0.6	1.1	0.2
650	0.0320	0.2007	0.672	4.2	4.0	5.9	3.6	1.0	0.9	1.9	1.2	-1.1	0.6	0.8	0.1
650	0.0500	0.1285	0.610	4.4	5.0	6.7	4.2	1.5	1.2	2.9	1.1	1.8	1.0	1.6	0.1
650	0.0800	0.0803	0.459	5.1	5.0	7.2	3.9	1.8	0.6	3.1	1.6	-1.7	-0.7	1.9	0.0
650	0.1300	0.0494	0.386	5.9	4.8	7.6	3.8	1.4	1.0	3.0	1.5	1.9	1.6	0.8	0.0
650	0.1800	0.0357	0.330	7.1	7.6	10.4	6.0	4.2	2.4	4.7	2.6	-1.9	-1.9	-2.9	0.0
650	0.2500	0.0257	0.204	9.5	11.1	14.6	6.8	3.5	3.2	8.7	5.1	5.2	2.9	3.8	0.0
650	0.4000	0.0161	0.134	10.4	14.4	17.8	8.5	6.7	3.8	11.6	2.9	-1.6	-3.3	-10.6	0.0
800	0.0080	0.9881	0.928	11.8	8.8	14.7	7.3	2.6	4.9	4.8	-0.2	-2.2	-2.2	-2.6	2.6
800	0.0130	0.6081	0.854	5.5	5.1	7.5	4.5	1.5	1.4	2.4	-0.2	-1.5	1.2	-1.2	0.8
800	0.0200	0.3953	0.710	5.3	4.6	7.0	3.7	0.2	1.5	2.6	1.6	-0.8	1.5	1.0	0.2
800	0.0320	0.2470	0.641	5.1	4.9	7.0	4.2	1.7	1.8	2.5	-1.6	-1.0	-1.2	-1.1	0.1
800	0.0500	0.1581	0.530	5.4	5.7	7.9	4.9	2.8	1.6	2.9	2.1	-1.7	0.3	1.2	0.1
800	0.0800	0.0988	0.434	6.2	5.0	8.0	4.4	2.7	0.5	2.5	0.9	1.8	-0.6	1.3	0.1
800	0.1300	0.0608	0.403	6.8	5.0	8.5	4.3	2.3	1.2	2.7	2.1	-1.1	0.1	1.1	0.0
800	0.1800	0.0439	0.304	8.3	8.3	11.8	6.6	4.7	1.9	5.1	4.2	-1.8	-1.8	-1.1	0.0
800	0.2500	0.0316	0.234	10.7	9.2	14.1	7.6	5.3	4.4	5.2	-2.7	-2.0	-3.9	-0.9	0.0
800	0.4000	0.0198	0.120	12.7	11.0	16.8	6.5	4.2	3.6	8.8	3.2	0.3	2.0	-8.0	0.0
1000	0.0130	0.7601	0.791	7.8	4.7	9.0	3.8	0.6	1.1	2.7	-1.6	-0.9	-1.2	0.6	1.4
1000	0.0200	0.4941	0.679	6.2	4.6	7.8	4.1	1.3	2.0	2.1	-1.3	-0.7	1.2	-0.8	0.3
1000	0.0320	0.3088	0.656	5.8	4.5	7.3	3.8	1.2	0.8	2.4	1.6	0.4	1.0	1.4	0.2
1000	0.0500	0.1976	0.560	5.9	4.0	7.1	3.5	0.8	0.3	1.9	-0.7	1.4	0.8	0.7	0.1
1000	0.0800	0.1235	0.470	6.8	5.1	8.5	4.1	2.0	1.2	3.0	2.0	-1.0	1.6	1.1	0.1
1000	0.1300	0.0760	0.377	8.0	5.1	9.5	4.4	1.7	2.2	2.4	-0.9	-1.5	0.8	1.5	0.0
1000	0.1800	0.0549	0.300	8.9	4.8	10.2	3.9	1.6	1.0	2.9	1.8	-1.0	-1.8	-0.8	0.0
1000	0.2500	0.0395	0.294	10.0	8.8	13.3	7.9	5.6	3.0	3.8	2.0	0.4	0.6	-3.1	0.0
1000	0.4000	0.0247	0.132	13.6	7.3	15.4	4.8	2.7	2.1	5.5	2.8	-3.4	-2.0	-2.7	0.0

Q^2 (GeV ²)	x	y	$\tilde{\sigma}_{NC}$	δ_{stat} (%)	δ_{sys} (%)	δ_{tot} (%)	δ_{unc} (%)	δ_{unc}^E (%)	δ_{unc}^h (%)	δ_{cor} (%)	δ_{cor}^{E+} (%)	$\delta_{cor}^{\theta+}$ (%)	δ_{cor}^{h+} (%)	δ_{cor}^{N+} (%)	δ_{cor}^{B+} (%)
1200	0.0130	0.9121	0.760	13.6	6.7	15.1	5.1	1.8	3.0	4.3	-1.2	-1.2	-2.7	1.9	2.2
1200	0.0200	0.5929	0.739	7.7	5.0	9.1	4.1	0.7	0.8	2.8	1.9	1.1	1.6	0.4	0.7
1200	0.0320	0.3706	0.627	7.0	4.4	8.2	3.9	0.5	1.8	1.9	1.0	-0.8	1.2	0.8	0.2
1200	0.0500	0.2372	0.539	6.9	4.0	8.0	3.7	1.2	0.8	1.5	-0.4	-0.9	0.9	0.7	0.1
1200	0.0800	0.1482	0.445	7.5	4.0	8.4	3.7	1.6	0.2	1.3	0.4	-0.4	0.9	-0.7	0.1
1200	0.1300	0.0912	0.402	8.6	4.9	9.9	4.2	2.4	0.7	2.6	0.9	-0.9	-1.7	1.5	0.0
1200	0.1800	0.0659	0.320	9.8	5.2	11.1	4.3	2.4	0.9	2.9	1.9	-1.9	-0.2	-1.1	0.0
1200	0.2500	0.0474	0.243	11.9	7.6	14.1	6.1	3.9	2.4	4.6	2.9	1.8	2.7	-1.4	0.0
1200	0.4000	0.0296	0.114	16.5	7.6	18.1	5.6	4.0	1.9	5.1	2.5	-2.3	-1.5	-3.5	0.0
1200	0.6500	0.0182	0.0137	30.2	24.6	38.9	13.9	11.0	6.7	20.3	7.0	-2.2	-5.2	-18.2	0.0
1500	0.0200	0.7411	0.648	10.2	5.8	11.7	4.4	1.1	1.1	3.7	-1.7	-1.9	-1.9	-1.5	1.1
1500	0.0320	0.4632	0.539	9.1	5.4	10.6	4.2	1.1	1.1	3.4	-2.3	-1.8	-1.1	1.0	0.3
1500	0.0500	0.2964	0.459	8.6	4.3	9.6	3.7	0.7	1.0	2.2	-0.5	-0.6	-1.6	-1.3	0.1
1500	0.0800	0.1853	0.473	8.3	5.5	10.0	5.1	3.7	0.8	2.0	1.2	-1.1	-1.2	0.4	0.1
1500	0.1300	0.1140	0.345	10.7	5.3	11.9	4.8	2.0	1.7	2.2	-1.1	-0.7	-1.1	1.3	0.1
1500	0.1800	0.0823	0.323	10.6	5.8	12.1	4.4	2.9	0.2	3.7	2.0	-1.8	-1.6	2.1	0.0
1500	0.2500	0.0593	0.263	12.3	8.0	14.7	7.1	5.6	2.6	3.6	3.4	-0.3	-0.4	-1.2	0.0
1500	0.4000	0.0371	0.117	18.6	8.1	20.3	6.8	5.3	2.7	4.4	1.7	0.8	-2.8	-2.8	0.0
1500	0.6500	0.0228	0.0121	35.4	26.8	44.4	12.8	8.6	8.7	23.5	10.1	-4.6	-3.3	-20.5	0.0
2000	0.0200	0.9881	0.652	17.1	7.4	18.6	6.0	1.7	4.3	4.2	2.1	1.6	-2.5	1.3	1.8
2000	0.0320	0.6176	0.520	10.7	4.6	11.7	4.3	0.4	1.6	1.4	1.0	-0.1	0.8	-0.3	0.6
2000	0.0500	0.3953	0.510	10.1	5.3	11.4	4.8	0.8	2.4	2.3	0.3	1.4	1.3	1.3	0.2
2000	0.0800	0.2470	0.438	9.6	5.3	11.0	4.7	2.3	0.6	2.4	1.0	-1.7	1.1	-0.9	0.1
2000	0.1300	0.1520	0.399	11.4	5.4	12.6	4.5	2.1	0.7	3.0	2.1	-0.8	1.3	-1.5	0.1
2000	0.1800	0.1098	0.297	13.0	4.2	13.7	3.8	0.6	1.0	1.9	0.7	0.3	0.3	1.7	0.1
2000	0.2500	0.0791	0.332	12.3	7.8	14.6	6.6	5.0	2.6	4.1	-0.6	-1.0	-2.2	-3.3	0.0
2000	0.4000	0.0494	0.144	18.6	10.6	21.4	8.8	6.4	4.9	5.8	4.4	-2.4	-2.0	2.2	0.0
2000	0.6500	0.0304	0.0266	30.2	26.8	40.3	15.2	13.6	5.9	22.0	8.1	3.2	-7.0	-19.0	0.0

Q^2 (GeV ²)	x	y	$\tilde{\sigma}_{NC}$	δ_{stat} (%)	δ_{sys} (%)	δ_{tot} (%)	δ_{unc} (%)	δ_{unc}^E (%)	δ_{unc}^h (%)	δ_{cor} (%)	δ_{cor}^{E+} (%)	$\delta_{cor}^{\theta+}$ (%)	δ_{cor}^{h+} (%)	δ_{cor}^{N+} (%)	δ_{cor}^{B+} (%)
3000	0.0320	0.9264	0.617	10.5	5.1	11.7	4.2	1.3	1.4	2.9	1.5	-1.8	-1.0	0.9	1.2
3000	0.0500	0.5929	0.511	8.6	5.2	10.0	4.9	1.4	2.1	1.6	-0.4	-0.4	1.1	0.8	0.4
3000	0.0800	0.3706	0.484	8.7	4.2	9.7	3.8	0.5	0.5	1.9	1.2	-1.0	0.9	-0.2	0.2
3000	0.1300	0.2280	0.318	11.4	6.1	13.0	4.6	2.8	0.6	4.0	2.9	2.3	0.8	1.4	0.1
3000	0.1800	0.1647	0.310	12.2	5.6	13.4	5.1	3.1	1.6	2.2	1.1	-1.6	1.0	-0.6	0.1
3000	0.2500	0.1186	0.221	13.4	6.1	14.7	4.8	2.6	0.8	3.7	2.8	0.9	0.6	2.2	0.0
3000	0.4000	0.0741	0.0892	19.6	11.8	22.9	10.3	8.5	3.0	5.9	-2.5	-3.0	-2.3	-3.8	0.0
3000	0.6500	0.0456	0.0104	40.9	21.8	46.4	13.6	10.6	7.1	17.0	10.9	5.8	6.0	-10.0	0.0
5000	0.0500	0.9881	0.480	14.5	5.1	15.4	4.2	1.3	1.2	2.8	-1.2	-1.3	-1.4	-0.5	1.7
5000	0.0800	0.6176	0.470	9.9	5.3	11.3	5.0	2.2	2.2	1.8	0.6	-1.0	1.2	0.6	0.4
5000	0.1300	0.3801	0.425	11.1	3.8	11.7	3.6	0.3	0.4	1.3	0.3	-0.2	0.9	0.8	0.2
5000	0.1800	0.2745	0.315	13.2	5.4	14.2	5.2	2.6	1.3	1.4	-0.6	-0.9	-0.8	0.0	0.1
5000	0.2500	0.1976	0.241	15.5	6.7	16.9	6.2	3.0	1.2	2.7	2.2	-1.4	-0.6	-0.5	0.1
5000	0.4000	0.1235	0.0752	25.0	10.4	27.1	8.9	7.4	3.6	5.3	3.8	2.0	-1.6	-2.7	0.0
5000	0.6500	0.0760	0.0165	40.9	33.8	53.0	31.8	30.2	6.7	11.4	7.7	-5.2	-4.2	-5.0	0.0
8000	0.0800	0.9881	0.390	24.8	6.8	25.7	5.9	3.9	2.3	3.4	-0.3	-1.3	-1.4	-1.0	2.6
8000	0.1300	0.6081	0.393	16.0	5.1	16.8	4.8	2.0	2.0	1.7	-0.5	-1.0	1.0	0.8	0.5
8000	0.1800	0.4392	0.282	17.5	6.6	18.7	6.5	5.1	0.9	1.6	0.8	-1.0	0.6	0.6	0.2
8000	0.2500	0.3162	0.136	25.1	7.9	26.3	7.5	6.5	0.5	2.5	2.0	1.0	-0.1	1.0	0.1
8000	0.4000	0.1976	0.110	25.1	11.4	27.5	11.2	10.4	1.5	1.8	1.1	0.8	1.2	0.2	0.1
8000	0.6500	0.1216	0.0227	40.9	41.9	58.5	39.3	36.9	12.4	14.4	8.4	4.8	-5.5	-9.2	0.1
12000	0.1300	0.9121	0.104	88.1	10.4	88.7	8.3	7.0	2.4	6.3	3.4	-2.1	3.6	-1.6	2.9
12000	0.1800	0.6588	0.264	28.4	5.5	28.9	5.0	3.2	0.4	2.2	-1.3	-0.8	-1.1	0.5	0.8
12000	0.2500	0.4743	0.122	35.8	8.0	36.7	7.8	6.6	1.5	1.9	1.6	-0.2	0.9	0.4	0.3
12000	0.4000	0.2964	0.174	27.8	16.0	32.0	15.4	14.9	0.1	4.1	3.8	1.4	-0.1	0.2	0.1
12000	0.6500	0.1824	0.0340	44.8	35.1	56.9	34.2	33.8	4.1	7.7	5.8	4.3	-2.1	-1.8	0.0
20000	0.2500	0.7905	0.119	59.7	5.2	59.9	4.9	3.1	0.0	1.7	0.5	-1.3	0.0	0.1	0.9
20000	0.4000	0.4941	0.149	41.1	14.5	43.5	14.2	13.6	1.6	2.5	2.0	1.0	1.0	0.3	0.3

Q^2 (GeV ²)	x	y	$\tilde{\sigma}_{NC}$	δ_{stat} (%)	δ_{sys} (%)	δ_{tot} (%)	δ_{unc} (%)	δ_{unc}^E (%)	δ_{unc}^h (%)	δ_{cor} (%)	$\delta_{cor}^{E^+}$ (%)	$\delta_{cor}^{\theta^+}$ (%)	$\delta_{cor}^{h^+}$ (%)	$\delta_{cor}^{N^+}$ (%)	$\delta_{cor}^{B^+}$ (%)
200	0.0032	0.6176	1.288	3.0	3.8	4.9	3.5	0.5	1.0	1.6	-0.6	-0.8	-0.6	0.2	0.9
200	0.0050	0.3953	1.158	2.4	4.8	5.4	3.9	1.0	1.0	2.8	-1.0	-1.7	-1.3	-1.4	0.3
200	0.0080	0.2470	1.019	2.3	4.1	4.7	3.5	0.2	1.0	2.1	0.4	-1.7	0.3	1.2	0.1
200	0.0130	0.1520	0.822	2.5	4.2	4.9	3.5	0.1	0.5	2.3	-1.0	-1.8	0.3	1.2	0.1
200	0.0200	0.0988	0.688	2.9	5.4	6.1	4.1	1.6	1.7	3.5	-0.3	-2.2	-1.6	-2.2	0.1
200	0.0320	0.0618	0.643	3.4	4.8	5.9	4.2	0.6	1.7	2.3	-1.4	-1.3	0.7	1.0	0.0
200	0.0500	0.0395	0.517	3.9	9.7	10.5	6.4	3.8	3.2	7.4	4.1	3.6	3.3	3.6	0.0
200	0.0800	0.0247	0.386	4.9	5.6	7.4	3.9	1.6	0.7	4.1	-1.3	-3.2	-1.1	-1.8	0.0
200	0.1300	0.0152	0.320	6.3	7.0	9.4	4.3	1.4	2.1	5.6	-4.0	-3.1	2.1	0.9	0.0
250	0.0050	0.4941	1.188	2.7	4.0	4.9	3.8	0.7	1.6	1.5	-0.4	-0.8	0.8	0.7	0.5
250	0.0080	0.3088	1.090	2.6	4.2	4.9	3.7	0.7	1.2	1.9	-0.6	-1.0	0.7	-1.2	0.2
250	0.0130	0.1900	0.782	2.8	5.2	5.9	4.4	1.7	1.5	2.9	1.3	-1.6	1.0	1.7	0.1
250	0.0200	0.1235	0.723	2.7	4.2	5.0	3.7	0.7	1.3	1.9	-0.7	-1.6	-0.2	0.6	0.1
250	0.0320	0.0772	0.582	3.2	4.3	5.3	3.8	0.8	1.2	2.0	1.4	-0.9	-0.6	-0.9	0.0
250	0.0500	0.0494	0.564	3.3	5.1	6.0	3.5	1.0	0.2	3.7	-1.4	-1.5	-1.0	2.9	0.0
250	0.0800	0.0309	0.457	3.6	5.0	6.1	4.0	1.8	1.1	3.0	0.6	-1.6	-1.2	-2.1	0.0
250	0.1300	0.0190	0.341	4.8	5.6	7.4	4.8	2.9	1.6	2.8	1.0	-2.4	-0.9	0.3	0.0
250	0.1800	0.0137	0.329	5.3	6.8	8.6	5.1	1.5	1.5	4.4	2.1	-1.9	-2.7	-2.2	0.0
300	0.0050	0.5929	1.145	3.8	3.9	5.4	3.5	0.5	0.8	1.7	-0.5	-1.4	-0.4	0.1	0.7

Table C.2: The NC e^+p double differential cross section $d^2\sigma_{NC}/dQ^2dx$ for LH polarised positrons ($P_e = -40.2\%$) with the statistical (δ_{stat}), systematic (δ_{sys}) and total (δ_{tot}) errors. Also shown are the total uncorrelated systematic (δ_{unc}) errors and two of its contributions: the electron energy error (δ_{unc}^E) and the hadronic energy error (δ_{unc}^h). The effect of the other uncorrelated systematic errors is included in (δ_{unc}). The table also provides the correlated systematic error (δ_{cor}) and its contributions from a positive variation of one standard deviation of the error on the electron energy ($\delta_{cor}^{E^+}$) and polar angle ($\delta_{cor}^{\theta^+}$), of the hadronic energy error ($\delta_{cor}^{h^+}$), of the error due to noise subtraction ($\delta_{cor}^{N^+}$) and background subtraction ($\delta_{cor}^{B^+}$) (δ_{unc}^h). The effect of the other correlated systematic errors is included in (δ_{cor}). The normalisation uncertainty of 1.4% is not included in the errors. The table continues on the next 4 pages.

Q^2 (GeV ²)	x	y	$\tilde{\sigma}_{NC}$	δ_{stat} (%)	δ_{sys} (%)	δ_{tot} (%)	δ_{unc} (%)	δ_{unc}^E (%)	δ_{unc}^h (%)	δ_{cor} (%)	$\delta_{cor}^{E^+}$ (%)	$\delta_{cor}^{\theta^+}$ (%)	$\delta_{cor}^{h^+}$ (%)	$\delta_{cor}^{N^+}$ (%)	$\delta_{cor}^{B^+}$ (%)
300	0.0080	0.3706	0.997	3.1	4.1	5.2	3.8	0.2	1.7	1.7	0.5	-1.4	0.7	0.6	0.2
300	0.0130	0.2280	0.916	3.0	3.9	4.9	3.6	0.9	0.6	1.6	0.5	-1.0	1.1	0.4	0.1
300	0.0200	0.1482	0.736	3.2	4.9	5.8	3.8	1.5	0.4	3.1	1.0	-2.6	0.5	1.3	0.1
300	0.0320	0.0926	0.608	3.4	5.3	6.3	4.1	2.2	0.6	3.4	1.6	-2.6	-0.6	1.4	0.0
300	0.0500	0.0593	0.586	3.8	4.9	6.2	4.2	2.5	0.5	2.5	1.0	-1.6	-0.4	1.7	0.0
300	0.0800	0.0371	0.520	3.7	4.6	5.9	3.8	1.4	0.9	2.6	-0.6	-1.2	-0.7	2.1	0.0
300	0.1300	0.0228	0.372	5.1	9.0	10.4	6.8	4.9	2.7	6.0	3.3	3.0	3.0	2.7	0.0
300	0.1800	0.0165	0.289	6.4	6.9	9.4	5.4	3.0	1.5	4.3	-2.7	-2.3	-1.4	-1.8	0.0
400	0.0050	0.7905	1.288	5.9	5.1	7.8	4.0	1.6	0.9	3.1	1.8	1.6	1.0	1.2	1.2
400	0.0080	0.4941	0.998	3.8	4.2	5.7	3.7	0.7	1.3	1.9	-0.3	-1.0	1.6	0.3	0.5
400	0.0130	0.3040	0.887	3.6	4.0	5.4	3.8	1.3	1.3	1.4	0.3	-1.2	-0.2	0.8	0.2
400	0.0200	0.1976	0.774	3.5	3.6	5.1	3.5	0.5	0.5	1.1	0.1	-0.9	-0.2	0.5	0.1
400	0.0320	0.1235	0.582	3.8	4.4	5.9	3.9	1.8	0.3	2.2	1.2	-1.6	0.7	0.6	0.1
400	0.0500	0.0791	0.548	4.2	5.3	6.8	4.4	2.2	1.0	3.0	1.2	1.4	1.2	2.0	0.1
400	0.0800	0.0494	0.479	4.2	5.2	6.7	4.3	1.8	1.4	3.0	-1.4	-1.8	-0.8	-1.8	0.0
400	0.1300	0.0304	0.362	5.5	6.6	8.6	5.2	3.4	1.9	4.1	3.6	-1.4	-1.0	0.9	0.0
400	0.1800	0.0220	0.302	7.1	6.0	9.3	5.3	3.7	1.8	2.9	2.0	-1.7	0.3	1.3	0.0
400	0.2500	0.0158	0.238	7.6	7.8	10.9	4.7	2.9	1.4	6.3	0.7	-2.4	-1.2	-5.6	0.0
500	0.0080	0.6176	1.067	4.8	4.7	6.7	4.3	1.3	1.7	2.0	-0.6	-1.3	-0.7	0.8	0.8
500	0.0130	0.3801	0.864	4.2	4.1	5.9	3.7	0.7	1.0	1.7	0.5	-0.9	0.7	1.2	0.2
500	0.0200	0.2470	0.775	4.1	3.9	5.7	3.6	0.9	1.0	1.4	0.6	-0.9	0.5	0.6	0.1
500	0.0320	0.1544	0.605	4.4	3.8	5.8	3.6	1.3	0.5	1.3	-0.8	-0.6	-0.7	0.3	0.1
500	0.0500	0.0988	0.570	4.6	5.7	7.3	4.8	3.2	1.0	2.9	2.0	-1.5	0.4	1.4	0.1
500	0.0800	0.0618	0.454	5.6	4.7	7.3	3.6	0.7	0.6	3.0	-1.0	-1.3	-0.3	2.5	0.0
500	0.1300	0.0380	0.427	5.6	5.2	7.7	4.6	3.1	0.2	2.4	1.3	-1.4	-0.6	-1.2	0.0
500	0.1800	0.0274	0.351	7.2	8.6	11.2	6.8	5.6	2.2	5.2	3.2	-2.3	-2.3	-2.5	0.0
500	0.2500	0.0198	0.205	9.1	5.1	10.5	4.1	1.5	1.4	3.0	-1.8	-1.7	-1.1	1.3	0.0
650	0.0080	0.8029	1.017	6.9	4.9	8.5	4.0	1.8	1.2	2.8	-1.3	-1.5	-0.4	1.4	1.2

Q^2 (GeV ²)	x	y	$\tilde{\sigma}_{NC}$	δ_{stat} (%)	δ_{sys} (%)	δ_{tot} (%)	δ_{unc} (%)	δ_{unc}^E (%)	δ_{unc}^h (%)	δ_{cor} (%)	δ_{cor}^{E+} (%)	$\delta_{cor}^{\theta+}$ (%)	δ_{cor}^{h+} (%)	δ_{cor}^{N+} (%)	δ_{cor}^{B+} (%)
650	0.0130	0.4941	0.903	4.9	4.3	6.5	3.6	0.6	1.2	2.3	1.3	-1.4	1.2	0.2	0.4
650	0.0200	0.3211	0.756	5.0	4.9	7.0	4.5	1.2	2.6	2.0	1.3	-0.9	0.7	1.1	0.2
650	0.0320	0.2007	0.610	5.1	4.2	6.6	3.6	1.1	1.0	2.0	1.3	-1.2	0.6	-0.8	0.1
650	0.0500	0.1285	0.530	5.5	5.1	7.5	4.2	1.6	1.2	2.9	1.2	2.0	1.0	1.4	0.1
650	0.0800	0.0803	0.429	6.1	5.0	7.9	3.9	1.8	0.5	3.1	1.6	-1.6	-0.6	2.0	0.0
650	0.1300	0.0494	0.381	6.6	4.7	8.1	3.8	1.4	1.0	2.8	1.5	1.9	1.4	0.7	0.0
650	0.1800	0.0357	0.284	8.7	7.6	11.5	6.0	4.1	2.4	4.7	2.8	-1.8	-1.8	-2.8	0.0
650	0.2500	0.0257	0.228	10.4	11.4	15.4	7.0	3.7	3.4	9.0	5.2	5.4	3.0	4.0	0.0
650	0.4000	0.0161	0.125	12.1	14.5	18.9	8.2	6.6	3.3	11.9	2.8	-1.5	-3.3	-11.0	0.0
800	0.0080	0.9881	0.964	13.1	8.7	15.7	7.0	2.1	4.7	5.2	-0.8	-2.0	-2.6	-2.9	2.7
800	0.0130	0.6081	0.804	6.4	5.1	8.2	4.5	1.4	1.4	2.4	-0.2	-1.5	1.2	-1.1	0.8
800	0.0200	0.3953	0.665	6.2	4.6	7.7	3.8	0.2	1.6	2.6	1.7	0.6	1.5	1.0	0.2
800	0.0320	0.2470	0.612	5.9	5.1	7.8	4.2	1.9	1.8	2.9	-2.0	-0.9	-1.4	-1.2	0.1
800	0.0500	0.1581	0.551	6.0	5.5	8.1	4.8	2.8	1.5	2.7	1.8	-1.5	0.4	1.1	0.1
800	0.0800	0.0988	0.468	6.9	5.0	8.6	4.4	2.6	0.7	2.5	1.1	1.8	-0.6	1.2	0.1
800	0.1300	0.0608	0.389	7.8	4.8	9.2	4.2	2.2	1.0	2.4	1.7	-1.3	0.1	1.1	0.0
800	0.1800	0.0439	0.289	9.7	8.0	12.6	6.3	4.6	1.8	4.9	4.1	-1.8	-1.7	-1.1	0.0
800	0.2500	0.0316	0.180	13.9	8.2	16.2	7.1	5.1	3.6	4.2	-1.9	-1.7	-3.3	0.3	0.0
800	0.4000	0.0198	0.102	15.6	10.9	19.0	6.5	4.2	3.7	8.7	3.0	-0.6	1.3	-8.1	0.0
1000	0.0130	0.7601	0.796	8.9	4.6	10.0	3.8	0.4	1.2	2.6	-1.5	-0.8	-1.0	0.6	1.5
1000	0.0200	0.4941	0.762	6.6	4.6	8.1	4.2	1.3	2.1	2.0	-1.2	-0.7	1.3	-0.7	0.3
1000	0.0320	0.3088	0.676	6.6	4.4	7.9	3.7	1.2	0.8	2.4	1.7	0.7	0.8	1.3	0.2
1000	0.0500	0.1976	0.531	7.0	4.0	8.0	3.5	0.8	0.3	1.9	-0.6	1.5	0.8	0.6	0.1
1000	0.0800	0.1235	0.473	7.8	5.1	9.3	4.1	2.1	0.9	3.1	2.0	-1.3	1.6	1.1	0.1
1000	0.1300	0.0760	0.373	9.2	4.9	10.4	4.2	1.3	1.9	2.6	-1.0	-1.3	0.7	1.8	0.0
1000	0.1800	0.0549	0.271	10.9	5.2	12.0	4.2	2.0	1.0	3.1	2.1	-1.1	-1.9	-0.6	0.0
1000	0.2500	0.0395	0.205	14.0	8.4	16.3	7.5	5.3	2.8	3.7	1.8	0.5	0.7	-3.1	0.0
1000	0.4000	0.0247	0.0967	18.3	7.7	19.8	5.1	3.0	2.3	5.8	2.9	-3.8	-2.0	-2.4	0.0

Q^2 (GeV ²)	x	y	$\tilde{\sigma}_{NC}$	δ_{stat} (%)	δ_{sys} (%)	δ_{tot} (%)	δ_{unc} (%)	δ_{unc}^E (%)	δ_{unc}^h (%)	δ_{cor} (%)	δ_{cor}^{E+} (%)	$\delta_{cor}^{\theta+}$ (%)	δ_{cor}^{h+} (%)	δ_{cor}^{N+} (%)	δ_{cor}^{B+} (%)
1200	0.0130	0.9121	0.703	16.1	6.3	17.3	4.7	1.2	2.7	4.2	-0.9	-1.3	-2.6	1.4	2.4
1200	0.0200	0.5929	0.686	8.9	4.8	10.1	4.1	0.8	0.7	2.5	1.6	1.0	1.4	0.2	0.7
1200	0.0320	0.3706	0.645	7.9	4.5	9.1	4.0	0.8	1.8	2.0	1.0	-0.8	1.1	0.9	0.2
1200	0.0500	0.2372	0.498	8.2	4.1	9.2	3.8	1.2	0.9	1.6	-0.2	-0.9	1.1	0.7	0.1
1200	0.0800	0.1482	0.409	8.9	3.9	9.7	3.7	1.6	0.1	1.1	0.4	-0.4	0.8	-0.6	0.1
1200	0.1300	0.0912	0.358	10.7	4.9	11.7	4.1	2.2	0.6	2.7	0.9	-0.9	-1.6	1.7	0.1
1200	0.1800	0.0659	0.317	11.2	5.2	12.4	4.4	2.5	1.1	2.9	1.9	-1.7	-0.6	-1.1	0.0
1200	0.2500	0.0474	0.238	13.8	7.9	15.9	6.2	4.1	2.4	4.9	2.8	2.1	2.9	-1.8	0.0
1200	0.4000	0.0296	0.146	16.7	7.7	18.4	5.7	4.2	1.9	5.2	2.5	-2.4	-1.2	-3.7	0.0
1200	0.6500	0.0182	0.0180	30.2	24.2	38.7	13.4	10.5	6.4	20.1	6.3	-2.4	-5.2	-18.2	0.0
1500	0.0200	0.7411	0.728	15.6	5.8	16.7	4.5	1.2	1.1	3.8	-1.6	-2.0	-2.1	-1.4	1.2
1500	0.0320	0.4632	0.558	10.2	5.2	11.5	4.2	0.8	1.3	3.0	-2.1	-1.7	0.9	0.9	0.3
1500	0.0500	0.2964	0.603	8.7	4.4	9.7	3.8	0.9	1.1	2.2	-0.7	-0.6	-1.6	-1.3	0.2
1500	0.0800	0.1853	0.537	11.8	5.6	13.1	5.2	3.9	0.7	2.1	1.4	-1.2	-1.0	0.3	0.1
1500	0.1300	0.1140	0.379	12.0	5.0	13.0	4.6	1.7	1.7	2.1	-0.8	-0.6	-0.9	1.6	0.1
1500	0.1800	0.0823	0.344	12.4	5.7	13.7	4.4	2.8	0.3	3.7	1.9	-1.7	-1.6	2.2	0.0
1500	0.2500	0.0593	0.199	16.2	7.8	18.0	7.0	5.6	2.6	3.3	3.0	-0.3	-0.5	-1.2	0.0
1500	0.4000	0.0371	0.133	20.0	7.8	21.5	6.4	4.8	2.6	4.4	1.6	-0.7	-2.9	-2.8	0.0
1500	0.6500	0.0228	0.0118	40.9	27.2	49.1	13.0	9.0	8.4	23.9	10.1	-4.8	-3.3	-20.8	0.0
2000	0.0200	0.9881	0.554	21.7	7.6	23.0	6.1	1.8	4.3	4.5	2.3	1.7	-2.4	1.4	2.1
2000	0.0320	0.6176	0.603	11.6	4.6	12.4	4.2	0.5	1.5	1.6	1.0	0.1	0.9	-0.6	0.7
2000	0.0500	0.3953	0.590	10.8	5.1	12.0	4.7	0.7	2.4	2.0	0.4	1.1	1.1	1.1	0.3
2000	0.0800	0.2470	0.381	12.0	5.3	13.1	4.7	2.0	0.6	2.4	1.0	-1.8	1.0	0.7	0.1
2000	0.1300	0.1520	0.331	14.6	5.4	15.6	4.7	2.3	0.5	2.8	2.2	-0.4	1.3	-1.0	0.1
2000	0.1800	0.1098	0.355	13.9	4.2	14.5	3.8	0.8	1.0	1.6	0.3	-0.1	0.2	1.6	0.1
2000	0.2500	0.0791	0.279	15.6	7.8	17.5	6.7	5.2	2.5	4.0	0.7	-1.1	-2.4	-2.9	0.0
2000	0.4000	0.0494	0.0668	31.7	10.6	33.4	9.0	6.8	4.7	5.5	4.2	-2.2	-2.2	1.8	0.0
2000	0.6500	0.0304	0.0170	44.8	27.8	52.7	15.4	14.0	5.0	23.2	8.2	4.0	-7.0	-20.1	0.0

Q^2 (GeV ²)	x	y	$\tilde{\sigma}_{NC}$	δ_{stat} (%)	δ_{sys} (%)	δ_{tot} (%)	δ_{unc} (%)	δ_{unc}^E (%)	δ_{unc}^h (%)	δ_{cor} (%)	δ_{cor}^{E+} (%)	$\delta_{cor}^{\theta+}$ (%)	δ_{cor}^{h+} (%)	δ_{cor}^{N+} (%)	δ_{cor}^{B+} (%)
3000	0.0320	0.9264	0.647	11.7	5.0	12.7	4.1	1.2	1.4	2.9	1.3	-1.8	-0.9	0.9	1.3
3000	0.0500	0.5929	0.495	10.0	5.2	11.3	5.0	1.4	2.2	1.6	0.4	-0.4	1.1	1.0	0.5
3000	0.0800	0.3706	0.389	11.1	4.2	11.9	3.8	0.6	0.6	1.8	1.3	-0.9	0.9	-0.2	0.2
3000	0.1300	0.2280	0.380	11.9	6.1	13.4	4.8	3.0	0.4	3.7	2.8	2.1	0.5	1.2	0.1
3000	0.1800	0.1647	0.315	13.8	5.5	14.8	5.0	3.0	1.7	2.3	1.2	-1.3	1.4	-0.4	0.1
3000	0.2500	0.1186	0.256	14.2	6.3	15.5	4.9	2.5	0.9	4.0	2.8	1.3	0.8	2.4	0.1
3000	0.4000	0.0741	0.123	19.3	12.0	22.7	10.5	8.7	3.2	5.8	-2.2	-3.0	-2.2	-3.8	0.0
3000	0.6500	0.0456	0.0162	37.8	22.4	44.0	13.1	10.4	6.4	18.1	11.0	6.1	6.5	-11.2	0.0
5000	0.0500	0.9881	0.525	15.5	5.2	16.4	4.3	1.6	1.3	3.0	-1.1	-1.2	-1.4	-0.5	2.0
5000	0.0800	0.6176	0.350	13.1	5.6	14.3	5.2	2.5	2.2	2.0	0.8	-1.0	1.3	0.7	0.5
5000	0.1300	0.3801	0.404	13.0	3.7	13.5	3.5	0.3	0.3	1.2	-0.3	-0.4	0.8	0.7	0.2
5000	0.1800	0.2745	0.228	17.8	5.4	18.6	5.2	2.6	1.4	1.3	-0.5	-1.0	-0.7	0.3	0.1
5000	0.2500	0.1976	0.268	16.7	7.1	18.1	6.4	3.1	1.5	3.0	2.3	-1.3	-0.9	-1.2	0.1
5000	0.4000	0.1235	0.0740	28.9	10.4	30.8	9.2	7.7	3.7	5.0	3.6	2.0	-1.8	-2.3	0.0
5000	0.6500	0.0760	0.0108	57.8	32.6	66.4	30.5	28.9	7.0	11.4	8.2	-5.4	-3.6	-4.8	0.0
8000	0.0800	0.9881	0.322	30.3	7.0	31.1	5.8	3.7	2.3	3.9	-0.6	-1.5	-1.5	-1.0	3.0
8000	0.1300	0.6081	0.198	25.6	5.4	26.2	5.2	2.8	2.0	1.7	-0.4	-0.8	1.0	0.9	0.6
8000	0.1800	0.4392	0.243	21.4	6.6	22.4	6.4	5.0	1.0	1.7	0.8	-1.0	0.7	0.6	0.2
8000	0.2500	0.3162	0.263	20.5	7.7	21.9	7.3	6.3	0.4	2.5	2.1	0.8	-0.4	1.0	0.1
8000	0.4000	0.1976	0.107	28.9	10.9	30.9	10.8	10.0	1.4	1.6	1.0	0.7	1.0	0.2	0.1
8000	0.6500	0.1216	0.0098	70.9	43.1	83.0	40.2	37.9	12.4	15.6	9.5	5.9	-5.6	-9.3	0.1
12000	0.1300	0.9121	0.217	64.2	10.5	65.1	8.0	6.7	2.2	6.8	3.4	-2.0	3.9	-1.5	3.6
12000	0.1800	0.6588	0.235	34.2	5.8	34.7	5.4	3.7	0.4	2.3	-1.3	-0.8	-1.3	0.5	1.0
12000	0.2500	0.4743	0.159	35.7	8.0	36.6	7.7	6.5	1.5	1.9	1.5	-0.3	0.9	0.4	0.3
12000	0.4000	0.2964	0.0170	101.8	15.9	103.0	15.4	14.9	0.0	4.0	3.8	1.3	-0.1	0.2	0.1
12000	0.6500	0.1824	0.0177	70.8	34.8	78.9	33.9	33.5	4.0	7.7	5.8	4.2	-2.1	-1.8	0.0

Q^2 (GeV ²)	x	y	$\tilde{\sigma}_{NC}$	δ_{stat} (%)	δ_{sys} (%)	δ_{tot} (%)	δ_{unc} (%)	δ_{unc}^E (%)	δ_{unc}^h (%)	δ_{cor} (%)	δ_{cor}^{E+} (%)	$\delta_{cor}^{\theta+}$ (%)	δ_{cor}^{h+} (%)	δ_{cor}^{N+} (%)	δ_{cor}^{B+} (%)
200	0.0032	0.6176	1.310	2.6	3.7	4.5	3.3	1.8	0.6	1.6	0.4	-1.0	0.3	0.8	0.9
200	0.0050	0.3953	1.106	2.0	3.9	4.4	3.2	0.5	1.4	2.3	-0.3	-2.0	0.8	0.6	0.3
200	0.0080	0.2470	0.969	2.0	3.4	4.0	2.8	0.9	1.0	2.0	0.4	-1.5	0.7	1.0	0.1
200	0.0130	0.1520	0.840	2.1	4.3	4.8	3.7	1.8	1.8	2.2	-0.6	-1.2	0.4	1.7	0.1
200	0.0200	0.0988	0.722	2.3	4.5	5.1	3.0	1.0	1.2	3.4	-1.6	-2.7	-1.0	0.5	0.1
200	0.0320	0.0618	0.542	2.9	6.0	6.6	4.6	1.6	2.3	3.8	-2.8	-1.6	-1.4	-1.4	0.0
200	0.0500	0.0395	0.510	3.1	5.6	6.4	3.9	2.0	1.8	4.0	-1.5	-1.8	0.9	3.1	0.0
200	0.0800	0.0247	0.436	3.5	4.9	6.0	3.7	1.8	2.0	3.2	-1.4	-2.7	0.7	-0.4	0.0
200	0.1300	0.0152	0.380	4.8	7.2	8.6	6.2	2.0	4.8	3.6	2.7	-0.6	-1.7	-1.6	0.0
250	0.0050	0.4941	1.092	2.4	3.2	4.0	2.8	0.3	1.0	1.6	0.1	-1.2	-0.5	-0.7	0.5
250	0.0080	0.3088	1.008	2.2	3.2	3.9	2.8	0.2	1.2	1.6	0.8	-1.0	0.9	-0.4	0.2
250	0.0130	0.1900	0.840	2.3	4.3	4.9	3.1	1.8	0.8	3.0	1.3	-2.3	1.0	0.9	0.1
250	0.0200	0.1235	0.722	2.3	3.5	4.2	2.8	0.8	1.0	2.1	0.6	-1.6	1.0	0.8	0.1
250	0.0320	0.0772	0.581	2.6	4.4	5.1	3.5	2.1	0.9	2.7	1.5	-1.8	-1.1	0.9	0.0
250	0.0500	0.0494	0.538	2.9	5.3	6.0	3.6	1.0	0.6	3.9	0.8	-1.7	-0.2	3.4	0.0
250	0.0800	0.0309	0.443	2.9	3.6	4.6	3.0	1.3	0.6	2.1	0.8	-0.7	-1.5	1.0	0.0
250	0.1300	0.0190	0.356	3.8	6.0	7.1	5.2	4.2	1.9	3.0	-2.2	-1.1	-1.4	1.1	0.0
250	0.1800	0.0137	0.329	4.3	5.9	7.4	4.4	2.7	0.3	4.0	1.5	-2.1	2.0	-2.3	0.0
300	0.0050	0.5929	1.235	3.2	3.6	4.8	2.9	0.6	1.2	2.2	0.3	-1.4	-0.6	1.2	0.8

Table C.3: The NC e^-p double differential cross section $d^2\sigma_{NC}/dQ^2dx$ for RH polarised electrons ($P_e = 37.0\%$) with the statistical (δ_{stat}), systematic (δ_{sys}) and total (δ_{tot}) errors. Also shown are the total uncorrelated systematic (δ_{unc}) errors and two of its contributions: the electron energy error (δ_{unc}^E) and the hadronic energy error (δ_{unc}^h). The effect of the other uncorrelated systematic errors is included in (δ_{unc}). The table also provides the correlated systematic error (δ_{cor}) and its contributions from a positive variation of one standard deviation of the error on the electron energy (δ_{cor}^{E+}) and polar angle ($\delta_{cor}^{\theta+}$), of the hadronic energy error (δ_{cor}^{h+}), of the error due to noise subtraction (δ_{cor}^{N+}) and background subtraction (δ_{cor}^{B+}) (δ_{unc}^h). The effect of the other correlated systematic errors is included in (δ_{cor}). The normalisation uncertainty of 2.1% is not included in the errors. The table continues on the next 4 pages.

Q^2 (GeV ²)	x	y	$\tilde{\sigma}_{NC}$	δ_{stat} (%)	δ_{sys} (%)	δ_{tot} (%)	δ_{unc} (%)	δ_{unc}^E (%)	δ_{unc}^h (%)	δ_{cor} (%)	δ_{cor}^{E+} (%)	$\delta_{cor}^{\theta+}$ (%)	δ_{cor}^{h+} (%)	δ_{cor}^{N+} (%)	δ_{cor}^{B+} (%)
300	0.0080	0.3706	1.007	2.6	4.7	5.3	3.8	1.8	1.2	2.8	-1.0	-1.8	-1.4	-1.3	0.2
300	0.0130	0.2280	0.826	2.6	3.5	4.4	3.0	0.8	0.8	1.9	0.7	1.0	0.8	1.2	0.1
300	0.0200	0.1482	0.747	2.7	3.7	4.6	3.4	2.4	0.2	1.3	0.6	-1.0	0.5	0.0	0.1
300	0.0320	0.0926	0.602	2.9	5.1	5.9	3.6	2.2	1.1	3.6	1.5	-2.6	-1.2	-1.7	0.0
300	0.0500	0.0593	0.502	3.3	5.0	6.0	3.9	2.6	0.8	3.1	0.8	-2.1	-1.1	1.9	0.0
300	0.0800	0.0371	0.454	3.3	5.3	6.2	3.6	2.1	1.4	3.8	-1.5	-2.3	-0.2	2.6	0.0
300	0.1300	0.0228	0.370	4.3	6.0	7.4	4.2	2.0	1.9	4.3	3.2	-2.1	1.1	1.7	0.0
300	0.1800	0.0165	0.313	5.0	6.9	8.5	5.2	3.6	1.8	4.6	-0.6	-2.2	-3.5	2.0	0.0
300	0.2500	0.0119	0.265	5.6	14.0	15.1	7.8	5.4	3.5	11.6	4.4	-2.8	3.0	-10.0	0.0
400	0.0050	0.7905	1.132	5.4	5.1	7.5	3.4	0.9	0.7	3.8	-0.8	-1.9	1.0	-2.8	1.2
400	0.0080	0.4941	1.016	3.4	3.2	4.6	2.8	0.8	1.0	1.5	0.7	-0.7	0.5	0.9	0.5
400	0.0130	0.3040	0.890	3.0	3.7	4.8	2.8	0.3	1.2	2.5	-1.4	-1.5	-1.2	-0.6	0.2
400	0.0200	0.1976	0.718	3.0	3.0	4.3	2.7	0.4	0.1	1.4	0.8	-0.9	0.3	0.8	0.1
400	0.0320	0.1235	0.626	3.1	3.7	4.8	3.1	1.9	0.2	1.9	1.3	-1.2	0.4	0.5	0.1
400	0.0500	0.0791	0.541	3.7	3.8	5.3	3.0	1.4	0.6	2.3	1.0	-1.2	-1.3	-1.2	0.1
400	0.0800	0.0494	0.445	3.8	3.8	5.3	2.8	1.1	0.5	2.6	-0.4	-1.1	1.0	2.1	0.0
400	0.1300	0.0304	0.392	4.6	5.9	7.5	4.6	3.4	1.3	3.7	2.7	-1.6	1.3	1.6	0.0
400	0.1800	0.0220	0.333	5.7	6.8	8.9	5.8	4.4	2.8	3.4	1.6	-2.2	-1.4	1.6	0.0
400	0.2500	0.0158	0.240	6.2	7.2	9.5	4.3	3.1	0.5	5.8	3.1	2.4	1.2	-4.1	0.0
500	0.0080	0.6176	0.936	4.2	2.9	5.1	2.6	0.7	0.7	1.2	-0.6	-0.5	0.4	-0.3	0.7
500	0.0130	0.3801	0.833	3.7	4.3	5.7	3.1	0.7	1.6	3.0	1.2	-2.3	1.4	0.5	0.2
500	0.0200	0.2470	0.722	3.7	4.3	5.6	3.8	1.7	1.1	2.0	0.9	1.5	-0.5	1.0	0.1
500	0.0320	0.1544	0.613	3.6	4.7	5.9	3.8	1.3	1.6	2.8	-1.2	-1.4	-1.4	1.6	0.1
500	0.0500	0.0988	0.510	4.1	5.0	6.4	4.3	3.2	0.8	2.5	1.8	1.4	0.8	0.7	0.1
500	0.0800	0.0618	0.497	4.1	4.9	6.4	3.5	0.6	2.4	3.4	0.5	-1.6	0.1	2.9	0.0
500	0.1300	0.0380	0.381	5.1	4.8	7.0	4.1	2.1	1.7	2.6	2.0	-0.8	-1.2	-0.8	0.0
500	0.1800	0.0274	0.342	6.0	6.8	9.0	5.0	4.1	1.4	4.5	2.6	-1.1	2.2	2.8	0.0
500	0.2500	0.0198	0.218	7.2	8.1	10.8	6.0	4.8	2.6	5.4	1.1	-2.5	-1.8	-4.3	0.0
500	0.4000	0.0124	0.123	10.3	19.2	21.8	7.9	6.7	3.1	17.5	3.9	-0.5	-2.1	-16.9	0.0

Q^2 (GeV ²)	x	y	$\tilde{\sigma}_{NC}$	δ_{stat} (%)	δ_{sys} (%)	δ_{tot} (%)	δ_{unc} (%)	δ_{unc}^E (%)	δ_{unc}^h (%)	δ_{cor} (%)	δ_{cor}^{E+} (%)	$\delta_{cor}^{\theta+}$ (%)	δ_{cor}^{h+} (%)	δ_{cor}^{N+} (%)	δ_{cor}^{B+} (%)
650	0.0080	0.8029	0.964	6.2	4.3	7.6	3.3	1.2	0.7	2.8	1.7	-1.5	-0.6	1.0	1.1
650	0.0130	0.4941	0.870	4.4	4.0	6.0	3.2	1.2	1.3	2.3	-0.4	-1.7	1.0	1.0	0.4
650	0.0200	0.3211	0.745	4.3	3.5	5.6	3.0	0.9	1.4	1.8	-0.5	-1.2	-0.9	0.9	0.2
650	0.0320	0.2007	0.609	4.3	3.1	5.3	3.0	1.4	0.7	1.0	0.4	-0.4	0.1	0.8	0.1
650	0.0500	0.1285	0.530	4.5	4.1	6.1	3.4	1.9	0.8	2.4	1.2	-1.8	0.5	-0.7	0.1
650	0.0800	0.0803	0.435	5.2	4.4	6.8	3.5	2.1	1.3	2.6	0.7	-0.8	0.8	2.3	0.0
650	0.1300	0.0494	0.395	5.7	6.2	8.4	4.9	3.9	1.5	3.8	2.7	-0.4	-1.3	2.2	0.0
650	0.1800	0.0357	0.298	7.0	8.0	10.6	6.0	3.7	3.9	5.2	3.0	-1.5	-3.0	-2.8	0.0
650	0.2500	0.0257	0.234	8.3	5.7	10.1	3.8	1.4	2.0	4.3	1.8	2.4	-2.9	1.0	0.0
650	0.4000	0.0161	0.131	10.8	18.0	21.0	9.6	7.6	5.0	15.2	3.0	-3.2	-2.5	-14.4	0.0
800	0.0080	0.9881	0.961	11.3	9.6	14.8	7.5	5.8	2.6	6.1	-2.0	-3.0	-3.5	-2.3	2.4
800	0.0130	0.6081	0.885	5.4	4.6	7.1	3.3	0.8	1.8	3.2	-1.2	-0.5	-1.3	-2.5	0.8
800	0.0200	0.3953	0.700	5.1	3.8	6.3	2.9	1.1	1.1	2.4	0.5	1.0	1.8	1.1	0.2
800	0.0320	0.2470	0.696	4.8	3.4	5.9	3.0	1.2	1.1	1.6	0.8	-1.2	-0.4	0.5	0.1
800	0.0500	0.1581	0.521	5.3	3.9	6.6	3.2	1.8	0.7	2.2	1.7	-0.4	1.4	-0.2	0.1
800	0.0800	0.0988	0.453	6.0	3.4	6.9	3.1	1.2	1.1	1.6	0.8	-0.6	-0.9	0.7	0.1
800	0.1300	0.0608	0.391	6.8	5.5	8.7	4.3	3.2	0.5	3.4	2.0	-1.8	-1.5	1.4	0.0
800	0.1800	0.0439	0.267	8.4	5.6	10.1	3.6	2.1	0.6	4.3	3.0	-1.6	2.3	-1.1	0.0
800	0.2500	0.0316	0.271	9.6	8.2	12.6	6.8	5.7	2.6	4.6	1.5	-2.3	-3.6	-0.7	0.0
800	0.4000	0.0198	0.129	12.0	12.6	17.4	8.2	6.0	4.8	9.6	1.1	-1.2	-2.2	-9.2	0.0
1000	0.0130	0.7601	0.855	7.4	5.1	9.0	4.0	1.9	1.2	3.1	-2.1	-1.0	1.0	1.0	1.6
1000	0.0200	0.4941	0.688	6.2	3.5	7.2	3.3	0.7	1.7	1.1	0.3	-0.5	0.4	0.8	0.3
1000	0.0320	0.3088	0.704	5.7	4.2	7.1	3.4	1.6	1.6	2.5	1.7	1.0	0.6	1.4	0.2
1000	0.0500	0.1976	0.531	6.1	4.1	7.3	3.3	0.6	0.6	2.5	0.5	-1.8	0.5	1.6	0.1
1000	0.0800	0.1235	0.419	7.0	4.7	8.4	4.1	3.0	0.8	2.3	1.7	-1.4	0.5	0.5	0.1
1000	0.1300	0.0760	0.417	7.4	3.9	8.4	2.9	0.9	0.9	2.6	-0.2	-2.1	-1.0	1.0	0.0
1000	0.1800	0.0549	0.352	8.5	8.1	11.7	7.1	5.6	3.5	3.9	2.2	1.1	-2.8	-1.3	0.0
1000	0.2500	0.0395	0.305	9.7	7.2	12.1	5.4	3.9	2.8	4.8	2.4	0.9	-0.8	-3.9	0.0
1000	0.4000	0.0247	0.150	12.9	10.8	16.8	7.9	5.5	4.4	7.3	4.9	1.5	3.8	-3.6	0.0

Q^2 (GeV ²)	x	y	$\tilde{\sigma}_{NC}$	δ_{stat} (%)	δ_{sys} (%)	δ_{tot} (%)	δ_{unc} (%)	δ_{unc}^E (%)	δ_{unc}^h (%)	δ_{cor} (%)	δ_{cor}^{E+} (%)	$\delta_{cor}^{\theta+}$ (%)	δ_{cor}^{h+} (%)	δ_{cor}^{N+} (%)	δ_{cor}^{B+} (%)
1000	0.6500	0.0152	0.0103	30.2	22.6	37.7	12.5	9.4	6.6	18.9	-4.8	-5.5	-4.9	-16.7	0.0
1200	0.0130	0.9121	0.911	11.7	5.1	12.8	4.1	1.0	2.5	3.0	0.8	-0.6	-1.4	1.1	2.3
1200	0.0200	0.5929	0.696	7.6	4.8	9.0	4.0	1.0	1.5	2.6	-0.5	-2.0	1.0	-1.0	0.7
1200	0.0320	0.3706	0.689	6.8	4.4	8.1	3.8	0.8	2.0	2.2	1.0	0.2	1.7	-0.9	0.2
1200	0.0500	0.2372	0.543	6.9	3.7	7.8	3.2	2.0	0.4	1.9	-0.3	-1.8	-0.6	0.3	0.1
1200	0.0800	0.1482	0.491	7.1	4.4	8.4	3.8	2.6	0.8	2.2	0.5	1.8	0.7	0.8	0.1
1200	0.1300	0.0912	0.378	9.2	3.6	9.8	2.9	1.0	1.2	2.0	1.6	-1.1	0.5	0.2	0.1
1200	0.1800	0.0659	0.274	10.5	4.6	11.5	4.0	2.5	1.7	2.2	1.4	-1.5	-0.8	0.4	0.0
1200	0.2500	0.0474	0.270	11.0	6.3	12.7	5.8	4.7	2.2	2.4	2.0	1.0	-1.0	-0.1	0.0
1200	0.4000	0.0296	0.129	15.4	11.1	19.0	6.9	6.2	1.2	8.6	3.6	-3.4	-2.2	-6.7	0.0
1200	0.6500	0.0182	0.0070	44.9	22.4	50.2	12.4	9.0	8.1	18.7	6.3	-2.6	-3.1	-17.1	0.0
1500	0.0200	0.7411	0.776	9.3	3.7	10.0	3.3	1.5	0.5	1.6	-0.6	0.3	0.4	-0.8	1.2
1500	0.0320	0.4632	0.600	8.5	3.3	9.1	3.0	0.8	1.1	1.4	0.2	-0.8	0.6	0.9	0.3
1500	0.0500	0.2964	0.586	7.8	4.1	8.8	3.6	1.5	1.0	2.0	-0.5	0.7	0.3	-1.8	0.2
1500	0.0800	0.1853	0.406	8.7	3.9	9.6	3.3	1.7	1.2	2.1	1.5	-1.0	0.4	1.1	0.1
1500	0.1300	0.1140	0.298	11.8	4.9	12.8	3.2	0.8	0.6	3.7	-2.4	1.3	-1.8	1.7	0.1
1500	0.1800	0.0823	0.271	11.8	4.8	12.7	3.8	2.6	0.5	2.8	2.2	1.2	1.3	-0.4	0.0
1500	0.2500	0.0593	0.283	11.9	5.4	13.1	4.4	3.4	0.8	3.2	1.2	-2.1	1.2	-1.8	0.0
1500	0.4000	0.0371	0.115	18.9	13.6	23.3	9.8	8.7	3.6	9.4	6.4	1.1	-4.4	-5.2	0.0
1500	0.6500	0.0228	0.0098	40.9	27.2	49.1	18.7	16.3	7.6	19.7	7.0	5.0	5.6	-16.8	0.0
2000	0.0200	0.9881	0.755	15.1	5.9	16.2	4.7	1.4	2.8	3.6	-0.8	-1.9	-2.3	-0.6	1.8
2000	0.0320	0.6176	0.641	9.6	4.6	10.6	4.3	0.5	2.3	1.6	0.4	-1.0	0.3	1.1	0.6
2000	0.0500	0.3953	0.517	10.3	4.9	11.4	4.1	1.1	2.0	2.7	2.0	0.9	1.0	1.2	0.2
2000	0.0800	0.2470	0.450	9.6	4.7	10.7	4.0	1.5	0.8	2.5	-1.3	-1.2	1.3	1.1	0.1
2000	0.1300	0.1520	0.338	12.8	5.4	13.9	4.7	2.8	1.7	2.7	2.1	-1.2	-0.8	0.8	0.1
2000	0.1800	0.1098	0.345	12.5	6.4	14.0	4.5	2.8	1.8	4.5	2.6	1.2	-2.9	1.9	0.1
2000	0.2500	0.0791	0.218	15.1	6.4	16.4	5.2	3.1	3.2	3.8	2.4	1.3	-1.5	-2.1	0.0
2000	0.4000	0.0494	0.153	18.6	11.2	21.7	7.6	6.8	1.8	8.2	6.2	1.8	3.1	-4.0	0.0
2000	0.6500	0.0304	0.0143	40.9	21.0	45.9	13.4	7.9	9.8	16.2	4.6	-4.3	-5.7	-13.8	0.0

Q^2 (GeV ²)	x	y	$\tilde{\sigma}_{NC}$	δ_{stat} (%)	δ_{sys} (%)	δ_{tot} (%)	δ_{unc} (%)	δ_{unc}^E (%)	δ_{unc}^h (%)	δ_{cor} (%)	δ_{cor}^{E+} (%)	$\delta_{cor}^{\theta+}$ (%)	δ_{cor}^{h+} (%)	δ_{cor}^{N+} (%)	δ_{cor}^{B+} (%)
3000	0.0320	0.9264	0.625	10.0	5.0	11.2	4.3	0.8	2.4	2.6	-1.1	-1.4	1.1	-1.2	1.1
3000	0.0500	0.5929	0.552	8.1	4.2	9.1	3.7	0.7	1.9	2.0	-0.3	-0.7	1.6	-0.9	0.5
3000	0.0800	0.3706	0.503	8.1	4.3	9.2	3.6	0.8	0.9	2.3	1.3	-1.6	0.8	-0.4	0.2
3000	0.1300	0.2280	0.373	10.5	5.1	11.7	4.3	2.0	1.8	2.7	2.3	0.6	-0.6	1.1	0.1
3000	0.1800	0.1647	0.272	12.4	5.6	13.6	3.4	1.2	0.8	4.4	-1.6	-1.6	-2.7	-2.7	0.1
3000	0.2500	0.1186	0.317	10.6	5.9	12.2	5.7	4.2	0.6	1.8	1.1	-0.6	-1.2	0.4	0.0
3000	0.4000	0.0741	0.0684	23.6	13.0	27.0	10.8	8.8	5.6	7.2	4.7	1.1	-2.6	-4.7	0.0
3000	0.6500	0.0456	0.0146	35.4	20.0	40.6	14.6	11.1	5.2	13.6	6.6	-6.1	-2.2	-10.0	0.0
5000	0.0500	0.9881	0.497	14.6	5.0	15.5	4.3	2.6	1.8	2.6	-1.0	-1.3	1.2	-0.2	1.6
5000	0.0800	0.6176	0.474	9.9	4.2	10.7	3.8	1.5	1.8	1.6	0.3	0.2	1.0	1.1	0.4
5000	0.1300	0.3801	0.380	11.2	4.2	11.9	3.9	2.0	1.2	1.5	0.7	0.8	0.4	1.0	0.2
5000	0.1800	0.2745	0.279	13.8	5.9	15.0	5.8	4.1	1.3	1.5	1.0	-0.5	-0.6	0.9	0.1
5000	0.2500	0.1976	0.224	15.5	7.0	17.0	6.4	5.6	1.2	2.7	1.7	1.4	-1.3	1.0	0.1
5000	0.4000	0.1235	0.133	18.6	9.0	20.7	8.2	7.0	1.6	3.7	3.1	-0.8	1.5	-1.0	0.0
5000	0.6500	0.0760	0.0130	50.1	40.9	64.7	35.8	33.9	7.6	19.7	10.3	8.7	-5.8	-13.1	0.0
8000	0.0800	0.9881	0.490	20.4	5.1	21.1	4.1	1.2	2.4	3.0	0.9	-1.7	-1.6	-0.7	1.6
8000	0.1300	0.6081	0.461	14.9	4.0	15.4	3.6	1.8	1.5	1.6	-0.7	-0.8	1.0	-0.7	0.4
8000	0.1800	0.4392	0.405	14.6	5.2	15.6	4.6	2.9	1.2	2.6	-1.8	-0.8	-1.6	-0.4	0.1
8000	0.2500	0.3162	0.286	16.5	10.0	19.3	9.2	8.4	2.0	4.0	3.7	-1.3	0.4	0.7	0.1
8000	0.4000	0.1976	0.121	21.9	11.2	24.6	10.6	10.0	2.0	3.4	-1.3	2.8	0.6	-1.3	0.1
8000	0.6500	0.1216	0.0286	37.8	37.8	53.5	35.1	34.5	5.8	13.9	10.9	0.4	-7.9	3.5	0.1
12000	0.1300	0.9121	0.796	28.7	7.2	29.6	6.2	3.1	4.3	3.7	-1.0	-1.8	-2.4	-1.1	1.6
12000	0.1800	0.6588	0.385	22.7	4.4	23.2	4.2	2.6	0.9	1.3	0.8	-0.8	0.5	0.3	0.4
12000	0.2500	0.4743	0.192	27.0	6.8	27.8	6.7	5.8	1.4	1.3	1.0	0.3	0.7	0.2	0.2
12000	0.4000	0.2964	0.230	23.0	15.8	27.9	15.3	14.9	0.8	4.3	2.8	1.3	2.2	1.9	0.1
12000	0.6500	0.1824	0.0184	57.8	39.7	70.1	38.0	37.4	5.6	11.5	8.4	6.2	2.8	-4.1	0.0
20000	0.2500	0.7905	0.340	35.8	5.1	36.2	4.8	3.6	0.0	1.8	0.7	-1.6	0.0	-0.1	0.4
20000	0.4000	0.4941	0.226	30.2	14.1	33.4	13.6	13.1	1.9	3.6	2.7	2.1	1.1	0.4	0.2
20000	0.6500	0.3040	0.0112	100.2	36.1	106.5	35.2	35.1	1.6	7.7	5.7	5.0	-1.1	-0.5	0.0

Q^2 (GeV ²)	x	y	$\tilde{\sigma}_{NC}$	δ_{stat} (%)	δ_{sys} (%)	δ_{tot} (%)	δ_{unc} (%)	δ_{unc}^E (%)	δ_{unc}^h (%)	δ_{cor} (%)	$\delta_{cor}^{E^+}$ (%)	$\delta_{cor}^{\theta^+}$ (%)	$\delta_{cor}^{h^+}$ (%)	$\delta_{cor}^{N^+}$ (%)	$\delta_{cor}^{B^+}$ (%)
200	0.0032	0.6176	1.325	1.6	3.6	4.0	3.3	1.7	0.6	1.6	0.4	-1.0	0.3	0.7	0.9
200	0.0050	0.3953	1.108	1.3	3.9	4.1	3.1	0.5	1.4	2.2	-0.3	-2.0	0.8	0.6	0.3
200	0.0080	0.2470	0.954	1.3	3.4	3.6	2.8	0.8	1.0	1.9	0.4	-1.5	0.6	0.9	0.1
200	0.0130	0.1520	0.829	1.4	4.3	4.5	3.7	1.8	1.8	2.2	0.6	-1.3	0.4	1.7	0.1
200	0.0200	0.0988	0.726	1.5	4.6	4.8	3.0	1.1	1.2	3.4	-1.7	-2.8	-1.0	0.5	0.1
200	0.0320	0.0618	0.566	1.9	6.0	6.3	4.6	1.6	2.3	3.8	-2.9	-1.6	-1.4	-1.4	0.0
200	0.0500	0.0395	0.499	2.1	5.7	6.1	4.1	2.2	1.8	4.0	-1.6	-1.8	0.9	3.1	0.0
200	0.0800	0.0247	0.395	2.4	5.0	5.6	3.8	1.9	2.0	3.2	-1.5	-2.8	0.7	0.4	0.0
250	0.0050	0.4941	1.115	1.6	3.2	3.5	2.8	0.2	1.0	1.5	0.2	-1.2	-0.4	-0.6	0.5
250	0.0080	0.3088	0.998	1.5	3.2	3.5	2.8	0.1	1.2	1.6	0.8	-1.0	0.9	-0.4	0.2
250	0.0130	0.1900	0.860	1.5	4.3	4.6	3.1	1.8	0.8	3.0	1.3	-2.3	1.0	0.9	0.1
250	0.0200	0.1235	0.725	1.5	3.5	3.8	2.8	0.8	1.0	2.0	0.5	-1.5	1.0	0.8	0.1
250	0.0320	0.0772	0.610	1.6	4.4	4.7	3.4	2.0	0.9	2.8	1.5	-1.8	-1.1	0.9	0.0
250	0.0500	0.0494	0.574	1.9	5.2	5.5	3.5	1.0	0.5	3.8	0.9	-1.7	-0.2	3.4	0.0
250	0.0800	0.0309	0.446	1.9	3.5	4.0	2.9	1.2	0.7	2.0	0.8	-0.6	-1.4	1.0	0.0
250	0.1300	0.0190	0.357	2.5	6.2	6.7	5.4	4.3	2.0	3.2	-2.2	-1.2	-1.5	-1.1	0.0
250	0.1800	0.0137	0.322	2.9	5.8	6.5	4.2	2.6	0.3	4.0	1.4	-2.0	2.1	-2.4	0.0
300	0.0050	0.5929	1.154	2.2	3.6	4.2	2.9	0.6	1.1	2.2	0.4	-1.5	-0.6	1.2	0.7

Table C.4: The NC e^-p double differential cross section $d^2\sigma_{NC}/dQ^2dx$ for LH polarised electrons ($P_e = -27.0\%$) with the statistical (δ_{stat}), systematic (δ_{sys}) and total (δ_{tot}) errors. Also shown are the total uncorrelated systematic (δ_{unc}) errors and two of its contributions: the electron energy error (δ_{unc}^E) and the hadronic energy error (δ_{unc}^h). The effect of the other uncorrelated systematic errors is included in (δ_{unc}). The table also provides the correlated systematic error (δ_{cor}) and its contributions from a positive variation of one standard deviation of the error on the electron energy ($\delta_{cor}^{E^+}$) and polar angle ($\delta_{cor}^{\theta^+}$), of the hadronic energy error ($\delta_{cor}^{h^+}$), of the error due to noise subtraction ($\delta_{cor}^{N^+}$) and background subtraction ($\delta_{cor}^{B^+}$) (δ_{unc}^h). The effect of the other correlated systematic errors is included in (δ_{cor}). The normalisation uncertainty of 2.1% is not included in the errors. The table continues on the next 4 pages.

Q^2 (GeV ²)	x	y	$\tilde{\sigma}_{NC}$	δ_{stat} (%)	δ_{sys} (%)	δ_{tot} (%)	δ_{unc} (%)	δ_{unc}^E (%)	δ_{unc}^h (%)	δ_{cor} (%)	$\delta_{cor}^{E^+}$ (%)	$\delta_{cor}^{\theta^+}$ (%)	$\delta_{cor}^{h^+}$ (%)	$\delta_{cor}^{N^+}$ (%)	$\delta_{cor}^{B^+}$ (%)
300	0.0080	0.3706	0.975	1.7	4.6	4.9	3.7	1.8	1.2	2.7	-0.9	-1.8	-1.4	-1.2	0.2
300	0.0130	0.2280	0.854	1.7	3.5	3.8	2.9	0.7	0.8	1.8	0.6	0.9	0.8	1.2	0.1
300	0.0200	0.1482	0.735	1.8	3.7	4.1	3.4	2.4	0.2	1.3	0.6	-1.1	0.5	0.2	0.1
300	0.0320	0.0926	0.574	1.9	5.1	5.4	3.6	2.2	1.0	3.6	1.5	-2.6	-1.1	-1.6	0.0
300	0.0500	0.0593	0.544	2.1	5.0	5.4	3.9	2.6	0.8	3.1	0.8	-2.0	-1.1	1.8	0.0
300	0.0800	0.0371	0.473	2.1	5.3	5.7	3.6	2.1	1.4	3.8	-1.6	-2.3	-0.3	2.6	0.0
300	0.1300	0.0228	0.382	2.8	6.1	6.7	4.2	2.0	1.9	4.4	3.2	-2.1	1.1	1.8	0.0
300	0.1800	0.0165	0.323	3.2	7.0	7.7	5.2	3.6	1.9	4.6	-0.7	-2.2	-3.5	2.0	0.0
300	0.2500	0.0119	0.252	3.7	13.9	14.4	7.6	5.4	3.4	11.6	4.4	-2.8	2.7	-10.0	0.0
400	0.0050	0.7905	1.150	3.7	5.1	6.3	3.3	0.9	0.8	3.8	-0.9	-1.9	0.9	-2.9	1.1
400	0.0080	0.4941	1.027	2.1	3.2	3.8	2.8	0.8	1.0	1.5	0.7	-0.7	0.5	0.8	0.4
400	0.0130	0.3040	0.899	1.9	3.8	4.2	2.8	0.3	1.2	2.6	-1.4	-1.5	-1.3	-0.7	0.2
400	0.0200	0.1976	0.744	2.0	3.0	3.6	2.7	0.4	0.1	1.5	0.8	-0.9	0.3	0.8	0.1
400	0.0320	0.1235	0.624	2.1	3.6	4.1	3.1	1.8	0.2	1.8	1.3	-1.2	0.4	0.5	0.1
400	0.0500	0.0791	0.514	2.5	3.8	4.6	3.0	1.4	0.5	2.4	1.0	-1.2	-1.4	-1.2	0.1
400	0.0800	0.0494	0.473	2.4	3.8	4.5	2.8	1.1	0.4	2.5	-0.5	-1.1	1.0	2.0	0.0
400	0.1300	0.0304	0.390	3.0	5.9	6.6	4.6	3.4	1.3	3.7	2.6	-1.5	1.3	1.6	0.0
400	0.1800	0.0220	0.354	3.7	6.8	7.7	5.9	4.5	2.8	3.4	1.7	-2.1	-1.4	1.6	0.0
400	0.2500	0.0158	0.242	4.1	7.2	8.3	4.3	3.1	0.5	5.8	3.1	2.4	1.3	-4.1	0.0
500	0.0080	0.6176	1.003	2.7	2.9	3.9	2.6	0.6	0.7	1.2	-0.6	-0.5	0.4	-0.3	0.7
500	0.0130	0.3801	0.894	2.3	4.4	4.9	3.1	0.6	1.6	3.1	1.4	-2.2	1.5	0.5	0.2
500	0.0200	0.2470	0.800	2.3	4.3	4.9	3.8	1.7	1.1	2.1	0.9	1.5	-0.5	1.0	0.1
500	0.0320	0.1544	0.624	2.3	4.7	5.2	3.8	1.3	1.6	2.7	-1.1	-1.4	-1.3	1.6	0.1
500	0.0500	0.0988	0.555	2.6	5.0	5.6	4.3	3.1	0.8	2.5	1.8	1.4	-0.8	0.6	0.1
500	0.0800	0.0618	0.477	2.8	5.0	5.7	3.6	0.7	2.6	3.4	0.7	-1.5	0.2	2.9	0.0
500	0.1300	0.0380	0.413	3.2	4.9	5.8	4.1	2.1	1.8	2.6	2.0	-0.8	-1.1	-0.9	0.0
500	0.1800	0.0274	0.332	4.1	6.8	8.0	5.0	4.1	1.4	4.6	2.5	-1.2	2.3	2.9	0.0
500	0.2500	0.0198	0.227	4.7	8.0	9.3	6.0	4.8	2.6	5.4	1.2	-2.3	-1.7	-4.4	0.0
500	0.4000	0.0124	0.144	6.3	19.4	20.4	8.0	6.7	3.2	17.7	3.9	-0.4	-2.1	-17.1	0.0

Q^2 (GeV ²)	x	y	$\tilde{\sigma}_{NC}$	δ_{stat} (%)	δ_{sys} (%)	δ_{tot} (%)	δ_{unc} (%)	δ_{unc}^E (%)	δ_{unc}^h (%)	δ_{cor} (%)	δ_{cor}^{E+} (%)	$\delta_{cor}^{\theta+}$ (%)	δ_{cor}^{h+} (%)	δ_{cor}^{N+} (%)	δ_{cor}^{B+} (%)
650	0.0080	0.8029	0.921	4.1	4.3	5.9	3.3	1.3	0.8	2.6	1.5	-1.5	-0.6	1.0	1.0
650	0.0130	0.4941	0.933	2.8	3.9	4.8	3.2	1.2	1.4	2.3	-0.5	-1.6	1.0	1.0	0.4
650	0.0200	0.3211	0.792	2.7	3.5	4.4	2.9	0.9	1.3	1.9	-0.5	-1.2	-1.0	0.9	0.2
650	0.0320	0.2007	0.650	2.7	3.1	4.1	2.9	1.4	0.8	1.0	-0.4	-0.4	0.1	0.7	0.1
650	0.0500	0.1285	0.513	3.0	4.0	5.0	3.3	1.8	0.8	2.3	1.2	-1.8	0.6	-0.8	0.1
650	0.0800	0.0803	0.464	3.2	4.4	5.5	3.5	2.1	1.3	2.7	0.7	-0.7	0.7	2.4	0.0
650	0.1300	0.0494	0.405	3.7	6.2	7.2	4.9	4.0	1.3	3.7	2.7	-0.5	-1.3	2.1	0.0
650	0.1800	0.0357	0.333	4.4	8.0	9.1	6.1	3.7	3.8	5.2	-3.0	-1.5	-2.8	-2.8	0.0
650	0.2500	0.0257	0.274	5.2	5.7	7.7	3.7	1.3	2.0	4.3	1.9	2.4	-2.9	0.9	0.0
650	0.4000	0.0161	0.123	7.3	17.7	19.2	9.4	7.4	4.8	15.0	2.8	-3.3	-2.3	-14.2	0.0
800	0.0080	0.9881	1.049	7.3	9.5	12.0	7.2	5.6	2.7	6.1	-1.9	-2.8	-3.6	-2.5	2.5
800	0.0130	0.6081	0.906	3.5	4.6	5.8	3.3	0.8	1.8	3.2	-1.2	-0.6	-1.3	-2.5	0.8
800	0.0200	0.3953	0.721	3.5	3.8	5.2	3.0	1.2	1.1	2.4	0.5	1.0	1.8	1.2	0.2
800	0.0320	0.2470	0.661	3.3	3.4	4.7	3.0	1.2	1.1	1.6	0.8	-1.2	-0.4	0.5	0.1
800	0.0500	0.1581	0.562	3.4	3.9	5.1	3.2	1.8	0.7	2.2	1.7	-0.3	1.4	0.2	0.1
800	0.0800	0.0988	0.445	3.9	3.4	5.2	3.1	1.2	1.1	1.6	0.8	-0.6	-1.0	0.8	0.1
800	0.1300	0.0608	0.397	4.4	5.3	6.9	4.2	3.1	0.5	3.2	2.0	-1.8	-1.5	1.2	0.0
800	0.1800	0.0439	0.338	5.0	5.7	7.5	3.6	2.0	0.6	4.4	3.1	-1.7	2.4	-1.1	0.0
800	0.2500	0.0316	0.300	6.1	8.2	10.2	6.8	5.7	2.5	4.6	1.2	-2.4	-3.7	-0.9	0.0
800	0.4000	0.0198	0.136	7.9	12.7	15.0	8.2	6.1	4.8	9.7	-1.3	-1.1	-2.1	-9.4	0.0
1000	0.0130	0.7601	0.905	4.8	5.2	7.1	4.1	1.9	1.3	3.2	-2.2	-1.1	0.9	1.2	1.6
1000	0.0200	0.4941	0.848	3.7	3.5	5.1	3.3	0.7	1.7	1.1	0.3	-0.4	0.4	0.8	0.3
1000	0.0320	0.3088	0.640	3.9	4.1	5.7	3.3	1.5	1.6	2.5	1.7	1.0	0.5	1.4	0.2
1000	0.0500	0.1976	0.524	4.0	4.1	5.7	3.2	0.6	0.7	2.5	0.4	-1.8	0.6	1.6	0.1
1000	0.0800	0.1235	0.442	4.4	4.6	6.4	4.0	2.9	0.8	2.2	1.6	-1.4	0.4	0.4	0.1
1000	0.1300	0.0760	0.361	5.2	3.9	6.5	2.9	0.9	0.9	2.6	0.3	-2.2	-1.0	1.0	0.0
1000	0.1800	0.0549	0.352	5.5	8.0	9.7	7.0	5.6	3.4	4.0	2.2	1.2	-2.8	-1.3	0.0
1000	0.2500	0.0395	0.307	6.4	7.1	9.6	5.3	3.7	2.8	4.6	2.3	0.9	-0.8	-3.9	0.0
1000	0.4000	0.0247	0.138	8.8	10.7	13.9	7.8	5.7	4.1	7.4	4.8	1.5	3.7	-3.8	0.0

Q^2 (GeV ²)	x	y	$\tilde{\sigma}_{NC}$	δ_{stat} (%)	δ_{sys} (%)	δ_{tot} (%)	δ_{unc} (%)	δ_{unc}^E (%)	δ_{unc}^h (%)	δ_{cor} (%)	$\delta_{cor}^{E^+}$ (%)	$\delta_{cor}^{\theta^+}$ (%)	$\delta_{cor}^{h^+}$ (%)	$\delta_{cor}^{N^+}$ (%)	$\delta_{cor}^{B^+}$ (%)
1000	0.6500	0.0152	0.0148	16.5	22.8	28.2	12.6	9.6	6.4	19.0	-4.8	-5.3	-5.2	-16.9	0.0
1200	0.0130	0.9121	0.886	7.9	5.2	9.4	4.2	1.2	2.5	3.1	0.8	-0.5	-1.5	1.2	2.2
1200	0.0200	0.5929	0.780	4.8	4.8	6.7	4.0	0.9	1.5	2.6	-0.6	-2.0	1.0	-1.0	0.7
1200	0.0320	0.3706	0.724	4.3	4.3	6.1	3.8	0.8	2.0	2.1	0.9	0.1	1.7	-0.8	0.2
1200	0.0500	0.2372	0.531	4.5	3.7	5.8	3.2	1.9	0.5	1.9	-0.2	-1.8	-0.6	0.4	0.1
1200	0.0800	0.1482	0.457	4.9	4.3	6.5	3.8	2.6	0.8	2.1	0.5	1.7	0.7	0.8	0.1
1200	0.1300	0.0912	0.370	6.0	3.6	7.0	3.0	1.1	1.2	2.1	1.7	-1.1	0.6	0.1	0.0
1200	0.1800	0.0659	0.332	6.2	4.5	7.6	3.9	2.4	1.5	2.2	1.4	-1.5	-0.8	0.3	0.0
1200	0.2500	0.0474	0.232	7.8	6.4	10.1	5.9	4.7	2.3	2.5	2.0	1.1	-1.0	0.1	0.0
1200	0.4000	0.0296	0.119	10.6	11.0	15.3	6.8	6.2	1.2	8.7	3.5	-3.5	-2.0	-6.9	0.0
1200	0.6500	0.0182	0.0169	18.9	22.5	29.4	12.6	9.1	8.4	18.6	6.4	-2.7	-3.0	-17.0	0.0
1500	0.0200	0.7411	0.889	5.8	3.7	6.9	3.3	1.5	0.5	1.7	-0.7	0.3	0.4	-0.8	1.2
1500	0.0320	0.4632	0.709	5.1	3.3	6.1	3.0	0.9	1.2	1.4	0.2	-0.8	0.5	0.9	0.3
1500	0.0500	0.2964	0.556	5.2	4.1	6.6	3.6	1.4	1.0	2.1	-0.6	0.6	0.3	-1.9	0.1
1500	0.0800	0.1853	0.481	5.3	3.8	6.5	3.2	1.6	1.2	2.1	1.4	-1.0	0.5	1.0	0.1
1500	0.1300	0.1140	0.381	6.8	4.9	8.4	3.3	0.9	0.7	3.7	-2.4	1.3	-1.8	1.7	0.1
1500	0.1800	0.0823	0.292	7.2	4.8	8.7	3.9	2.6	0.5	2.8	2.2	1.2	1.3	-0.4	0.0
1500	0.2500	0.0593	0.227	8.7	5.4	10.2	4.4	3.4	0.9	3.1	1.2	-2.0	1.1	-1.6	0.0
1500	0.4000	0.0371	0.145	11.0	13.3	17.3	9.5	8.5	3.4	9.3	6.2	1.0	-4.4	-5.2	0.0
1500	0.6500	0.0228	0.0118	24.3	27.2	36.5	18.8	16.3	7.5	19.7	7.0	5.0	5.4	-16.9	0.0
2000	0.0200	0.9881	0.916	9.0	5.9	10.8	4.7	1.5	2.9	3.6	-0.9	-1.9	-2.3	-0.7	1.6
2000	0.0320	0.6176	0.621	6.4	4.6	7.9	4.3	0.6	2.4	1.6	0.3	-1.0	0.3	1.0	0.6
2000	0.0500	0.3953	0.591	6.3	5.1	8.1	4.3	1.3	2.0	2.8	1.9	0.9	1.2	1.4	0.2
2000	0.0800	0.2470	0.482	6.1	4.7	7.7	4.0	1.5	0.8	2.6	-1.3	-1.3	1.3	1.2	0.1
2000	0.1300	0.1520	0.371	8.0	5.3	9.6	4.6	2.8	1.6	2.5	2.0	-1.0	-0.8	0.7	0.1
2000	0.1800	0.1098	0.365	8.0	6.5	10.3	4.6	2.9	1.9	4.6	2.6	1.3	-2.9	1.9	0.1
2000	0.2500	0.0791	0.269	8.9	6.4	11.0	5.1	3.0	3.3	3.8	2.4	1.5	-1.5	-2.1	0.0
2000	0.4000	0.0494	0.151	12.2	11.3	16.6	7.7	6.8	1.9	8.3	6.2	1.8	3.1	-4.1	0.0
2000	0.6500	0.0304	0.0100	31.7	20.1	37.5	12.5	7.0	9.6	15.7	4.4	-4.2	-5.6	-13.4	0.0

Q^2 (GeV ²)	x	y	$\tilde{\sigma}_{NC}$	δ_{stat} (%)	δ_{sys} (%)	δ_{tot} (%)	δ_{unc} (%)	δ_{unc}^E (%)	δ_{unc}^h (%)	δ_{cor} (%)	δ_{cor}^{E+} (%)	$\delta_{cor}^{\theta+}$ (%)	δ_{cor}^{h+} (%)	δ_{cor}^{N+} (%)	δ_{cor}^{B+} (%)
3000	0.0320	0.9264	0.801	5.8	5.0	7.7	4.3	0.9	2.4	2.6	-1.1	-1.4	1.0	-1.2	1.0
3000	0.0500	0.5929	0.653	4.9	4.2	6.5	3.7	0.8	1.9	2.0	0.3	-0.7	1.6	-0.9	0.4
3000	0.0800	0.3706	0.448	5.7	4.3	7.1	3.6	0.9	0.9	2.2	1.3	-1.6	0.7	-0.4	0.1
3000	0.1300	0.2280	0.413	6.6	5.1	8.3	4.3	2.0	1.8	2.6	2.2	0.5	-0.7	1.2	0.1
3000	0.1800	0.1647	0.308	7.7	5.4	9.4	3.3	1.0	0.7	4.2	-1.4	-1.5	-2.6	-2.5	0.1
3000	0.2500	0.1186	0.235	8.1	5.9	10.0	5.6	4.1	0.7	1.8	1.1	-0.6	-1.3	0.3	0.0
3000	0.4000	0.0741	0.145	10.7	13.0	16.8	10.8	8.8	5.6	7.1	4.6	1.2	-2.5	-4.6	0.0
3000	0.6500	0.0456	0.0119	25.8	20.1	32.8	14.6	11.2	5.1	13.8	6.7	-6.2	-2.3	-10.1	0.0
5000	0.0500	0.9881	0.704	8.0	5.1	9.5	4.5	2.8	1.9	2.5	-1.0	-1.3	1.2	-0.2	1.4
5000	0.0800	0.6176	0.559	6.0	4.1	7.3	3.8	1.4	1.8	1.6	0.3	-0.2	1.0	1.1	0.3
5000	0.1300	0.3801	0.474	6.6	4.1	7.7	3.8	1.8	1.2	1.5	0.7	0.8	0.4	1.0	0.1
5000	0.1800	0.2745	0.381	7.8	5.8	9.7	5.6	3.9	1.2	1.5	1.0	-0.4	0.5	0.9	0.1
5000	0.2500	0.1976	0.252	9.6	6.8	11.8	6.3	5.6	1.2	2.6	1.6	1.3	-1.2	1.0	0.1
5000	0.4000	0.1235	0.0992	14.2	9.1	16.8	8.2	6.9	1.7	3.9	3.3	-0.8	1.6	-0.9	0.0
5000	0.6500	0.0760	0.0210	25.8	40.8	48.3	35.8	33.8	7.6	19.6	9.6	8.8	-5.6	-13.6	0.0
8000	0.0800	0.9881	0.575	12.6	5.1	13.6	4.2	1.2	2.4	3.0	1.0	-1.7	-1.6	-0.7	1.4
8000	0.1300	0.6081	0.592	8.7	4.0	9.6	3.6	1.7	1.5	1.7	-0.7	-0.8	1.0	-0.7	0.3
8000	0.1800	0.4392	0.367	10.2	5.2	11.5	4.6	3.0	1.3	2.4	-1.8	-0.8	-1.4	-0.4	0.1
8000	0.2500	0.3162	0.296	10.8	9.9	14.6	9.2	8.3	2.1	3.9	3.6	-1.3	0.4	0.7	0.1
8000	0.4000	0.1976	0.139	13.5	11.0	17.4	10.4	9.8	2.0	3.4	-1.2	2.8	0.6	-1.3	0.1
8000	0.6500	0.1216	0.0208	28.9	36.8	46.8	34.3	33.8	5.6	13.2	10.5	-0.4	-7.4	2.7	0.1
12000	0.1300	0.9121	0.575	22.9	7.1	24.0	6.0	2.6	4.4	3.7	-1.0	-1.9	-2.5	-1.1	1.4
12000	0.1800	0.6588	0.579	12.4	4.3	13.1	4.1	2.4	0.9	1.3	0.7	-0.8	0.5	0.3	0.4
12000	0.2500	0.4743	0.325	13.8	6.7	15.4	6.6	5.7	1.4	1.3	1.0	0.3	0.6	0.2	0.1
12000	0.4000	0.2964	0.198	16.5	15.9	22.9	15.3	15.0	0.8	4.4	2.9	1.3	2.3	2.0	0.1
12000	0.6500	0.1824	0.0136	44.8	39.5	59.7	37.8	37.2	5.4	11.6	8.3	6.2	2.6	-4.4	0.0
20000	0.2500	0.7905	0.553	18.4	5.1	19.1	4.8	3.6	0.0	1.7	0.7	-1.6	0.0	-0.1	0.3
20000	0.4000	0.4941	0.185	21.9	14.0	26.0	13.6	13.0	2.0	3.6	2.7	2.1	1.2	0.4	0.1
20000	0.6500	0.3040	0.0243	44.8	36.2	57.6	35.4	35.2	1.6	7.7	5.6	5.0	-1.1	-0.5	0.0

Q^2 (GeV ²)	$d\sigma_{NC}/dQ^2$ (pb/GeV ²)	δ_{stat} (%)	δ_{sys} (%)	δ_{tot} (%)	δ_{unc} (%)	δ_{unc}^E (%)	δ_{unc}^h (%)	δ_{cor} (%)	$\delta_{cor}^{E^+}$ (%)	$\delta_{cor}^{\theta^+}$ (%)	$\delta_{cor}^{h^+}$ (%)	$\delta_{cor}^{N^+}$ (%)	$\delta_{cor}^{B^+}$ (%)
200	$1.830 \cdot 10^1$	0.9	3.8	3.9	3.4	0.2	0.4	1.8	-0.3	-1.7	-0.2	-0.2	0.2
250	$1.090 \cdot 10^1$	0.9	3.9	4.0	3.5	0.9	0.2	1.6	0.7	-1.5	0.1	0.2	0.2
300	$7.174 \cdot 10^0$	1.0	4.2	4.4	3.7	1.6	0.0	2.0	0.9	-1.8	0.1	0.0	0.2
400	$3.469 \cdot 10^0$	1.2	3.9	4.1	3.6	1.5	0.1	1.4	0.7	-1.3	0.0	0.1	0.2
500	$2.137 \cdot 10^0$	1.4	3.9	4.2	3.7	1.4	0.1	1.3	0.7	-1.0	-0.2	0.2	0.2
650	$1.118 \cdot 10^0$	1.7	4.0	4.4	3.6	1.4	0.2	1.7	1.2	-1.2	0.3	0.3	0.2
800	$6.269 \cdot 10^{-1}$	2.1	4.2	4.7	4.0	2.0	0.1	1.4	0.8	-1.1	0.1	-0.1	0.3
1000	$3.632 \cdot 10^{-1}$	2.4	3.6	4.3	3.5	0.9	0.1	0.8	0.4	-0.6	0.2	0.2	0.3
1200	$2.266 \cdot 10^{-1}$	2.9	4.0	4.9	3.7	1.3	0.2	1.4	0.9	-0.9	0.4	0.3	0.3
1500	$1.196 \cdot 10^{-1}$	3.6	4.4	5.6	4.0	1.8	0.7	1.7	0.8	-0.8	-1.0	-0.7	0.3
2000	$5.995 \cdot 10^{-2}$	4.2	4.4	6.0	4.2	1.5	0.1	1.3	0.9	0.7	0.5	0.2	0.4
3000	$1.950 \cdot 10^{-2}$	4.1	4.5	6.1	4.3	1.8	0.5	1.3	1.1	-0.3	0.3	0.4	0.4
5000	$5.056 \cdot 10^{-3}$	5.3	4.6	7.0	4.5	2.2	0.3	1.0	0.7	-0.6	-0.2	-0.2	0.5
8000	$1.132 \cdot 10^{-3}$	8.9	6.3	10.9	6.2	5.0	0.0	1.1	1.0	-0.2	0.0	0.2	0.6
12000	$2.961 \cdot 10^{-4}$	16.0	8.3	18.0	8.1	7.1	0.1	1.7	1.5	-0.2	0.0	0.0	0.8
20000	$4.380 \cdot 10^{-5}$	32.1	11.4	34.1	11.3	10.6	0.1	1.8	1.6	0.2	0.1	0.0	0.6

Table C.5: The NC e^+p single differential cross section $d\sigma_{NC}/dQ^2$ for RH polarised positrons ($P_e = 33.6\%$) with the statistical (δ_{stat}), systematic (δ_{sys}) and total (δ_{tot}) errors. Also shown are the total uncorrelated systematic (δ_{unc}) errors and two of its contributions: the electron energy error (δ_{unc}^E) and the hadronic energy error (δ_{unc}^h). The effect of the other uncorrelated systematic errors is included in (δ_{unc}). The table also provides the correlated systematic error (δ_{cor}) and its contributions from a positive variation of one standard deviation of the error on the electron energy ($\delta_{cor}^{E^+}$) and polar angle ($\delta_{cor}^{\theta^+}$), of the hadronic energy error ($\delta_{cor}^{h^+}$), of the error due to noise subtraction ($\delta_{cor}^{N^+}$) and background subtraction ($\delta_{cor}^{B^+}$) (δ_{unc}^h). The effect of the other correlated systematic errors is included in (δ_{cor}). The normalisation uncertainty of 1.4% is not included in the errors.

Q^2 (GeV ²)	$d\sigma_{NC}/dQ^2$ (pb/GeV ²)	δ_{stat} (%)	δ_{sys} (%)	δ_{tot} (%)	δ_{unc} (%)	δ_{unc}^E (%)	δ_{unc}^h (%)	δ_{cor} (%)	δ_{cor}^{E+} (%)	$\delta_{cor}^{\theta+}$ (%)	δ_{cor}^{h+} (%)	δ_{cor}^{N+} (%)	δ_{cor}^{B+} (%)
200	$1.883 \cdot 10^1$	1.0	3.8	4.0	3.4	0.3	0.4	1.8	-0.4	-1.7	-0.2	-0.3	0.2
250	$1.116 \cdot 10^1$	1.0	3.8	4.0	3.5	0.8	0.2	1.6	0.7	-1.4	-0.1	0.1	0.2
300	$7.460 \cdot 10^0$	1.2	4.3	4.4	3.8	1.7	0.0	2.0	0.9	-1.8	0.1	0.0	0.2
400	$3.597 \cdot 10^0$	1.4	3.9	4.2	3.7	1.5	0.1	1.4	0.7	-1.2	0.1	0.2	0.2
500	$2.108 \cdot 10^0$	1.6	3.9	4.2	3.7	1.4	0.1	1.3	0.7	-1.0	-0.3	0.2	0.2
650	$1.065 \cdot 10^0$	2.0	4.0	4.5	3.6	1.4	0.2	1.8	1.2	-1.2	0.3	0.3	0.2
800	$6.098 \cdot 10^{-1}$	2.4	4.2	4.8	3.9	1.9	0.1	1.4	0.8	-1.1	0.0	-0.2	0.3
1000	$3.594 \cdot 10^{-1}$	2.8	3.7	4.6	3.5	1.0	0.1	1.0	0.5	-0.7	0.2	0.2	0.3
1200	$2.177 \cdot 10^{-1}$	3.4	4.0	5.2	3.7	1.4	0.3	1.4	0.9	-0.9	0.4	-0.3	0.3
1500	$1.310 \cdot 10^{-1}$	4.4	4.3	6.2	4.0	1.8	0.7	1.6	0.8	-0.9	-0.9	-0.6	0.3
2000	$5.763 \cdot 10^{-2}$	5.0	4.4	6.6	4.2	1.6	0.1	1.3	0.9	0.6	0.4	-0.2	0.4
3000	$1.989 \cdot 10^{-2}$	4.6	4.6	6.5	4.4	2.0	0.5	1.4	1.2	-0.4	0.3	0.5	0.4
5000	$4.460 \cdot 10^{-3}$	6.4	4.7	8.0	4.6	2.3	0.3	1.1	0.7	-0.6	-0.2	-0.3	0.5
8000	$9.834 \cdot 10^{-4}$	10.8	6.4	12.6	6.3	5.1	0.0	1.3	1.0	-0.2	0.0	0.2	0.7
12000	$2.122 \cdot 10^{-4}$	21.6	8.5	23.2	8.3	7.3	0.1	1.8	1.5	-0.2	0.0	0.0	1.0
20000	$5.015 \cdot 10^{-6}$	114.2	11.6	114.8	11.5	10.8	0.1	1.9	1.7	0.2	0.1	0.0	0.8

Table C.6: The NC e^+p single differential cross section $d\sigma_{NC}/dQ^2$ for LH polarised positrons ($P_e = -40.2\%$) with the statistical (δ_{stat}), systematic (δ_{sys}) and total (δ_{tot}) errors. Also shown are the total uncorrelated systematic (δ_{unc}) errors and two of its contributions: the electron energy error (δ_{unc}^E) and the hadronic energy error (δ_{unc}^h). The effect of the other uncorrelated systematic errors is included in (δ_{unc}). The table also provides the correlated systematic error (δ_{cor}) and its contributions from a positive variation of one standard deviation of the error on the electron energy (δ_{cor}^{E+}) and polar angle ($\delta_{cor}^{\theta+}$), of the hadronic energy error (δ_{cor}^{h+}), of the error due to noise subtraction (δ_{cor}^{N+}) and background subtraction (δ_{cor}^{B+}) (δ_{unc}^h). The effect of the other correlated systematic errors is included in (δ_{cor}). The normalisation uncertainty of 1.4% is not included in the errors.

Q^2 (GeV ²)	$d\sigma_{NC}/dQ^2$ (pb/GeV ²)	δ_{stat} (%)	δ_{sys} (%)	δ_{tot} (%)	δ_{unc} (%)	δ_{unc}^E (%)	δ_{unc}^h (%)	δ_{cor} (%)	$\delta_{cor}^{E^+}$ (%)	$\delta_{cor}^{\theta^+}$ (%)	$\delta_{cor}^{h^+}$ (%)	$\delta_{cor}^{N^+}$ (%)	$\delta_{cor}^{B^+}$ (%)
200	$1.858 \cdot 10^1$	0.8	3.2	3.3	2.6	0.5	0.4	1.8	-0.4	-1.8	0.2	0.4	0.2
250	$1.099 \cdot 10^1$	0.8	3.2	3.4	2.8	1.2	0.1	1.7	0.8	-1.5	0.2	-0.2	0.2
300	$7.154 \cdot 10^0$	1.0	3.6	3.8	3.1	1.7	0.4	1.9	0.9	-1.6	-0.4	-0.4	0.2
400	$3.582 \cdot 10^0$	1.2	3.2	3.4	2.8	1.2	0.1	1.5	0.9	-1.2	-0.2	-0.3	0.2
500	$2.024 \cdot 10^0$	1.4	3.4	3.7	3.0	1.6	0.3	1.6	0.8	-1.3	0.3	0.2	0.2
650	$1.056 \cdot 10^0$	1.7	3.3	3.7	3.0	1.5	0.2	1.5	0.8	-1.2	-0.2	0.2	0.2
800	$6.377 \cdot 10^{-1}$	2.0	3.1	3.7	2.8	1.3	0.2	1.4	0.8	-1.0	0.2	-0.2	0.3
1000	$3.732 \cdot 10^{-1}$	2.4	3.2	4.0	3.0	1.6	0.1	1.1	0.7	-0.7	-0.1	0.2	0.4
1200	$2.315 \cdot 10^{-1}$	2.9	3.4	4.5	3.1	1.5	0.1	1.5	0.8	-1.2	-0.2	-0.2	0.3
1500	$1.232 \cdot 10^{-1}$	3.5	3.2	4.8	3.1	1.6	0.2	0.9	0.8	-0.1	0.1	0.3	0.3
2000	$6.030 \cdot 10^{-2}$	4.2	3.8	5.7	3.4	1.5	0.4	1.7	1.3	-0.8	-0.4	0.4	0.4
3000	$2.098 \cdot 10^{-2}$	3.8	3.7	5.3	3.5	1.0	0.6	1.4	0.8	-0.6	-0.5	-0.6	0.4
5000	$4.880 \cdot 10^{-3}$	5.3	4.2	6.8	4.1	2.6	0.5	1.1	0.6	0.4	0.6	0.5	0.4
8000	$1.520 \cdot 10^{-3}$	7.4	5.0	9.0	4.9	3.8	0.3	1.2	1.0	-0.3	-0.4	-0.2	0.4
12000	$4.638 \cdot 10^{-4}$	12.2	7.8	14.5	7.6	7.0	0.3	1.5	1.2	0.3	0.5	0.5	0.5
20000	$9.105 \cdot 10^{-5}$	21.5	9.7	23.6	9.6	9.1	0.0	1.6	1.6	0.3	0.0	0.0	0.3

Table C.7: The NC e^-p single differential cross section $d\sigma_{NC}/dQ^2$ for RH polarised electrons ($P_e = 37.0\%$) with the statistical (δ_{stat}), systematic (δ_{sys}) and total (δ_{tot}) errors. Also shown are the total uncorrelated systematic (δ_{unc}) errors and two of its contributions: the electron energy error (δ_{unc}^E) and the hadronic energy error (δ_{unc}^h). The effect of the other uncorrelated systematic errors is included in (δ_{unc}). The table also provides the correlated systematic error (δ_{cor}) and its contributions from a positive variation of one standard deviation of the error on the electron energy ($\delta_{cor}^{E^+}$) and polar angle ($\delta_{cor}^{\theta^+}$), of the hadronic energy error ($\delta_{cor}^{h^+}$), of the error due to noise subtraction ($\delta_{cor}^{N^+}$) and background subtraction ($\delta_{cor}^{B^+}$) (δ_{unc}^h). The effect of the other correlated systematic errors is included in (δ_{cor}). The normalisation uncertainty of 2.1% is not included in the errors.

Q^2 (GeV ²)	$d\sigma_{NC}/dQ^2$ (pb/GeV ²)	δ_{stat} (%)	δ_{sys} (%)	δ_{tot} (%)	δ_{unc} (%)	δ_{unc}^E (%)	δ_{unc}^h (%)	δ_{cor} (%)	δ_{cor}^{E+} (%)	$\delta_{cor}^{\theta+}$ (%)	δ_{cor}^{h+} (%)	δ_{cor}^{N+} (%)	δ_{cor}^{B+} (%)
200	$1.840 \cdot 10^1$	0.6	3.2	3.3	2.6	0.6	0.4	1.8	-0.4	-1.7	0.2	0.4	0.2
250	$1.113 \cdot 10^1$	0.6	3.2	3.3	2.8	1.2	0.1	1.6	0.7	-1.4	0.2	-0.2	0.2
300	$7.160 \cdot 10^0$	0.7	3.6	3.7	3.1	1.7	0.4	1.9	0.9	-1.6	-0.3	-0.3	0.2
400	$3.625 \cdot 10^0$	0.8	3.1	3.2	2.8	1.2	0.2	1.5	0.9	-1.1	-0.2	-0.3	0.2
500	$2.128 \cdot 10^0$	0.9	3.4	3.5	3.0	1.6	0.3	1.6	0.8	-1.3	0.3	0.3	0.2
650	$1.104 \cdot 10^0$	1.1	3.3	3.4	2.9	1.5	0.2	1.4	0.8	-1.2	-0.2	0.2	0.2
800	$6.617 \cdot 10^{-1}$	1.3	3.1	3.4	2.8	1.2	0.3	1.3	0.8	-1.0	0.2	-0.2	0.3
1000	$3.779 \cdot 10^{-1}$	1.6	3.2	3.6	3.0	1.5	0.1	1.1	0.7	-0.7	-0.1	0.2	0.3
1200	$2.354 \cdot 10^{-1}$	1.9	3.4	3.9	3.1	1.4	0.1	1.4	0.7	-1.2	-0.2	-0.2	0.3
1500	$1.352 \cdot 10^{-1}$	2.2	3.2	3.9	3.1	1.5	0.2	0.9	0.8	-0.1	0.0	0.3	0.3
2000	$6.501 \cdot 10^{-2}$	2.7	3.7	4.6	3.4	1.4	0.4	1.6	1.3	-0.8	-0.3	0.4	0.4
3000	$2.257 \cdot 10^{-2}$	2.4	3.7	4.4	3.4	0.9	0.6	1.3	0.8	-0.6	-0.5	-0.6	0.3
5000	$5.919 \cdot 10^{-3}$	3.2	4.1	5.2	4.0	2.4	0.4	1.1	0.6	0.4	0.6	0.5	0.4
8000	$1.649 \cdot 10^{-3}$	4.7	4.9	6.8	4.7	3.6	0.3	1.2	1.0	-0.3	-0.3	-0.2	0.4
12000	$5.502 \cdot 10^{-4}$	7.5	7.6	10.7	7.5	6.8	0.3	1.5	1.2	0.4	0.5	0.5	0.4
20000	$1.090 \cdot 10^{-4}$	12.9	9.7	16.1	9.5	9.0	0.0	1.6	1.6	0.3	0.0	0.0	0.2

Table C.8: The NC e^-p single differential cross section $d\sigma_{NC}/dQ^2$ for LH polarised electrons ($P_e = -27.0\%$) with the statistical (δ_{stat}), systematic (δ_{sys}) and total (δ_{tot}) errors. Also shown are the total uncorrelated systematic (δ_{unc}) errors and two of its contributions: the electron energy error (δ_{unc}^E) and the hadronic energy error (δ_{unc}^h). The effect of the other uncorrelated systematic errors is included in (δ_{unc}). The table also provides the correlated systematic error (δ_{cor}) and its contributions from a positive variation of one standard deviation of the error on the electron energy (δ_{cor}^{E+}) and polar angle ($\delta_{cor}^{\theta+}$), of the hadronic energy error (δ_{cor}^{h+}), of the error due to noise subtraction (δ_{cor}^{N+}) and background subtraction (δ_{cor}^{B+}) (δ_{unc}^h). The effect of the other correlated systematic errors is included in (δ_{cor}). The normalisation uncertainty of 2.1% is not included in the errors.

Q^2 (GeV ²)	x	$x\tilde{F}_3$	δ_{stat}	δ_{sys}	δ_{tot}
1500	0.020	0.0384	0.018	0.024	0.029
1500	0.032	0.0691	0.018	0.031	0.036
1500	0.050	0.0505	0.025	0.041	0.048
1500	0.080	0.0456	0.037	0.061	0.071
1500	0.130	-0.0650	0.061	0.082	0.102
1500	0.180	-0.1173	0.079	0.110	0.135
1500	0.250	-0.0846	0.097	0.145	0.174
1500	0.400	0.1937	0.113	0.202	0.231
1500	0.650	-0.1207	0.046	0.079	0.091
5000	0.050	0.1010	0.016	0.017	0.023
5000	0.080	0.0876	0.014	0.018	0.023
5000	0.130	0.1215	0.021	0.026	0.033
5000	0.180	0.0721	0.027	0.032	0.042
5000	0.250	0.0678	0.033	0.048	0.058
5000	0.400	0.0500	0.035	0.052	0.063
5000	0.650	0.0149	0.015	0.029	0.033
12000	0.180	0.1707	0.038	0.015	0.041
12000	0.250	0.1534	0.029	0.017	0.034
12000	0.400	0.1179	0.031	0.037	0.048
12000	0.650	-0.0107	0.015	0.019	0.024
Q^2 (GeV ²)	x	$xF_3^{\gamma Z}$	δ_{stat}	δ_{sys}	δ_{tot}
1500	0.020	0.34	0.16	0.21	0.26
1500	0.032	0.62	0.16	0.28	0.33
1500	0.050	0.36	0.06	0.06	0.08
1500	0.080	0.32	0.05	0.06	0.08
1500	0.130	0.44	0.08	0.09	0.12
1500	0.180	0.37	0.07	0.05	0.08
1500	0.250	0.37	0.06	0.04	0.07
1500	0.400	0.29	0.06	0.08	0.10
1500	0.650	-0.01	0.03	0.04	0.05

Table C.9: The upper part of the table shows the generalised structure function $x\tilde{F}_3$ with statistical (δ_{stat}), systematic (δ_{sys}) and total (δ_{tot}) absolute errors. The normalisation uncertainties of the e^+p and e^-p data are included in the systematic error. The lower part of the table shows the averaged structure function $xF_3^{\gamma Z}$ at $Q^2 = 1500$ GeV². To define the average, the measurements at higher Q^2 have been corrected down to $Q^2 = 1500$ using a QCD model (see section 9.5)

List of Figures

2.1	Diagrams of electron proton scattering via photon or Z exchange for neutral current interactions (a) and W exchange for charged current interactions (b). The four-momentum vectors of the particles are given in parentheses.	6
2.2	Observation of scaling: independence of the structure function $\nu W_2 = F_2$ of Q^2 . The Bjorken variable x is kept fixed, $x = 0.25$	9
2.3	Loop diagrams.	11
2.4	Measurement of the proton structure function $F_2(x, Q^2)$ (solid points) as a function of Q^2 at fixed x by H1 and fixed target experiments BCDMS and NMC. The result are compared with the corresponding Standard Model expectation determined from the H1 PDF 2000 fit [85] (error bands).	13
2.5	Schematic representation of photon-proton scattering for increasing photon virtuality Q^2 . As Q^2 increases, the photon probes smaller transverse distances and is able to resolve the structure of the proton. With further increase in Q^2 , more quarks and gluons are resolved inside the proton.	14
2.6	Sketch of the variation of F_2 as a function of x and Q^2	15
2.7	Factorisation in QCD.	15
2.8	Splitting functions P_{ij} , denoting the probabilities for a parton j with momentum fraction y to emit a parton i with momentum fraction x	16
2.9	The H1 PDF 2000 fit [85] for the valence quarks xu_v and xd_v , the sea quarks xS and the gluon xg . The distributions are shown at $Q^2 = 10 \text{ GeV}^2$. The bands represent estimates of the experimental and theoretical uncertainties. Gluon and sea quark densities are scaled down by a factor of 20.	17
2.10	Helicity and angular momentum conservation at the hadronic vertex in Quark Parton Model (QPM) and Quantum Chromodynamics (QCD).	18
2.11	Q^2 dependence of κ_Z , the ratio of the couplings and propagators of the Z^0 to those of the photon, and of κ_Z^2	20
2.12	Measurement of the CC cross section term ϕ_{CC} by H1 as function of $(1 - y)^2$, together with a NLO QCD fit [84].	23
2.13	The Q^2 dependencies of the NC (circles) and CC (squares) cross sections $d\sigma/dQ^2$, measured with the H1 detector [85]. The e^+p collisions are shown as full symbols, e^-p as open symbols. The results are compared to the Standard Model expectations determined from the H1 PDF 2000 fit (bands).	24
2.14	The dependence of the e^-p and e^+p CC cross sections on the lepton beam polarisation, P_e . The data [117, 118] are compared to the Standard Model prediction obtained using the H1 2000 PDF fit.	25

2.15	NC cross sections $d^2\sigma/dxdQ^2$ at $x = 0.2$ as a function of Q^2 for different charge and polarisation assignments. The left part shows the cross sections normalised to the one-photon exchange which is independent of charge and polarisation, right part displays the absolute cross sections [49].	26
2.16	Results of the fit to vector and axial-vector electroweak couplings of light quarks for up -quarks assuming fixed $down$ -quark couplings (left) and for $down$ -quarks assuming fixed up -quark couplings with different degree of longitudinal polarisation [49].	26
2.17	Diagrams showing the different LO QED corrections to the Born diagram.	27
3.1	The HERA storage ring with two collider experiments (H1, ZEUS) and two fixed target experiments (HERA-B [44], HERMES [45]). On the right-hand side of the picture an enlarged view of the pre-accelerators for HERA (DESY II/III and PETRA) is shown.	30
3.2	The H1 integrated luminosity as function of time for HERA I and HERA II periods, up to the end of the year 2005.	31
3.3	The left half of the rotator pair in the East hall (HERMES experiment). The magnets BH03 and BH02 are not part of the rotator, but are needed to complete the spin rotation into the longitudinal direction. On the opposite side of the IP a similar magnet arrangement with reversed radial fields (BF and BG magnets) brings the polarisation back to the vertical direction.	34
3.4	Schematic view of the HERA ring after upgrade.	35
3.5	Typical HERA II longitudinal and transverse polarisation as a function of time.	36
3.6	Schematic overview of the Longitudinal Polarimeter in the HERA East section.	36
3.7	Layout of the longitudinal polarimeter at HERA. The laser beam is brought inside the electron vacuum beam pipe by an entrance window. Compton photons are scattered back in the direction of the electron beam within a very narrow angular cone. The back-scattered photons escape the beam pipe through an exit window located at the end of the right section and enter a calorimeter ≈ 60 m downstream from the laser beam-electron interaction point. An optical bench is located on the other side of the interaction point to stop the laser beam and to measure the light polarisation.	37
3.8	Spectra collected in multi-photon mode for the spin- $\frac{1}{2}$ (dashed histogram) and spin- $\frac{3}{2}$ (solid histogram) configurations for a specific electron bunch with polarisation of 0.59.	38
3.9	Synchrotron radiation in the horizontal plane in the region around the H1 detector shown as tangential lines. Angles with respect to the H1 z -axis are enlarged. The high amount of synchrotron radiation leads to a increased pressure near the absorber.	39
3.10	Schematic view of the H1 detector. The H1 coordinate system is indicated in the top right corner.	41

3.11	Longitudinal cross section of the LAr calorimeter. The upper half shows the sampling structure with the orientation of absorber plates. The read-out cell structure is indicated in the lower part. “WWP” denotes the nominal interaction point.	45
3.12	Transverse cross section of a central barrel (CB2) wheel of the LAr calorimeter, viewed along the proton beam direction.	45
3.13	The profile of lead sheets (electromagnetic SpaCal).	48
3.14	The module of the electromagnetic SpaCal calorimeter.	48
3.15	Principle of drift and multiwire proportional chambers: Charged particles interact with the gas molecules and produce positive ions and electrons. With HV applied between the anode wires and the cathode plane the ionised electrons are accelerated towards the anode wire and positive ions drift to the cathode.	50
3.16	The side view of the tracking system.	50
3.17	Cross-section view of the central track detector.	52
3.18	Illustration of mirror tracks in the central track detector, resulting from the left-right ambiguity in drift chambers. The tilted anode wire planes cause mirror track segments to neither link with track segments in neighbouring drift cells nor to point to the event vertex, allowing for mirror tracks to be easily identified.	53
3.19	Side view of the CIP chamber in the rz -plane: The charged particle deposits charge, that cannot discharge immediately due to the high resistance of the carbon coating. Thus, a current is induced on the cathode pad near the accumulation of the charge.	54
3.20	The Forward Tracking Detector.	54
3.21	Division of the central muon system into modules.	55
3.22	The ToF system.	56
3.23	Layout of the Photon Detector in the tunnel: the γ beam axis is 13 cm below the proton beam pipe. An absorber of roughly $2X_0$ reduces the amount of synchrotron radiation (and the produced heat) directly hitting the presampler and the main calorimeter. All the detectors are mounted on a vertically movable table.	57
3.24	Illustration of the four-level trigger system of the H1 experiment. The status of the pipelines buffering the event information is shown as well as the dead-time generated by the different trigger levels during nominal operation of the H1 experiment.	59
3.25	Schematic overview of the H1 LAr trigger. See text for details.	61
3.26	Arrangement of Big Towers in the LAr calorimeter. Each tower points toward the nominal interaction vertex.	62
3.27	The projective geometry of the CIP is shown. The event vertex is reconstructed by building a histogram of the possible z origins of tracks and identifying the event vertex as lying in the bin with the highest population.	64
3.28	A schematic overview of the data storage levels used by the H100 Project.	68
4.1	Examples of leading order diagrams for direct (left) and resolved (right) photoproduction, contributing to NC DIS background.	72
4.2	Leading order diagram for lepton-pair production.	73

4.3	Leading order diagrams for the production of real W bosons via neutral current $ep \rightarrow eWX$ processes at HERA and the subsequent decay $W \rightarrow f\bar{f}'$	73
5.1	The resolution of reconstructed Q^2 (a) and x (b) as a function of y for different reconstruction methods. Q_{rec}^2 (Q_{gen}^2) and x_{rec} (x_{gen}) refer to the reconstructed (generated) values of Q^2 and x respectively.	79
5.2	The HERA coverage of the kinematic plane in comparison to previous fixed-target experiments.	80
6.1	Schematic view of the electron identification envelope cone.	82
6.2	Electron finding efficiency for data (full points) and simulation (histogram) as a function of the electron z impact (a) and φ angle between the electron impact point and the closest φ -crack (b).	84
6.3	Mean z_{vtx} as a function of run number in bins of equal luminosity.	85
6.4	The z_{vtx} distribution for data and Monte Carlo events before (a) and after reweighting of the MC (b). The simulation is normalised to the luminosity of the data.	86
6.5	An NC event with a nuclear interaction in the beam pipe by the hadronic final state. Tracks from the hadronic final state point to the vertex of the nuclear interaction. The electron track is originating from the primary ep interaction vertex.	86
6.6	Distribution of the z vertex for NC events with no DTRA electron track. The vertices determined from the hadronic final state give rise to the right tail of the z_{vtx} distribution caused by nuclear interactions in the beam pipe.	87
6.7	Distribution of the z “DTNV vertex”. The “DTNV vertex” is calculated from the extrapolation of the scattered electron DTNV track to the run average vertex. This vertex does not depend on nuclear interactions with the beam pipe by hadronic final state and is used for the vertex and electron track link efficiency studies.	88
6.8	Vertex and track link efficiency as a function of γ_h before (left) and after (right) MC correction. The data are shown by full points and simulation by open points.	88
6.9	Vertex and track link efficiency (left) and efficiency ratio of data to MC (right) as a function of polar, θ_{elec} , (top) and azimuthal, φ_{elec} , (bottom) angles of the scattered electron for data (full points) and simulation after correction (open points).	89
6.10	Vertex and track link finding efficiency in (Q^2, x) bins for the data (points) and for the MC after correction (curve).	90
6.11	Schematic view of the BBE octant. The filled areas indicate the regions where there is no overlap with the CB1 wheel viewed along the z axis. The hatched areas in the plot corresponds to the non-instrumented part of the BBE.	92
6.12	Illustration of the $\Delta\phi$ method.	93
6.13	Illustration of the $\Delta\varphi$ -method. $\Delta\varphi = \varphi_{track} - \varphi_{cluster}$, as a function of φ of the track for the z slice $-100 \text{ cm} < z_{LAr} < -80 \text{ cm}$, shown for data (full points). The curve represents results of the alignment fit.	94

6.14	Track cluster matching before (left) and after (right) alignment for data (full points), compared to the simulation (open points). The shifts Δx and Δy , determined using the $\Delta\phi$ -method, and Δz , using the $\Delta\theta$ -method, are shown as function of the z impact position of the scattered electron in the LAr calorimeter.	95
6.15	The track-cluster θ_e difference as a function of φ_e (a) and as a function of z impact position (b), shown for data (full points) and simulation (open) points.	96
6.16	Beam tilt: the inclination of the beam with respect to the H1 coordinate system in the $x - z$ (a) and the $y - z$ (b) plane.	96
6.17	Mean values of the ratio E_e/E_{DA} as a function of the stack number for data (full circles) and MC (open circles) before calibration.	98
6.18	Mean values of the ratio E_e/E_{DA} as a function of the z position of the electron impact point for data (full circles) and MC (open circles) before calibration. Bin zero corresponds to $z = -190$ cm.	98
6.19	Electron energy measurement after calibration for the data from 2004-05. The mean values of the ratio E_e/E_{DA} as a function of the stack number (see text) (a) and the z position of electron impact point (b). The ratio E_e/E_{DA} as a function of the φ angle between the electron impact point and closest φ -crack for BBE (c) and CB1-CB3 (d).	99
6.20	The resolution of the electron energy measurement as a function of the z -position of the impact point before calibration for data (full circles) and MC (open circles).	100
6.21	The resolution of the electron energy measurement as a function of the z -position of the impact point after calibration and a gaussian smearing of the energy in simulation.	100
6.22	Relative contributions from LAr calorimeter, tracks and SpaCal to the total y_h and the suppressed noise contribution relative to the measured y_h	102
6.23	Examples: The behaviour of the HADROO2 algorithm, given three starting situations involving tracks and clusters. On the first line, a 10 GeV track measured with a 4 % accuracy is kept and all the calorimetric information is removed. In the second line the track information is still kept, however the cylinder energy of 15 GeV is determined to contain a neutral component and it is reduced by the track energy. In the third line the track is not well measured (15 % accuracy) and the calorimetric information is used.	104
6.24	Distribution of p_T^{bal} for data and Monte Carlo events as function of the hadronic polar angle γ_h (upper two plots) and p_T^{DA} (bottom two plots) before (left) and after (right) the jet calibration. The dotted lines represent a $\pm 2\%$ uncertainty around unity.	105
6.25	The mean values of the transverse momentum balance, p_t^h/p_t^e , as a function of the transverse momentum of the scattered electron, p_t^e , (left) and y balance with respect to the double angle reference, y_h/y_{da} , as a function of γ_h . The error bands correspond to a 2% systematic uncertainty.	106
6.26	The efficiency to fire the <i>LAr_electron_1</i> TE by the scattered electron (a) and by the hadronic final state (b), presented in a $z - \varphi$ grid, using the 2005 e^-p data.	108

6.27	The efficiency of the trigger element $LAr_electron_1$, presented in a $z - \varphi$ grid using the 2005 e^-p data. The hatched areas indicate regions which are excluded because of low efficiency of the $LAr_electron_1$ TE.	109
6.28	T0 trigger efficiencies as a function of (a) φ_e and (b) z_{LAr} for the 2003-04 e^+p data period.	110
6.29	T0 trigger efficiencies as a function of (a) φ_e and (b) z_{LAr} for the 2004-05 e^-p data period.	110
6.30	Veto trigger efficiencies as a function of φ_e for (a) e^+p 2003-04 and (b) for e^-p 2005.	111
6.31	Trigger efficiency in the $z - \varphi$ plane of the electron impact position, shown for the 2003-04 e^+p (a) and for the 2005 e^-p (b) data taking periods. The hatched areas indicate regions which are excluded because of low trigger efficiency.	113
6.32	Distribution of p_T balance for events found by the background finders 0-8 (points). The line corresponds to genuine NC events from MC (see text).	114
6.33	Distribution of p_T balance for events found by background finders which are rejected by a pair of background finders (see text). The line corresponds to genuine NC events from MC.	116
7.1	The luminosity weighted polarisation profile for the 2003-04 e^+p (a) and the 2005 e^-p (b) data.	118
7.2	The event yield per nb^{-1} , shown as a function of the run number (a) for the 2003-04 e^+p and (c) for the 2005 e^-p data, and the event yield projection (b) for the 2003-04 e^+p and (d) for the 2005 e^-p	119
7.3	Distributions of the electron energy E'_e (left) and the polar angle θ_e (right) shown for selected events in the RH (a,b) and LH (c,d) e^+p data sets, and in the RH (e,f) and LH (g,h) e^-p data sets. The Monte Carlo (MC) contributions from the neutral current (NC) process and the ep background (bkg) processes are shown as open histograms with the latter contribution alone being shown as shaded histograms.	122
7.4	Distribution of electron energy E'_e in logarithmic scale. The contribution of the ep background, shown as shaded histogram, is very small and appears mainly at low electron energies.	123
7.5	Distribution of the electron azimuthal angle φ_e (a). The z impact position of the scattered electron in the LAr calorimeter shown in the ranges $-200 < z_{LAr} < 0$ cm (b), and $0 < z_{LAr} < 200$ cm (c).	123
7.6	Distributions of the longitudinal momentum balance $E - P_z$ (left) and the transverse momentum balance $P_{T,h}/P_{T,e}$ (right), shown for selected events in the RH (a,b) and LH (c,d) e^+p data sets, and in the RH (e,f) and LH (g,h) e^-p data sets. The Monte Carlo (MC) contributions from the neutral current (NC) process and the ep background (bkg) processes are shown as open histograms, with the latter contribution alone being shown as shaded histograms.	124

- 8.1 Schematic view of the migrations dynamics. The arrows show the path of an event from the GEN level to the REC level, thick squares are bins inside the measured phase-space, dotted squares are bins outside the measured phase-space; (a) is an illustration of the situation where an event has the same GEN and REC bin; (b) shows a GEN event being lost from the REC sample by being reconstructed outside of the measured phase-space; (c) illustrates an event smearing out of a GEN bin into a different REC bin; finally, (d) shows an event smearing into a REC bin from outside of the GEN phase-space, i.e. the generated quantities do not satisfy the x, Q^2 cut applied. 127
- 8.2 Acceptance (solid points), purity (open points) and stability (triangles) as function of x in bins of Q^2 . The solid lines indicate the minimum purity and stability of 30% and the dashed lines the required 20% for the acceptance. 129
- 8.3 Comparison of the reduced cross section measurements $\tilde{\sigma}(x, Q^2)$ using the $e\Sigma$ method (solid points) and DA method (open points) for the reconstruction of the kinematic variables method. 132
- 9.1 The NC reduced cross section $\tilde{\sigma}_{NC}(x, Q^2)$ for e^+p scattering with positive (full points) and negative (open points) longitudinal positron polarisation (data from years 2003-04). The inner and outer error bars represent the statistical and total errors, respectively. The 1.4% normalisation uncertainty is not included in the error bars. The curves show the predictions from the H1 2000 PDF fit. 136
- 9.2 The NC reduced cross section $\tilde{\sigma}_{NC}(x, Q^2)$ for e^-p scattering with positive (full points) and negative (open points) longitudinal electron polarisation (data from year 2005). The inner and outer error bars represent the statistical and total errors, respectively. The 2.1% normalisation uncertainty is not included in the error bars. The curves show the predictions from the H1 2000 PDF fit. 137
- 9.3 The unpolarised reduced cross sections $\tilde{\sigma}^\pm(x, Q^2)$ shown for the HERA II data (open/solid points) compared to the Standard Model (solid/dashed curves). The inner error bars represent the statistical uncertainties and the outer error bars represent the total errors. The normalisation uncertainties of 1.4% for e^+p data and 2.1% for e^-p data respectively are not included in the error bars. 138
- 9.4 The Q^2 dependence of the NC cross sections $d\sigma/dQ^2$ cross sections for e^+p scattering with positive longitudinal positron polarisation (a). The ratio of cross sections for data and theory is shown in (b). The data (full points) are compared to the predictions from the H1 2000 PDF fit (solid curve). The inner and outer error bars represent the statistical and total errors, respectively. The 1.4% normalisation uncertainty is not included in the error bars and indicated by the dashed lines in (b). 140

- 9.5 The Q^2 dependence of the NC cross sections $d\sigma/dQ^2$ cross sections for e^+p scattering with negative longitudinal positron polarisation (a). The ratio of cross sections for data and theory is shown in (b). The data (full points) are compared to the predictions from the H1 2000 PDF fit (solid curve). The inner and outer error bars represent the statistical and and total errors, respectively. The 1.4% normalisation uncertainty is not included in the error bars and indicated by the dashed lines in (b). 141
- 9.6 The Q^2 dependence of the NC cross sections $d\sigma/dQ^2$ cross sections for e^-p scattering with positive longitudinal electron polarisation. The ratio of cross sections for data and theory is shown in (b). The data (full points) are compared to the predictions from the H1 2000 PDF fit (solid curve). The inner and outer error bars represent the statistical and and total errors, respectively. The 2.1% normalisation uncertainty is not included in the error bars and indicated by the dashed lines in (b). 142
- 9.7 The Q^2 dependence of the NC cross sections $d\sigma/dQ^2$ cross sections for e^-p scattering with negative longitudinal electron polarisation (a). The ratio of cross sections for data and theory is shown in (b). The data (full points) are compared to the predictions from the H1 2000 PDF fit (solid curve). The inner and outer error bars represent the statistical and and total errors, respectively. The 2.1% normalisation uncertainty is not included in the error bars and indicated by the dashed lines in (b). 143
- 9.8 The Q^2 dependence of the NC (open symbols) and CC (solid symbols) unpolarised cross sections $d\sigma/dQ^2$ are shown for the 2003-04 e^+p (stars) and 2005 e^-p (triangles) measurements. The data are compared to the Standard Model expectations determined from the H1 PDF 2000 fit. The normalisation uncertainties of 1.4% for e^+p data and 2.1% for e^-p data respectively are not included in the error bars. 144
- 9.9 The Q^2 dependence of the NC cross section ratio $\frac{d\sigma}{dQ^2}$ (RH) / $\frac{d\sigma}{dQ^2}$ (LH) for the (a) e^+p scattering and (b) e^-p scattering. The inner error bars represent the statistical uncertainties and the outer error bars represent the total errors. The normalisation uncertainty is not included in the error bars and is instead shown as dashed lines. The data (solid points) are compared to the Standard Model prediction (solid curve). 146
- 9.10 The Q^2 dependence of the combined $e^\pm p$ LH and RH NC cross section ratio R . The inner error bars represent the statistical uncertainties and the outer error bars represent the total errors. The normalisation uncertainty is not included in the error bars and is instead shown as dashed lines. The data (solid points) are compared to the Standard Model prediction. 147
- 9.11 Measurements of the polarisation asymmetries A^\pm by this analysis (a) and combined with ZEUS (b). The error bars denote the total uncertainty which is dominated by the uncorrelated error contributions. The curves describe the theoretical prediction using the H1 PDF 2000 fit. 148

- 9.12 Unpolarised reduced cross sections $\tilde{\sigma}^{\pm}(x, Q^2)$ function of x for various values of Q^2 are shown in (a) for the HERA II data (open/solid points) compared to the Standard Model (solid/dashed curves). The structure function $x\tilde{F}_3$ evaluated using the HERA II data is shown in (b) (solid points) compared to the Standard Model (solid curve). The inner error bars represent the statistical uncertainties and the outer error bars represent the total errors. The normalisation uncertainty is included in the error bars for (b) only. 149
- 9.13 The structure function $x F_3^{\gamma Z}$ extracted from HERA II data (solid and open points) is shown in (a) for three Q^2 bins together with the Standard Model expectation (full, dashed and dotted curves). In (b) the data are transformed to $Q^2 = 1500 \text{ GeV}^2$ and combined in each x bin. The inner error bars represent the statistical uncertainties and the outer error bars represent the total errors. The normalisation uncertainty is included in the error bars. 151
- 9.14 The structure function $x\tilde{F}_3$ evaluated using combined HERA I and HERA II data is shown in (a) (solid points) compared to the Standard Model (solid curve). The structure function $x F_3^{\gamma Z}$ extracted from HERA I and HERA II data (solid and open points) is shown in (b) together with the Standard Model expectation (solid curve). The inner error bars represent the statistical uncertainties and the outer error bars represent the total errors. The normalisation uncertainty is included in the error bars. 152
- 9.15 The structure function $x F_3^{\gamma Z}$ extracted from all HERA I and the HERA II H1 and ZEUS data (solid and open points) is shown in (a) for three Q^2 bins together with the Standard Model expectation (full, dashed and dotted curves). In (b) the data are transformed to $Q^2 = 1500 \text{ GeV}^2$ and combined in each x bin. The inner error bars represent the statistical uncertainties and the outer error bars represent the total errors. The normalisation uncertainty is included in the error bars. 153
- B.1 Example of a NC event with high Q^2 in the H1 Detector from 2003-05 data taking. 161
- B.2 Example of a CC event with high Q^2 in the H1 detector from 2003-05 data taking. 161
- B.3 Cosmic (top) and halo-muon (bottom) events in the H1 detector. . . 162
- B.4 Beam-gas event in the H1 detector. 162

List of Tables

3.1	Operational parameters of HERA I and HERA II as it was achieved in 2000 and 2005, respectively.	32
3.2	Geometrical acceptances of the individual tracking detectors in the forward, central and backward regions of the H1 detector; the minimum and maximum polar angles of charged particles within the detector acceptances are referring to the nominal interaction point.	51
3.3	The significance is set to the given value if the number of tracks in the central region is S times higher than the number of backward and forward tracks.	64
3.4	The multiplicity is set to the described values if the number of tracks (M) is higher than the presented threshold.	65
6.1	The estimator variables used by the electron finding algorithm. Each estimator is briefly described and the cut values are noted (see text).	83
6.2	The alignment parameters of the LAr calorimeter.	94
6.3	NC trigger elements and their monitor triggers	107
6.4	Veto efficiencies.	112
6.5	Background finding algorithms [98] for halo-muons and cosmic muons.	115
7.1	Table of luminosities and luminosity weighted average longitudinal polarisations, for the data sets presented in this analysis.	118
7.2	Run selection requirements related to data taking conditions and operational status of the detector systems.	119
8.1	Binning in x and Q^2	125
8.2	The combination of the Q^2 bins for the extraction of the structure function xF_3 . Given are the Q^2 bin centres of the initial bins, Q_1^2, Q_2^2 and Q_3^2 , and the bin centres of the combined bins Q_c^2 . The last column lists the bin centres in x	133
A.1	Regions excluded from the analysis due to low trigger efficiency. . . .	159

C.1 The NC e^+p double differential cross section $d^2\sigma_{NC}/dQ^2dx$ for RH polarised positrons ($P_e = 33.6\%$) with the statistical (δ_{stat}), systematic (δ_{sys}) and total (δ_{tot}) errors. Also shown are the total uncorrelated systematic (δ_{unc}) errors and two of its contributions: the electron energy error (δ_{unc}^E) and the hadronic energy error (δ_{unc}^h). The effect of the other uncorrelated systematic errors is included in (δ_{unc}). The table also provides the correlated systematic error (δ_{cor}) and its contributions from a positive variation of one standard deviation of the error on the electron energy ($\delta_{cor}^{E^+}$) and polar angle ($\delta_{cor}^{\theta^+}$), of the hadronic energy error ($\delta_{cor}^{h^+}$), of the error due to noise subtraction ($\delta_{cor}^{N^+}$) and background subtraction ($\delta_{cor}^{B^+}$) (δ_{unc}^h). The effect of the other correlated systematic errors is included in (δ_{cor}). The normalisation uncertainty of 1.4% is not included in the errors. The table continues on the next 4 pages. . 164

C.2 The NC e^+p double differential cross section $d^2\sigma_{NC}/dQ^2dx$ for LH polarised positrons ($P_e = -40.2\%$) with the statistical (δ_{stat}), systematic (δ_{sys}) and total (δ_{tot}) errors. Also shown are the total uncorrelated systematic (δ_{unc}) errors and two of its contributions: the electron energy error (δ_{unc}^E) and the hadronic energy error (δ_{unc}^h). The effect of the other uncorrelated systematic errors is included in (δ_{unc}). The table also provides the correlated systematic error (δ_{cor}) and its contributions from a positive variation of one standard deviation of the error on the electron energy ($\delta_{cor}^{E^+}$) and polar angle ($\delta_{cor}^{\theta^+}$), of the hadronic energy error ($\delta_{cor}^{h^+}$), of the error due to noise subtraction ($\delta_{cor}^{N^+}$) and background subtraction ($\delta_{cor}^{B^+}$) (δ_{unc}^h). The effect of the other correlated systematic errors is included in (δ_{cor}). The normalisation uncertainty of 1.4% is not included in the errors. The table continues on the next 4 pages. . 169

C.3 The NC e^-p double differential cross section $d^2\sigma_{NC}/dQ^2dx$ for RH polarised electrons ($P_e = 37.0\%$) with the statistical (δ_{stat}), systematic (δ_{sys}) and total (δ_{tot}) errors. Also shown are the total uncorrelated systematic (δ_{unc}) errors and two of its contributions: the electron energy error (δ_{unc}^E) and the hadronic energy error (δ_{unc}^h). The effect of the other uncorrelated systematic errors is included in (δ_{unc}). The table also provides the correlated systematic error (δ_{cor}) and its contributions from a positive variation of one standard deviation of the error on the electron energy ($\delta_{cor}^{E^+}$) and polar angle ($\delta_{cor}^{\theta^+}$), of the hadronic energy error ($\delta_{cor}^{h^+}$), of the error due to noise subtraction ($\delta_{cor}^{N^+}$) and background subtraction ($\delta_{cor}^{B^+}$) (δ_{unc}^h). The effect of the other correlated systematic errors is included in (δ_{cor}). The normalisation uncertainty of 2.1% is not included in the errors. The table continues on the next 4 pages. . 174

C.4 The NC e^-p double differential cross section $d^2\sigma_{NC}/dQ^2dx$ for LH polarised electrons ($P_e = -27.0\%$) with the statistical (δ_{stat}), systematic (δ_{sys}) and total (δ_{tot}) errors. Also shown are the total uncorrelated systematic (δ_{unc}) errors and two of its contributions: the electron energy error (δ_{unc}^E) and the hadronic energy error (δ_{unc}^h). The effect of the other uncorrelated systematic errors is included in (δ_{unc}). The table also provides the correlated systematic error (δ_{cor}) and its contributions from a positive variation of one standard deviation of the error on the electron energy ($\delta_{cor}^{E^+}$) and polar angle ($\delta_{cor}^{\theta^+}$), of the hadronic energy error ($\delta_{cor}^{h^+}$), of the error due to noise subtraction ($\delta_{cor}^{N^+}$) and background subtraction ($\delta_{cor}^{B^+}$) (δ_{unc}^h). The effect of the other correlated systematic errors is included in (δ_{cor}). The normalisation uncertainty of 2.1% is not included in the errors. The table continues on the next 4 pages. 179

C.5 The NC e^+p single differential cross section $d\sigma_{NC}/dQ^2$ for RH polarised positrons ($P_e = 33.6\%$) with the statistical (δ_{stat}), systematic (δ_{sys}) and total (δ_{tot}) errors. Also shown are the total uncorrelated systematic (δ_{unc}) errors and two of its contributions: the electron energy error (δ_{unc}^E) and the hadronic energy error (δ_{unc}^h). The effect of the other uncorrelated systematic errors is included in (δ_{unc}). The table also provides the correlated systematic error (δ_{cor}) and its contributions from a positive variation of one standard deviation of the error on the electron energy ($\delta_{cor}^{E^+}$) and polar angle ($\delta_{cor}^{\theta^+}$), of the hadronic energy error ($\delta_{cor}^{h^+}$), of the error due to noise subtraction ($\delta_{cor}^{N^+}$) and background subtraction ($\delta_{cor}^{B^+}$) (δ_{unc}^h). The effect of the other correlated systematic errors is included in (δ_{cor}). The normalisation uncertainty of 1.4% is not included in the errors. 184

C.6 The NC e^+p single differential cross section $d\sigma_{NC}/dQ^2$ for LH polarised positrons ($P_e = -40.2\%$) with the statistical (δ_{stat}), systematic (δ_{sys}) and total (δ_{tot}) errors. Also shown are the total uncorrelated systematic (δ_{unc}) errors and two of its contributions: the electron energy error (δ_{unc}^E) and the hadronic energy error (δ_{unc}^h). The effect of the other uncorrelated systematic errors is included in (δ_{unc}). The table also provides the correlated systematic error (δ_{cor}) and its contributions from a positive variation of one standard deviation of the error on the electron energy ($\delta_{cor}^{E^+}$) and polar angle ($\delta_{cor}^{\theta^+}$), of the hadronic energy error ($\delta_{cor}^{h^+}$), of the error due to noise subtraction ($\delta_{cor}^{N^+}$) and background subtraction ($\delta_{cor}^{B^+}$) (δ_{unc}^h). The effect of the other correlated systematic errors is included in (δ_{cor}). The normalisation uncertainty of 1.4% is not included in the errors. 185

- C.7 The NC e^-p single differential cross section $d\sigma_{NC}/dQ^2$ for RH polarised electrons ($P_e = 37.0\%$) with the statistical (δ_{stat}), systematic (δ_{sys}) and total (δ_{tot}) errors. Also shown are the total uncorrelated systematic (δ_{unc}) errors and two of its contributions: the electron energy error (δ_{unc}^E) and the hadronic energy error (δ_{unc}^h). The effect of the other uncorrelated systematic errors is included in (δ_{unc}). The table also provides the correlated systematic error (δ_{cor}) and its contributions from a positive variation of one standard deviation of the error on the electron energy ($\delta_{cor}^{E^+}$) and polar angle ($\delta_{cor}^{\theta^+}$), of the hadronic energy error ($\delta_{cor}^{h^+}$), of the error due to noise subtraction ($\delta_{cor}^{N^+}$) and background subtraction ($\delta_{cor}^{B^+}$) (δ_{unc}^h). The effect of the other correlated systematic errors is included in (δ_{cor}). The normalisation uncertainty of 2.1% is not included in the errors. 186
- C.8 The NC e^-p single differential cross section $d\sigma_{NC}/dQ^2$ for LH polarised electrons ($P_e = -27.0\%$) with the statistical (δ_{stat}), systematic (δ_{sys}) and total (δ_{tot}) errors. Also shown are the total uncorrelated systematic (δ_{unc}) errors and two of its contributions: the electron energy error (δ_{unc}^E) and the hadronic energy error (δ_{unc}^h). The effect of the other uncorrelated systematic errors is included in (δ_{unc}). The table also provides the correlated systematic error (δ_{cor}) and its contributions from a positive variation of one standard deviation of the error on the electron energy ($\delta_{cor}^{E^+}$) and polar angle ($\delta_{cor}^{\theta^+}$), of the hadronic energy error ($\delta_{cor}^{h^+}$), of the error due to noise subtraction ($\delta_{cor}^{N^+}$) and background subtraction ($\delta_{cor}^{B^+}$) (δ_{unc}^h). The effect of the other correlated systematic errors is included in (δ_{cor}). The normalisation uncertainty of 2.1% is not included in the errors. 187
- C.9 The upper part of the table shows the generalised structure function $x\tilde{F}_3$ with statistical (δ_{stat}), systematic (δ_{sys}) and total (δ_{tot}) absolute errors. The normalisation uncertainties of the e^+p and e^-p data are included in the systematic error. The lower part of the table shows the averaged structure function $x\tilde{F}_3^{\gamma Z}$ at $Q^2 = 1\,500\text{ GeV}^2$. To define the average, the measurements at higher Q^2 have been corrected down to $Q^2 = 1\,500$ using a QCD model (see section 9.5) 188

Bibliography

- [1] E. D. Bloom *et al.* Phys. Rev. Lett. **23**, 930, 1969.
- [2] M. Bretenbach *et al.* Phys. Rev. Lett. **23**, 935, 1969.
- [3] E. Rutherford. The Scattering of α and β Particles by Matter and the Structure of the Atom. *Philosophical Magazine*, **21**, page 669, 1911.
- [4] J. D. Bjorken, Phys. Rev. **148**, 1467, 1966.
- [5] J. D. Bjorken. Phys. Rev. **179**, 1547, 1969.
- [6] F. Halzen and Alan D. Martin. Quarks and Leptons: An Introductory Course in Modern Particle Physics. New York, USA: Wiley (1984) 396p.
- [7] Particle Data Group, S. Eidelman *et al.*, Physics Letters **B592**, 1 (2004).
- [8] R. Frisch, O. Stern, Z. Physik **85** (1933) 4.
- [9] R. Hofstadter, Rev. Mod. Phys. **28** (1956) 214.
- [10] M. Gell-Mann, Phys. Lett. **8**, 214 (1964).
- [11] C. Zweig, CERN Report Nos. TH 401, 402 (1964).
- [12] C. G. Callan and D. J. Gross. High-Energy Electroproduction and the Constitution of the Electric Current. *Phys. Rev. Lett.*, **22**, pages 156-159, 1969.
- [13] A. A. Glazov Measurement of the Proton Structure Functions $F_2(x, Q^2)$ and $F_L(x, Q^2)$ with the H1 Detector at HERA, PhD thesis, Berlin.
- [14] CDHS Collaboration, H. Abramowicz *et al.*, Z. Phys. C **17** (1983) 283.
- [15] R. Brandelik *et al.* (TASSO collaboration), Evidence for Planar Events in e^+e^- Annihilation at High Energies, Phys. Lett. **B86**, 243-249, 1979.
- [16] Sterman *et al.* Handbook of Perturbative QCD, Rev. Mod. Phys., Vol. 67, No. 1, January 1995.
- [17] Yuri L. Dokshitzer, Calculation of the Structure Functions for Deep Inelastic Scattering and e^+e^- Annihilation by Perturbation Theory in Quantum Chromodynamics. Sov. Phys. JETP, 46:641-653, 1977.
- [18] V. N. Gribov and L. N. Lipatov. e^+e^- Pair Annihilation and Deep Inelastic ep Scattering in Perturbation Theory. Yad. Fiz., 15:1218-1237, 1972.
- [19] V. N. Gribov and L. N. Lipatov. Deep Inelastic ep Scattering in Perturbation Theory. Yad. Fiz., 15:781-807, 1972.

- [20] Guido Altarelli and G. Parisi. Asymptotic Freedom in Parton Language. Nucl. Phys., B126:298, 1977.
- [21] E. A. Kuraev, L. N. Lipatov, and Victor S. Fadin. Multi - Reggeon Processes in the Yang-Mills Theory. Sov. Phys. JETP, 44:433-450, 1976.
- [22] I. I. Balitsky and L. N. Lipatov. The Pommeranchuk Singularity in Quantum Chromodynamics. Sov. J. Nucl. Phys., 28:822-829, 1978.
- [23] Marcello Ciafaloni. Coherence Effects in Initial Jets at Small Q^2/s . Nucl. Phys., B296:49, 1988.
- [24] S. Catani, F. Fiorani, and G. Marchesini. QCD Coherence in Initial State Radiation. Phys. Lett. B234:339, 1990.
- [25] S. Catani, F. Fiorani, and G. Marchesini. Small x Behavior of Initial State Radiation in Perturbative QCD. Nucl. Phys., B336:18, 1990.
- [26] CTEQ Collaboration, edited by G. Sterman, HandBook of Perturbative QCD, Fermilab-Pub-93/094.
- [27] G. Altarelli and G. Martinelli. Transverse Momentum of Jets in Electroproduction from Quantum Chromodynamics. *Phys. Lett.*, **B76**, page 89, 1978.
- [28] R. G. Roberts. The Structure of the Proton. Cambridge University Press, 1990.
- [29] A. M. Cooper-Sarkar *et al.* Measurement of the Longitudinal Structure Function and the Small x Gluon Density of the Proton. *Z. Phys.*, **C39**, page 281, 1988.
- [30] BCDMS Collaboration, A. C. Benvenuti *et al.* A High Statistics Measurement of the Proton Structure Functions $F_2(x, Q^2)$ and R from Deep Inelastic Muon Scattering at High Q^2 . *Phys. Lett.*, **B223**, page 485, 1989.
- [31] NMC Collaboration, M. Arneodo *et al.* Measurement of the Proton and the Deuteron Structure Functions F_2^p and F_2^d . *Phys. Lett.*, **B364**, pages 107-115, 1995.
- [32] S. A. Rabinowitz *et al.* CCFR Collaboration. Measurement of the Strange Sea Distribution Using Neutrino Charm Production. *Phys. Rev. Lett.*, **70**, pages 134-137, 1993.
- [33] H. Abramowitz *et al.* CDHS Collaboration. Measurement of Neutrino and Antineutrino Structure in Hydrogen and Iron. *Z. Phys.*, **C25**, pages 29-43, 1984.
- [34] P. Berge *et al.* CDHS Collaboration. A Measurement of differential cross-sections and nucleon structure functions in charged-current neutrino interactions on iron. *Z. Phys.*, **C49**, pages 187-223, 1991.
- [35] A. D. Martin, R. G. Roberts, W. J. Stirling, R. S. Thorne, Eur. Phys. J. **C23** (2002) 73.
- [36] J. Pumplin, D. R. Stump, J. Huston, H. L. Lai, P. Nadolsky, W. K. Tung, JHEP **0207**, 012 (2002).
- [37] S. I. Alekhin, Phys. Rev. **D68** (2003), 014002.

- [38] D. I. Kazakov and A. V. Kotikov, Phys. Lett. **B291**, 171 (1992); W. L. van Neeven and E. B. Zijlstra, Phys. Lett. **B272**, 127 (1991).
- [39] A. Retey and J. A. Vermaseren, Nucl. Phys. **B604**, 281 (2001).
- [40] S. Alekhin, K. Melnikov, F. Petriello Fixed Target Drell-Yan Data and NNLO QCD Fits of Parton Distribution Functions, 2006, [hep-ph/0606237].
- [41] Griffiths, David J. Introduction to Elementary Particles. Wiley, John & Sons, Inc. ISBN 0-471-060386-4, 1987.
- [42] The H1 Collaboration, see <http://www-h1.desy.de/>.
- [43] The ZEUS Collaboration, see <http://www-zeus.desy.de/>.
- [44] The HERA-B Collaboration, see <http://www-hera-b.desy.de/>.
- [45] The HERMES Collaboration, see <http://www-hermes.desy.de/>.
- [46] A. A. Sokolov and I. M. Ternov, Sov. Phys. Dokl. 8 No. 12 (1964) 1203.
- [47] V. N. Baier, V. M. Katkov, Sov. Phys. JETP, **25**, 944 (1967).
- [48] V. Chekelian, C. Gwenlan and R. S. Thorne, The Structure Functions and Low x Working Group Summary, 2006. Proceedings of the DIS 2006, Tsukuba, Japan.
- [49] R. J. Cashmore *et al.*, Future Physics at HERA, Proceedings of the Workshop 1995/96, p. 163.
- [50] H. Spiesberger, Physics at High Q^2 With HERA II, Proceedings of the Ringberg Workshop, 2001.
- [51] G. Z. M. Berglund Spin-Orbit Maps and Electron Spin Dynamics for the Luminosity Upgrade Project at HERA, PhD thesis, Stockholm, 2001.
- [52] D. P. Barber *et al.*, The First Achievement of Longitudinal Spin Polarization in a High Energy Electron Storage Ring, Phys. Letts., **B343**, p.436 (1995).
- [53] J. Böhme, Precession Measurement with the Transverse Polarimeter at HERA II, Eur. Phys. J. **C 33**, 1067-1069 p, 2004
- [54] M. Beckmann *et al.* The Longitudinal Polarimeter at HERA, Nucl. Instr. Meth. **A 479**, 334 p, 2002 [arXiv:physics/0009047]
- [55] Z. Zhang, Electron Polarisation Measurement Using a Fabry-Perot Cavity at HERA, Proceedings of the 2001 HEP, [hep-ex/0201033]
- [56] H1 Collaboration: “The Luminosity upgrade 2000-2002”, see: <http://www-h1.desy.de/h1det/>.
- [57] V. Andreev *et al.* [H1 background working group], “Technical Report on the Beam Induced Backgrounds in the H1 Detector”, H1 note H1-IN-606 (10/2002).
- [58] V. Andreev *et al.* [H1 background working group], “Further Report on the Beam Induced Backgrounds in the H1 Detector”, H1 note H1-IN-607 (01/2003).

- [59] A. T. Doyle, G. Grindhammer, G. Ingelman, and H. Jung, editors. Lepton Pair Monte Carlo Generators for HERA Physics, 1999. Proceedings of the workshop Monte Carlo Generators for HERA Physics, DESY, Hambrug.
- [60] B. Heinemann, Measurement of Charged Current and Neutral Current Cross Sections in Positron Proton Collisions at $\sqrt{s} \approx 300\text{GeV}^2$, PhD thesis, Hamburg, 1999.
- [61] A. Mehta, New Track Based Electron Finder. Talk given at the High Q^2 Analysis meeting, Hamburg, October 2003.
- [62] H. Wellisch, J. Kubenka, H. Oberlack, and P. Schacht. H1 Internal Note H1-02/94-346.
- [63] I. Abt *et al.* "The Tracking, calorimeter and muon detectors of the H1 experiment at HERA." Nucl. Instrum. Meth. A 386, 1997.
- [64] B. Andrieu *et al.* "Electron/Pion Separation With the H1 LAr Calorimeters". Nucl. Instr. Meth. A, 344:492, 1994.
- [65] B. Andrieu *et al.* [H1 Calorimeter Group Collaboration], "The H1 Liquid Argon Calorimeter System", Nucl. Instrum. Meth. A 336:460, 1993.
- [66] B. Andrieu *et al.* Results From Pion Calibration Runs For the H1 Liquid Argon Calorimeter and Comparisons With Simulations. Nucl. Instr. Meth. A, 336:499, 1993.
- [67] K. Hagiwara *et al.* [Particle Data Group Collaboration], "Review of Particle Physics", Phys. Rev. D 66 (2002) 010001.
- [68] V. Shekelyan. "Simulation and Reconstruction in H1 Liquid Argon calorimetry". H1-internal note H1-04/93-288, 1993.
- [69] L. Goerlich and H. P. Wellisch. "Documentation of the LAr Clustering". H1-internal note H1-12/91-204, 1991.
- [70] C. Issever, K. Bornas, and D. Wegener. "An Improved Weighting Algorithm to Achieve Software Compensation in a Fine Grained LAr Calorimeter". H1-internal note H1-03/03-608, 2003.
- [71] H1: "Series of Tests of Fine Mesh Photomultiplier Tubes in Magnetic Fields of up to 1.2 Tesla", DESY-97-070, 1997.
- [72] H1: "The LED based Calibration System of the H1 Lead/Scintillating-Fiber Calorimeter", Nucl. Instr. Meth.
- [73] J. Ferencei "SpaCal cells after lumi upgrade modifications", HyperNews System of H1, 2001, Aug 22.
- [74] J. Bürger *et al.* "The Central Jet Chamber of the H1 Experiment." Nucl. Instrum. Meth., A 279, pages 217-222, 1989.
- [75] H. Bethe and W. Heitler. "On the Stopping of Fast Particles And On The Creation of Positive Electrons". Proc. Roy. Soc. Lond. A, 146:83, 1934.

- [76] M. Ch. Urban, The new CIP2k z -Vertex Trigger for the H1 Experiment at HERA, PhD thesis, Zürich, 2004.
- [77] J. K. Kohne *et al.* Nucl. Instrum. Meth. A 389 (1997) 128.
- [78] J. C. Bizot *et al.*, “Stratagy Studies for the H1 Topological L2-Trigger (L2TT)”, H1 internal note H1-IN-508 (01/1997).
- [79] T. Nicholls *et al.*, IEEE Trans. Nucl. Sci. 45 (1998) 810.
- [80] A. Baird *et al.*, IEEE Trans. Nucl. Sci. 48, (2001) 1276, hep-ex/0104010.
- [81] A. D. Martin, R. G. Roberts and W. J. Stirling. Parton distributions update. Phys. Lett., **B306**, pages 145-150, 1993. Erratum, Phys. Lett. **B309**, 1993, page 492.
- [82] S. Aid *et al.* [H1 Collaboration], Nucl. Phys. **B470** (1996) 3.
- [83] S. Aid *et al.* [H1 Collaboration], Phys. Lett. **B379** (1996) 319.
- [84] C. Adloff *et al.* [H1 Collaboration], Measurement of Neutral and Charged Current Cross-Sections in Positron-Proton Collisions at Large Momentum Transfer, arXiv:hep-ex/9908059.
- [85] C. Adloff *et al.* [H1 Collaboration], “Measurement and QCD Analysis of Neutral and Charged Current Cross Sections at HERA”, arXiv:hep-ex/0304003.
- [86] C. Adloff *et al.* Multi-Jet Event Rates in Deep Inelastic Scattering and Determination of the Strong Coupling Constant. Eur. Phys. J., C6:575-585, 1999.
- [87] H. Spiesberger A. Kwiatkowski and H.J.Mohring. HERACLES: An Event Generator for ep Interactions at HERA Energies Including Radiative Processes: Version 1.0. Comp. Phys. Comm., 69, pages 155-172, 1992.
- [88] G. A. Schuler and H. Spiesberger. DJANGO: The Interface for Event Generators HERACLES and LEPTO. In W. Buchmueller and G. Ingelman, Proceedings of the Workshop: Physics at HERA, volume 3, page 1419. DESY. 1992.
- [89] T. Sjostrand, L. Lonnblad and S. Mrenna, (2001), hep-ph/0108264.
- [90] G. Ingelman, Proceedings of the Workshop “Physics at HERA”, vol.3 eds. W. Buchmüller, G. Ingelman, DESY (1992) 1366.
- [91] L. Lönnblad, Comput. Phys. Commun. **71** (1992) 15.
- [92] T. Sjöstrand and M. Bengtsson, Comput. Phys. Commun. **43** (1987) 367.
- [93] U. Baur, J. A. M. Vermaseren, and D. Zeppenfeld, Nucl. Phys. **B375**, 3 (1992).
- [94] H. Spiesberger, Proceedings of the Workshop “Future Physics at HERA”, vol. I, eds. G. Ingelman, A. De. Roeck, R. Klancer, DESY (1996) 227.
- [95] C. Berger and P. Kandel, Prepared for Workshop on Monte Carlo Generators for HERA Physics, Hamburg, Germany, 27-30 Apr. 1998.
- [96] The H1 Collaboration, available at <https://www-h1.desy.de/icas/immanuals/h1rec/h1rec9/h1rec.html>.

- [97] M. Peez, B. Portheault, E. Sauvan, H1 Internal Note H1-01/05-616
- [98] C. Veelken, “H1NoneepBgFinder - Rejection of cosmic muon and beam-halo events in the H1OO framework”, H1 Internal Note H1-09/02-603.
- [99] J. Meyer. Guide for the H1 simulation program H1SIM. Internal Software-Note 03-11/89, DESY, 1989.
- [100] R. Brun *et al.* GEANT User’s Guide. CERN-DD/EE-84-1, 1987.
- [101] M. Peters. Die parametrisierte Simulation elektromagnetischer Schauer. Dissertation, MPI München, 1992.
- [102] M. Rudowicz. Hadronische Schauersimulation für den H1-Detektor. Dissertation, MPI München, 1992.
- [103] A. Dubak Measurement of the e^+p Neutral Current DIS Cross Section and the F_2 , F_L , xF_3 Structure Functions in the H1 Experiment at HERA., PhD thesis, München, 2003.
- [104] H1 Calorimeter Group, B. Andrieu *et al.* Beam tests and calibration of the H1 liquid argon calorimeter with electrons. Nucl. Instrum. Meth. **A 350**, pages 57-72, 1994.
- [105] S. Bentvelsen *et al.* Reconstruction of (x, Q^2) and extraction of structure functions in neutral current scattering at HERA. In W. Buchmüller and G. Ingelmann, Proceedings of the Workshop: Physics at HERA, volume 1, pages 23-40. DESY. 1992.
- [106] A. Blondel and F. Jacquet. In U. Amaldi, Proceedings of the Study of an ep Facility for Europe, page 391. DESY 79/48, 1979.
- [107] U. Bassler and G. Gernardi. On the Kinematic Reconstruction of Deep Inelastic Scattering at HERA. Nucl. Instrum. Meth., **A361**, pages 197-208, 1995.
- [108] U. Bassler and G. Gernardi. Structure Function Measurements and Kinematic Reconstruction at HERA. Nucl. Instrum. Meth., **A426**, pages 583-598, 1999.
- [109] R. Brun and F. Rademakers, Nucl. Instrum. Meth. **A389**, 81 (1997), available at <http://root.cern.ch>.
- [110] The H1OO Group, available at <https://www-h1.desy.de/icas/oop/current/oo/>.
- [111] P. Laycock, A Measurement of the Diffractive Reduced Cross Section $\sigma_r^D(3)$ at High Q^2 with the H1 Detector at HERA, PhD thesis, Liverpool, 2003.
- [112] P. Bruel, Recherche d’interactions au-dela du Modele Standard a HERA, PhD thesis, Orsay, 1998.
- [113] V. Andreev *et al.*, H1 Internal Note H1-06/98-544.
- [114] V. Andreev *et al.*, Nucl. Instrum. Meth. **A494**, 45 (2002).
- [115] H1 and ZEUS Collaborations, Electroweak Neutral Currents at HERA, H1prelim-06-142, ZEUS-prel-06-022, July 2006.

-
- [116] R. Placakyte First Measurement of Charged Current Cross Sections with Longitudinally Polarised Positrons at HERA, PhD thesis, München, 2006.
- [117] H1 Collaboration, Charged Current Interactions in ep Scattering at HERA With Longitudinally Polarised Electrons, ZEUS-prel-06-002, ICHEP06, July 2006.
- [118] ZEUS Collaboration, Measurement of High- Q^2 Charged Current Deep Inelastic Scattering Cross Sections With a Longitudinally Polarised Electron Beam at HERA, ICHEP06, July 2006.
- [119] H1 Collaboration, Neutral Current in e^\pm Scattering with Longitudinally Polarised Leptons, ICHEP06, July 2006.
- [120] W. Lorenzon [HERMES Collaboration], DESY-HERMES-97-68, 7th International Workshop on Polarised Gas Targets and Polarised Beams, Urbana, IL, 18-22 Aug 1997; F. Corriveau *et al.* [TPOL Polarimeter Group], “A Calibration of the HERA Transverse Polarimeter for the 2003/2004 Data”, available at <http://www.desy.de/pol2000/documents/documents.html>.
- [121] NuTeV Collaboration, D. Mason, NuTeV Strange / Antistrange Sea Measurements From Neutrino Charm Production, AIP, Conf. Proc. **792** (2005) 851.
- [122] E. Rizvi and T. Sloan, Eur. Phys. J. **C3** (2001) N2 [hep-ex/0101007]

Acknowledgements

At this point I want to express my sincere gratitude to all those I was working together with and I could profit from during my time as Ph.D student. I enjoyed the friendly and professional atmosphere in the H1 collaboration. In my opinion, working in such an environment is a real experience for a lifetime.

I would like to express my sincere gratefulness to my “doctor father” Prof. Dr. Christian Kiesling, for the critical reading of this thesis and valuable suggestions, for his support during my PhD years and his willingness in answering all my questions.

It is a great pleasure for me to thank Vladimir Chekelian for possibility to work on this thesis under his supervision. His support was invaluable, I have benefited considerably from his large experience and wide physics knowledge. I have learned a lot from daily work with him, during all those hours of discussions about physics at high Q^2 , low Q^2 and no Q^2 at all.

I thank all the members of the H1 collaboration, especially the members of the ELAN working group, who contributed with ideas and opinions to the analysis presented in this thesis. Among many others, I specially want to thank to Eram Rizvi, Emmanuel Sauvan, Zhiqing Zhang and Sasha Glazov.

Working at DESY has given me the opportunity to get to know many people whose friendship I value, and whose help and support has been indispensable. Particularly, I would like to express my thanks to Juraj Bracinik for his patience, willingness to help and answer questions, for interesting and fruitful discussions and of course for exceptionally nice tea. I also thank him for careful reading and helping me correcting the manuscript. Many thanks to Zuzana Rurikova and Adil Aktas for outdoor activities and having good times in the spare time.

For a friendly atmosphere, very pleasant to work in, I owe thanks to members of MPI H1 group: Biljana Antunović, Alexei Babaev, Ana Dubak, Günter Grindhammer, Andrej Liptaj, Bob Oliver, Sebastian Schmidt.

I owe special thanks to Ringailė Plačakytė for all her support and sympathy and for a beautiful time.

Last but not least I would like to thank my family and especially my parents, who gave me their love and continuous support during my whole life. Thank you very, very much.